

A parametric study of thermomechanical 3D finite
element simulations of subduction zones and its
application to the Central Andes using realistic
geometries

Dissertation

zur Erlangung des akademischen Grades doctor rerum naturalium
(Dr. rer. nat.)

vorgelegt dem Rat der Chemisch-Geowissenschaftlichen Fakultät der
Friedrich-Schiller-Universität Jena

von Diplom-Physiker Chris Salomon
geboren am 30.04.1986 in Jena

Gutachter:

1. PD Dr. Thomas Jahr, Institut für Geowissenschaften, FSU Jena
2. Prof. Dr. Kamil Ustaszewski, Institut für Geowissenschaften, FSU Jena

Tag der öffentlichen Verteidigung: 18.11.2020

Zusammenfassung

Der westliche Rand von Zentral-Südamerika zählt zu den am besten untersuchten Gebieten von Subduktionszonen. Die ozeanische Nazca-Platte taucht entlang eines, in Richtung des Ozeans konkav gekrümmten, Tiefseegrabens (Trench) unter die kontinentale Südamerikanische Platte ab. Diese Form des Trench ist einzigartig auf der Erde und führte zur Entstehung der Anden, dem größten magmatisch aktiven Orogen dass durch Subduktion entstand. Hier widme ich mich einem dreidimensionalen thermomechanischen Finite-Elemente-Modell des Nordchilenischen Kontinentalrandes zwischen 17°S - 24°S und 61°W - 78°W .

Im ersten Teil dieser Dissertation wird ein Referenzmodell erstellt, dessen Geometrie auf einem vereinfachten Querschnitt durch das Untersuchungsgebiet basiert. Es verwendet eine elasto-viskoplastische Rheologie und beinhaltet die Erzeugung von Scherwärme entlang des Plattenkontaktes. Das Modell umfasst eine Fläche von $1380\text{ km} \times 400\text{ km}$ und reicht bis in 400 km Tiefe. Es beinhaltet somit sowohl die Lithosphäre als auch Asthenosphäre. Der Subduktionsprozess wird für $1,6 \cdot 10^5$ Jahre simuliert. Diese Zeitspanne ist vergleichsweise kurz gegenüber den die Anden erzeugenden orogenen Prozessen, die seit mehr als 40 Millionen Jahren andauern. Das Referenzmodell ist daher nicht zur Untersuchung von Langzeitprozessen geeignet aber die Ergebnisse spiegeln den aktuellen Stand der Subduktion wieder und können mit Beobachtungen verglichen werden. Trotz der einfachen Geometrie stimmen die erhaltenen Hebungsdaten bereits in erster Ordnung mit Messungen der Paläohebung überein. Das Modell erlaubt zudem eine Abschätzung der zu erwartenden Randeffekte, was genutzt wird um das finale Modell von Zentral-Südamerika zu verbessern. In einer Langzeitrechnung, die $1,6 \cdot 10^6$ Jahre simuliert, wird Scherwärme beobachtet mit einem maximalen Temperaturanstieg von 45 K der konsistent mit Beobachtungen ist. Des Weiteren ist erkennbar, dass der Wärmefluss entlang der ozeanischen Platte ca. 1 Ma benötigt um ein stabiles thermodynamisches Gleichgewicht zu erreichen.

Das Referenzmodell nach $1,6 \cdot 10^5$ Jahren wird analysiert im Rahmen einer Parameterstudie. Demnach sind die wichtigsten Parameter Konvergenz- und Slab-Pull-Geschwindigkeit, Art und Anzahl der Elemente des Finite-Elemente-Gitters, Art der Rheologie, also elastisch, elasto-plastisch oder elasto-viskoplastisch, Kohäsion, Reibungskoeffizient, maximale Schwellspannung und Winkel der inneren Reibung. Aufgrund der geringeren Mächtigkeit der ozeanischen Kruste wird sie generell stärker von den Änderungen dieser Parameter beeinflusst als die kontinentale Kruste.

Die Anwendung einer Slab-Pull-Geschwindigkeit am unteren Ende des Slab, verursacht ein signifikantes Absinken des gesamten Modells um mehrere hundert Meter. Die Scherspannungen entlang der Reibungszone zwischen den Platten werden um mehr als 100 MPa verringert. Der Wärmefluss in den ozeanischen Abschnitten der Kopplungszone wird erhöht, hingegen in den kontinentalen Abschnitten um einen ähnlichen Betrag verringert. Schiefe Subduktion der ozeanischen Platte bewirkt deutliche Modelländerungen im Gebiet um die Reibungszone, jedoch geringe Variationen im restlichen Modell. Ein Wechsel der Elementart von hexaedrisch zu tetraedrisch als auch eine Erhöhung der Anzahl der Elemente, liefert konsistente Ergebnisse. Jedoch sind die Randeffekte für das aus Tetraedern bestehende Modell stärker als für das Modell mit einer erhöhten Anzahl von Hexaedern. Wird die Kohäsion im Modell von $20\text{ MPa} - 50\text{ MPa}$ auf $200\text{ MPa} - 500\text{ MPa}$ erhöht, beobachtet man mehr Subsidenz in der Kruste sowie eine leichte Verringerung von Scherspannung und Wärmefluss entlang der

Reibungszone. Eine Änderung der Kohäsion zu höheren oder niedrigeren Werten scheint das Modell kaum zu beeinflussen. Wird die Kohäsion gemeinsam mit dem Winkel der inneren Reibung variiert, so bewirkt eine Erhöhung des Winkels eine Verstärkung der durch die Kohäsion verursachten Änderungen, jedoch eine Verringerung des Winkels eine deutliche Abschwächung dieser Modelländerungen. Eine maximale Schwellspannung kann eingeführt werden um ein Bleib-Gleit (stick-slip)-Verhalten zwischen den Platten zu simulieren. Die entsprechenden Ergebnisse sind nahezu identisch mit einer Reduktion des Reibungskoeffizienten und verursachen ausschließlich Änderungen um die Reibungszone herum. In einer weiteren Untersuchung, wird die Viskosität durch Dislokationskriechen definiert anstatt unabhängig von Temperatur und Deformationsrate zu sein, wie in allen übrigen Modellen. Die Modelländerungen sind zunächst unwesentlich, werden aber verstärkt sobald der Winkel der inneren Reibung zusätzlich verringert wird.

Das Endmodell enthält eine realistische Geometrie und Dichteverteilung, in welche viele Randbedingungen aus den Gebieten der Geophysik, Geologie und Petrophysik eingegangen sind. Es beinhaltet jedoch keine Topografie und Bathymetrie. Ähnlich zum Referenzmodell reicht es bis in 410 km Tiefe und simuliert 100.000 Jahre des Subduktionsprozesses.

Die Geometrie hat einen großen Einfluss auf die Modellergebnisse. Die Krümmung des Trench, die schiefe Subduktion der Nazca-Platte sowie die Tiefe der kontinentalen Moho und Lithosphären-Asthenosphären-Grenze (LAB) verursacht signifikante Unterschiede zwischen den nördlichen und südlichen Teilen des Modells. Die durchschnittlichen kontinentalen Hebungsraten sind im Süden zwischen 1 mm/a und 2 mm/a höher im Vergleich zum Norden. Die maximale Hebungsrates liegt in der Nähe des Trench und beträgt 11 mm/a, während der mittlere Wert entlang der kontinentalen Kruste bei 1,0 mm/a bis 2,8 mm/a liegt. Bis zu einer Entfernung von 500 km östlich des Trench stimmen die berechneten Geschwindigkeiten in östlicher Richtung gut mit GPS-Messungen überein. Die Geschwindigkeiten in nördlicher Richtung sind dagegen in meinem Modell deutlich geringer im Vergleich zu den Beobachtungen. Die Verteilung von mitteltiefen Erdbeben mit hoher Magnitude ($M \geq 6,0$) im Untersuchungsgebiet korreliert gut mit den im Modell erhaltenen Verteilungen von Scherspannung und Deformationsrate. Diese Korrelation kann auch durch höhere numerische Ungenauigkeiten in bestimmten Regionen verursacht worden sein und ist daher womöglich besser oder schlechter als die vom Modell Vorhergesagte. Die Verteilung der Deformationsrate und des Wärmeflusses entlang der kontinentalen Platte zeigen Maximalwerte an denjenigen Orten an denen die größte Krustendicke und die höchste Position der LAB vorliegt und werden damit eindeutig von der Geometrie beeinflusst. Der Wärmefluss ist zudem im Süden höher als im Norden, aber die Deformationsrate zeigt keine bedeutenden Änderungen zwischen südlichen und nördlichen Teilen. Des Weiteren ist die Deformationsrate an der Oberfläche in guter Übereinstimmung mit dem Global Strain Rate-Modell und erreicht Werte bis zu $80 \cdot 10^{-9}/a$. In Ähnlicher Weise entspricht der Wärmefluss an der Oberfläche in meinem Modell gut der entsprechenden Verteilung von globalen Modellen in meinem Untersuchungsgebiet. Sein Maximalwert von $72,2 \text{ mWm}^{-2}$ liegt am magmatischen Bogen, ist aber geringer im Vergleich zu den globalen Modellen, da die Erzeugung von Schmelzen wie auch Konvektion nicht im Modell enthalten sind.

Das Finale Modell der Zentral-Südamerikanischen Subduktionszone ist teilweise in guter Übereinstimmung mit geologischen, geodätischen und geophysikalischen Beobachtungen. Trotz der Verwendung einer rein elastischen Rheologie ist die Nutzung einer realistischen Geometrie und Dichteverteilung für Finite-Elemente-Simulationen ein erfolgreicher Ansatz

für Subduktionszonen. Diese Art der Modelle kann dabei helfen, zukünftige geodynamische Modellierungen deutlich zu verbessern.

Summary

The western margin of central South America is one of the best studied regions of subduction zones. The oceanic Nazca plate descends beneath the continental South American plate at an oceanward concave trench. This form of the trench is unique on Earth and lead to the formation of the Andes, the largest magmatic active orogen caused by subduction. Here, I focus on a three-dimensional thermomechanical finite element model along the north Chilean margin between 17°S - 24°S and 61°W - 78°W .

In the first part of this thesis a reference model is created whose geometry is based on a simplified cross-section through the study area. It makes use of an elasto-viscoplastic rheology including shear heating along the plate interface. The model comprises an area of 1380 km by 400 km and reaches down to 400 km depth. It thus includes the lithosphere and asthenosphere. The subduction process is simulated for $1.6 \cdot 10^5$ years. This timescale is short compared to the orogenic processes forming the Andean mountain range, which are ongoing for more than 40 million years. The reference model is, therefore, not suitable for the study of long-term processes but the results reflect the recent state of subduction and can be compared to observations. Despite its simple geometry the uplift rates obtained are already in first-order agreement with measurements from paleoelevation. The model also allows for an estimation of the expected boundary effects, which is used to enhance the final model of central South America. In a long-term run simulating $1.6 \cdot 10^6$ years shear heating is observed with a maximum temperature increase of 45 K consistent with observations. It further reveals that the heat flux along the oceanic plate needs approximately 1 Ma to reach a stable thermodynamic equilibrium.

The reference model after $1.6 \cdot 10^5$ years is analyzed within the framework of a parametric study. According to this, the most important parameters are convergence and slab pull velocity, type and numbers of elements of the finite element mesh, type of rheology, i.e. elastic, elasto-plastic or elasto-viscoplastic, cohesion, friction coefficient and maximum threshold shear stress, and angle of internal friction. Because of its lower thickness the oceanic crust is generally more affected by changes in these parameters than the continental crust.

The application of a slab pull velocity at the lower end of the slab results in significant subsidence by several hundred metres of the overall model. The shear stresses along the zone of frictional coupling between the plates are reduced by more than 100 MPa. The heat flux within the oceanic parts of the coupling zone is increased but decreased by a similar degree within the continental parts. Oblique subduction of the oceanic plate causes substantial model changes around the zone of friction but only minor variations for the remaining model. A switch of the type of elements from hexahedrons to tetrahedrons as well as an increase in the number of elements yields consistent model results. However, the boundary effects for the model using tetrahedrons are more dominant than for a model with an increased number of hexahedral elements. If the cohesion within the model is raised from 20 MPa – 50 MPa to 200 MPa – 500 MPa more subsidence of the crust, and a slight decrease in shear stress and heat flux within the frictional coupling zone is observed. A change in cohesion to higher or lower values does not seem to affect the model results. If, however, the cohesion is simultaneously varied together with the angle of internal friction, an increase in the angle amplifies the model changes due to the variation in cohesion, while a decrease in the angle significantly weakens the respective model changes. A maximum threshold shear

stress can be introduced to simulate stick-slip behaviour between the plates. The results of this are almost the same as a reduction in the friction coefficient and only cause model variations around the zone of friction. In an additional analysis the viscosity is defined via dislocation creep rather than being independent of strain-rate and temperature as for all other models. While the model changes are insignificant they become important as soon as the angle of internal friction is additionally decreased.

The final model includes a realistic geometry and density distribution that is based on a well constrained density model, but does not consider topography and bathymetry. It consists out of 16 parts in total and only accounts for elastic deformations. Similar to the reference model it reaches down to 410 km depth and simulates 100,000 years of subduction.

The geometry has a major impact on the model results. The curvature of the trench, the oblique subduction of the Nazca plate as well as the depth of the continental Moho and lithosphere-asthenosphere boundary (LAB) cause significant differences between the northern and southern parts of the model. The average continental uplift rates are about 1 mm/a up to 2 mm/a higher in the south compared to the north. The maximum uplift rate occurs near the trench with 11 mm/a, while the mean value along the continental crust is between 1.0 mm/a and 2.8 mm/a. Up to a distance of 500 km east of the trench the simulated east velocities of the continental plate fit to GPS measurements. The north velocities, however, are much smaller in my model compared to observations. The distribution of high magnitude ($M \geq 6.0$) intermediate depth earthquakes in the study area correlates well with the acquired distributions of shear stress and strain rate obtained in my model. This correlation can also be caused by higher numerical uncertainties in specific regions and may, thus, be better or worse than predicted by the model. The distributions of strain rate and heat flux along the continental plate show maximum values at the positions of highest crustal thickness and highest places of the LAB and are, therefore, strongly affected by the geometry of the model. The heat flux is additionally higher in the south compared to the north, whereas the strain rate does not show significant differences between southern and northern parts. Furthermore, the onshore surface strain rate is in good agreement with the Global Strain Rate Model and reaches maximum values of $80 \cdot 10^{-9}/\text{a}$. Similarly the surface heat flux of my model is in accordance with the respective distribution for the study area proposed by global heat flux models. Its maximum values of up to 72.2 mWm^{-2} are found at the magmatic arc but are lower compared to global models because the generation of melts and convection are not included in my model.

The final model of the central South American subduction zone is partially in good agreement with geological, geodetical and geophysical observations. Despite the application of a purely elastic rheology, it is hence a successful approach to use a realistic geometry and density distribution for finite element simulations of subduction zones. These types of models can help to significantly improve future geodynamic models.

Contents

Zusammenfassung	II
Summary	V
1 Introduction	1
2 The subduction zone of Northern Chile	5
2.1 Geotectonics of the Andes	5
2.2 Forces acting throughout subduction	9
2.3 Density model of the study area	10
2.4 Seismic velocities	13
2.5 Surface kinematics	13
2.6 Strain Rate Model	14
2.7 Surface heat flow	14
3 Physical and numerical background	19
3.1 Conservation equations	19
3.1.1 Conservation of mass	19
3.1.2 Conservation of momentum	20
3.1.3 Conservation of energy	20
3.2 Small strain constitutive equations	21
3.2.1 Linear elasticity	22
3.2.2 Viscoplasticity	23
3.3 Return mapping algorithm	25
3.4 Numerical discretization	27
3.4.1 Finite element method	28
3.4.2 Abaqus	29
4 Reference model	30
4.1 Initial and boundary conditions	30
4.2 Surface interactions	32
4.3 Material parameters	34

4.4	Assumptions	37
4.5	Results	38
4.5.1	Short-term simulation	38
4.5.2	Long-term simulation	41
4.5.3	Summarizing interpretation	44
5	Parameter study	47
5.1	Changes in parameters	47
5.2	Results	49
5.2.1	Overview	49
5.2.2	Rheology	53
5.2.3	Yield function	54
5.2.4	Frictional coupling	56
5.2.5	Velocity	58
5.2.6	Viscosity	60
5.2.7	Mesh	62
6	Modelling South America's subduction zone	64
6.1	Construction of geometry and mesh	64
6.2	Model properties	65
6.3	Results	68
6.3.1	Final Stage	68
6.3.2	Temporal evolution	74
6.3.3	Slab Pull velocity	78
6.3.4	Discussion	80
7	Conclusions and Outlook	84
	References	87
	Appendix	i
A	Voigt notation and formulary	i
A.1	Voigt notation	i
A.2	Formulary for Drucker-Prager viscoplasticity	ii
B	Results of parameter changes	v

C Finite element modelling of the geodynamic processes of the central Andes subduction zone: A Reference Model	ix
Acknowledgements	xvi
Selbständigkeitserklärung	xvii

1 Introduction

The Earth's lithosphere is composed of several rigid and highly viscous plates moving relative to each other on top of a hotter asthenospheric mantle. Those plates slide past each other at transform faults and are continuously deformed while descending or subducting at trenches, while new plates are formed at mid-ocean ridges (Condie, 2011). There, adjacent plates diverge from each other and hot mantle material ascends to fill the gap (Turcotte and Schubert, 2014). As the hot material moves away from the ridge it cools down, densifies and thickens, forming a new plate. This process of seafloor spreading is counterbalanced by the process of subduction, where an oceanic plate descends below a less dense continental or oceanic plate. Because of friction and asperities between the plates and the surrounding hotter mantle material, large amounts of heat are generated resulting in dehydration and partial melting of the subducting plate material. The released volatiles rise up to the mantle wedge in the upper plate lithosphere, causing melting processes. Along the descending oceanic plate melting results in a two-layer decomposition with a thin $\sim 3 - 7$ km thick basaltic crust and a several tens of kilometres thick depleted lithospheric mantle (Condie, 2011; Cramer et al., 2019). Along the upper plate melted material rises up forming a volcanic belt at the surface. If the upper plate is oceanic the volcanoes are formed at the seafloor forming an island arc such as the Aleutian arc west of Alaska or the Izu-Bonin arc southeast of Japan. In case of a continental plate, the volcanoes grow onshore, for example east of the Cascadia subduction zone in North America. Large orogens develop landwards of the arcs such as the Andes in South America. The subduction process usually leads to strong earthquakes (subduction megaquakes) and all of the largest ones measured so far, i.e. South Chile 1960 ($M_W=9.5$), Alaska 1964 ($M_W=9.2$), Sumatra 2004 ($M_W=9.1$), Tohoku 2011 ($M_W=9.1$), did occur at the frictional interface of subduction zones.

The Andes are one of the largest orogens on Earth with a North-South extension of about 8000 km, a width of up to 800 km, and heights of up to 7 km. They are the result of the subducting oceanic Nazca plate below the continental South American plate leading to some of the strongest earthquakes measured so far, e.g. the Valdivia and Maule earthquake in 1960 and 2010 in South Chile with magnitudes of $M_W=9.5$ and $M_W=8.8$, respectively. Although the convergence rates differ only slightly (6.0 – 7.9 cm/a, Syracuse et al., 2010) and the azimuth of movement of $\sim 74^\circ$ (e.g. Norabuena et al., 1998) is almost constant along-strike (N-S), there are considerable variations in several geophysical and geological features such as rheology, plate geometry, volcanism, topography, and tectonics. This is unique to the subduction zone of South America (e.g. Hoffmann-Rothe et al., 2006; Oncken et al., 2006; Warren, 2014; Horton, 2018).

The main parameters that control these features are still debated. The most promising are (see for example Ramos, 2010; Sepulveda et al., 2015): length of the Wadati-Benioff zone, relative convergence rate, age of the descending slab, slab dip angle, direction of magmatic mantle flow, absolute motion of the overriding plate, slab retreat, climatic conditions and frictional coupling between the Nazca and South American plate. Temporal variations in those parameters during ongoing subduction resulted in highly variable rates of uplift and shortening since ~ 50 Ma (see also section 2.1). The collision with oceanic ridges, such as the Juan-Fernandez ridge or the Nazca ridge, additionally resulted in local changes of stress

and tectonics (Ramos and Kay, 1992; Gutscher et al., 2000; Yañez et al., 2001; Ranero et al., 2006; Kay and Coira, 2009).

The main goal of the present work is, thus, to find a suitable set of parameters to be used for a realistic numerical simulation of the actual state of the subduction process. Within the framework of a parametric study, the impact of the parameters on the model controlling shear heating, uplifting, and state of stress and deformation is analyzed. This information is used to define the parameters for a model with realistic geometries of a region in northern Chile between 17°S–24°S (fig. 1.1). The area includes a concave trench, a significant relief comprising the Altiplano-Puna plateau being one of the biggest and highest plateaus on Earth, a high crustal thickness of about 60 km on average (Assumpção et al., 2013), and an age of the subducting Nazca plate of about 50 Ma (Müller et al., 2008). Furthermore, a lot of research has been done (e.g. Oncken et al., 2006) concerning the physical and geological properties of the region, being essential to define a sufficiently realistic numerical model.

Due to the size and complexity of subduction zones, field observations can only cover very small parts of the regions of interest. Laboratory experiments can be scaled to apprehend larger structures, however, they are only able to consider near surface processes with comparatively high strain rates of 10^{-6} s^{-1} compared to typical strain rates of 10^{-15} s^{-1} in reality (see Karato, 2010). Numerical modelling, however, is capable to simulate large structures over long time periods under realistic conditions. Nevertheless, this is restricted by hard- and software capabilities making it impossible to take into account every physical or chemical aspect at unlimited precision. Therefore, every numerical simulation is concentrated on specific features of the region of interest.

Several numerical studies about the subduction zone of central South America are available. For example Sobolev and Babeyko (2005) studied the Cenozoic tectonic shortening of the South American plate. Among other aspects, they found that a model with a thick continental crust in the backarc and a friction coefficient of ≈ 0.05 reproduces the Andean orogeny in the long-term range. Hampel and Pfiffner (2006) established that upper plate motion together with a frictional coupling of the plates is essential for modelling of topographically high mountain belts, such as the Andes. Kellner (2007) developed 2D-thermal and 3D-mechanical models of the study area up to a depth of 200 km using simple geometries to study the effects of different model parameters on the deformation of the Chilean fore-arc. Based on this, she investigated a model that is consistent to first order observations. Babeyko and Sobolev (2008) used a refined 2D-thermomechanical model of Sobolev and Babeyko (2005) and found two compressional as well as one extensional zone within the slab. Bonnardot et al. (2008) analyzed the effects of oblique subduction using a 3D-mechanical model. Convex plate boundaries cause an accumulation of the subducted material beneath the upper plate inducing uplift, while in case of concave boundaries the material escapes and the fore-arc region subsides. Gerbault et al. (2009) performed a 2D-parametric study to identify the rheological parameters corresponding to models describing different regions of the Andean subduction zone. They showed that the weaker the continental crust is, the broader the developing upper-plate orogen will be. Applied to South America, they hence concluded that the strength of its fore-arc crust increases from north to south. Zeumann and Hampel (2015) studied the tectonic evolution of fore-arcs affected by ridge subduction with the help of 3D-mechanical models. Their results showed that displacement and strain fields above migrating and non-migrating ridges tend to be asymmetric with respect to the position of the ridge axis, unless both ridge and plate convergence direction are perpendicular to the trench.

However, these studies were either interested in the long-term evolution of the subduction process or were only interested in certain parts of the involved regions such as ridges or did only consider the continental plate. Zeumann (2013), Gutknecht et al. (2014), and Zeumann et al. (2014) used a 3D density model of the study area of the present thesis to create a 3D-mechanical model with realistic geometry (see section 2.3). They assumed an initial lithostatic pressure and simulated the subduction process for a geologically short time scale to model the present state of subduction in the Nazca and South American plate. One of their main results was a good correlation between the computed stress distribution and the distribution of large earthquakes in the corresponding area. Although they did not include temperature and mainly considered elastic material behaviour, they found good correlations between observational data and numerical results.

In this thesis a similar but extended approach as in Zeumann (2013) is pursued. Using a recent 3D density model of the central Andes, a realistic geometry is created for use in a dynamic thermomechanical subduction simulation. The model will include a gravitational force, friction as well as shear heating between the upper and lower plate, radiogenic heat production along the continental crust and elasto-viscoplastic deformations depending on the recent state of deformation and temperature. It simulates the subduction process for about 10^5 years down to 410 km depth and thus includes the continental and oceanic lithosphere and asthenosphere. Furthermore, the oceanic Nazca plate is supposed to move towards the northeast (fig. 1.1) resulting in oblique convergence at a concave trench. Due to the use of a realistic geometry, the continental crust thickens towards the back-arc.

The simulated timespan of 10^5 years is short compared to typical tectonic processes lasting over several millions of years. Therefore, the overall geometry will be almost fixed and temperature changes due to forced convection induced by plate movements are expected to be very small. The final temperature distribution is consequently determined by the initial distribution and may not reflect a recent state. However, the distributions of heat flux, stress, strain, and movement are considered to reflect the latest state of subduction in the study area and can be compared to observations.

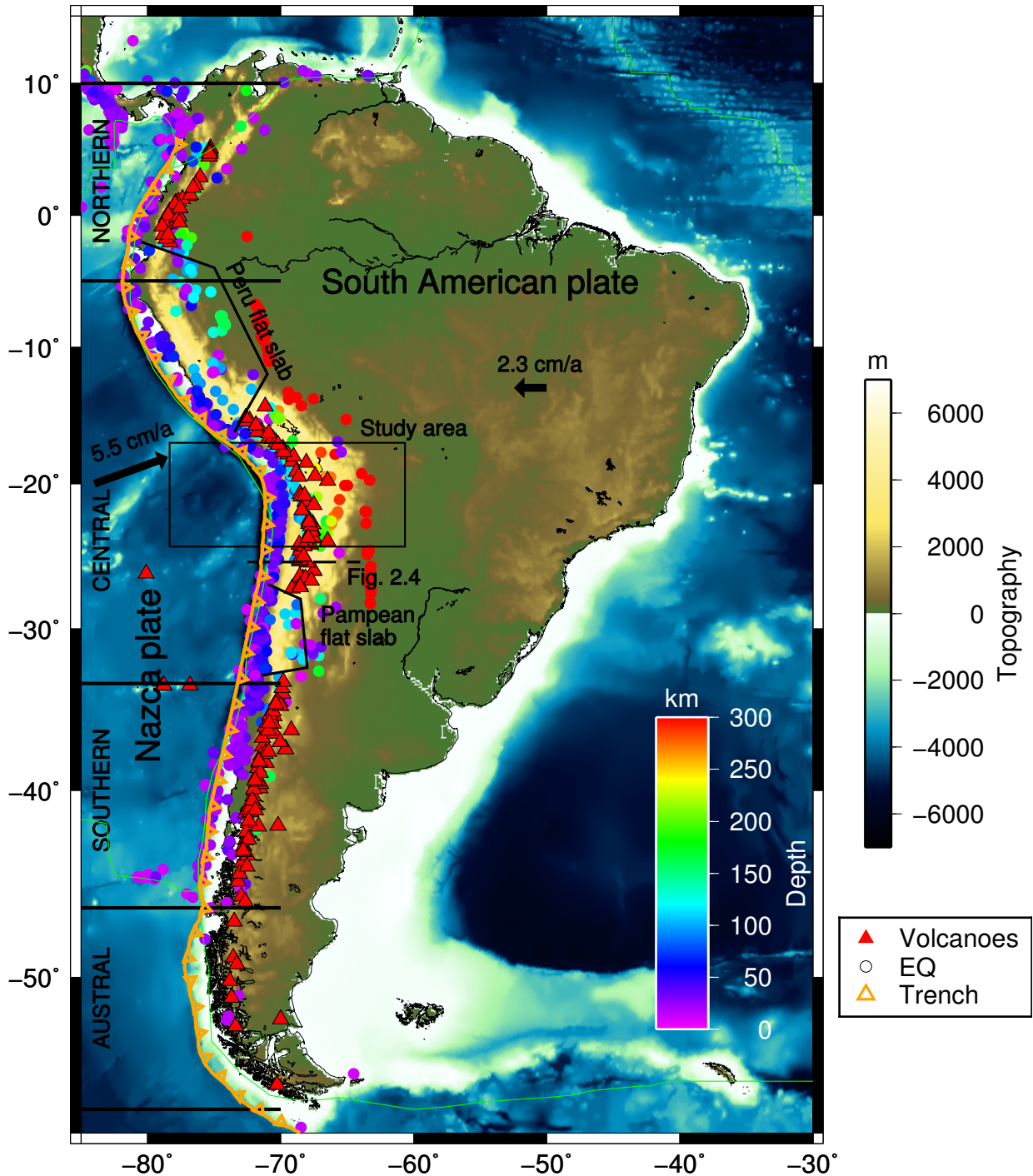


Figure 1.1: Topographic map (ETOPO5; National Geophysical Data Center, 1993) of South America. The rectangle marks the area under investigation, red triangles denote volcanoes (<https://www.ngdc.noaa.gov/hazard/volcano.shtml>), circles show earthquakes with magnitudes ≥ 6.0 since 1960-01-01 (USGS), green lines show the plate boundaries (DeMets et al., 1994), the orange line shows the position of the trench, black arrows indicate the plate velocities (Kremer, 2009), and the dashed line shows the approximate position of the cross-section in figure 2.4. The subduction zone is subdivided into the four segments Northern, Central, Southern, and Austral (see section 2.1). The outlines for the Peru and Pampean flat slab regions are chosen according to Ramos and Folguera (2009).

2 The subduction zone of Northern Chile

Numerical simulations always suffer from the fact that they can only be as reliable as the worst known model parameters for the region of interest. Nevertheless, they allow for an estimation of several observables at once at a regional scale, which would otherwise be impossible. The following chapter summarizes the most important tectonic features of the study area in northern Chile. After a brief review of the main driving forces a description of the geometric and density model to be used for the final model is given. In association with the seismic velocities for the region of interest the elastic properties are determined, defining the major deformations to occur throughout the simulation. The remaining sections provide an overview of the surface kinematics, strain rate and heat flow that will be compared with the final model results of this study for the purpose of evaluating and interpreting the outcome of the numerical model.

2.1 Geotectonics of the Andes

The Andean mountain belt at the western coast of South America has formed due to the subduction of the oceanic Nazca plate underneath the continental South American plate since at least 200 Ma (e.g. Pardo-Casas and Molnar, 1987; Mpodozis and Ramos, 1989; Somoza, 1998; Sobolev and Babeyko, 2005). This lead to a highly segmented margin with strong along-strike variations in e.g. topography, tectonics, volcanism, and subduction geometry (e.g. Isacks, 1988; Mpodozis and Ramos, 1989; Kley et al., 1999; Stern, 2004; Oncken et al., 2006; Alvarez et al., 2019), separating the Andean Cordillera into a northern (10°N - 5°S), central (5°S - 33.5°S), southern (33.5°S - 46.5°S), and austral (46.5°S - 56°S) part (fig. 1.1; Tassara, 2005). The central Andes reach about 7 km in height and 800 km in width (fig. 1.1). The Alitplano-Puna plateau, as one of the most prominent features, is the second largest and highest plateau on Earth, but its formation is still debated (e.g. Oncken et al., 2006; DeCelles et al., 2015). From the centre of the study area the age of the oceanic lithosphere decreases to the North and South to near 0 Ma (fig. 2.1; Müller et al., 2008), while topographic height and width decrease as well reaching a minimum throughout the austral part (< 150 km width, < 2500 m height).

The development of relative plate motion of the Nazca plate with respect to stable South America has been studied by Pardo-Casas and Molnar (1987) and Somoza (1998). According to them, the convergence rate during the middle Eocene and early Oligocene ($\approx 50 - 26$ Ma) varied between $5 - 10$ cm/a in SW-NE direction with an almost constant obliquity of about 40° . At around 25 Ma the foremost Farallon plate broke up into the Nazca and Cocos plates (Lonsdale, 2005), leading to a sudden change in direction with an obliquity of 10° and an increase in velocity to 15 cm/a for about 5 Ma. Since early Miocene (< 20 Ma) the convergence rate has its present value of ≈ 7.5 cm/a at an obliquity of 20° (Silver et al., 1998; Norabuena et al., 1999; Angermann et al., 1999; Vigny et al., 2009) (fig. 2.2).

The central Andean segment is subdivided into the three trench parallel tectonic units fore-arc, magmatic arc, and back-arc (fig. 2.4; Tassara et al., 2006). The fore-arc is comprised of

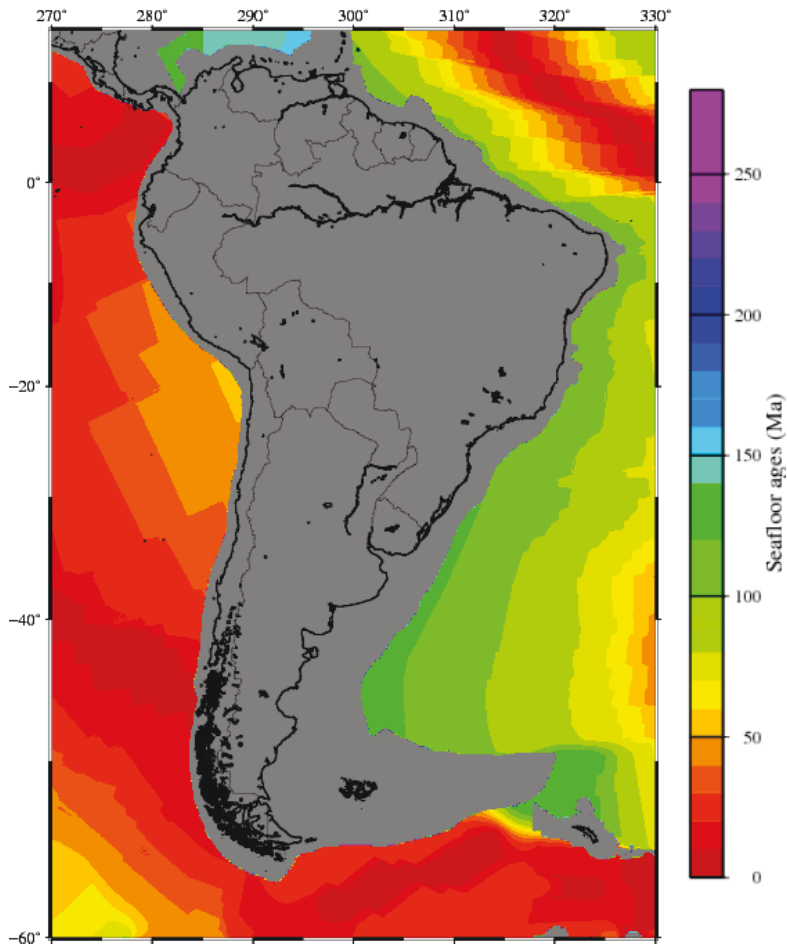


Figure 2.1: Age of the oceanic seafloor (from Müller et al., 2008)

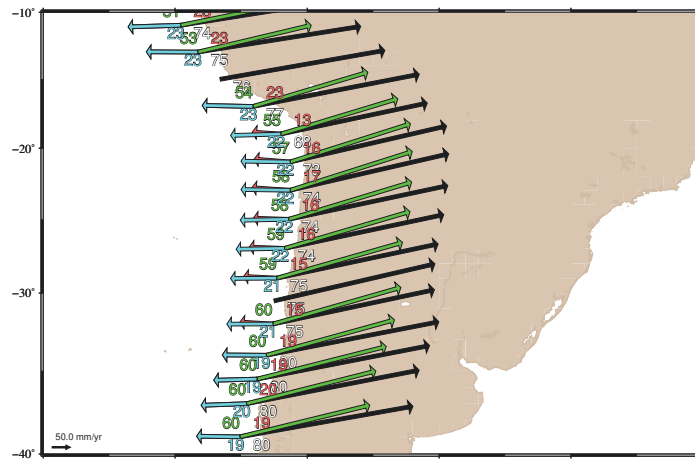


Figure 2.2: Plate velocities throughout the central Andean subduction zone. Black arrows show subduction velocity, trench absolute motion given in red, upper plate absolute motion in blue, subducting plate absolute motion in green. The velocities are given according to the reference frame GSRM-APM1 of the global strain rate model project (Kreemer, 2009). Figure generated with Submap 4.3 (Heuret and Lallemand, 2005).

the 1 – 3 km high Coastal Cordillera, the longitudinal valley, and the Precordillera (fig. 2.3) with altitudes up to 4 km. Along the Coastal Cordillera and Precordillera the more than 1000 km long trench-parallel Atacama Fault Zone (AFZ) and Precordilleran Fault System (PFS, also referred to as Domeyko fault system) are located. Both are relatively inactive in terms of seismicity since the Neogene with slip rates below 1 mm/a (Dewey and Lamb, 1992; Hoffmann-Rothe et al., 2006; González et al., 2015) and while the AFZ was formed during the late Jurassic (163 – 145 Ma) along the magmatic arc, the PFS initiated in the late Eocene (37 – 34 Ma) (Scheuber and Andriessen, 1990; Reutter et al., 1996).

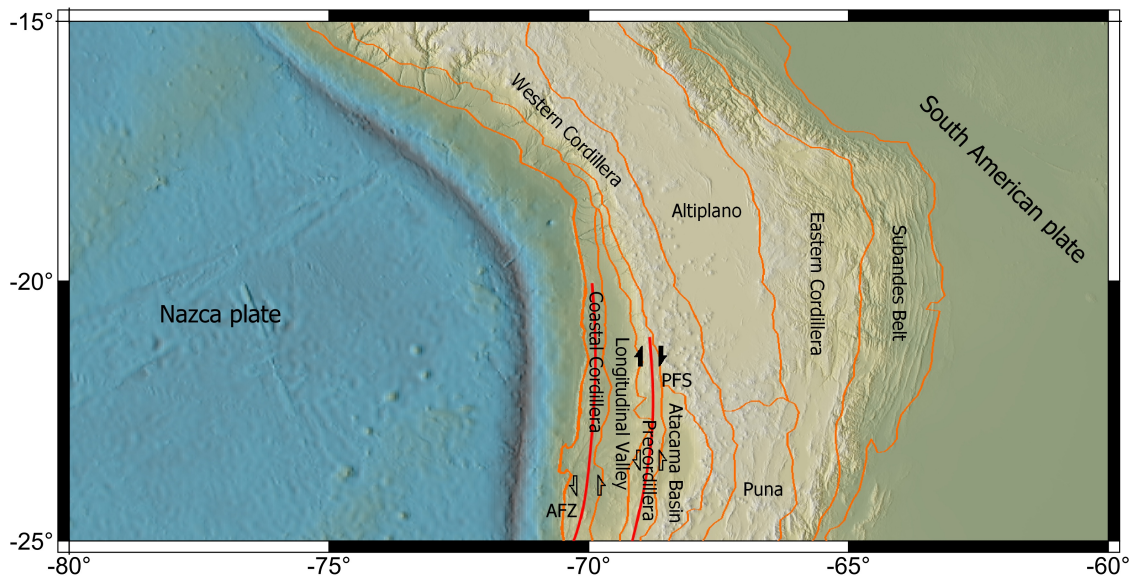


Figure 2.3: Major tectonic provinces after Mpodozis and Ramos (1989). AFZ-Atacama Fault Zone, PFS-Precordilleran Fault System after Hoffmann-Rothe et al. (2006).

The AFZ is mainly composed of left-lateral strike-slip faults ranging from meter to kilometer scales (Mitchell and Faulkner, 2009). Its peak activity is dated at ~ 150 Ma and ~ 126 Ma (Scheuber et al., 1995) and was subjected to heating and fluid infiltration along the magmatic arc that triggered localized deformation. In the late Cretaceous (100 – 66 Ma) the magmatic activity migrated further to the east and the type of deformation changed from ductile to brittle sinistral (left-lateral) strike-slip (Brown et al., 1993; Taylor et al., 1998). During the Neogene (23 – 2.5 Ma) parts of the AFZ have been reactivated due to the uplift of the Coastal Cordillera. Nowadays the fault zone is dominated by normal faults and some regional sinistral and local dextral (right-lateral) strike-slip movements (e.g. Delouis et al., 1998; Pelz, 2000; González et al., 2003; Allmendinger and González, 2010). The most recent deformations are dated to ~ 400 ka and ~ 5 ka (González et al., 2006; Cortés et al., 2012).

The PFS is a complex system of steeply dipping strike-slip, normal, and reverse faults. It is similar in length to the AFZ and has a width of 40 km to 60 km (Reutter et al., 1991; Reutter et al., 1996). It has been active since the late Eocene (34 – 38 Ma) within the Eocene-Oligocene magmatic arc and controlled the formation of some of the largest porphyry copper deposits on Earth (Ossandón et al., 2001). Initially a dextral strike-slip movement was followed by several reactivations showing a sinistral displacement associated with lower convergence rates (Lindsay et al., 1995; Reutter et al., 1996). Within the Neogene the sense of movement switched to normal and dextral strike-slip (Tomlinson and Blanco, 1997). The

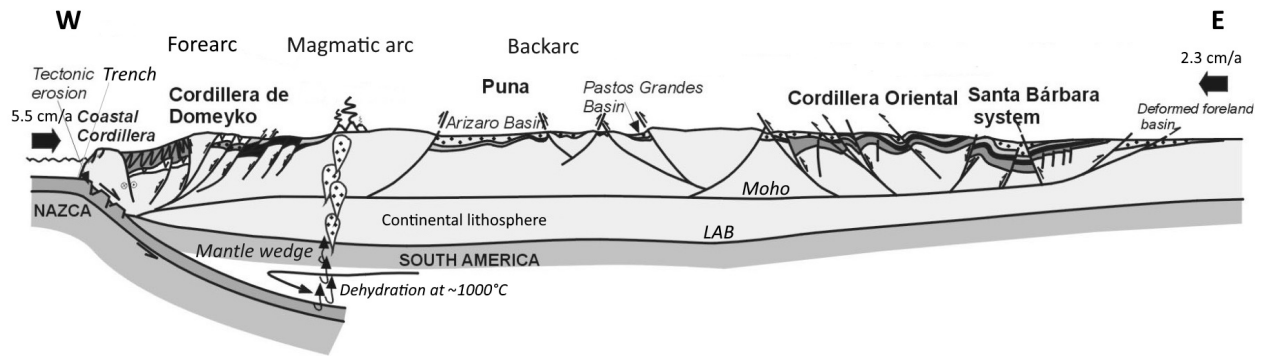


Figure 2.4: Schematic cross-section through the Central Andes at 25.5°S modified from Muñoz et al. (2005). Shown are the main tectonic provinces including the major fault zones within the fore-arc and continental hinterland. Moho marks the Mohorovičić discontinuity and LAB the lithosphere-asthenosphere boundary.

present-day seismic activity shows that the fault system includes dextral- and reverse-faulting kinematics (Salazar, 2011; Bloch et al., 2014).

The magmatic arc contains the Central Andean Volcanic Zone on top of the Western Cordillera reaching a maximum elevation of about 7 km at 32.5°S . In the northern and southern parts of the subduction zone flat subduction is observed (fig. 1.1) with dipping angles of $5^{\circ} - 10^{\circ}$ at intermediate depths (70–120 km), whereas normal subduction ($\sim 30^{\circ}$ dip) occurs between $15^{\circ} - 27^{\circ}\text{S}$ (e.g. Tassara, 2005; Espurt et al., 2008). Within the flat subduction regions, gaps in the volcanic arc are observed where no volcanism occurs (fig. 1.1). According to Gutscher et al. (2000), Gutscher et al. (2000) and Gutscher (2001) the low dipping angle of flat subduction displaces the asthenospheric wedge away from the trench, decreasing the temperature in both plates. Therefore the strength of the upper plate as well as the width of the seismogenic zone (Tichelaar and Ruff, 1993; Oleskevich et al., 1999) increases, resulting in a volcanic gap. East of the Western Cordillera lies the Altiplano-Puna plateau with a mean elevation of 3800 m (Tassara, 2005). Here the Andean orogen is up to 700 km wide with a 70–75 km thick crust (e.g. Yuan et al., 2000; ANCORP Working Group, 2003). The back-arc east of the Altiplano-Puna region consists of the 4–6 km high Eastern Cordillera and the shallower Subandean ranges.

The central segment is also a prominent example of subduction (also: tectonic) erosion (e.g. Kukowski and Oncken, 2006; Stern et al., 2011; Horton, 2018). The subducting Nazca plate removes crustal material from the fore-arc of the South American plate which is seen by several characteristic features. For example the low sediment thickness of less than 300 m (Straume et al., 2019), the lack of an accretionary wedge (Kulm et al., 1977; Scholl and von Huene, 2007), a high roughness of the Nazca plate (von Huene et al., 1999; von Huene and Ranero, 2003) or the eastward migration of the volcanic arc (Rutland, 1971; Stern, 1991) are indicators for subduction erosion. It is a fundamental process to recycle the continental material back into the Earth's mantle. Frontal erosion takes place at the trench and, thus, at the tip of the fore-arc. Basal subduction erosion removes material from the base of the overriding fore-arc (Kukowski and Oncken, 2006). Most of this material is transported deep into the mantle, however, some of it may be reattached via crustal underplating as suggested by Adam and Reuther (2000) for the central Andean margin south of 14°S .

The amount of shortening of the overriding South American plate can yield insights into the formation of the Andean orogen and the structure of the Nazca slab. Tectonic reconstruc-

tions and balanced cross sections allow to identify deformation patterns during the temporal evolution throughout the entire orogen (e.g. Oncken et al., 2006; Schepers et al., 2017). In general the maximum amount of shortening during the last ~ 50 Ma is found along the central Altiplano-Puna plateau reaching up to 420 km (Schepers et al., 2017) decreasing to about 150 km to the north and south (e.g. Kley and Monaldi, 1998; Oncken et al., 2006; Arriagada et al., 2008; Eichelberger and McQuarrie, 2015; Schepers et al., 2017, and references therein). According to Oncken et al. (2006) the temporal evolution for the central Andean segment can be summarized as follows: The shortening in the Precordillera and Western Cordillera started 46 Ma ago with a rate of about 1 mm/a dropping to near zero at 30 Ma and reaching about 16 km of shortening. The western and central Altiplano were shortened by 1 – 30 km during the Oligocene (35 – 25 Ma) followed by a phase of lower shortening below 1 km during the early Miocene (25 – 20 Ma) and were shortened by 17 – 30 km during the late Miocene (20 – 10 Ma). The eastern Altiplano experienced the same stages of deformation but with generally lower rates of shortening. In the Eastern Cordillera the shortening continuously increased between 40 to 25 Ma reaching a maximum shortening rate of 9 mm/a but ceased between 12 – 8 Ma. At the same time the Subandean belt was initiated and shortened by 40 – 70 km. The present day shortening rate in the Subandes is in the range of 8 – 13 mm/a (Bevis et al., 2001; Brooks et al., 2011; Parks and McQuarrie, 2019).

At around 40 Ma the Western and Eastern Cordillera were separated by today's Altiplano-Puna plateau, which had an elevation of ~ 1 km (Lamb and Hoke, 1997; Lamb et al., 1997; Gregory-Wodzicki, 2000; Saylor and Horton, 2014; Armijo et al., 2015; Lamb, 2016). Until 25 Ma the plateau subsided to near sea-level, whereas the Eastern Cordillera rose up to an elevation of 2.5 – 3.5 km and the Western Cordillera experienced no significant uplift until ~ 16 Ma (e.g. Saylor and Horton, 2014; Lamb, 2016; Scott et al., 2018) at an elevation of ~ 2 km. At ~ 20 Ma and ~ 16 Ma the Altiplano-Puna plateau attained significantly higher uplift rates compared to the Cordilleras (Lamb, 2016) reaching near today's elevations together with the Eastern Cordillera at around 10 Ma, while the Western Cordillera was uplifted by 1 km since 10 Ma (Lamb, 2016; Scott et al., 2018). The resulting modern uplift rate is at around 0.1–0.2 mm/a from the coast up to the Precordillera increasing to 0.3 mm/a towards the Altiplano-Puna plateau (Gregory-Wodzicki, 2000; Kukowski and Oncken, 2006; Saylor and Horton, 2014; Melnick, 2016).

2.2 Forces acting throughout subduction

Nowadays there is an ongoing debate about the relative importance of forces driving and resisting subduction (e.g. Forsyth and Uyeda, 1975; Conrad et al., 2004; Bilek, 2008; Billen, 2008; Wessel and Müller, 2015). The major driving forces are ridge push, slab pull and slab suction. The ridge push force or gravitational sliding is due to the cooling and densification of the oceanic plate as it moves away from mid-ocean ridges. The slab pull force arises from the colder and denser subducting plate resulting in a negative thermal buoyancy and can be enhanced by the phase transition from olivine to the more dense spinel. Related to this is slab suction. Because of the lower temperature of the slab it is stiffer than the surrounding mantle material. On descending it induces a viscous corner flow in the mantle lifting the oceanic plate towards the surface. This in turn, balances the slab pull force keeping the plate at a finite descent angle (Stevenson and Turner, 1977; Turcotte and Schubert, 2014; Wessel and Müller, 2015). The resisting forces are due to the frictional coupling between upper and

lower plate, bending of the oceanic lithosphere and viscous shear forces at the base of the slab due to convection in the mantle.

The relative importance of these forces depends on the specific conditions of subduction such as age of the oceanic lithosphere, dipping angle of the slab, rheology, i.e. thermal and mechanical properties, as well as size and geometry of the involved plates and duration of subduction (e.g. Billen, 2008; Wessel and Müller, 2015). In the models to be presented ridge push and slab pull are considered to be the only driving mechanisms. Several authors (e.g. Forsyth and Uyeda, 1975; Conrad et al., 2004; Conrad and Lithgow-Bertelloni, 2004; Schellart, 2004; Turcotte and Schubert, 2014) state that slab pull may be the dominant driving mechanism being up to twice as high as the ridge push force. Conrad et al. (2004) and van Summeren et al. (2012) were furthermore able to reproduce the movement of certain tectonic plates without the use of ridge push forces. On the other hand, if the resistive viscous forces become large enough they may balance out the slab pull forces resulting in the ridge push force to become as important as slab pull (Coblentz et al., 1995; Sandiford et al., 1995; Lithgow-Bertelloni and Richards, 1998; van Summeren et al., 2012). In the present work the effects of ridge push and slab pull are investigated in section 5.2.5.

2.3 Density model of the study area

Various density models of the central South American subduction zone are available nowadays (Strunk, 1990; Kirchner et al., 1996; Kösters, 1998; Tassara et al., 2006; Prezzi et al., 2009; Tassara and Echaurren, 2012; Meeßen et al., 2018; Ibarra et al., 2019). While most of them are developed on a regional scale, the model provided by Tassara et al. (2006) and Tassara and Echaurren (2012) includes the overall central and most parts of the southern Andean segment between 5°S to 45°S. The model therefore reaches down to a depth of 410 km including the overall lithosphere and asthenosphere between 60°W to 85°W (fig. 2.5). This model was chosen for the present work because it allows to construct a large sized numerical model using a well known geometry down to the lithosphere-asthenosphere boundary for the overall study area.

The density model of Tassara and Echaurren (2012) is an upgraded version of Tassara et al. (2006) for the region between 18°S to 45°S with twice the resolution of Tassara et al. (2006) of about 25 km. To compute the Bouguer anomaly the Earth Gravitational Model 2008 (EGM2008; Pavlis et al., 2012) is used as well as seismic constraints incorporated in Tassara et al. (2006) and later constraints published until 2011. The EGM2008 contains terrestrial, altimetry-derived, airborne and satellite derived gravity data acquired over more than 20 years. It includes satellite data obtained by the Gravity Recovery And Climate Experiment (GRACE), the Digital Topographic Model DTM2006.0 (Pavlis et al., 2007), satellite altimetry-derived gravity anomalies derived at the Danish National Space Center (DNSC) and at Scripps Institution of Oceanography (SIO/NOAA). EGM2008 covers the entire earth's surface with a spatial resolution of ca. 10 km and has been released as a spherical harmonic representation being complete until degree and order 2159. The seismic data includes results from several local seismic networks, active source seismic profiles and teleseismic reflections acquired over the last 30 years. Many of these results were acquired in the framework of the collaborative research project SFB267 "Deformation Processes in the Andes". Further constraints come from the heat flow map provided by Hamza and Munoz

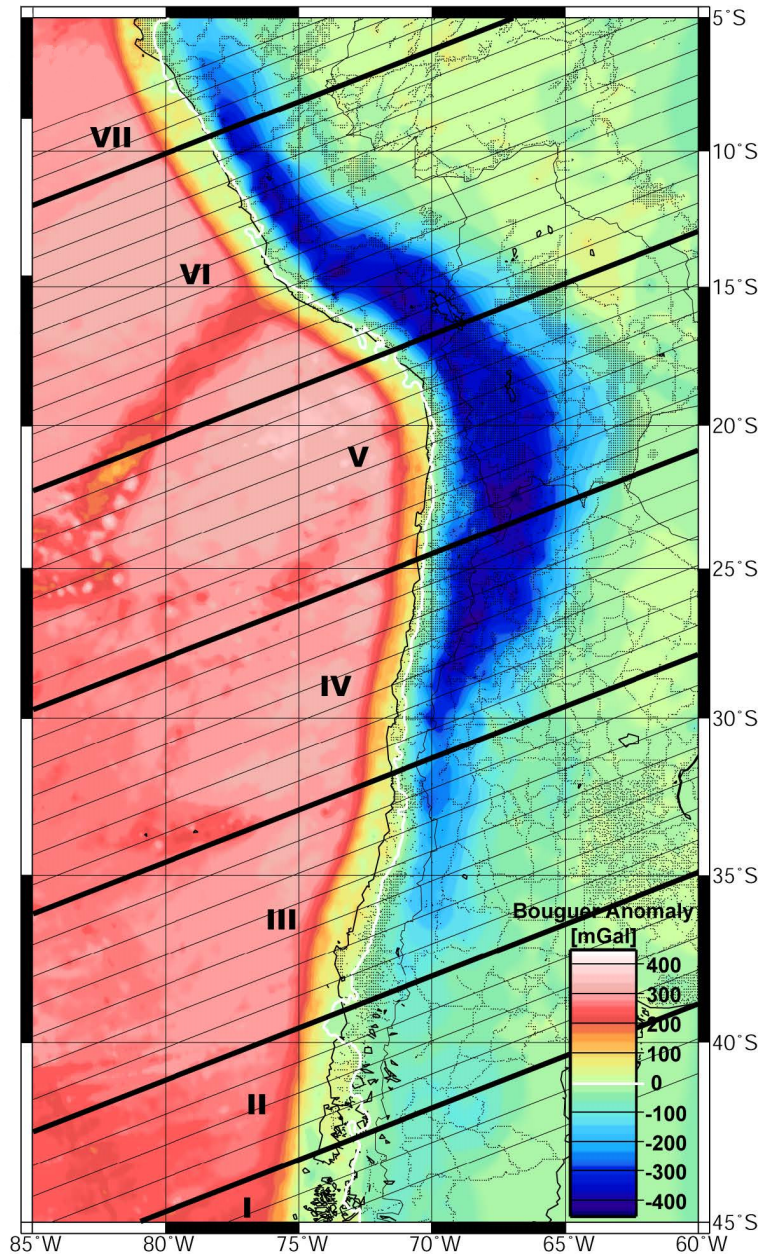


Figure 2.5: Map showing the Bouguer anomaly from Tassara et al. (2006): Thin lines mark the 43 vertical cross-sections of the density model. Thick lines correspond to cross-sections dividing the density model into several segments.

(1996) and different seismic tomography models (see Tassara et al. 2006 and Tassara and Echaurren 2012 for additional informations).

The density model is described by a number of three-dimensional bodies of constant density defining the structure of the Nazca plate, the slab and South American plate (fig. 2.6). The densities are based on a petrophysical analysis (Tassara, 2006) considering lateral variations of composition and pressure-temperature conditions. Before using the software IGMAS (Götze and Lahmeyer, 1988; Schmidt and Götze, 1998; Schmidt et al., 2010) to define those bodies, the density structure of the Tassara et al. (2006) model was triangulated to the region considered in Tassara and Echaurren (2012). Afterwards the Bouguer anomaly resulting

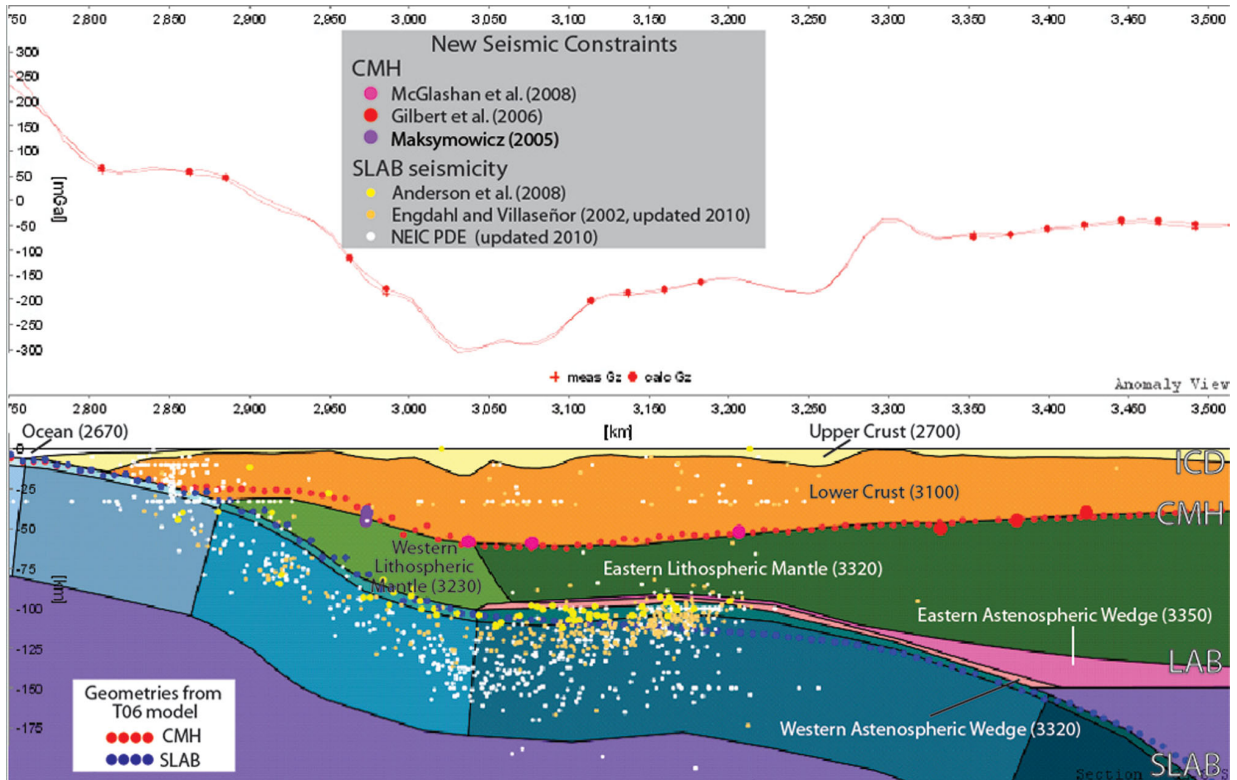


Figure 2.6: Cross-section of the density model at 32.8°S from Tassara and Echaurren (2012): In the upper panel measured and calculated Bouguer anomalies along the cross section are shown. The lower panel depicts the structure of the density model down to 200 km depth. Values of densities are shown in parentheses in units of kg m^{-3} . Circles denote new seismic constraints for continental Moho and slab upper surface used to modify the geometries of the model by Tassara et al. (2006).

from the density structure along 55 cross sections is computed. By iteratively changing the geometry of the bodies within IGMAS using the seismic constraints, the computed Bouguer anomaly is visually compared with the observed one until an optimal fit is found.

In comparison to Tassara et al. (2006) the differences in the Bouguer anomalies between the models are below the average uncertainty reported by Tassara et al. (2006). Furthermore the geometries are very similar within the study area of the present work. Only the depth of the continental Moho between 20°S to 22°S along the margin has been corrected by up to 20 km due to new seismic constraints. The models are thus in good agreement and because the average error in the Bouguer anomaly reported by Tassara et al. (2006) was ± 20 mGal the model by Tassara and Echaurren (2012) is expected to represent the structures of the subduction zone reasonably well.

2.4 Seismic velocities

The most important material parameters, besides the density of the rocks, are the Young's moduli E and Poisson ratios ν , which are defined as

$$E = \rho v_s^2 \frac{3v_p^2 - 4v_s^2}{v_p^2 - v_s^2}, \quad \nu = \frac{v_p^2 - 2v_s^2}{2(v_p^2 - v_s^2)} \quad (2.1)$$

with the density ρ and the seismic velocities v_p and v_s . Many studies determined the seismic velocities in Central South America during the 1990's within the framework of the projects CINCA 95 (Crustal Investigations off- and onshore Nazca/Central Andes; Patzwahl et al., 1999), ANCORP 96 (ANdean COntinental Research Program to image an active subduction zone; ANCORP Working Group, 1999; ANCORP Working Group, 2003) and SFB 267 (e.g. Rietbrock and Scherbaum, 1998; Schurr, 2001). Several active source seismic profiles were analyzed and arrays of seismic stations were installed between 20°S and 25°S. The seismic velocities used for the present work are taken from ANCORP Working Group (2003), Koulakov et al. (2006) and Dorbath et al. (2008). ANCORP Working Group (2003) collected the data results for the seismic reflection and refraction profiles at 21°S obtained during ANCORP 96 and CINCA 95 to cover a profile length of more than 800 km in total ranging from the trench up to the eastern boundary of the Altiplano-Puna plateau. Koulakov et al. (2006) used seismic velocities previously obtained by other authors and developed an inversion algorithm to compute the three-dimensional seismic structure in the area of 20°S to 26°S and 65°W to 71°W. Dorbath et al. (2008) used the seismic data of 2052 events collected by a seismic network consisting out of 43 stations situated near the coast between 18°S to 19.5°S. With this they were able to relocate the hypocentral positions of the earthquakes and similar to Koulakov et al. (2006) they received the 3D seismic structure of the subduction zone.

For the present work the P wave velocities down to a depth of 100 km provided by ANCORP Working Group (2003) are used for the oceanic crust and continental lithosphere. The S wave velocities as well as the remaining P wave velocities down to 200 km depth were taken from Koulakov et al. (2006) and Dorbath et al. (2008). Because the finite element model is divided into several parts each with constant material properties average velocities were chosen from these authors (fig. 2.7). Due to the lack of information below 200 km a P wave velocity of 8.5 km/s and S wave velocity of 4.9 km/s was used for the oceanic and continental asthenosphere. The material properties used for this study are given in table 6.1.

2.5 Surface kinematics

The use of Global Navigation Satellite Systems (GNSS like GPS or GLONASS) makes it possible to derive recent crustal deformations on a continental scale with high spatial resolution. The velocity model VEMOS2017 (Sanchez and Drewes, 2016; Drewes and Sanchez, 2017) describes the state of deformation on the South American continent and the Caribbean between January 2014 and January 2017. During this time 515 GNSS stations took measurements, which were used to derive the surface kinematics between 120°W, 55°S to 35°W, 32°N. A least squares collocation method was used to interpolate the station velocities to a $1^\circ \times 1^\circ$ continuous grid (Sanchez and Drewes, 2016).

The main input data are provided by the Geocentric Reference System for the Americas (Sistema de Referencia Geocéntrico para las Américas, SIRGAS). SIRGAS consists out of a core network of GNSS stations with good continental coverage and high long-term stability as well as several local networks for improved densification of the core network. Further data are provided by the International GNSS Service (IGS), UNAVCO and the US National Geodetic Service (NGS). To acquire a multi-year solution (fig. 2.8) at first daily solutions by all stations from NGS and UNAVCO and some stations of the SIRGAS core network are computed. Next the weekly station positions of all stations are derived and combined to a multi-year solution (Sanchez and Drewes, 2016). The average uncertainty is ± 1.0 mm/a in the north-south and ± 1.7 mm/a in the east-west direction. Maximum uncertainties up to ± 15 mm/a occur at the regions of recent strong earthquakes (e.g. near Maule in 2010, near Iquique in 2014).

2.6 Strain Rate Model

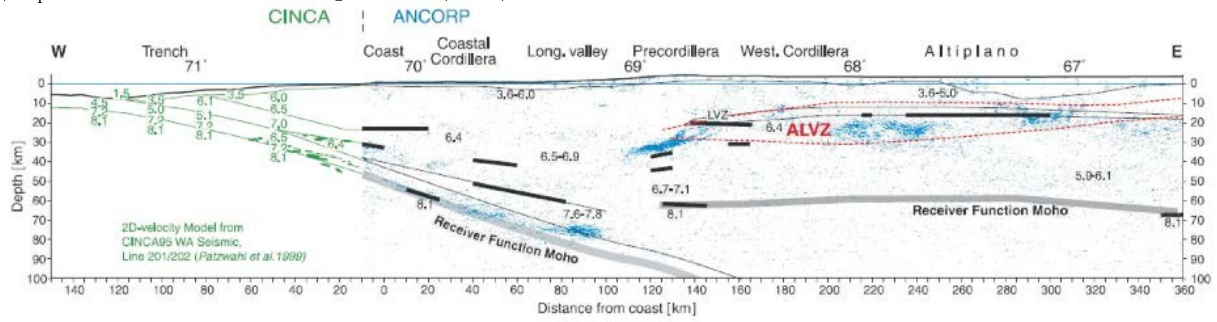
The tectonic plates are most often considered as rigid plates separated by narrow boundaries. This concept of plate tectonics is true for most cases but about $\sim 15\%$ of the Earth's surface are covered by diffuse plate boundary zones (Gordon and Stein, 1992). Modern day GNSS observations allow for the determination of velocity and velocity gradients all along the plate boundaries and provide constraints for plate motions and deformations. Kreemer et al. (2014) compiled a global strain rate model using more than 20.000 velocities gathered between January 1996 and December 2013. Most are GNSS derived velocities but also velocities derived from DORIS (Détermination d'Orbite et Radiopositionnement Intégrés par Satellite; Tavernier et al., 2006), VLBI (Very Long Baseline Interferometry), trilateration and submarine markers have been used (see Kreemer et al. 2014 for further information). The resolution of the mesh is 0.2° by 0.25° and covers 50 rigid plates and micro-plates. The strain rates (fig. 2.9) are computed using the method of Haines and Holt (e.g. Haines and Holt, 1993; Holt et al., 2000; Beavan and Haines, 2001) which further allowed Kreemer et al. (2014) to compute the standard deviations of their model. For the Global Strain Rate Model (GSRM) v2.1 (Kreemer et al., 2014) the velocities for some of the plates differ from previous models (Kreemer et al., 2003; Argus et al., 2010; DeMets et al., 2010; Altamimi et al., 2012). This is because Kreemer et al. (2014) neglected the translation rate of their reference frame origin, they did take care of stations affected by glacial isostatic adjustment (e.g. Whitehouse, 2018) more than previous studies, and used GNSS derived instead of geologically derived velocities. In comparison to GSRM v1 (Kreemer et al., 2003) the strain rates are in good agreement in the 1st order pattern. Along oceanic ridges, however, the rates are higher in GSRM v2.1. For GSRM v2.1 more tectonic plates were used and the mesh resolution has been increased resulting in a more refined local pattern of the strain rate.

2.7 Surface heat flow

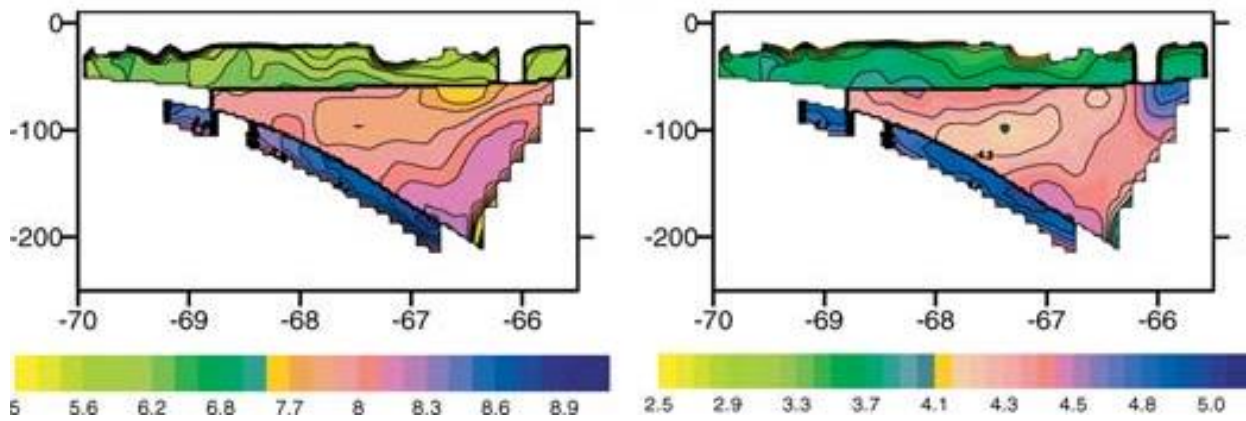
Measurements of the surface heat flow can yield insights into the Earth's interior dynamics. It is dependent on thermal conductivity, heat productivity such as radiogenic heating, and convective mantle flow. Studying the surface heat flow on a global scale is, therefore, important to understand the processes in great depths. Pollack et al. (1993) compiled a heat flow

database including about 25.000 observations. Up to now this database has grown to ca. 61.000 oceanic and terrestrial measurements and is available at <http://www.heatflow.org/> (see Hasterok and Chapman, 2008; Hasterok, in prep). Based on the database of Pollack et al. (1993) Lucazeau (2019) maintained the New Global Heat Flow (NGHF) database actually being the most complete database containing about 30.000 marine and 40.000 terrestrial measurements. The mean oceanic heat flow is $78.8 \pm 76.0 \text{ mWm}^{-2}$ and the mean continental heat flow $67.1 \pm 47.1 \text{ mWm}^{-2}$, while the mean oceanic heat loss is estimated to 23.78 TW and the mean continental heat loss is 14.90 TW. Because these data are unevenly distributed and do not cover the entire Earth's surface, Lucazeau (2019) applied the similarity method suggested by Goutorbe et al. (2011). A global grid with cell sizes of 0.5° by 0.5° is generated. The cells are categorized into several proxies for example age, elevation or distance to specific geological features. Two cells are similar if they belong to the same category. With this a weight is specified for each of the cells which is used to define the average heat flow and its standard deviation for the cells. The greater the number of proxies, the smaller the misfit between measurements and heat flow predicted by the similarity method (Lucazeau, 2019). However, with increasing number of observables the number of artifacts increases at positions where no heat flow measurements are available. The optimum number of observables was found to be 14 or 19 depending on which proxies were used (fig. 2.10). The results are consistent with previous studies (e.g. Pollack et al., 1993; Hamza et al., 2008; Goutorbe et al., 2011; Davies, 2013; Mareschal et al., 2017) although significant differences in oceanic heat flow are observed compared to Pollack et al. (1993) due to new measurement techniques. The differences decrease in average for plate ages younger than 65 Ma. For older oceanic plates previous heat flow models could not simultaneously explain subsidence and heat flow due to sparse data coverage at hot spots sites and large igneous provinces. Lucazeau (2019) did a Monte Carlo simulation of finite element models to find an optimal heat flow model with a constant heat flow of 36.4 mWm^{-2} at the base of a 114 km thick lithosphere and a mantle temperature of 1235°C .

a) v_p from ANCORP Working Group (2003)



b) v_p (left) and v_s (right) from Koulakov et al. (2006)



c) v_p (top) and v_s (bottom) from Dorbath et al. (2008)

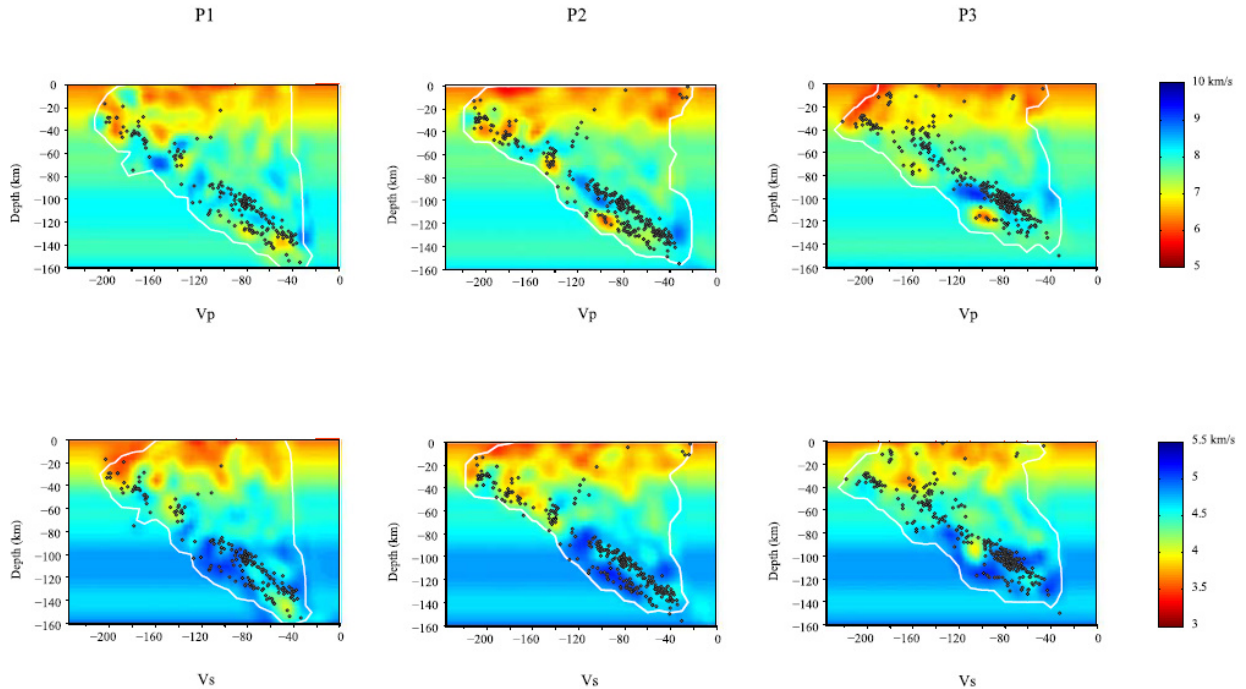


Figure 2.7: Seismic velocity models used throughout this study. a) P wave velocities at 21°S from ANCORP Working Group (2003), b) P and S wave velocities at 23.5°S from Koulakov et al. (2006), c) P and S wave velocities at three different profiles P1, P2, P3 between 18°S and 19°S from Dorbath et al. (2008).



Figure 2.8: Velocity field VEMOS2017 with respect to the South American plate from Drewes and Sanchez (2017).

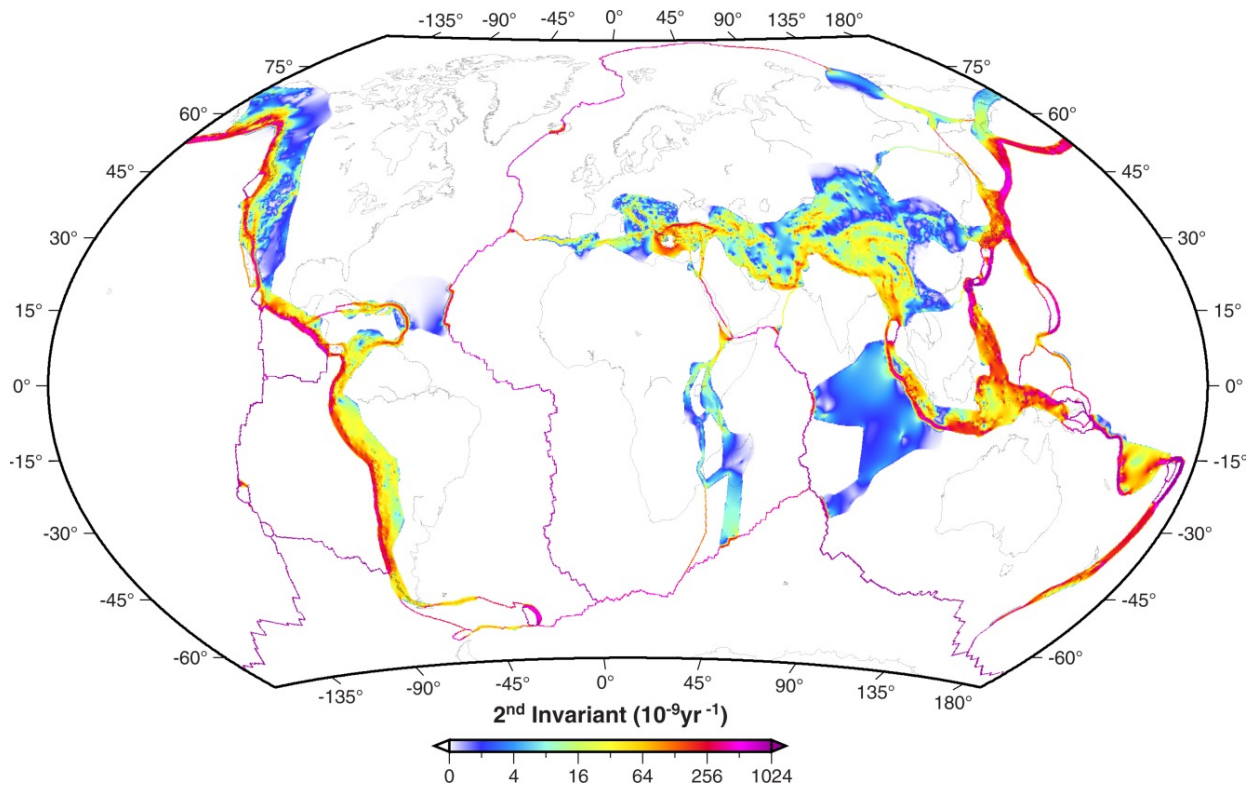


Figure 2.9: Second invariant of the strain rate field of the Global Strain Rate Model (GSRM) v2.1 from Kreemer et al. (2014). White areas represent rigid plates where no strain rates have been computed.

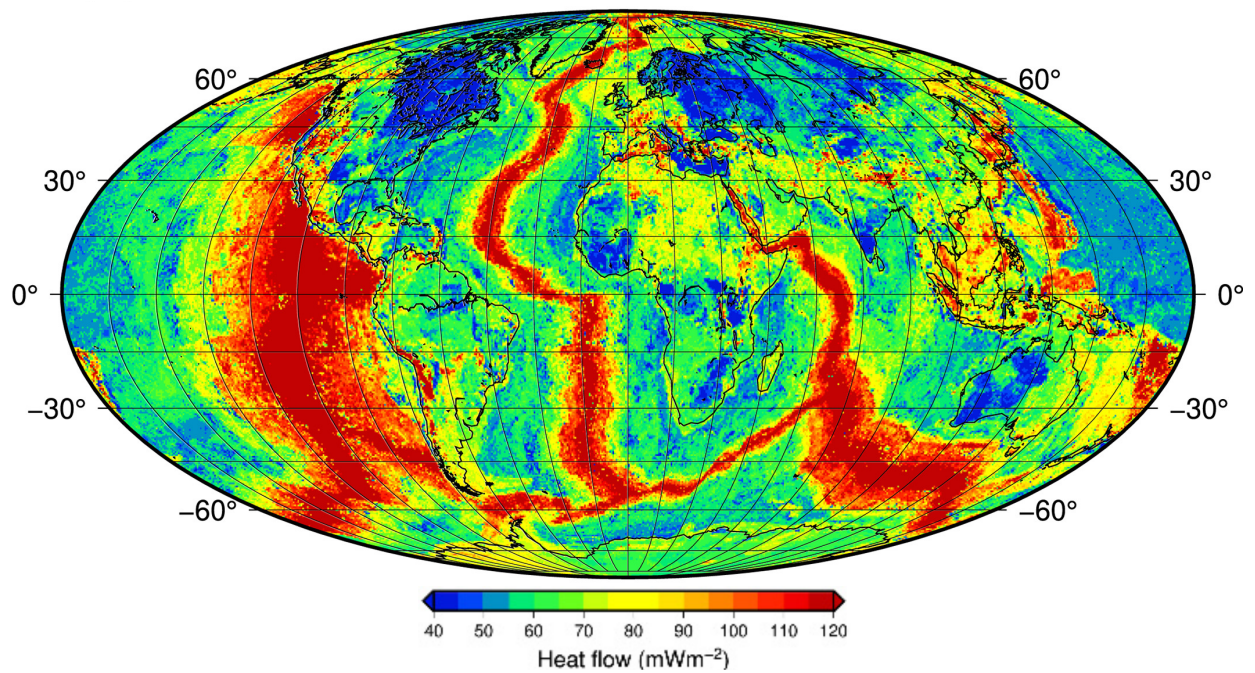


Figure 2.10: Map of global surface heat flow based on 14 observables adapted from Lucazeau (2019).

3 Physical and numerical background

To be able to numerically study subduction processes, the basic theory of continuum mechanics is presented. This includes the conservation equations as well as the material or constitutive equations describing the internal state of a body. The third part of this chapter is about the approximate, i.e. numerical, solution of these equations with the main focus on solving the constitutive equations via the return mapping algorithm.

3.1 Conservation equations

This section provides a short derivation of the conservation equations of continuum mechanics needed for this study, which are the fundamental differential equations defining the movement, deformation and temperature distribution of a physical object.

3.1.1 Conservation of mass

To achieve conservation of mass the amount of material moving through the surface ∂V of a volume V must equal the rate of change in mass inside the volume. The total mass is given by

$$M = \int_V \rho dV$$

while the amount of material flowing out of ∂V is given by

$$\int_{\partial V} \rho v_i dS_i$$

with the mass density ρ , the velocity components v_i of the moving material and the component in i -direction of the surface element dS_i . The conservation of mass is thus expressed as

$$\frac{dM}{dt} = \frac{d}{dt} \int_V \rho dV = - \int_{\partial V} \rho v_i dS_i$$

Using the divergence theorem of Gauß this results in

$$\int_V \left[\frac{\partial \rho}{\partial t} + \partial_i(\rho v_i) \right] dV = 0$$

from an Eulerian point of view, i.e. if we assume the volume to be fixed in space; herein $\partial_i := \partial/\partial x_i$ with the coordinate x_i in i -direction. This relation must hold for every arbitrary volume finally resulting in the *continuity equations*

$$\frac{\partial \rho}{\partial t} + \partial_i(\rho v_i) = 0 \tag{3.1}$$

3.1.2 Conservation of momentum

Now consider a fluid as a sample material, flowing through V . The force of the fluid acting on V is given by $-\int_{\partial V} p dS_i$, which according to Gauß' theorem is the same as

$$-\int_V \partial_i p dV$$

with the hydrostatic pressure p . Therefore $-\partial_i p$ is the force per unit volume acting on a volume element dV . By definition this force is equivalent to

$$-\partial_i p = \rho \frac{dv_i}{dt} + \rho f_i$$

where dv_i/dt denotes the material time derivative given by

$$\frac{dv_i}{dt} = \frac{\partial v_i}{\partial t} + (v_k \partial_k) v_i$$

and ρf_i is an external force such as gravity. For a more general approach we introduce the shear stress tensor τ_{ik} and replace the pressure by the stress tensor

$$\sigma_{ik} = -p \delta_{ik} + \tau_{ik}$$

resulting in

$$\rho \left(\frac{\partial v_i}{\partial t} + (v_k \partial_k) v_i \right) = \frac{\partial \sigma_{ik}}{\partial x_k} + \rho g_i \quad (3.2)$$

with the identity tensor δ_{ik} . Eqn. (3.2) is also known as *Eulers equation*.

3.1.3 Conservation of energy

The total energy decomposes into mechanical work and thermal energy. If P_W is the work per unit time (short: work rate) and P_Q the rate of increase of thermal energy (short: heat rate), conservation of energy requires that

$$P_W + P_Q = 0 \quad (3.3)$$

The work rate originates from forces acting on the surface ∂V and from external volume forces, i.e.

$$P_W = \int_{\partial V} \sigma_{ik} v_k dS_i + \int_V \rho g_i v_i dV$$

Applying the divergence theorem on the surface integral and using Eulers equation we have

$$P_W = \int_V \left[\rho \frac{\partial v_k}{\partial t} v_k + \sigma_{ik} \frac{\partial v_i}{\partial x_k} \right] dV$$

With the continuity equation one can show (e.g. Kennett and Bunge, 2008) that

$$\frac{\partial}{\partial t} \int_V \rho \psi dV = \int_V \rho \frac{d\psi}{dt} dV \quad (3.4)$$

for any scalar, vector or general tensor quantity ψ . Due to the fact that

$$\frac{\partial v_k}{\partial t} v_k = \frac{1}{2} \frac{\partial (v_k v_k)}{\partial t}$$

the mechanical work rate is given by

$$P_W = \int_V \left(\frac{\rho}{2} \frac{d(v_i v_i)}{dt} + \sigma_{ik} \frac{\partial v_i}{\partial x_k} \right) dV$$

The heat rate P_Q can as well be decomposed into components on the surface through heat conduction and volume sources. Heat conduction is defined via the heat flux vector q_i as given by Fouriers law

$$q_i = -\kappa \frac{\partial T}{\partial x_i}$$

with the thermal conductivity κ and temperature T , while a possible source for heat production H is radioactivity. Thus the heat rate is given by

$$P_Q = \int_V H dV + \int_{\partial V} \kappa \frac{\partial T}{\partial x_i} dS_i$$

or using the divergence theorem

$$P_W = \int_V \left(H + \frac{\partial}{\partial x_i} \left(\kappa \frac{\partial T}{\partial x_i} \right) \right) dV$$

The total energy is furthermore the sum of the kinetic and internal energy and its conservation thus implies

$$\frac{\partial}{\partial t} \int_V \rho u dV = \int_V \left(\sigma_{ik} \frac{\partial v_i}{\partial x_k} + H + \frac{\partial}{\partial x_i} \left(\kappa \frac{\partial T}{\partial x_i} \right) \right) dV$$

On using (3.4) the *conservation of energy* finally implies

$$\rho \frac{du}{dt} = \sigma_{ik} \frac{\partial v_i}{\partial x_k} + H + \frac{\partial}{\partial x_i} \left(\kappa \frac{\partial T}{\partial x_i} \right) \quad (3.5)$$

because the volume V is arbitrary.

3.2 Small strain constitutive equations

The constitutive equations are the material equations of continuum mechanics and establish a connection between stress and strain or strain rate. In this work the small strain approach is used, being valid for slowly deforming bodies and for deformations $\ll 100\%$. Because of the low velocities of tectonic plates of some cm/a typical strain-rates are on the order of 10^{-15} to 10^{-13} s^{-1} . Thus after 10^5 years, which is the time scale to be considered for this study, the strain is expected to be $\lesssim 10\%$ i.e. $\ll 100\%$. In large-scale geodynamical problems such as subduction zones, temperature leads to successive creep of rocks due to microphysical lattice defects. Therefore a viscoplastic type of deformation is added to account for inelastic deformations.

3.2.1 Linear elasticity

At the time $t = 0$ the position in i -direction of an element of the undeformed body is $r_i(t = 0) = x_i$. After a certain time t it is translated by $s_i(\vec{x})$ to

$$r_i(t) = x_i + s_i(\vec{x})$$

Now consider a neighbouring element at $x_i + dx_i$ translated by $s_i(\vec{x} + d\vec{x})$ to

$$r_i(t) + dr_i(t) = x_i + dx_i + s_i(\vec{x} + d\vec{x})$$

Because dx_i is infinitesimal small the difference in shift s_i is ds_i and therefore

$$dr_i(t) = dx_i + ds_i = dx_i + \frac{\partial s_i}{\partial x_i} dx_i = \left(\delta_{ik} + \frac{\partial s_i}{\partial x_i} \right) dx_i$$

with the deformation gradient

$$F_{ik} = \frac{\partial s_i}{\partial x_i}$$

From now on the Einstein summation convention will be used, i.e. repeated indices are implicitly summed over. The deformation of the element is characterized by the line element $ds_i ds_i = dr_i dr_i - dx_i dx_i$ given by

$$ds_i ds_i = 2\epsilon_{ik} dx_i dx_k$$

with the strain tensor

$$\epsilon_{ik} = \frac{1}{2} \left(\frac{\partial s_i}{\partial x_k} + \frac{\partial s_k}{\partial x_i} + \frac{\partial s_n}{\partial x_i} \frac{\partial s_n}{\partial x_k} \right)$$

For small deformations this reduces to

$$\epsilon_{ik} = \frac{1}{2} \left(\frac{\partial s_i}{\partial x_k} + \frac{\partial s_k}{\partial x_i} \right)$$

In the case of rigid rotations the stress tensor σ_{ik} is symmetric (Kennett and Bunge, 2008) and therefore $\sigma_{ik} \partial v_i / \partial x_k = \sigma_{ik} \partial v_k / \partial x_i$ implying the strain tensor to be symmetric too. From section 3.1.3 we can conclude that the stress power per unit volume is given by

$$p_s = \sigma_{ik} \dot{\epsilon}_{ik}$$

with $\dot{\epsilon}$ defined as

$$\dot{\epsilon} = \frac{\partial \Phi}{\partial t}$$

With this it is verified that (Simo and Hughes, 1998; Banerjee, 2006; Kennett and Bunge, 2008)

$$\sigma_{ik} = \frac{\partial w}{\partial \epsilon_{ik}} \tag{3.6}$$

with the strain rate tensor $\dot{\epsilon}_{ik}$ and the work per unit volume w . Eqns. (3.6) are the general constitutive equations for small strain elasticity. A first order Taylor series expansion results in *Hooke's law*

$$\sigma_{ik} = \sigma_{0,ik} + C_{iklm}\epsilon_{lm}$$

with the initial stress state $\sigma_{0,ik}$ (usually assumed to be = 0) and the elastic stiffness tensor C_{iklm} . In the special case of an isotropic cubic crystalline material one finds

$$C_{iklm} = \mu(\delta_{il}\delta_{km} + \delta_{im}\delta_{kl}) + \lambda\delta_{ik}\delta_{lm}$$

with the well known Lamé constants μ (also: shear modulus) and λ .

3.2.2 Viscoplasticity

Viscoplasticity means rate-dependent inelastic deformations without damaging the material. According to Lee (1969) the total strain is given by the sum of elastic and inelastic strains. For our rate-dependent material we use the total strain rate instead

$$\dot{\epsilon}_{ik} = \dot{\epsilon}_{ik}^{(el)} + \dot{\epsilon}_{ik}^{(vp)}$$

whereat $\dot{\epsilon}_{ik}^{(el)}$ denotes the elastic and $\dot{\epsilon}_{ik}^{(vp)}$ the viscoplastic strain rate. The stress tensor is defined using Hooke's Law, i.e.

$$\sigma_{ik} = C_{iklm}\epsilon_{lm}^{(el)} = C_{iklm}(\epsilon_{lm} - \epsilon_{lm}^{(vp)})$$

On using the Clausius-Duhem inequality together with the principle of maximum dissipation (e.g. Simo and Hughes, 1998; Banerjee, 2007) the viscoplastic strain rate is derived as

$$\dot{\epsilon}_{ik}^{(vp)} = \lambda^{(vp)} \frac{\partial f}{\partial \sigma_{ik}} \quad (3.7)$$

with a Lagrange multiplier $\lambda^{(vp)}$ (also: consistency parameter in case of plasticity) and the yield function $f(\sigma_{ik})$. Eqn. (3.7) is called associated flow rule but it is known from laboratory studies (e.g. Miller and Cheatham Jr., 1972; Senseny et al., 1983) that these types of models predict higher volumetric expansion due to inelastic strain (dilatancy) as compared to observations from shear tests. To simulate geophysical problems the plastic potential $g(\sigma_{ik})$ is thus introduced to replace $f(\sigma_{ik})$ in eqn. (3.7) resulting in the *non-associated flow rule* (3.8)

$$\dot{\epsilon}_{ik}^{(vp)} = \lambda^{(vp)} \frac{\partial g}{\partial \sigma_{ik}} \quad (3.8)$$

The yield function $f(\sigma_{ik})$ describes the fundamental type of deformation, i.e. elastic or inelastic. If the stresses reach a certain limit, the materials deformation does not stop although the stresses do not increase or may even decrease. This phenomenon is known as yielding and the following holds true:

$$\begin{aligned} \text{elastic deformation:} & \quad f(\sigma_{ik}) < 0 \\ \text{plastic deformation:} & \quad f(\sigma_{ik}) = 0 \\ \text{viscoplastic deformation:} & \quad f(\sigma_{ik}) > 0 \end{aligned}$$

The yield function and the plastic potential are user defined functions depending on the type of material considered. For this study the Drucker-Prager yield function is used, given by

$$f(\sigma_{ik}) = \alpha I_1 + \sqrt{J_2} - \tau_Y \quad (3.9)$$

whereat

$$\begin{aligned} \alpha &= \frac{2 \sin \phi}{\sqrt{3}(3 - \cos \phi)} \\ \tau_Y &= \frac{6C \cos \phi}{\sqrt{3}(3 - \sin \phi)} \\ I_1 &= \sigma_{11} + \sigma_{22} + \sigma_{33} \\ J_2 &= \sigma_{12}^2 + \sigma_{13}^2 + \sigma_{23}^2 + \frac{1}{6} [(\sigma_{11} - \sigma_{22})^2 + (\sigma_{22} - \sigma_{33})^2 + (\sigma_{33} - \sigma_{11})^2] \end{aligned}$$

with the angle of internal friction ϕ , the cohesion C , the yield stress τ_Y , the first invariant of the stress tensor I_1 and the second invariant of the stress deviator J_2 . For more information have a look at Jiang and Xie (2011). The plastic potential $g(\sigma_{ik})$ is nearly the same with the exception that ϕ is replaced by the dilatancy angle ϕ_{dil} .

Finally we have to define the Lagrange multiplier $\lambda^{(vp)}$. To ensure that the maximum dissipation principle (Simo and Hughes, 1998, Sec. 2.6) is fulfilled, the Karush-Kuhn-Tucker relations (Kuhn and Tucker, 1951) must hold true

$$\begin{aligned} \lambda^{(vp)} &\geq 0 \\ \tilde{f}(\sigma_{ik}) &\leq 0 \\ \lambda \cdot \tilde{f}(\sigma_{ik}) &= 0 \end{aligned}$$

In the present thesis the approach proposed by Perzyna (1966) is employed by introducing the overstress function $\Phi(f)$ and the alternative yield function $\tilde{f}(\sigma_{ik})$ resulting in

$$\begin{aligned} \lambda^{(vp)} &= \frac{1}{\eta} \langle \Phi(f) \rangle \\ \tilde{f}(\sigma_{ik}) &= f(\sigma_{ik}) - \Phi(f) \end{aligned}$$

with the McCauley brackets defined by

$$\langle \Phi(f) \rangle = \begin{cases} \Phi(f), & f(\sigma_{ik}) \geq 0 \\ 0, & f(\sigma_{ik}) < 0 \end{cases}$$

and the effective viscosity η . More specifically a power-law model with

$$\Phi(f) = \tau_Y \left(\frac{f}{\tau_Y} \right)^N$$

is utilized and the viscosity is defined via dislocation creep (see section 4.3) as

$$\eta(T) = \frac{1}{2} A_D^{-1/N} \dot{\epsilon}_{II}^{1/N-1} \exp\left(\frac{E_{act}}{RT}\right) \quad (3.10)$$

with a prefactor A_D , the power-law exponent N , the second invariant of the strain rate $\dot{\epsilon}_{II}$, the creep activation energy E_{act} , the universal gas constant R and temperature T .

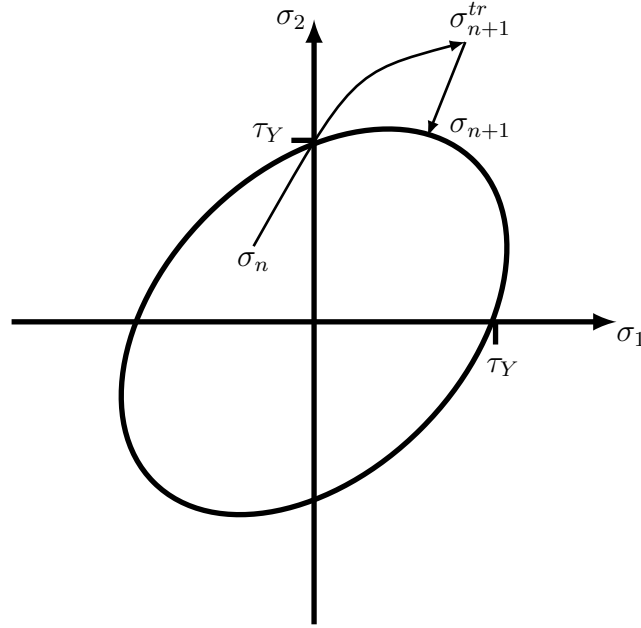


Figure 3.1: Schematic illustration of the return mapping algorithm in two dimensions

3.3 Return mapping algorithm

The constitutive equations presented in section 3.2 are non-linear equations for the stress components σ_{ik} at a time t given the total strain components ϵ_{ik} at that time. Therefore the return mapping algorithm, first proposed by Maenchen and Sacks (1964) and Wilkins (1964), is used to solve the equations. The method is based on the idea that for small strains the inelastic strains at time t are nearly the same as for the time $t + \Delta t$ with $\Delta t \ll t$. On discretizing the time interval we can introduce a trial stress at the time t_{n+1} as

$$\sigma_{ik,n+1}^{tr} = C_{ijkl}(\epsilon_{kl,n+1} - \epsilon_{kl,n}^{vp})$$

For simplification we consider the case of plasticity instead of viscoplasticity for now. Then the yield function must fulfill

$$f(\sigma_{ik,n+1}) \leq 0$$

In general on inserting the trial stress we are outside the yield surface, i.e. $f(\sigma_{ik,n+1}^{tr}) > 0$ (see fig. 3.1), which requires some correction. The elastic strains are given by

$$\epsilon_{ik,n+1}^{el} = \epsilon_{ik,n}^{el} + \Delta\epsilon_{ik,n+1} - \Delta\epsilon_{ik,n+1}^{pl}$$

and on using eqn. (3.8) we have to solve the implicit system of equations

$$\sigma_{ik,n+1} = \sigma_{ik,n+1}^{tr} - \lambda_{n+1}^{pl} \frac{\partial g}{\partial \sigma_{ik,n+1}}$$

for $\sigma_{ik,n+1}$.

Following Zienkiewicz and Taylor (2000, Sec. 3.4) we enforce

$$f(\sigma_{ik,n+1}) = 0$$

and define the residuals

$$R_{ik} = \Delta\epsilon_{ik,n} - C_{ijkl}^{-1}\Delta\sigma_{ik,n+1} - \lambda^{pl} \frac{\partial g}{\partial\sigma_{ik,n+1}}$$

$$r = -f(\sigma_{ik,n+1})$$

to satisfy $R_{ik} = 0$ and $r = 0$. Here $\Delta\epsilon_{ik,n}$ is a constant given by the finite element solution and thus linearization results in

$$R_{ik} = \left(C_{ikmn}^{-1} + \lambda_{n+1}^{pl} \frac{\partial^2 g}{\partial\sigma_{ik,n+1}\partial\sigma_{mn,n+1}} \right) \Delta\sigma_{mn,n+1} + \frac{\partial g}{\partial\sigma_{mn,n+1}} \Delta\lambda_{n+1}^{pl}$$

$$r = \frac{\partial f}{\partial\sigma_{ki,n+1}} \Delta\sigma_{ik,n+1}$$

On neglecting the second derivatives the solution is found to be

$$\Delta\sigma_{ik,n+1} = C_{ikmn} R_{mn} - \frac{1}{H} \left[C_{ikmn} \frac{\partial g}{\partial\sigma_{mn,n+1}} \frac{\partial f}{\partial\sigma_{pq,n+1}} C_{opqr} R_{qr} - r \right] \quad (3.11)$$

$$\Delta\lambda^{pl} = \frac{1}{H} \left[\frac{\partial f}{\partial\sigma_{ik,n+1}} C_{ikmn} R_{mn} - r \right] \quad (3.12)$$

with the denominator

$$H = \frac{\partial f}{\partial\sigma_{ik,n+1}} C_{ikmn} \frac{\partial g}{\partial\sigma_{mn,n+1}}$$

To perform an implicit finite element method the consistent tangent modulus is required (ABAQUS 6.14, 2014), i.e. the derivative of stress increments with respect to strain increments. From (3.11) we find this to be

$$C_{ikmn}^{pl} = C_{ikmn} - \frac{1}{H} C_{ikop} \frac{\partial g}{\partial\sigma_{op,n+1}} \frac{\partial f}{\partial\sigma_{rq}} C_{qrmn}$$

Doing a similar analysis for viscoplasticity we finally arrive at (Zienkiewicz and Taylor, 2000)

$$R_{ik} = \Delta\epsilon_{ik,n} - C_{ijkl}^{-1}\Delta\sigma_{ik,n+1} - \lambda_{n+1}^{vp} \frac{\partial g}{\partial\sigma_{ik,n+1}}$$

$$r = -\Phi(f) + \lambda_{n+1}^{vp} \frac{\eta}{\Delta t_n}$$

$$\Delta\lambda_{n+1}^{vp} = \frac{1}{H} \left[\frac{d\Phi}{df} \frac{\partial f}{\partial\sigma_{ik,n+1}} C_{ikmn} R_{mn} - r \right]$$

$$\Delta\sigma_{ik,n+1} = C_{ikmn} R_{mn} - C_{ikmn} \frac{\partial g}{\partial\sigma_{mn,n+1}} \Delta\lambda_{n+1}^{vp}$$

$$C_{ikmn}^{vp} = C_{ikmn} - \frac{1}{H} C_{ikop} \frac{\partial g}{\partial\sigma_{op,n+1}} \frac{d\Phi}{df} \frac{\partial f}{\partial\sigma_{rq,n+1}} C_{qrmn}$$

$$H = \frac{d\Phi}{df} \frac{\partial f}{\partial\sigma_{ki,n+1}} C_{ikmn} \frac{\partial g}{\partial\sigma_{mn,n+1}} + \frac{\eta}{\Delta t_n}$$

with the increment in time Δt_n . The entire algorithm (adapted from Simo and Hughes (1998, Sec. 3.7)) is given below:

1. Initialization

$$a = 0, \lambda^{vp(0)} = 0, \Delta\sigma_{ik,n}^{(0)} = C_{ikmn} (\Delta\epsilon_{ik,n} - \Delta\epsilon_{ik,n}^{vp}), \epsilon_{ik,n+1}^{vp} = \epsilon_{ik,n}^{vp}$$

2. Compute trial stress

$$\sigma_{ik,n+1}^{(0)} = C_{ikmn} (\epsilon_{mn,n+1} - \epsilon_{mn,n}^{vp})$$

3. Check yield condition

$$\text{IF } f(\sigma_{ik,n+1}^{(a)}) \leq 0$$

$$C_{ikmn}^{vp} = C_{ikmn}, \sigma_{ik,n+1} = \sigma_{ik,n+1}^{(a)}$$

EXIT

ELSE:

4. Return mapping algorithm

a) Compute residuals

$$R_{ik}^{(a)} = \Delta\epsilon_{ik,n} - C_{ijkl}^{-1} \Delta\sigma_{ik,n+1}^{(a)} - \lambda^{vp(a)} \frac{\partial g^{(a)}}{\partial \sigma_{ik,n+1}}$$

$$r^{(a)} = -\Phi(f^{(a)}(\sigma_{ik,n+1})) + \lambda^{vp(a)} \frac{\eta}{\Delta t_n}$$

$$H^{(a)} = \frac{d\Phi^{(a)}}{df} \frac{\partial f^{(a)}}{\partial \sigma_{ki,n+1}} C_{ikmn} \frac{\partial g^{(a)}}{\partial \sigma_{mn,n+1}} + \frac{\eta}{\Delta t_n}$$

b) Check convergence

$$\text{IF } |R_{ik}^{(a)}| < \text{Tol}_1 \text{ and } |r^{(a)}| < \text{Tol}_2$$

$$\sigma_{ik,n+1} = \sigma_{ik,n+1}^{(a)}$$

$$\epsilon_{ik,n+1}^{vp} = \lambda^{vp(a)} \frac{\partial g^{(a)}}{\partial \sigma_{ik,n+1}}$$

$$C_{ikmn}^{vp} = C_{ikmn} - \frac{1}{H^{(a)}} C_{ikop} \frac{\partial g^{(a)}}{\partial \sigma_{op,n+1}} \frac{d\Phi^{(a)}}{df} \frac{\partial f^{(a)}}{\partial \sigma_{rq,n+1}} C_{qrmn}$$

EXIT

ELSE:

c) Compute increments

$$\Delta\lambda^{vp(a)} = \frac{1}{H^{(a)}} \left[\frac{d\Phi^{(a)}}{df} \frac{\partial f^{(a)}}{\partial \sigma_{ik,n+1}} C_{ikmn} R_{mn}^{(a)} - r^{(a)} \right]$$

$$\Delta\sigma_{ik,n}^{(a)} = C_{ikmn} R_{mn}^{(a)} - C_{ikmn} \frac{\partial g^{(a)}}{\partial \sigma_{mn,n+1}} \Delta\lambda^{vp(a)}$$

d) Update stresses

$$\sigma_{ik,n+1}^{(a+1)} = \sigma_{ik,n+1}^{(a)} + \Delta\sigma_{ik,n}^{(a)}$$

$$\lambda^{vp(a+1)} = \lambda^{vp(a)} + \Delta\lambda^{vp(a)}$$

$$a = a + 1$$

GO TO 3.

The above algorithm has been used to write the UMAT subroutine implementing the viscoplastic and temperature dependent Drucker-Prager constitutive equations in Abaqus. More information on this can be found in appendix A.2.

3.4 Numerical discretization

Solving the coupled system of partial differential equations (3.1), (3.2), and (3.5) including several boundary conditions is mostly done using numerical discretization methods. All of

these methods are only approximations to reality and the corresponding results are at best as good as the worst known material parameters. Furthermore the accuracy is controlled by the distance between neighbouring integration points, the stability of the algorithm and the complexity of the geometry to consider. Modern numerical software often provide very stable methods that can efficiently handle difficult deformations and so the most limiting factors are the amount of memory of the computing machine and the computational time needed to solve the equations.

Depending on the type of boundary conditions to be fulfilled and the size and geometries of the problem, various numerical methods exist, such as finite differences (FDM), pseudo-spectral (PSM), discrete element (DEM), finite volume (FVM) and finite element methods (FEM). While finite difference and pseudospectral methods can be very effectively used for simple geometries (e.g. Wicht, 2002; Gerya and Yuen, 2007; Gerya, 2010; FLAC, 2018), they are difficult to apply for more complex ones. Discrete element, finite volume and finite element methods can be used for almost any geometry but depending on their specific implementation the computational time and the amount of memory needed can be larger and the accuracy may be lower as compared to a similar simulation using the FDM or PSM.

Due to their high flexibility the DEM, FVM and FEM are widely used methods for geophysical simulations. In DEM simulations the geometry is represented by a set of bonded rigid particles where each particle interacts with its nearest neighbours. With this it is possible to study e.g. crack and fault propagations (e.g. Groh et al., 2011; Chu et al., 2015; Liu and Konietzky, 2018). In finite volume methods the geometry is splitted into small volumes and the conservation equations are solved in integral rather than differential form. Thus all variables are averaged and located within the volume. The method is mostly used for coupled fluid dynamics simulations including convection and diffusion (e.g. Bessemoulin-Chatard, 2012; Zhang et al., 2016; Filbet and Herda, 2017).

3.4.1 Finite element method

The finite element method is possibly the most widely used technique for geodynamical simulations (e.g. Faccenna et al., 2018; Gerbault et al., 2018; Pelecanos et al., 2018; Rummel et al., 2018) because it can handle surface interactions and even more complex geometries than FVM. The general idea is that the geometry can be represented by a set of small elements, called the mesh. These elements have simple elementary forms, such as a cuboid, a tetrahedron or a wedge and are characterized by their nodes and edges. If $u(x)$ denotes an unknown function of position x , e.g. displacement or temperature, it can be approximated within an element by

$$u(x) = \sum_{i=1}^m N_i(x)u_i \quad (3.13)$$

where u_i are the values of u at the m nodes and $N_i(x)$ are the values of the shape functions at the nodes. The shape functions $N_i(x)$ are used to approximate the non-nodal values in

the elements interior by interpolation of the nodal values and depend on the specific shape of the element. They are characterized by the following conditions:

$$\begin{aligned} N_i(x)N_k(x) &= \delta_{ik} \\ \sum_{i=1}^m N_i(x) &= 1 \end{aligned}$$

On writing a partial differential equation (PDE) in integral form we can make use of its weak formulation by multiplying the function $u(x)$ in the PDE with an arbitrary function $v(x)$. If $A(u) = 0$ denotes the PDE in the volume V and $B(u) = 0$ the condition at the boundary ∂V , the weak fomulation states

$$\int_V v A(u) dV + \int_{\partial V} v B(u) dS = 0 \quad (3.14)$$

If we approximate $u(x)$ by eqn. (3.13), (3.14) only holds true at the nodes of an element. To determine the m unknowns u_i we must therefore solve the system of equations

$$\int_V v_i A(u_i) dV + \int_{\partial V} v_i B(u_i) dS = 0, \quad i \in \{1, \dots, m\}$$

For finite element simulations one makes use of the *Galerkin method* with $v_i(x) = N_i(x)$, while for FVM one uses $v_i(x) = 1$ (*subdomain collocation*). In matrix notation we thus obtain

$$K_{ik}^e u_k = f_i^e, \quad i, k \in \{1, \dots, m\}$$

with the local stiffness matrix components K_{ik}^e containing all terms related to the PDE and the vector components f_i^e containing all terms related to the boundary conditions at the element. Finally to obtain a system of equations for the whole geometry consisting of several elements, the equations above must be added up with care because neighbouring elements share some of their nodes. For more informations on the finite element method see for example Zienkiewicz and Taylor (2000).

3.4.2 Abaqus

The commercial software Abaqus 6.14 (ABAQUS 6.14, 2014) is used to conduct the FE simulations including mesh creation, model definition, solution of the PDE system and post-processing of the results. It provides many possibilities for element types, rheologies, boundary conditions and solution controls. During mesh creation the user can define local seeds as well as different element types and meshing algorithms to different regions of the model to create a very robust mesh even for complex geometries. The geometries can be imported from CAD software such as AutoCAD using the ACIS SAT file format, allowing the user to use a wide range of geometries. Furthermore there are several algorithms available to calculate contact interactions between surfaces and the user is allowed to define e.g. its own boundary conditions, rheologies, contact interaction types or element types. These sub-routines also allow for changes in material properties during the simulation depending on the actual results. Abaqus can carry out thermomechanical, thermoelectrical and coupled fluid dynamic static and transient analysis and it can interact with external software during the computation via co-simulation. Moreover, the software is very well documented (see ABAQUS 6.14, 2014) significantly facilitating the process of model creation and simulation. Therefore, the software is widely used for engineering, industrial and scientific purposes.

4 Reference model

The following chapter describes the specifications of the reference model representing a simplified version of the final model of northern Chile (chapter 6). This model is an updated version of Salomon (2018, see appendix C) and has been used to figure out all relevant numerical settings needed to achieve a stable thermomechanical subduction simulation in Abaqus, for testing purposes of the user material subroutine UMAT (section 3.3), and to study the effects due to changes in various physical and numerical parameters (chapter 5). The system of units used during the simulation is based on the international system (SI) but with lengths defined in 1 km and masses in 10^9 kg resulting in stresses defined in 1 MPa. The simulation runs for $1.6 \cdot 10^5$ years, which is short compared to typical subduction related timescales of several millions of years. The resulting deformations are expected to be very small, i.e. on the order of 1% and the same is true for changes in temperature and heat flux. However, the changes in shear stresses shall be significant because of the plate interactions especially along the zone of frictional coupling. The final shear stresses are, thus, expected to reflect the recent state. Therefore, the final model (chapter 6) can be compared with observations of e.g. uplift rate and positions of recent earthquakes.

For the geometry of the oceanic plate a smoothed version of the cross section at 20°S of the slab geometry provided by the density model of Tassara and Echaurren (2012) is used with the dip angle increasing from 10° near the trench to 35° in the asthenosphere. For the continental plate a horizontal layering is chosen (fig. 4.1). The cross section has been extended by 400 km in z-direction (south to north) resulting in a 2.5-dimensional geometry with changes in x- and y- but not z-direction. The vertical extension (y-direction) is 400 km, i.e. down to the olivine to wadsleyite transition zone, to avoid having to consider major phase transformations. The total dimensions are thus 1380 km (x) by 400 km (y) by 400 km (z). The mesh is created using hexahedral elements (see section 4.1). If the dimensions of some elements of the mesh compared to the dimensions of surrounding elements becomes too small, the resulting deformations of the small elements can become unrealistically high and the model may fail. Hence, the first 100 km of the continental plate east of the trench are neglected to avoid numerical instabilities due to very small elements.

4.1 Initial and boundary conditions

Before the subduction simulation an initial lithostatic stress and the initial temperature distribution (fig. 4.2) must be computed during a static analysis.

To calculate the initial stress the overall model is fixed in x- and z-direction. The bottom is additionally fixed in y-direction to ensure that vertical movements are the only ones possible. By default all stresses are zero and by applying gravity the model subsides by several kilometres. In perfect isostatic equilibrium all normal stresses are equal to the vertical normal stresses, i.e. σ_{yy} , and no shear stresses are present resulting in a lithostatic pressure distribution. The model geometry is situated in a free space, i.e. no pressure is applied at its surroundings, and is thus deforming. As a result shear stresses are present and the normal

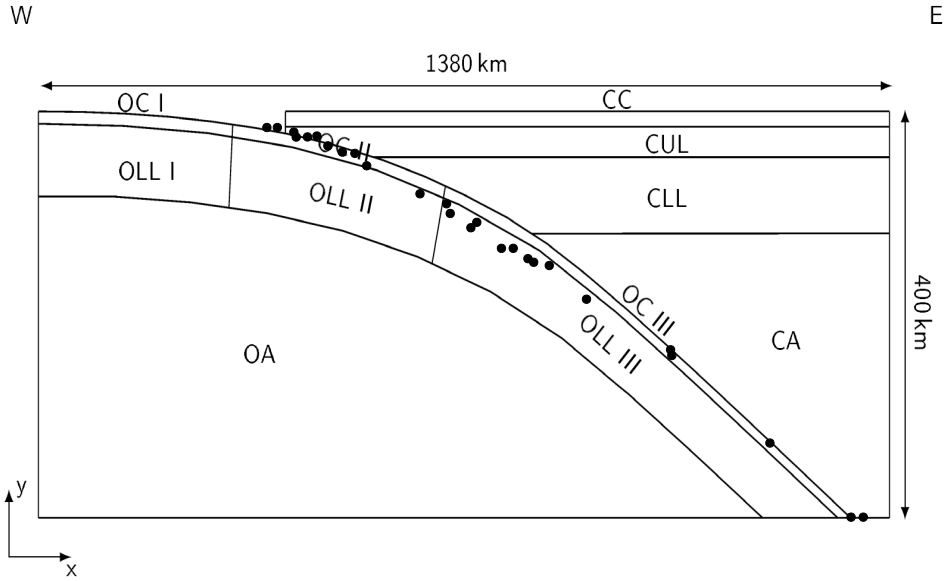


Figure 4.1: Geometrical cross section of the reference model showing the different parts of the model. The black dots denote vertices provided by Tassara and Echaurren (2012). Abbreviations: CC-continental crust, CUL-continental upper lithosphere, CLL-continental lower lithosphere, CA-continental asthenosphere, OC-oceanic crust, OLL-oceanic lower lithosphere, OA-oceanic asthenosphere

stresses σ_{xx} , σ_{zz} differ from σ_{yy} . Therefore, after the static calculation a new initial stress is defined where all normal components are set equal to σ_{yy} and all shear stresses to zero. This procedure is applied until the resulting subsidence is minimized, i.e. no significant changes in subsidence between two subsequent analyses are present and isostatic equilibrium is thus reestablished.

To simulate the initial temperature distribution a surface temperature of 273 K and a temperature of 1523 K at the continental and oceanic LAB is assumed. Constant radiogenic heating is applied throughout the continental crust and remaining upper lithosphere with typical mean values (e.g. Ranalli, 1995; Currie et al., 2002; van Keken et al., 2002; Afonso and Ranalli, 2004; Babeyko and Sobolev, 2008) of $H = 1.3 \mu\text{Wm}^{-3}$ and $H = 0.35 \mu\text{Wm}^{-3}$, respectively. In Abaqus convection is represented by a mass flow rate, which according to the manual (ABAQUS 6.14, 2014), can only be applied to hexahedral elements. In the model this is assumed to occur inside the slab and at the continental LAB. The mass flow rate can be approximated by

$$\dot{m} \approx \rho \vec{v}$$

$$\vec{v} = (v_x, v_y, v_z)^T = (v \cos \phi \cos \theta, v \sin \theta, v \sin \phi \cos \theta)^T$$

with the mass density ρ and the velocity vector \vec{v} of the continental or oceanic plate given in spherical coordinates where v is the velocity magnitude, ϕ the dipping angle and θ the angle between the movement direction and z-axis, i.e. in case of oblique subduction.

The boundary conditions during the subduction simulation include no-slip and free-slip conditions (fig. 4.3) as well as gravity. Both the continental and oceanic plate are moving towards each other with convergence velocities of 3.3 cm/a and 6.5 cm/a, respectively. At

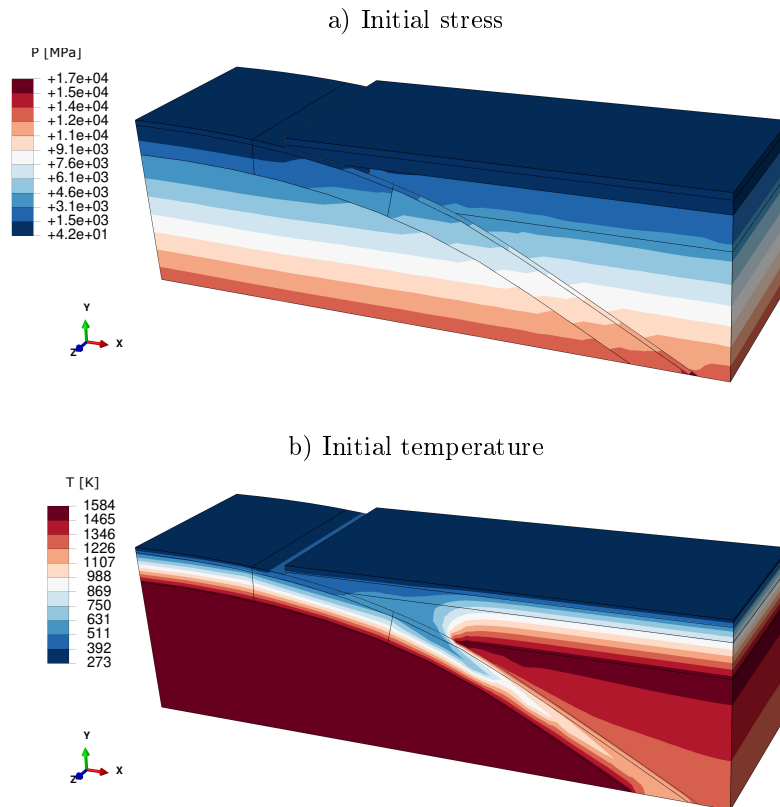


Figure 4.2: Initial lithostatic stress (a), and temperature distribution (b) of the reference model.

the eastern and western boundary of the asthenosphere a pressure corresponding to the lithostatic pressure is applied, while at the bottom large parts of the oceanic asthenosphere are fixed in vertical direction. At the bottom of the subducting slab and surrounding regions a Winkler foundation condition (Winkler, 1867; Winkler, 1867) is applied. If a beam, lying on an elastic foundation, is under external loading, its deflection leads to reaction forces $f(x)$ of the foundation that are proportional to the deflection $w(x)$, i.e.

$$f(x) = kw(x)$$

with k the modulus of foundation. During an elastic foundation condition these forces are assumed to balance, i.e. minimize, the deflection by defining an appropriate modulus k . The same applies to the deflection of a plate and according to e.g. Capitanio and Morra (2012) a good approximation for k is the corresponding lithostatic pressure as given by the initial stress model, i.e. $k = 13570$ MPa for my reference model. In z-direction (south to north) the model is completely fixed.

4.2 Surface interactions

The geometry used for this reference model (fig. 4.1) consists of 11 parts in total. Numerically, these parts are separated by default, i.e. there is no exchange of information about any variables between them. In subduction zones the upper and lower plate interact via

is in agreement with the study by Hoffmann-Rothe et al. (2006) about the Andes subduction zone. For the reference model no subduction channel is introduced and therefore a moderate value of $\mu = 0.2$ is chosen.

To define the numerical contact between two surfaces in Abaqus a primary and secondary surface is needed. The primary surface acts as reference while the position of the nodes of the secondary surface are adapted to fit with the ones of the primary surface. For this study the general contact algorithm is used. By default the positions of the secondary nodes are averaged using neighbouring nodes of both surfaces (surface-to-surface discretization) resulting in a more robust contact definition. Depending on the accuracy of the mesh the surfaces may not come into contact at certain regions. For this case the user can provide a position tolerance to increase the default size of the region used to average the secondary nodal positions. For the reference model an optimum value of 80 m is found. The amount of information transferred between the surfaces depends on the contact pressure as defined by the pressure-overclosure relationship. Here the linear penalty method is used, i.e. the contact pressure linearly increases with decreasing distance between the surfaces or increasing overclosure respectively.

4.3 Material parameters

The material parameters presented in this section do correspond to the area in northern Chile (fig. 1.1) such that the final state of the reference model represents the local state. Most of the stresses will result from elastic strains, due to the typically very low strain rates between 10^{-15} and 10^{-13} s^{-1} and the comparatively short simulated timescale of 10^5 years, and therefore density, Young's modulus, and Poisson's ratio are the most important parameters. The densities provided by Tassara and Echaurren (2012) result from petrophysical analysis done by Tassara et al. (2006) and are well constraint for the continental plate and oceanic crust. For the remaining parts, including oceanic lithosphere, slab, and asthenosphere, they are first order estimates. For simplicity the Poisson ratio is assumed to be 0.25 in the overall model although it is known to reach values of about 0.30 in the continental lithosphere (e.g. Koulakov et al., 2006). For the Young moduli the values provided by Zeumann (2013) are used for the current model, including the seismic velocity profile of the ANCORP ("Andean Continental Research Project 1996") project (ANCORP Working Group, 2003). The angle of internal friction ϕ (section 3.2) determines the amount of shear stresses needed for inelastic deformations to occur, given that the cohesion is zero. Byerlee (1978) found $\phi \approx 30^\circ$ for different kinds of rocks at pressures up to 1.7 GPa, a value often used for geodynamical simulations (e.g. Vermeer and de Borst, 1984; Sobolev and Babeyko, 2005; Burg and Schmalholz, 2008; Schmalholz et al., 2009; Baumann and Kaus, 2015; Gerbault et al., 2018; Gülcher et al., 2019). However, due to high uncertainties (see the review by Burov, 2011) deeper rocks may have lower values (Brace and Kohlstedt, 1980; Kohlstedt et al., 1995) and therefore in this study the angles of friction as proposed by Dorbath et al. (2008) and Gerbault et al. (2009) are used (table 4.1). To account for dilatancy the actual dilatancy angle is needed describing the degree of compressibility (Burov, 2011). Referring to Michelis (1981) and Vermeer and de Borst (1984) typical values for most rocks at low pressures are in the range $12^\circ \leq \phi_{dil} \leq 20^\circ$ decreasing to 0° with increasing pressure. The values used for the cohesive strength C are between 20 MPa for the crust up to 50 MPa in the asthenosphere (e.g. Byerlee, 1978; Schön, 1983; Sobolev et al., 2006; Kennett and Bunge,

2008; Burov, 2011). The specific heat capacity C_P is nearly constant from the crust down to 400 km depth with values of 1200 to 1250 J kg⁻¹ K⁻¹ (e.g. Stacey, 1977; Sobolev et al., 1994; Afonso and Ranalli, 2004; Whittington et al., 2009) while the thermal conductivity κ increases with depth from about 2.5 to 3.0 W m⁻¹ K⁻¹ in the crust up to 6.9 W m⁻¹ K⁻¹ in the asthenosphere (e.g. Stacey, 1977; Ranalli, 1995; McKenzie et al., 2005; Emmerson and McKenzie, 2007; Whittington et al., 2009).

Table 4.1: Material parameters used for the reference model: The Poisson ratio is set to 0.25, the thermal expansion coefficient to 0.0 K⁻¹ and the specific heat capacity to 1250 J kg⁻¹ K⁻¹ in the overall model.

Part	$\rho^{(1)}$ (kg m ⁻³)	E ⁽²⁾ (GPa)	$\phi^{(3)}$ (°)	$\phi_{dil}^{(4)}$ (°)	C ⁽⁵⁾ (MPa)	N ⁽⁶⁾ (1)	log(η_0) ⁽⁷⁾ (Pas)	$\kappa^{(8)}$ (W m ⁻¹ K ⁻¹)
CC	2700	80	20	10	20	3.5	25	2.5
CUL	3100	100	10	0	20	3.5	21	2.5
CLL	3320	150	10	0	30	3.5	21	2.5
CA	3430	180	10	0	50	3.5	19	6.9
OC I	3050	98	20	10	20	3.5	25	2.5
OC II	3300	116	20	10	20	3.5	25	2.5
OC III	3550	125	20	10	20	3.5	25	2.5
OLL I	3350	183	20	10	30	3.5	21	2.5
OLL II	3400	186	20	10	30	3.5	21	2.5
OLL III	3500	191	20	10	30	3.5	21	2.5
OA	3411	205	20	10	50	3.5	19	6.9

References: (1) Tassara and Echaurren (2012), (2) Zeumann (2013), (3) Gerbault et al. (2009), (4) Michelis (1981), Vermeer and de Borst (1984), (5) Byerlee (1978), Schön (1983), Sobolev et al. (2006), (6) Kirby and Kronenberg (1987), Hirth and Kohlstedt (2003), Bürgmann and Dresen (2008), Turcotte and Schubert (2014), (7) Ranalli (1995), Karato (2010), Turcotte and Schubert (2014), (8) Stacey (1977), Afonso and Ranalli (2004), Whittington et al. (2009)

One possible source for data about the viscosity is the macrophysical viewpoint, i.e. observations of post-glacial rebound, geoid anomalies and earth's rotational period (Ranalli, 1995). The resultant viscosities are valid in case of a viscoelastic Maxwell body with relaxation times on the order of $\geq 10^3$ years. Although mantle viscosities can be derived by those observations, the assumption to treat mantle rocks as fluids with Newtonian viscosity is a rough simplification. Results from microphysics at the atomic scale reveal significant deviations and are used to simulate different kinds of geodynamic processes (e.g. Burov, 2010; Fuchs et al., 2015; Popov et al., 2012; Liao et al., 2018; Osei Tutu et al., 2018; Reuber et al., 2018). The dominant creep mechanisms in the mantle are diffusion creep for low stresses and small grain sizes and dislocation creep for high stresses and large grain sizes (Ranalli, 1995). If crystal grains are subjected to low stresses, diffusion between the grain boundaries occurs and deforms the grains. This leads to a linear increase in strain rate with increasing stress,

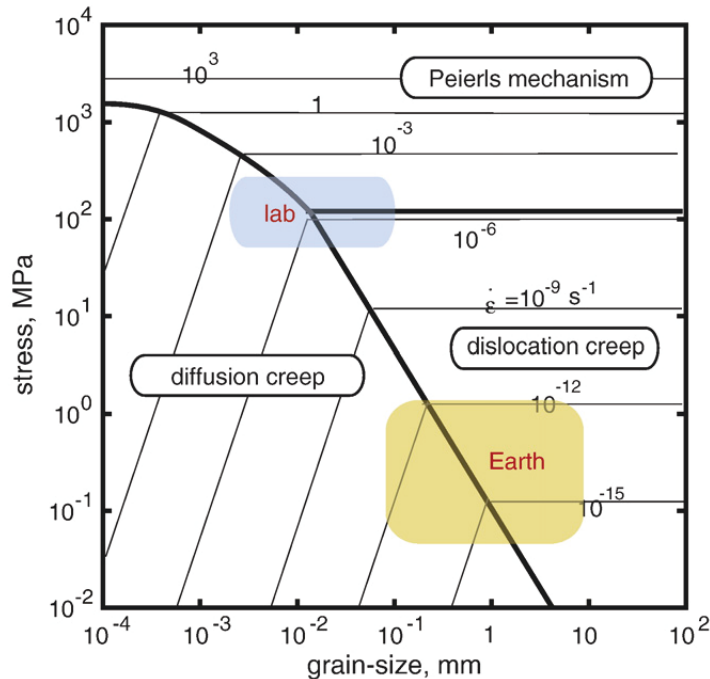


Figure 4.4: Creep mechanisms for dry olivine and the resulting strain rates after Karato (2010)

but also to a significant decrease with increasing grain size. At high stresses, dislocations in the crystal lattice move, resulting in a nonlinear increase of strain-rate with stress, which depends on grain size. The resulting creep strain-rate is given by Karato et al. (1986)

$$\dot{\epsilon} = A\sigma^N s^m \exp\left(-\frac{E_{act} + V_{act}p}{RT}\right)$$

with a factor A , stress σ , stress exponent N , grain size s , grain size exponent m , activation energy E_{act} , activation volume V_{act} , pressure p , universal gas constant R and temperature T . According to Kameyama et al. (1999) the Peierls mechanism is another creep mechanism that is important in the shallow portion of a subducting slab where low temperature plasticity occurs. Figure 4.4 shows the dependence of strain-rate on stress and grain size for the three types of creep for dry olivine.

Typical strain-rates in subduction zone modelling are on the order of 10^{-16} s^{-1} to 10^{-14} s^{-1} so that for simplicity dislocation creep is the only mechanism considered in this work, i.e. it is assumed that $m = 0$. Furthermore, the dependence on the creep activation volume V_{act} is neglected and the effective viscosity is introduced as

$$\eta = \frac{1}{2} \frac{\sigma}{\dot{\epsilon}}$$

resulting in equation (3.10). For the reference model a constant viscosity η_0 is employed, which is independent of strain-rate and temperature and which is later on compared with a model containing a more realistic viscosity distribution (see section 5.2.6). On average the viscosity in the upper mantle is found to be $10^{20} - 10^{22} \text{ Pas}$ increasing up to 10^{27} Pas (e.g. Ranalli, 1995; Karato, 2010; Turcotte and Schubert, 2014) in the crust. In the upper

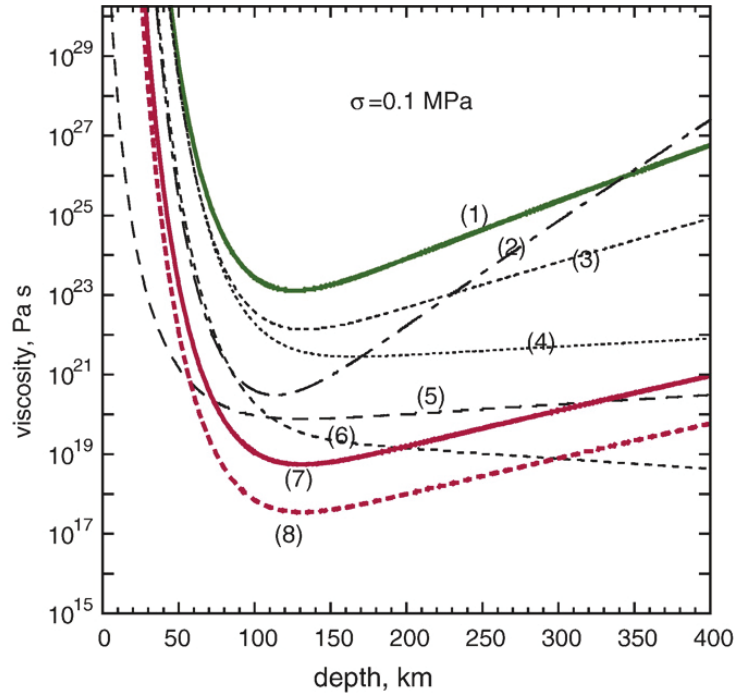


Figure 4.5: Upper mantle viscosity after different data sources (from Karato, 2010).

part of the asthenosphere it may reach values of 10^{19} Pa s, however the scatter in the data is large (see fig. 4.5) due to different measuring systems (see Karato, 2010 for a review) and the results obtained are valid for strain-rates of 10^{-6} to 10^{-4} s^{-1} , i.e. up to 10 orders of magnitude higher than typical strain-rates of geodynamic processes. For this reason typical mean values of viscosity (table 4.1) are used here. For the reference model the power-law exponent N is only needed for the definition of the overstress function $\Phi(f)$ (eqn. (3.2.2)). A typical value for dry olivine is $N = 3.5 \pm 0.5$ (e.g. Kirby and Kronenberg, 1987; Hirth and Kohlstedt, 2003; Bürgmann and Dresen, 2008; Turcotte and Schubert, 2014), which is used here, too.

4.4 Assumptions

Subduction processes typically last for more than 10^8 years over areas of several 10^6 km^2 and down to depths of about 700 km or even further. Many aspects, which are currently not well understood, play an important role for surface and subsurface processes that occur during subduction. Examples are erosion, phase transitions, convection, fluid migration, generation of melts, and plate coupling. Therefore, assumptions must be made with care to simplify the numerical model while still being able to compare the results with observations. In the following section I give a description of the most important assumptions made during this study.

The geometry is possibly the most limiting quantity for this study. Because it is based on a two dimensional cross section there are no variations in north-south direction. Nevertheless it allows to study surface coupling effects between the plates instead of line coupling in a purely two dimensional analysis. Furthermore, it allows for studying the effects of oblique

subduction during the parametric study (section 5.2.5). Due to the limited size of the model the major phase transitions of olivine do typically occur in depths larger than those considered here (e.g. Woodward, 1977; Kirby, 1996; Negredo et al., 2004; Carminati et al., 2005; Liu and Zhang, 2015; Goes et al., 2017) and are thus neglected. The short time scale of about 10^5 years restricts the model to a present-day situation. Significant temperature changes due to convection start to occur on time scales of 10^6 to 10^7 years and are thus not considered in this work. However, long-term shear heating in the plate coupling zone is included allowing for a temperature increase during inelastic deformation.

A further restriction is the flat Earth approximation used here as well as in many other studies (e.g. Sobolev et al., 2006; Kellner, 2007; Babeyko and Sobolev, 2008; Zeumann, 2013; Popov et al., 2012; Baumann and Kaus, 2015; Lin and Kuo, 2016). The surface of the model is assumed to be flat, which is only reasonable if the model dimensions are small enough. Assuming a spherical shape of the Earth the distance between two points along a great circle is given by

$$D = 2R \operatorname{asin} \left(\frac{d}{2R} \right)$$

with Earth radius R and the distance d in case of a flat Earth. Using a Taylor expansion of $\operatorname{asin}(x)$ the difference between both distances is

$$\Delta = D - d \approx \frac{d^3}{24R^2}$$

with $\Delta \approx 3$ km for $d = 1380$ km being a negligible value compared to the total dimensions of the model. The maximum height difference from the centre of the model is given by

$$\Delta h = R \left(1 - \cos \frac{\alpha}{2} \right) = 2R \sin^2 \frac{\alpha}{4}$$

with the angle $\alpha \approx d/R$ yielding a maximum of $\Delta h = 9$ km at the model boundaries. Thus when studying very long trenches, such as along the overall Indian, Nazca and Pacific plate, the flat-earth approximation can lead to significant deviations (e.g. Antonioli et al., 1998; Morra et al., 2009).

Fluid transport is an important aspect leading to melting processes connected with the development of volcanic arcs as found along the Andes mountain belt (fig. 1.1). Moreover the addition of fluids implies additional chemical phase transitions and would thus significantly increase the complexity of the model. Erosion, glaciation and uplift are the main mountain building processes. While erosion is restricted to the surface, glaciation results in postglacial rebound affecting large parts of the lithosphere. Both aspects depend on the local climate conditions, which is not the intention of this work and therefore fluids, erosion and glaciation are ignored.

4.5 Results

4.5.1 Short-term simulation

The following section describes the results of the reference model obtained after simulating $1.6 \cdot 10^5$ years of subduction under the conditions mentioned in the previous sections.

Figure 4.6 shows the main results obtained for the reference model after $1.6 \cdot 10^5$ years of subduction. Most parts of the model show minor vertical movement, but the eastern continental and oceanic plate show subsidence of up to 1.7 km above the bottom edge of the slab. From here towards the trench the overriding plate is uplifted relative to this position, reaching a maximum of 100 m east of the trench, while the trench itself shows subsidence of up to 90 m similar to most parts of the subducting plate. Only the eastern and western boundaries of the model are uplifted significantly by up to 3.7 km. These uplifted regions are boundary effects due to the applied constant velocities and should be neglected in any geological or geophysical interpretation. Because of the conservation of mass (section 3.1.1) the strongly subsided areas are the result of mass compensation between the upper and lower plate.

Looking at the horizontal movement the motion of the oceanic plate dominates large parts of the model, i.e. the western and middle parts of the continental plate including the trench move towards the east, while only about 300 km of the eastern part move towards the west. Although no velocities are applied to the asthenosphere and it is fixed at the bottom, it does show horizontal movement by up to 4 km.

The shear stresses in the model are rather high compared to long-term studies (e.g. Babeyko and Sobolev, 2008; Gerbault et al., 2009; Kaus et al., 2009; Capitanio and Morra, 2012; Farrington et al., 2014; Jaquet and Schmalholz, 2018), reaching values of about 200 MPa in the continental trench-near regions. The highest shear stresses occur in the lower oceanic and continental lithosphere, with several GPa decreasing towards the middle of the slab to about 300 MPa in depths of 150 km. According to Lamb (2006) and Copley (2017) typical shear stresses in the seismogenic zone are ≤ 15 MPa for subduction megathrust estimates and no larger than ≤ 50 MPa, due to the typically very low coefficients of friction of $\mu \leq 0.05$. In this study a much higher value of $\mu = 0.2$ is assumed, because the plates are in frictional contact rather than interacting via a subduction channel (see also section 4.2). However, this is still below the suggested maximum of ≈ 0.3 (Craig et al., 2014). For $\mu = 0.2$ the shear stress at the lower end of the zone of friction estimates to $\tau \approx 200$ MPa at a depth of 40 km similar to the values obtained in the model. Therefore the simulated timespan of $1.6 \cdot 10^5$ years is sufficient to represent the actual model state before the occurrence of a large earthquake.

The horizontal shear strains are significantly increased around the eastern and western LAB compared to most parts of the overall lithosphere, reaching values of up to 0.08 and -0.07 respectively. Those strains affect large parts of the surrounding asthenosphere while the central regions are nearly unaffected. The upper part of the zone of friction in the continental plate shows slightly higher shear strains compared to its surroundings.

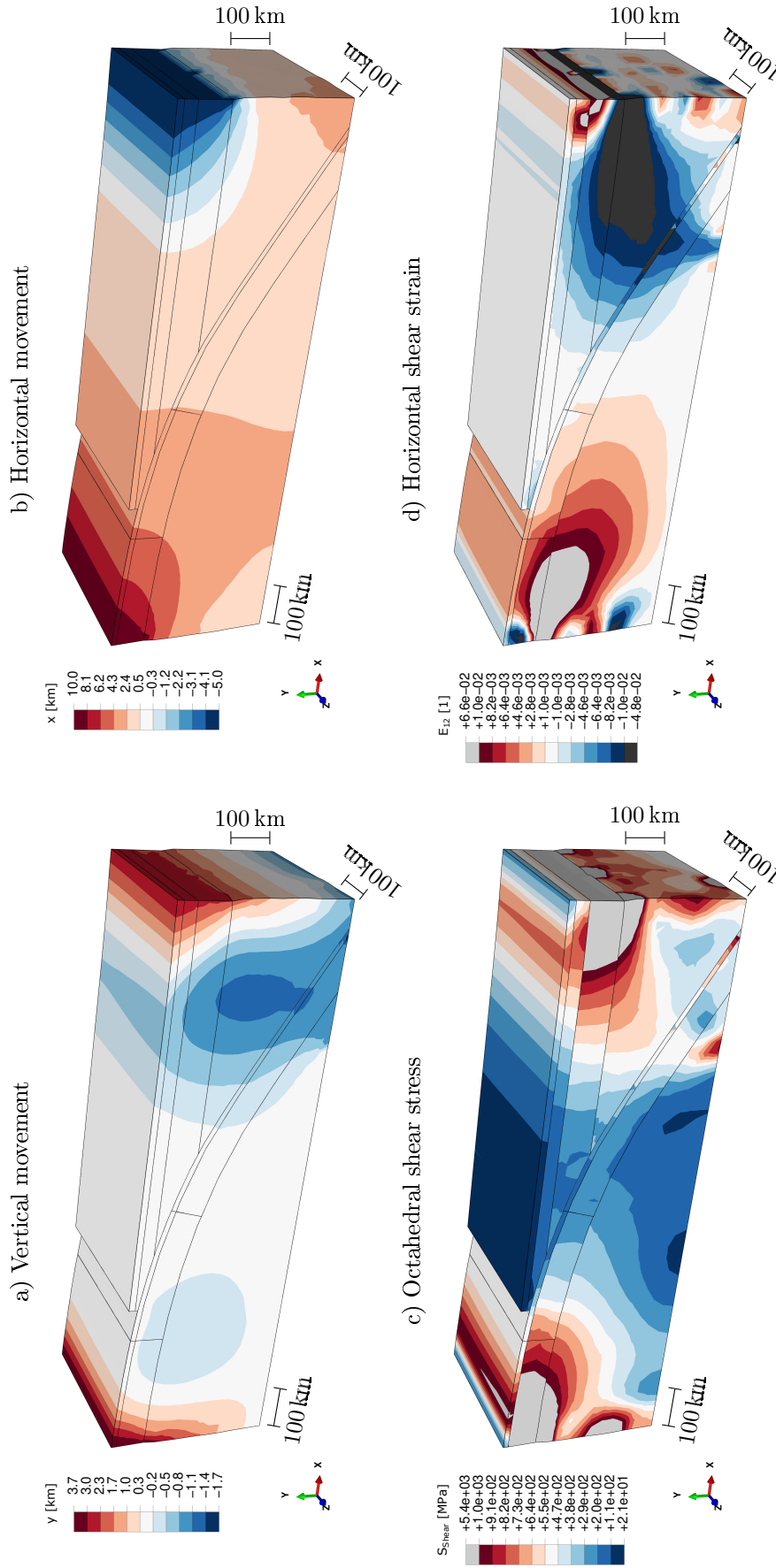


Figure 4.6: Results for the reference model after 160 ka. Top: Vertical (a) and horizontal (b) movement. Bottom: Octahedral shear stresses (c), i.e. $\sqrt{2J_2}/3$ with J_2 the second invariant of the deviatoric stress tensor, and horizontal shear strains (d).

The temperature in the model has hardly changed after $1.6 \cdot 10^5$ years, which is to be expected (fig. 4.7). The most significant changes do occur at the uppermost layer of the oceanic crust as well as at the intersection between slab and continental lithosphere and asthenosphere. While the temperature in the oceanic crust increases by up to 27 K, the temperature at the intersection decreases by up to 17 K. During the subduction simulation no temperature constraints are applied to the model. Therefore the crust, as the coldest region in the model, experiences the highest temperature changes due to conduction. Because of the higher temperature gradient within the oceanic plate the temperature increase is higher compared to the continental plate. The decrease at the intersection is caused by the cold oceanic slab. At the uppermost region of the frictional coupling zone a slight temperature increase of up to 4 K in the oceanic plate is observed. This can already be attributed to frictional shear heating due to inelastic deformations.

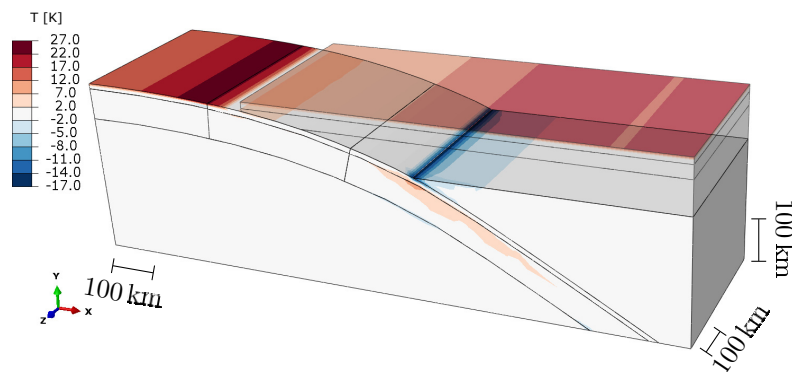


Figure 4.7: Temperature changes with respect to initial temperature distribution of the reference model after $1.6 \cdot 10^5$ years

4.5.2 Long-term simulation

Besides the short-term simulation of $1.6 \cdot 10^5$ years, I computed a long-term run simulating $1.6 \cdot 10^6$ years to have a look at the further evolution of the model. All results must be interpreted with care, because the built-up shear stresses along the zone of friction are not limited by a subduction channel (Scholl et al., 1977; Shreve and Cloos, 1986) as in other studies (e.g. Billen and Hirth, 2007; Babeyko and Sobolev, 2008; Gerbault et al., 2009; Popov et al., 2012; Baumann and Kaus, 2015) or by the occurrence of earthquakes. The analysis of this and of the results in chapter 5 will be done along the paths shown in figure 4.8.

Figure 4.9 shows the temporal evolution of vertical movement, temperature, heat flux and shear stress along the paths in figure 4.8. With ongoing subduction the influence of the velocity boundary conditions applied to the eastern and western ends of the lithosphere increases, resulting in significant uplift of those regions. For this reason the area that can be interpreted with confidence is significantly reduced (fig. 4.9a). The continental crust shows an increasing topography with a wavelength of about 600 km and a minimum uplift of 800 m east of the trench. The continental crust beneath the trench is raised by 1 km, while 350 km east of it a maximum uplift of more than 3 km is observed. In the oceanic crust a similar topographic evolution can be observed with nearly the same wavelength but different amplitudes. While the coupling zone is nearly in steady state for up to $1 \cdot 10^6$ yrs, it starts to

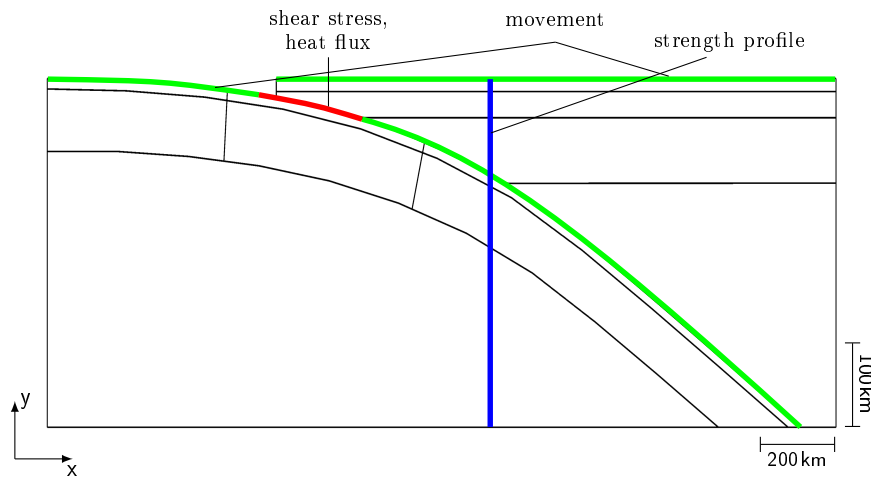


Figure 4.8: Paths along the centre of the model. The results obtained for the movement are analyzed along the continental and oceanic crust (green), while shear stresses and heat fluxes are evaluated along the zone of frictional coupling (red). The central blue path is used to conduct a strength profile (see section 5.2.6)

subside later on. The area 300 km east of the trench is uplifted by 2 km, but further to the east the amount of subsidence increases to 2.5 km after $1.6 \cdot 10^6$ years. While after $1.6 \cdot 10^5$ years the lower end of the slab subsided by 1 km, it is uplifted by several 100 m at the end of the long-term run.

The shear stresses generally increase with ongoing subduction along the upper and lower plate frictional interface (fig. 4.9b). In the continental plate the shear stress is below 200 MPa near the trench and raises significantly with time towards the downdip end. After $1.6 \cdot 10^5$ years the maximum shear stress is 180 MPa, but after $1.6 \cdot 10^6$ years it is at 2500 MPa. In the oceanic plate the shear stresses are about twice as high compared to the continental plate and towards the lower end of the coupling zone the stresses increase non-linearly with time reaching values up to 5000 MPa. The reason for such high shear stresses is probably that no subduction channel is used within the zone of friction. This channel would be significantly weaker than the surrounding materials and is able to lower the shear stresses.

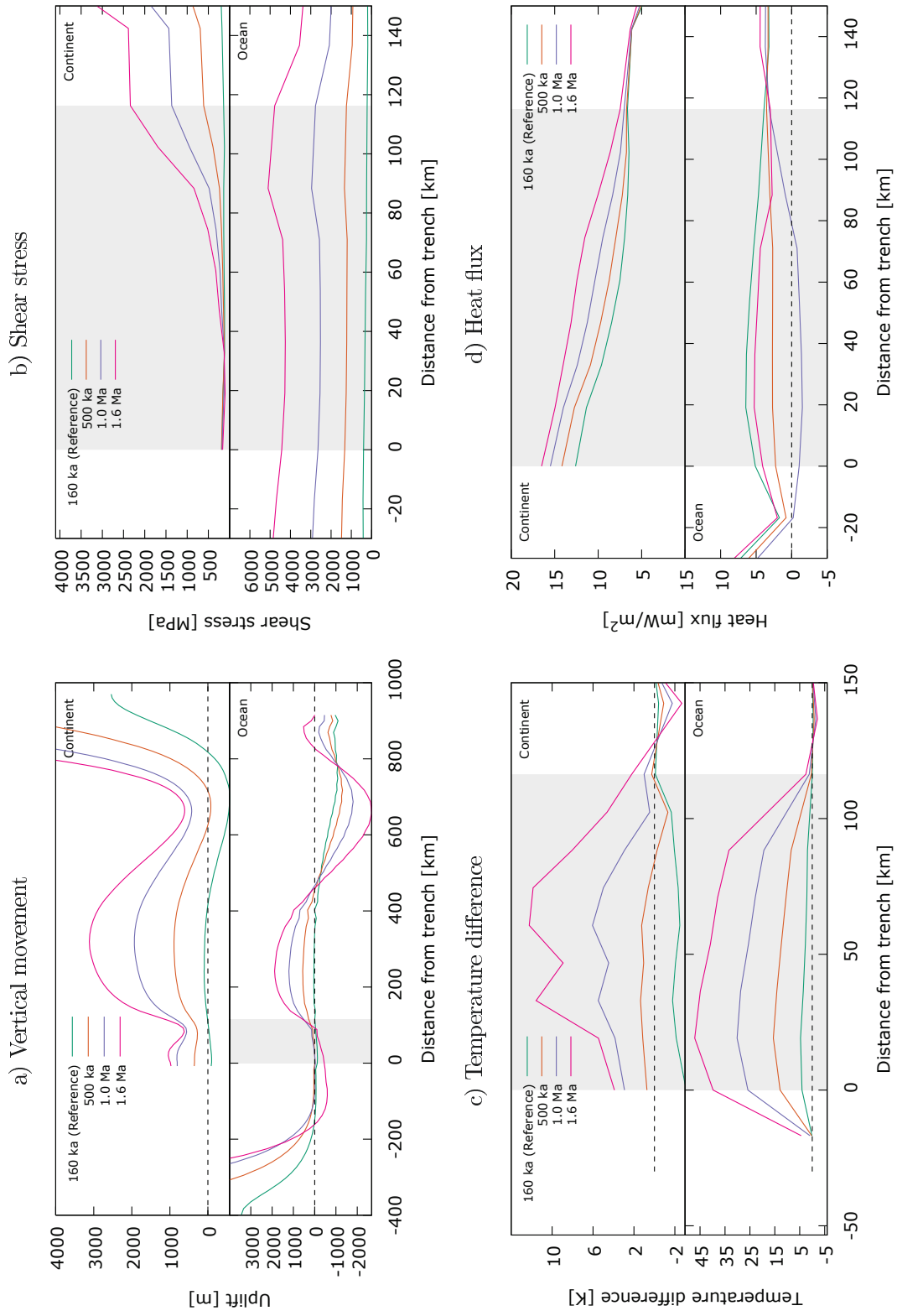


Figure 4.9: Evolution of vertical movement along the continental (top panel) and oceanic (bottom panel) crust (green paths in fig. 4.8; a) as well as shear stress (b), temperature (c) and vertical heat flux component (d) along the zone of friction (red paths in fig. 4.8). The grey shaded area marks the zone of friction between the plates.

In figure 4.9c the temperature distribution along the zone of coupling is shown. There is a clear increase in temperature inside the zone of coupling that decreases towards the outside. After $1.6 \cdot 10^5$ years the temperature in the continental plate has decreased by about 2K inside the zone while it is constant outside of it. The temperature increased by up to 13K at 30 km and 60 km east of the trench after $1.6 \cdot 10^6$ years, while in between the increase is slightly lower with about 10 K. The reason for this might be the low spatial resolution of the mesh. In the oceanic plate the temperature already starts to increase at the beginning of the subduction process and increases by up to 45K after $1.6 \cdot 10^6$ years. This highest increase occurs 20 km east of the trench, while for most of the remaining parts of the coupling zone the increase is between 35K and 45 K. This results in a steep temperature gradient west of it. 90 km east of the trench the increase starts to drop reaching near 0 K at the lower end of the zone of coupling. At the beginning of the subduction process the inelastic deformations are near zero, while there are significant temperature differences between upper and lower plate (fig. 4.2). Therefore, heat conduction is the dominant mechanism, increasing the temperature in the oceanic but decreasing it in the continental plate. After about $5 \cdot 10^5$ years the inelastic deformations along the frictional coupling zone are significantly increased allowing for shear heating to dominate over heat conduction in the continental plate. In the oceanic plate shear heating leads to an additional temperature increase as shown in figure 4.9c.

The vertical heat flux (fig. 4.9d) is the dominant component of heat transport in the model. In the upper plate coupling zone the flux decreases continuously from the upper towards the lower end, while it generally increases by up to 4 mWm^{-2} between $1.6 \cdot 10^5$ and $1.6 \cdot 10^6$ years of subduction. Further to the east the heat flux is nearly the same for all times but still decreases with increasing distance to the trench. In the lower plate the heat flux decreases over time for up to $1.0 \cdot 10^6$ yrs. After $1.6 \cdot 10^6$ years it has nearly reached the values obtained after $1.6 \cdot 10^5$ years again. Inside the zone of coupling the flux is nearly constant for up to $5.0 \cdot 10^5$ years. Later the flux changes more rapidly towards the downdip end, while approaching constant values further to the east. 20 km west of the coupling zone the heat flux reaches its minimum, while increasing with higher distances. This increase might be due to boundary effects.

4.5.3 Summarizing interpretation

Due to the frictional coupling the trench-near regions of the continental plate move in the same direction as the oceanic plate. Additionally, the continental plate is pushed towards the west, i.e. perpendicular with respect to the oceanic plate but with only half the velocity (fig. 4.6b). As a result the continental trench-near regions experience most of the shear strain (fig. 4.6d). Because of the short time scales and high viscosities only small inelastic deformations occur. The continental plate is therefore folded in a similar way as suggested by Biot (1961) and Ramberg (1962). According to their results the dominant wavelength of the fold is given by

$$L_d \propto H \cdot R^n$$

with the thickness H of the deforming geological unit, the viscosity ratio R between the upper and lower unit viscosity and the exponent n ranging between $1/3$ and $2/3$ (see the review by Schmalholz and Mancktelow, 2016). In the reference model the viscosities are

nearly constant, while the thickness H of the lithosphere, and therefore the wavelength L_d as well, increase from the trench towards the east, which is consistent with figure 4.9a. The shear stresses are not limited in the coupling zone, and thus the wavelength decreases with time (fig. 4.9a). Nevertheless, the possible back-arc zone in the continental plate 300 km east of the trench shows reasonable uplift rates of 2 mm/a at maximum and -0.4 mm/a of subsidence at 100 km east of the trench. Compared to observations of the Andean subduction zone (e.g. Gregory-Wodzicki, 2000; Lamb, 2016; Scott et al., 2018), the values obtained in this study are a factor of 10 higher on average. Several studies of rocks found along fault zones (Maino et al., 2015; Mori et al., 2015; Fukumura et al., 2019) show evidence for long-term shear heating with local temperature increases of about 40 K to 100 K suggesting a friction coefficient of about $\mu \approx 0.4$. In the reference model of this study an increase by up to 45 K is observed after $1.6 \cdot 10^6$ years for $\mu = 0.2$. This shows that although the model presented is quite simple compared to reality, it is already in good agreement with first order observations.

The results show that after $1.6 \cdot 10^5$ years, boundary effects affect about 300 km of the model from the position where the velocities are applied towards the center of the model (fig. 4.6a, 4.6c). Trench-near regions of the continental plate are thus unaffected because the plate's horizontal extension is sufficient. However, above the position of the applied Winkler foundations (fig. 4.3), the continental plate subsides due to conservation of mass although no subsidence in the continental plate is observed in reality (Gregory-Wodzicki, 2000). In reality surrounding materials would flow into these regions to balance the amount of subsidence, which is not considered for the numerical model. The Winkler foundation is also the reason for the overall subsidence of the model. The foundation modulus is constant in time and can not be varied throughout the simulation. Its value is chosen as the corresponding lithostatic pressure of the underlying mantle material. However, at the beginning of the subduction simulation all boundary conditions are suddenly switched on resulting in significantly higher strain rates and stresses compared to the remaining simulation duration (see the discussion in section 6.3.2). During this warm-up time the foundation modulus is, thus, lower than actually needed and large parts of the model subside by several hundreds of meters until a state of dynamic equilibrium is reached.

During the subduction simulation no temperature conditions, except for the initial distribution, are applied. Therefore heat conduction is the dominant heat transport mechanism, heating up the overall continental and oceanic lithosphere including the surface (fig. 4.7, 4.9c). In many other studies (e.g. Billen and Hirth, 2007; Gerbault et al., 2009; Popov et al., 2012; Marot et al., 2014; Baes et al., 2018) the temperature of the surface as well as the LAB or model bottom are fixed. The intention for the present study was to analyze a fully dynamic model. However, this approach may lead to additional uncertainties because in reality the surface temperature is controlled by atmospheric conditions as well and the LAB is a dynamic boundary changing its position over time. None of this is included in the model and for the final model (chapter 6) fixed temperatures at the surface and LAB are to be used. The permanent increase in heat flux over time along the continental zone of friction seems to correlate with the respective temperature increase and is an indicator for increased shear heating in the model. Along the oceanic part of the coupling zone the temperature increases as well but to a much higher degree because of the higher temperature gradient between the upper crust and asthenosphere with respect to the continental plate. In contrast to this the heat flux decreases for the first about 10^6 years of subduction until it starts to increase as well. Thus, this is the time needed for the temperature along the oceanic crust

to reach a stable equilibrium due to thermal conduction. Afterwards shear heating becomes the dominant heating process.

5 Parameter study

During the parametric study several physical and numerical parameters were changed to study their effects on the final result. In the beginning of this chapter the ranges applied for the different parameters are discussed and a general overview of the results is given. The second part discusses the model changes with respect to the reference model for the most important parameters, while further results can be found in appendix B.

5.1 Changes in parameters

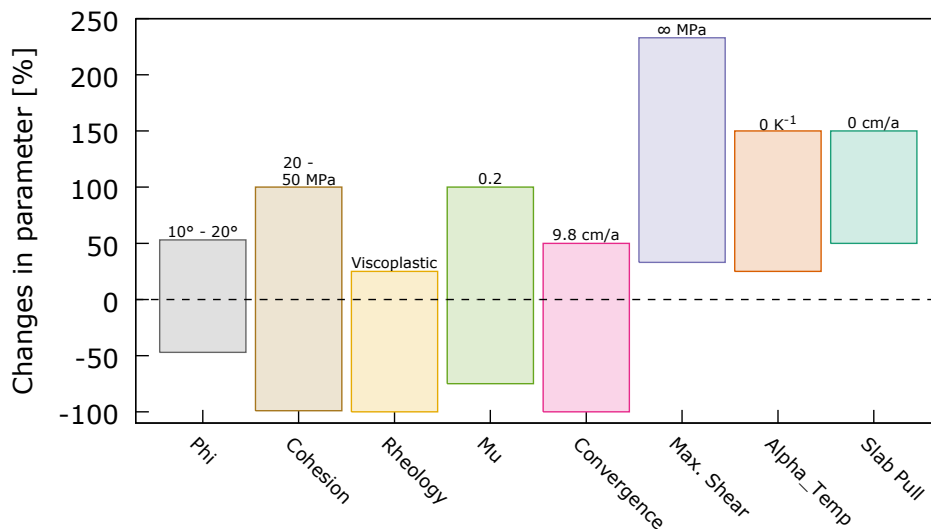


Figure 5.1: Parameter ranges considered during the parametric study. The values above the bins denote the values used in the reference model. Phi-angle of internal friction, Cohesion-cohesion, Rheology-dominant type of rheology, Mu-friction coefficient, Convergence-convergence velocity, Max. Shear-maximum threshold shear stress up to which friction takes place, Alpha_Temp-linear thermal expansion coefficient, Slab Pull-slab pull velocity

Figure 5.1 shows the considered variations of all physical parameters with respect to the values used in the reference model. All parameters were varied by at least $\pm 50\%$. In case of the thermal expansion coefficient, maximum threshold stress, and slab pull velocity, a value of 100% corresponds to $4 \cdot 10^{-5} \text{ K}^{-1}$, 60 MPa, and 6.5 cm/a, respectively. The dominant type of rheology means the possible type of deformations, i.e. elasto-viscoplastic in the reference model. A value of -100% corresponds to a purely elastic deformation, while +100% means elasto-plastic. For values in between only parts of the model deformation are changed to either elastic or elasto-plastic.

The angle of internal friction is essential for controlling the amount of inelastic deformation in the model. As such it is expected to have a significant influence on the results of the

reference model. A typical value under dry conditions is $\phi = 30^\circ$ corresponding to the high pressure regime of Byerlee's law (Byerlee, 1978). Depending on the resolution of the model, the upper crust may split into sediment- and quartz-rich types of rocks. Including sediments means accounting for fluids that effectively reduce the normal stress by the pore pressure. By defining the ratio λ between pore fluid pressure and lithostatic pressure, the friction coefficient μ can be replaced with an effective coefficient $\mu' = \mu(1 - \lambda)$. Assuming the critical taper theory (Dahlen, 1990), the angle ϕ is similarly reduced to an effective angle ϕ' . Sediments and other fluid-rich types of rocks are transported along the slab interface effectively reducing ϕ in deeper parts of the model as well. Therefore, ϕ has been varied by $\pm 5^\circ$ and $\pm 10^\circ$.

The thermal expansion coefficient typically varies between $2 \cdot 10^{-5}$ and $4 \cdot 10^{-5} \text{ K}^{-1}$ (Afonso et al., 2005) depending on the type of material, temperature, and pressure whereas $\alpha_{th} = 3 \cdot 10^{-5} \text{ K}^{-1}$ is the typically used value (e.g. McKenzie et al., 2005; Burg and Schmalholz, 2008; Babeyko and Sobolev, 2008; Gerbault et al., 2009; Popov et al., 2012; Lin and Kuo, 2016). Depending on the temperature α_{th} reduces the density of the material and the amount of deformation, whereas the reduction in deformation is given by $\alpha_{th}\Delta T$ and thus depends on the changes in temperature with time. For a short-term simulation, the temperature is nearly constant with minor changes occurring in the zone of frictional coupling. Because the same coefficient is applied in the overall model, changes in density are expected to be the same relative to each other leading to insignificant changes. Thus the value is set to 0 K^{-1} in the reference model and varied during the parameter study between $1 \cdot 10^{-5}$ and $6 \cdot 10^{-5}$.

The cohesion controls the amount of inelastic deformation in the model as does the angle of internal friction ϕ . For high normal stresses the effect of ϕ is higher (see eq. (3.9)) and therefore it may only affect the upper parts of the model. For the cohesion typical values are 0 MPa in the crust and up to 50 MPa in the lower lithosphere (e.g. Byerlee, 1978; Schön, 1983), but it may also reach several 100 MPa (Afrouz, 1992; Marone, 1995). In this study it is therefore varied by up to several orders of magnitude.

Due to the short time scale of $1.6 \cdot 10^5$ years, viscoplastic deformations are very small and the model is assumed to be nearly purely elastic. To evaluate the influence of those inelastic deformations the type of deformation is varied between purely elastic and elasto-viscoplastic but with an elasto-plastic deforming crust.

Along the zone of friction in reality shear stresses are built up until a threshold value is reached and the shear stress suddenly drops causing earthquakes. This stick-slip behaviour can be simulated by introducing a maximum threshold shear stress. If the shear stress is below this threshold friction takes place, while otherwise the plates slide past each other. Typical values are in the range of 20 MPa to 100 MPa (e.g. Molnar and England, 1990; Peacock, 1992; Tichelaar and Ruff, 1993; Peacock, 1996; Lamb, 2006; Krien and Fleitout, 2008; Seno, 2009; Luttrell et al., 2011; Bletery et al., 2017). Those shear stress values are, however, not directly comparable with the values needed for this study because the authors did not account for viscoplastic deformations. Thus, the maximum threshold shear stress to be applied is possibly higher than the values given and therefore the shear stresses needed to generate a similar amount of inelastic deformations as for the plastic case are generally higher. Hence, the range considered for this study is 20 MPa to 140 MPa.

As already mentioned in section 4.3, the friction coefficient may reach values no larger than $\mu = 0.3$ (Craig et al., 2014) but typically one assumes $\mu \lesssim 0.1$ depending on whether

a subduction channel is used or not. The range considered for the parametric study is therefore $0.05 \leq \mu \leq 0.3$.

Besides the material parameters, kinematic and numerical parameters are altered as well. The convergence velocity in the reference model is 9.8 cm/a (fig. 4.3), i.e. 30% higher than what is observed for the South American subduction zone (e.g. Norabuena et al., 1998; Angermann et al., 1999; Vigny et al., 2009). Due to the nondimensional character of the conservation equations (section 3.1), an increase in velocity by a factor of f should result in a model state corresponding to the simulation time considered but increased by this factor f , as long as f is not too large. In the reference model the simulation time is $1.6 \cdot 10^5$ years corresponding to $2.1 \cdot 10^5$ years of subduction of the Nazca plate. This scaling is important to reduce the computational time of the final models and thus the convergence velocity is varied by up to $\pm 50\%$.

The slab pull velocity can only be acquired by comparing numerical results with observations in the field. However, the numerical models depend on many different kinds of parameters and therefore it is hard to estimate this velocity. In a recent study van Summeren et al. (2012) estimated the amount of slab pull by introducing a "slab pull fraction" f_{sp} varying between 0% and 100%, which is multiplied by the total slab pull force. They found good correlations in comparison with the NNR-NUVEL-1A plate velocities (DeMets et al., 1994) for $f_{sp} \gtrsim 50\%$. Nevertheless the slab pull velocity remains unknown and many authors (e.g. Sobolev and Babeyko, 2005; Gerbault et al., 2009; Zeumann, 2013) assume it to be the same as the ridge push velocity of the oceanic plate although this may be an oversimplification assuming a steady state subduction. In this study the slab pull velocity is therefore varied in a wide range of $\pm 50\%$ around the corresponding ridge push velocity of 6.5 cm/a.

The mesh is always one of the most important aspects in finite element modelling, because it represents the geometry and defines the spatial resolution and numerical accuracy. Hence a model with a higher number of elements has been tested and in a second model the type of elements have been changed from hexahedrons to tetrahedrons.

5.2 Results

5.2.1 Overview

Figures 5.2 and 5.3 give an overview of the main results obtained by changing single model parameters in the ranges shown in figure 5.1. All results shown in this chapter are obtained along the paths presented in figure 4.8. The vertical movement is presented along the crust (green paths) whereas the paths are shortened by 300 km to neglect boundary effects. The shear stress and vertical heat flux are only discussed around the zone of frictional coupling (red path). The histograms reveal that most model runs yield very similar results (deviation $\lesssim 10\%$) compared to the reference model. In some cases however, the deviations are more significant. The relevant parameters are thus the angle of internal friction ϕ , cohesion, type of rheology, maximum threshold shear stress, friction coefficient μ , convergence velocity, and slab pull velocity. Results obtained due to variations in the coefficient of thermal expansion α_T are therefore not discussed in the following.

In general the differences in the oceanic crust are higher due to its lower thickness compared to the continental crust. The heat flux only shows minor changes of no more than 12%

along the frictional coupling zone, while the variations in shear stress reach up to 55% for the same region. The vertical movement along the crust is the most affected variable with changes of up to several 100%. Although the results shown in the histograms are not directly comparable with each other because they are obtained at different paths through the model, some parameters do generally affect multiple aspects of the model. The convergence velocity is the most important parameter affecting both the continental and oceanic crust with significant deviations in vertical movement, shear stress and heat flux. The vertical movement is furthermore significantly influenced by the slab pull velocity and also affects the vertical heat flux in both plates (section 5.2.5). If the dominant rheology of the oceanic and continental crust is defined as elasto-plastic instead of elasto-viscoplastic, the vertical movement and shear stress change substantially, whereas the movement in the oceanic crust is the most affected (section 5.2.2). The angle of internal friction and the cohesion only cause the vertical movement to change but not the heat flux and shear stress along the frictional coupling zone (section 5.2.3). Varying the friction coefficient mostly changes the oceanic crust, while in the continental crust the shear stress is the only significantly affected variable. Applying a maximum threshold shear stress does not influence the movement of the continental crust. Heat flux and shear stress in the zone of coupling do change, while in the oceanic crust the shear stress is unaffected but heat flux and movement change (section 5.2.4).

Besides changes in a single model parameter, several combined parameter changes were tested to see if there are additional effects. For most cases the differences with respect to the reference model are the sum of the differences of the corresponding single parameter changes. By simultaneously varying the angle of internal friction and the cohesion as well as by varying the angle of internal friction and the viscosity, additional effects can be observed (section 5.2.3 and 5.2.6). Finally, the finite element mesh has been edited and it is found that an increase in the number of elements as well as a change in the type of elements yield results that are consistent with the reference model (section 5.2.7).

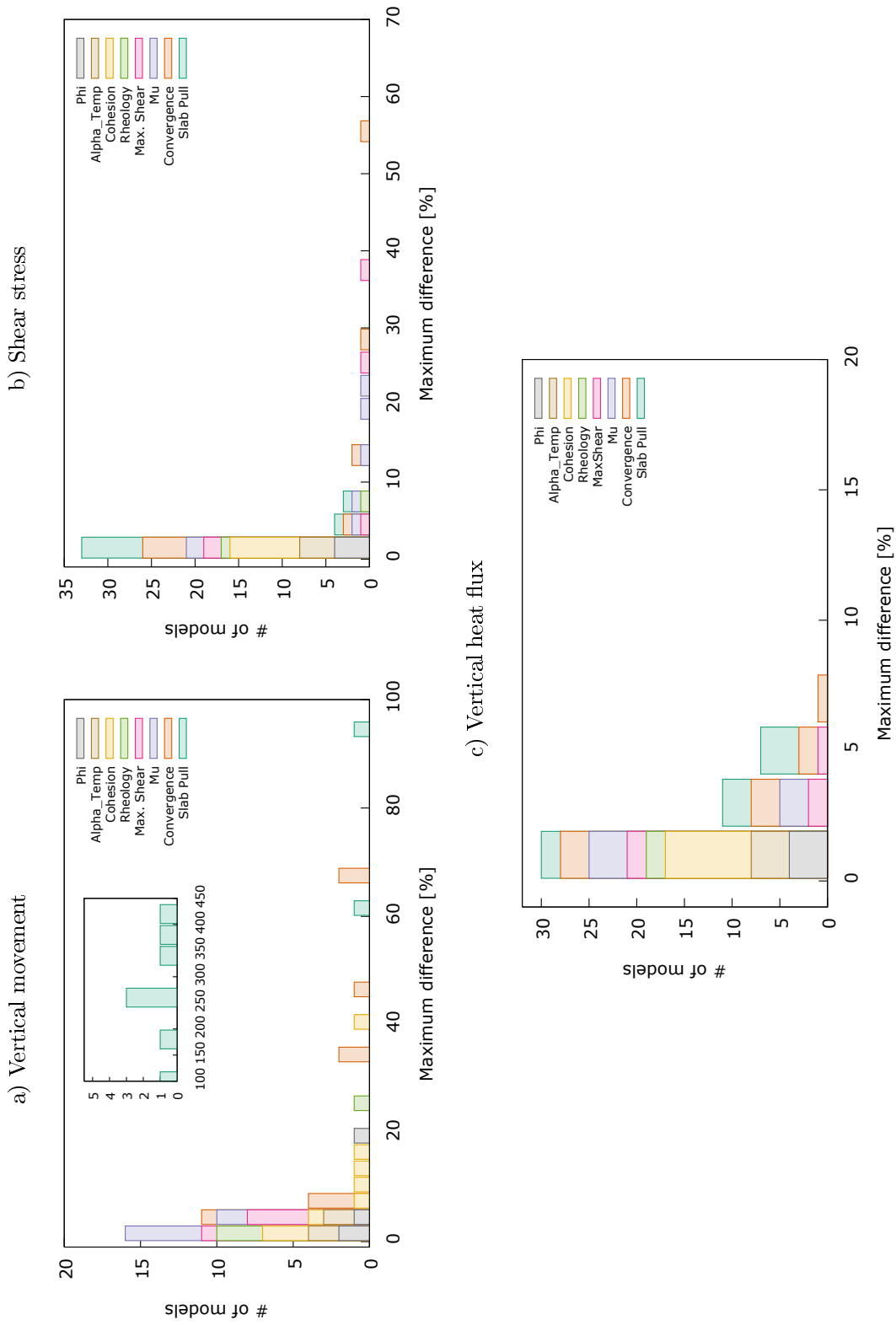


Figure 5.2: Number of models with differing material parameters and their corresponding maximum relative difference in vertical movement, shear stress, and vertical heat flux along the paths in figure 4.8 with respect to the reference model for the continental crust. For the changes in vertical movement the paths were shortened by 300 km to neglect boundary effects.

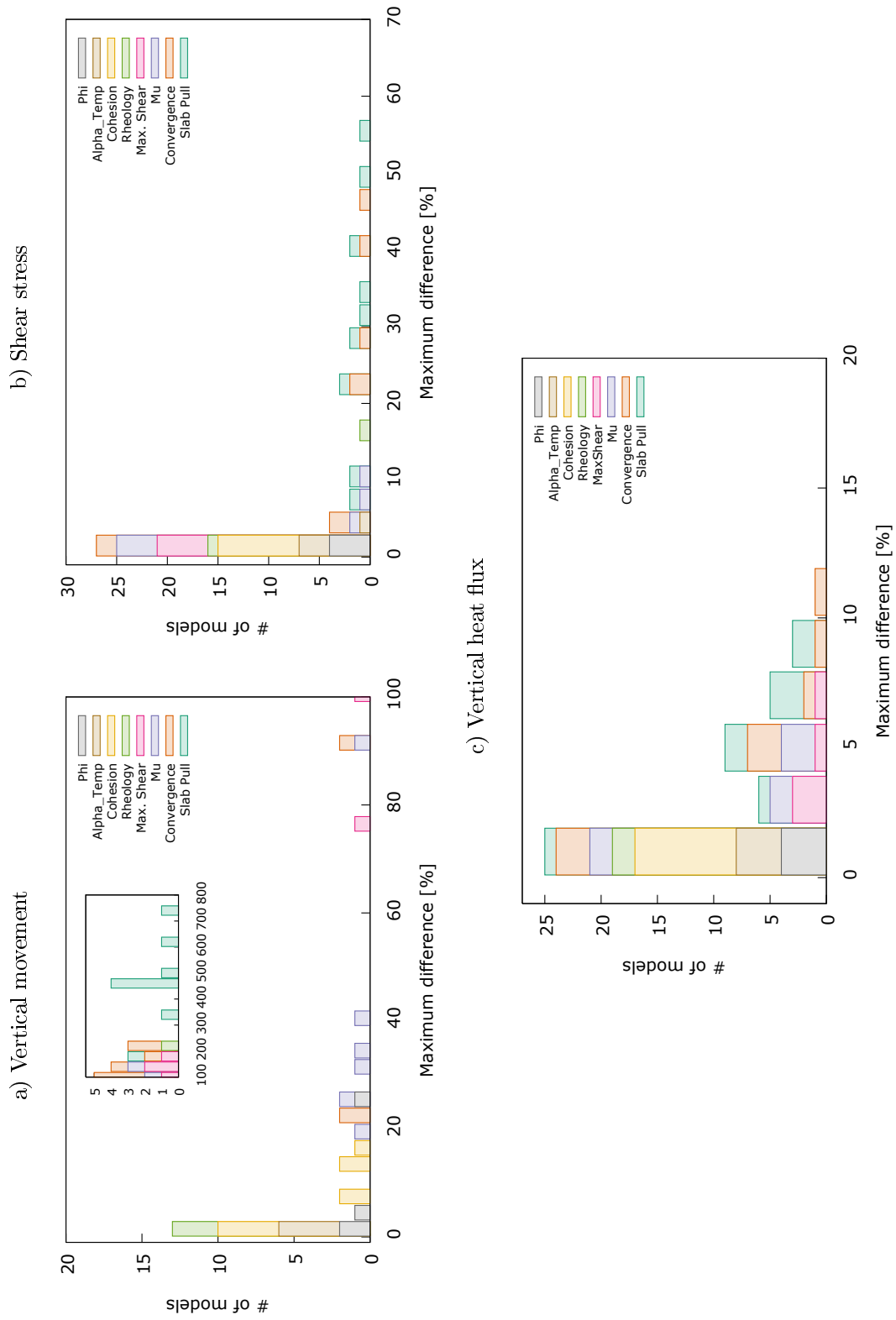


Figure 5.3: Same as figure 5.2 for the oceanic crust.

5.2.2 Rheology

The type of rheology fundamentally defines the deformation. In the reference model all regions undergo elasto-viscoplastic deformations, i.e. if the yield function (eqn. 3.9) is below zero elastic deformations do occur but viscoplastic deformations in all other cases. By varying the type of rheology one is able to study the effects caused by inelastic deformations, which is important to understand the influences caused by a change in any other physical or mathematical parameter. Here the results for a completely elastic model and a model with an elasto-plastic instead of an elasto-viscoplastic continental and oceanic crust are presented.

Figure 5.4 shows the model differences with respect to the reference model. In case of a completely elastic model the changes in vertical movement, shear stress, and heat flux are negligible and thus the reference model is nearly in a fully elastic state. If the continental and oceanic crust undergoes elasto-plastic deformations the results change significantly. For both plates the changes in vertical movement along the crust are very similar except far to the east and at the trench. In the east, the continental plate is additionally uplifted by more than 50 m while the oceanic plate subsides by about 10 m. At the trench the continental plate shows subsidence by 10 m while at the oceanic plate the heights do not change. East of the trench a maximum uplift of about 20 m is observed along both plates, i.e. inside the coupling zone and above respectively, decreasing to almost zero at 200 km to 250 km east of the trench.

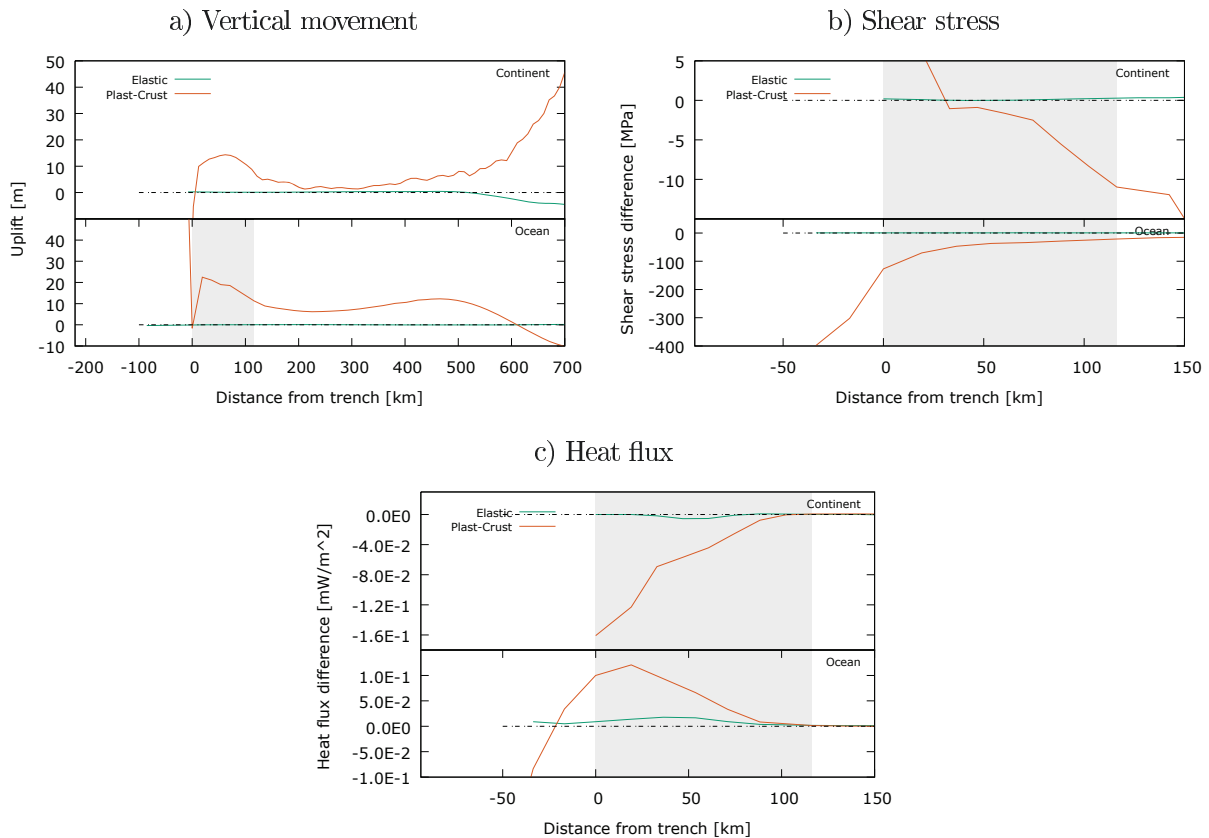


Figure 5.4: Differences in vertical movement (a), shear stress (b) and vertical heat flux (c) due to a completely elastic model and a model with an elasto-plastic instead of an elasto-viscoplastic crust.

The changes in shear stress around the coupling zone differ significantly between upper and lower plate. In the upper plate the shear stress increases by 15 MPa at the trench but decreases by a similar amount at the downdip end and east of it. Around the center of the coupling zone the differences are almost zero. In the lower plate the shear stress decreases by up to 400 MPa west of the trench, still reaching 150 MPa right at the trench. Towards the east the decrease drops down to similar values as observed in the upper plate of about 20 MPa at the downdip end.

The changes in vertical heat flux are similar in magnitude for both plates but with differing signs. Along the continental plate a decrease by up to 0.16 mWm^{-2} at the trench is observed, while along the oceanic plate an increase at the same position of 0.10 mWm^{-2} occurs but the maximum is at 0.11 mWm^{-2} 15 km east of the trench. For both plates the changes in heat flux are continuously reduced to zero towards the downdip end.

5.2.3 Yield function

Besides the type of rheology the yield function determines if there are elastic or inelastic deformations. From eqn. (3.9) it follows that a decrease in either the angle of internal friction ϕ or the cohesion should result in more inelastic deformations. The influence of ϕ is expected to be the most significant one.

In figure 5.5 the results for varying ϕ and the cohesion are presented. By increasing ϕ the model approaches the fully elastic model as expected and by decreasing ϕ the changes are partially similar to the case of an elasto-plastic crust, but with lower magnitudes. While the changes in shear stress and heat flux are negligible, the changes in vertical movement are about half as large as for the elasto-plastic crust model. The most important difference is that the region around the trench is almost unaffected by changes in ϕ whereas at 300 km distance to the east additional uplift is observed in the continental crust. Along the oceanic crust a small uplift is observed between 300 km and 500 km distance to the trench followed by subsidence of a few meters similar to figure 5.4 but only for a decrease in ϕ by 10° . For a decrease by 5° the resulting curve becomes smoother and the position of maximum increase in elevation is shifted to the east by 200 km for both plates. The maximum additional uplift is increased in the continental but decreased in the oceanic crust for a change in ϕ by 5° compared to a change by 10° .

For changes in the cohesion C the results are not as expected. For a decrease or large increase in cohesion the models do behave nearly elastic as expected. But for a moderate increase by factors between 3 and 20, significant differences can be observed. The amount of differences in vertical movement, shear stress and heat flux to the reference model, increases with increasing changes in C up to a factor of 15. For higher factors the differences are decreasing approaching the elastic model results. Both plates show subsidence along the crust for a moderate increase in C . Around the coupling zone and above, a similar amount of subsidence up to 300 km east of the trench with a maximum of about 9 m at 300 km distance and 3 m to 5 m of subsidence around the trench can be found in both plates. Further to the east the vertical movement along the oceanic plate approaches the reference model, leading to a slight uplift at around 600 km distance of no more than 2 m. Along the continental plate the amount of subsidence increases up to 27 m. For both plates the positions of maximum uplift along the oceanic and maximum subsidence along the continental crust are shifted to the east with increasing changes in C . The shear stresses along the zone of coupling are

decreasing with increasing cohesion suggesting more inelastic deformation. Compared to the case of an elasto-plastic crust, the changes along the continental plate are very similar but along the oceanic plate the decrease in shear stress is more than one magnitude smaller. The differences in vertical heat flux are very similar to the ones caused by an elasto-plastic crust (fig. 5.4) as well, but similar to the shear stress they are about one magnitude smaller.

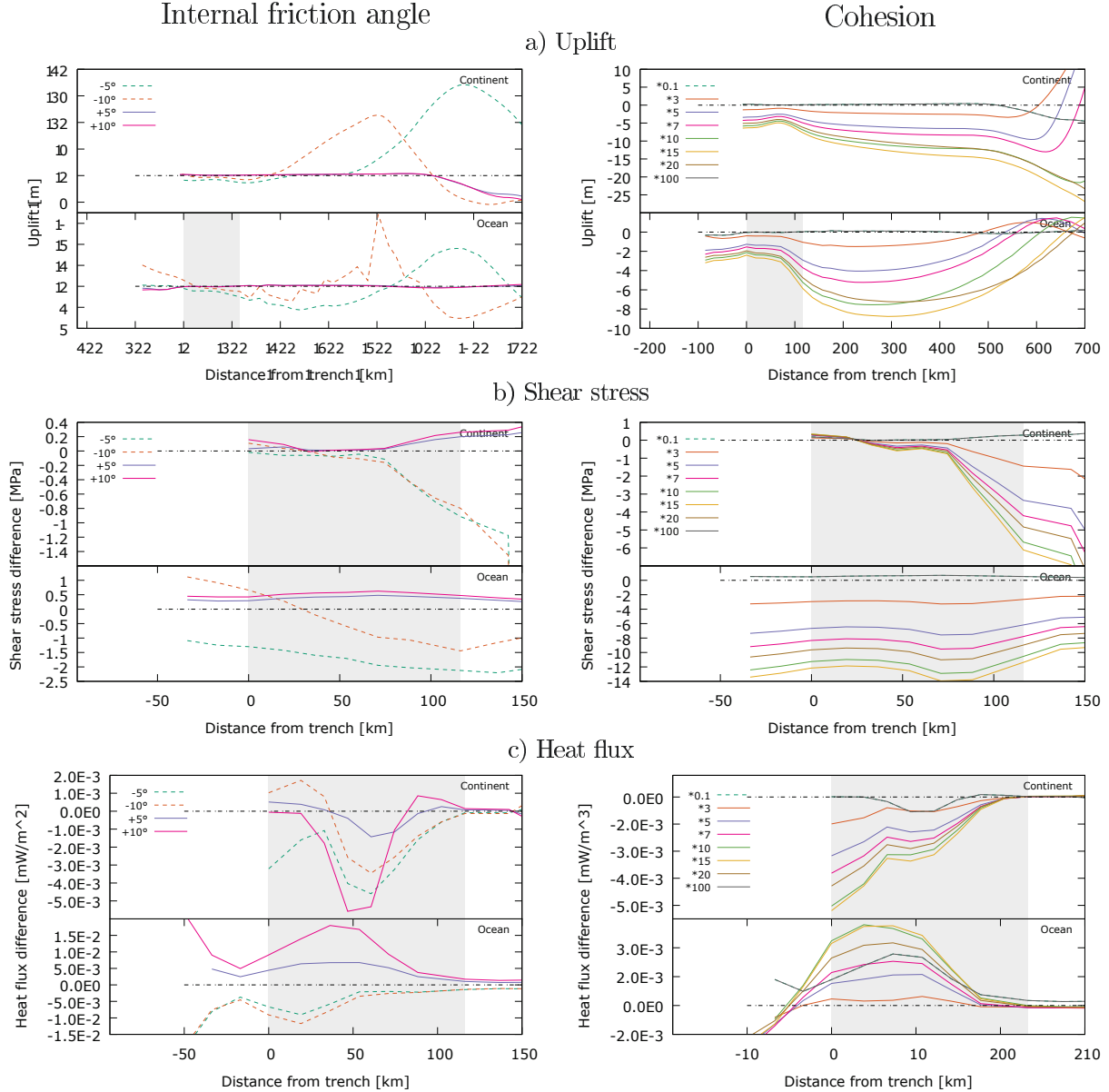


Figure 5.5: Model differences due to a variation in the angle of internal friction by up to $\pm 10^\circ$ (left column) and the cohesion by factors between 1/10 and 100 (right column).

When simultaneously varying both parameters (fig. 5.6) effects additional to the ones observed in figure 5.5 can be distinguished. For simplicity the cohesion has been increased by a factor of 10 while ϕ has been varied as before. On increasing ϕ the model tends to become more elastic, i.e. the effects for a moderate increase in cohesion are significantly reduced. A decrease in ϕ significantly amplifies nearly all effects due to the increase in cohesion, whereas the changes by the sole decrease of ϕ only influence the easternmost parts of the model. Here,

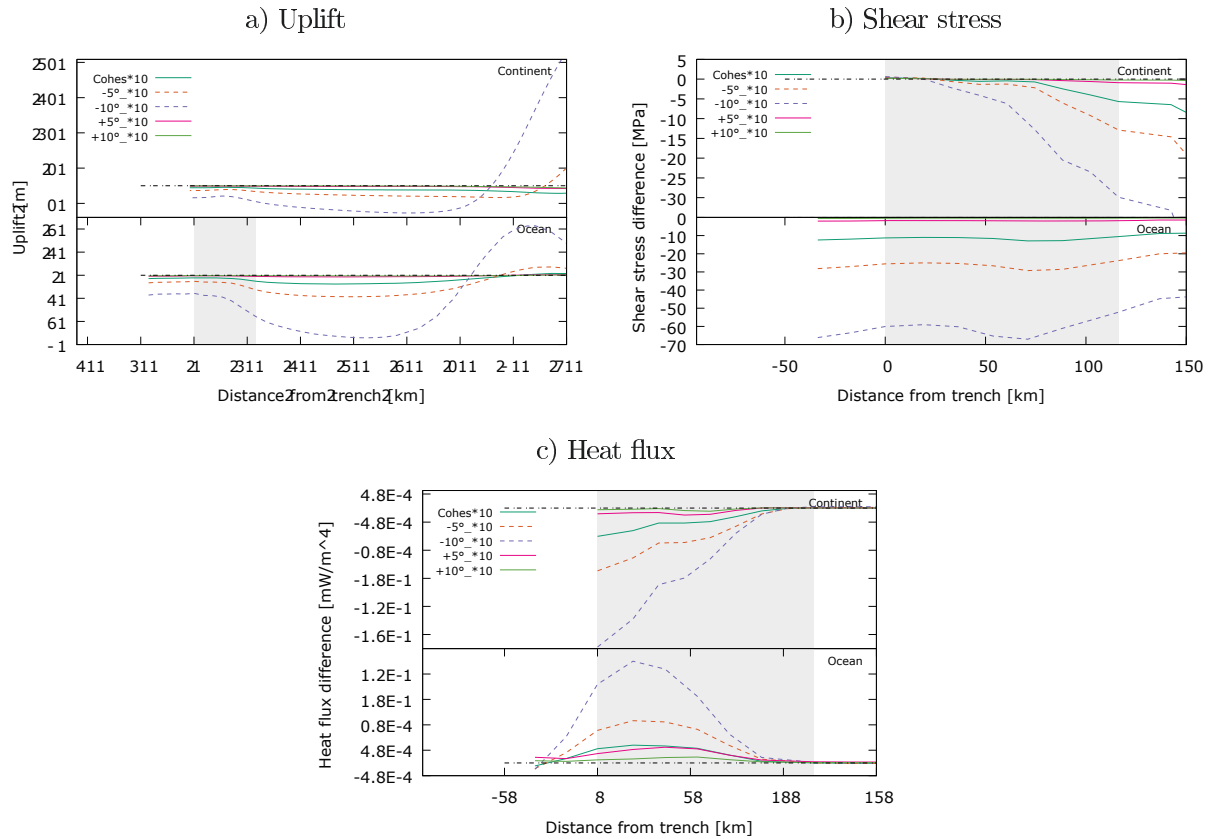


Figure 5.6: Model differences for simultaneously increasing the cohesion by a factor of 10 and varying the angle of internal friction by up to $\pm 10^\circ$.

a high uplift of the continental crust is observed: about 50 m for a decrease in ϕ by 5° but about 370 m for a decrease by 10° at 700 km distance to the trench. Along the oceanic crust the amount of uplift at the east is much smaller being 10 m for a 5° decrease and about 60 m for 10° decrease in ϕ .

5.2.4 Frictional coupling

In the reference model there is no mechanism, such as a subduction channel, to limit the amount of built up shear stresses along the zone of friction. Abaqus provides the possibility to introduce a maximum threshold shear stress to simulate stick-slip behaviour (section 5.1) between the plates. In the reference model this shear stress is assumed to be infinite, i.e. friction always takes place, and so the expectation is that for a decreasing threshold value the differences to the reference model will become larger but only around the zone of friction. Besides this, the friction coefficient μ determines the speed of the increase in shear stress and therefore, both parameters necessarily control the deformation along the zone of friction.

Figure 5.7 shows the corresponding results. At a first glance one observes that the introduction of a threshold shear stress and a variation in μ mainly affect the regions around the zone of coupling as expected. Furthermore, all changes for decreasing μ are very similar in magnitude and curve-shape compared to the models with a decreasing threshold stress,

while for the models with a higher value of μ the signs are reversed and the changes are approaching limiting values, which is to be expected.

For a decrease in μ or the threshold stress the changes in vertical movement along the oceanic and continental crust are nearly the same. The trench-near regions are uplifted by up to several tens of metres. Towards the east, twice the amount of subsidence is found near the downdip end of the coupling zone and above, while another 100 km to the east less than 5 m uplift occurs approaching the values of the reference model further east. While the highest uplift is always observed at the trench, the maximum subsidence is shifted towards the downdip end with decreasing μ or threshold stress.

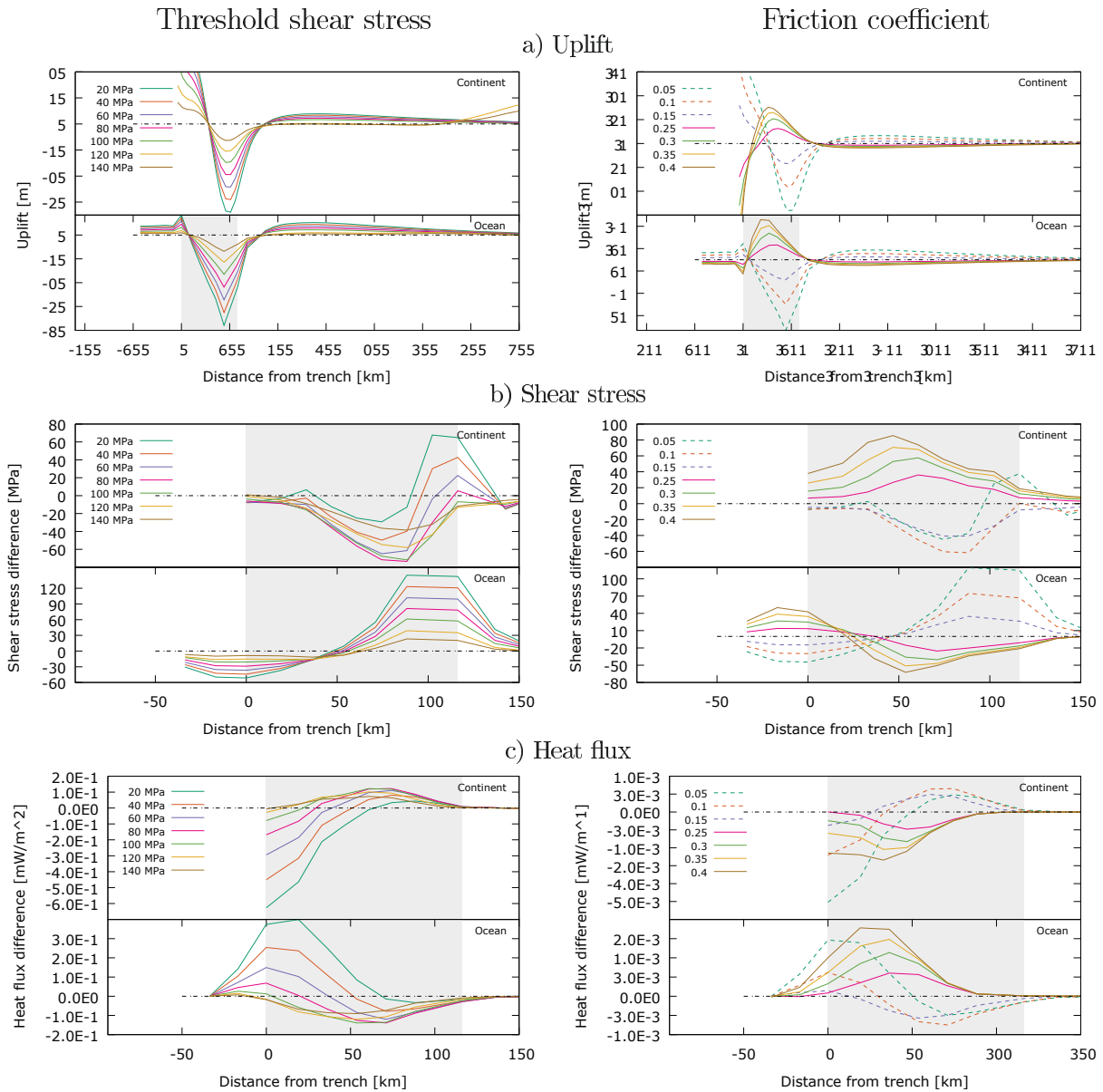


Figure 5.7: Model differences due to the introduction of a maximum threshold shear stress between 20 MPa and 140 MPa (left column) and to varying the friction coefficient between 0.05 and 0.4. (right column)

The shear stress mainly decreases with decreasing μ along the continental coupling zone, whereas at $\mu = 0.1$ or a threshold stress of 80 MPa the maximum decrease is reached with 60

and 75 MPa, respectively, near the lower end of the zone. To the east the shear stress increases with decreasing parameter values but quickly approaches the reference values outside the shear zone. Along the oceanic plate the shear stress only decreases near the trench with decreasing parameter values. To the east the differences approach 0 MPa at around 45 km distance to the trench, whereas at the lower end of the shear zone, between 80 km and 115 km distance, the shear stresses show a maximum increase twice as high as the maximum decrease at the trench. In all cases the maximum is reached for the minimum in μ or the threshold shear stress.

The changes in vertical heat flux are slightly higher along the continental plate coupling zone compared to the oceanic plate and with differing sign. At the trench the flux decreases in the continental plate by up to 0.5 mWm^{-2} or 0.6 mWm^{-2} for $\mu = 0.05$ or a threshold stress of 20 MPa, respectively. Towards the center of the coupling zone the heat flux increases, whereas the maximum increase is observed for $\mu = 0.1$ or 80 MPa of threshold stress, similar to the maximum decrease in shear stress. Further to the east and west of the coupling zone the differences are quickly approaching zero in both plates.

5.2.5 Velocity

The plate velocities together with the simulation time determine the considered subduction duration. By varying the convergence velocity the considered duration can be up- and downscaled up to a certain limit, which is important to reduce the simulation duration for more realistic models.

Currently, the movement of the bottom of the slab is controlled by buoyancy forces and by the Winkler foundation applied. As discussed in section 4.5.3 the numerical simulation has a warm-up time and during this time the applied foundation modulus is too low, while after that its value is the correct one. By applying a slab pull velocity in movement direction of the slab's bottom the model might become more realistic. The simulation is able to account for thermal buoyancy of the slab. However, the model is capped at 400 km depth whereas in reality the slab may reach depths below 1000 km (e.g. Bijwaard et al., 1998; Li et al., 2008; Fukao and Obayashi, 2013; Scire et al., 2017). The thermal buoyancy achieved in the model is, thus, lower than expected from these observations additionally favoring the application of a slab pull velocity.

In figure 5.8 the results are shown. Compared to figure 4.9, all changes in vertical movement, shear stress, and heat flux fit with the observations of the long-term study, showing that an in- or decrease in velocity by up to $\pm 50\%$ leads to the corresponding later or earlier stage of subduction as expected. A velocity increase by e.g. 25% results in 55 m additional uplift of the trench along the continental crust, while for a 50% increase the amount of additional uplift is at 110 m.

If the oceanic plate has a north component with an angle between 20° and 60° , different results are observed. With increasing north-directed movement, the total (i.e. sum of continental and oceanic) west-east component of the velocity decreases and both crusts do subside. However, the amount of subsidence for both plates is not comparable with previous results. The trench remains nearly unaffected but the nearest regions to the east show subsidence of about 50 m to 70 m for both plates. Between 450 km and 550 km to the east, the state of the reference model is achieved. At greater distances the continental crust subsides by more than 100 m for a north directed angle between 45° and 60° . For 20° the model

changes are negligible. Along the oceanic crust the differences in vertical movement far away from the trench are below 20 m for all angles. The shear stresses along the zone of friction show contradicting results concerning the continental and oceanic plates. Along the continental coupling zone the shear stress increases with increasing angle to the north, from the trench towards the center of the zone. For 20° the maximum increase is at 40 MPa, while for an angle of 60° it is at 100 MPa. Towards the downdip end and below the shear stresses are decreasing, whereas outside the zone of friction a threshold value seems to be reached. Along the oceanic zone of friction the shear stresses are generally decreasing on including a north-directed velocity component. The amount of decrease is higher than expected because for an angle of e.g. 20° the total west-east velocity is reduced by 4% but the decrease in shear stresses is similar to a reduction by 25%. The decrease is highest below the trench with about 160 MPa, continuously decreasing towards the downdip end to 70 MPa for an angle of 20° and to 50 MPa for 60°. Although the total west-east velocity is reduced with increasing angles to the north, the changes in vertical heat flux are similar to the models with increased west-east velocity. For example in case of an angle of 20° all changes along the continental and oceanic coupling zone are nearly the same as for solely increasing the west-east velocity by 25%. With increasing the angle of northward plate velocity the heat flux increases along the continental, and decreases along the oceanic plate accordingly. Similar observations are found by a general study about oblique subduction by Ji and Yoshioka (2015). Their results reveal that the temperature at the plate interface as well as the heat flux at the surface is rising with increasing obliquity. In contrast to this, Morishige and van Keken (2014, 2017) observed a temperature increase as well, while the surface heat flux has barely changed.

Including a slab pull velocity results in the largest differences observed during this parameter study. If the slab pull velocity is the same as the oceanic plate velocity, i.e. 6.5 cm/a, significant subsidence in both plates is observed, continuously increasing to the east up to 1300 m at 700 km distance. With only 50% of the oceanic plate velocity the maximum subsidence is still about 500 m in both plates. The shear stresses along the zone of coupling are decreasing if a slab pull velocity is included. Along the continental plate coupling zone the shear stress is hardly affected around the trench whereas towards the downdip end the effect increases up to a reduction by 90 MPa. Further to the east the shear stress is continuously decreasing. Along the oceanic plate the decrease diminishes towards the downdip end with values of 180 MPa around the trench and 120 MPa at the lower end of the zone. For only half the slab pull velocity the values are about 45 MPa at maximum along the continental plate and 60 MPa down to 40 MPa along the oceanic plate. The changes in heat flux are similar to the ones observed for an elasto-plastic crust (fig. 5.4). With increasing slab pull the heat flux near the trench within the coupling zone decreases along the continental plate, while increasing with similar magnitudes along the oceanic plate. Towards the downdip end the results of the reference model are achieved. For half the slab pull velocity almost the same magnitudes, compared to the model with an elasto-plastic crust, of 0.2 mWm^{-2} within the continental and oceanic plate are reached.

If a slab pull velocity is applied the overall slab undergoes more subsidence and is stretched with respect to the reference model. Due to mass compensation the upper plate takes part in this process, showing a similar amount of subsidence. The stretching of the oceanic plate reduces the coupling between the plates and the shear stress in both plates as well as the amount of shear heating in the continental plate decreases. Furthermore, the thickness of the oceanic plate is decreased, which increases the temperature gradient and finally the heat

flux. Thus, the heat flux decreases within the continental and increases within the oceanic part of the coupling zone.

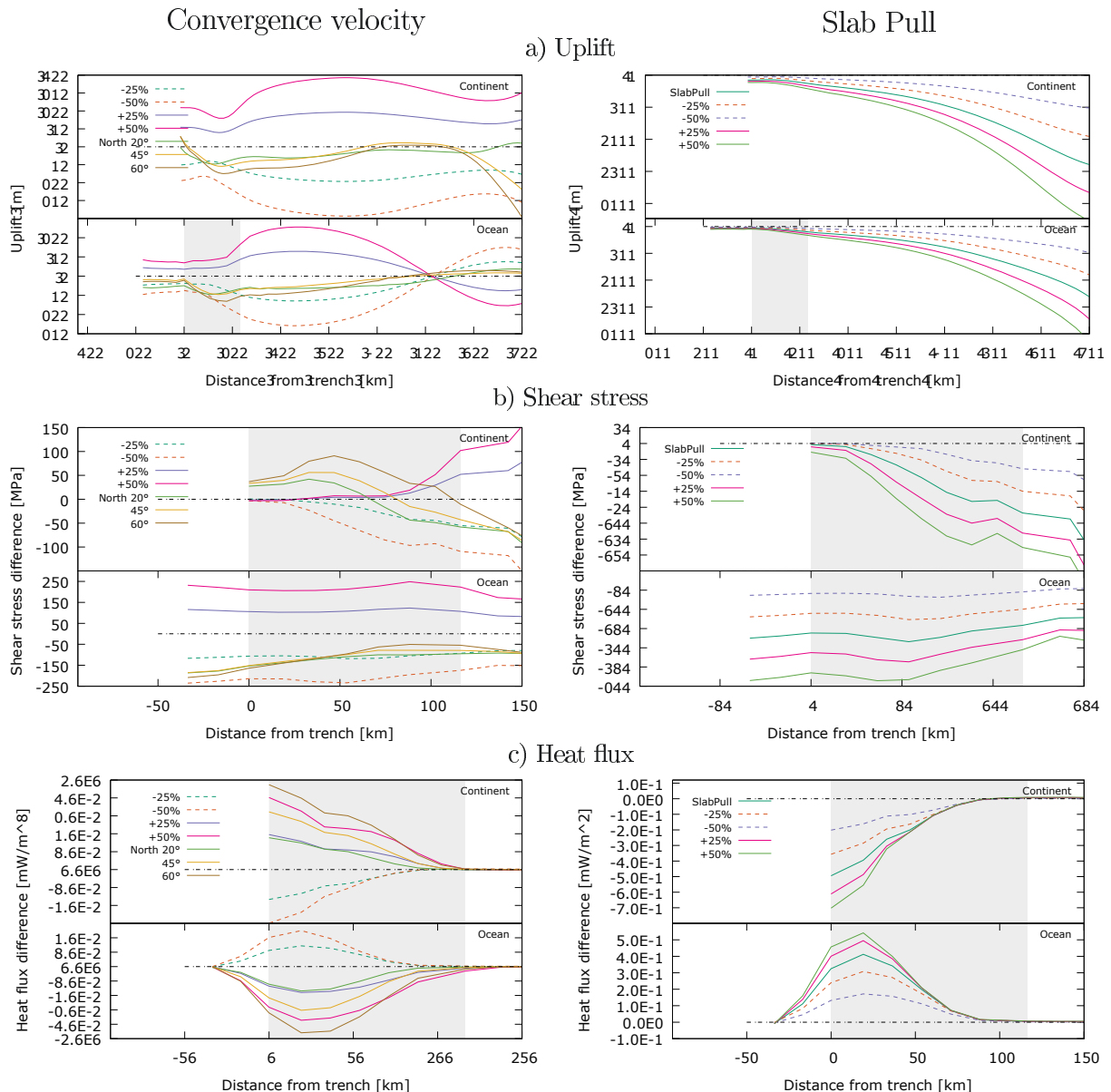


Figure 5.8: Model differences due to changes in convergence velocity by up to $\pm 50\%$, by including a north-directed component of the oceanic plate velocity (left column) and to an additional slab pull velocity varying between $\pm 50\%$ around the oceanic plate velocity (right column).

5.2.6 Viscosity

Due to the high viscosities used, typical Maxwell relaxation times are on the order of 10^5 to 10^6 years in the lithosphere and because of the short simulation timescale of $1.6 \cdot 10^5$ years the model is not expected to change significantly for changes in viscosity. To test whether this is true or not, instead of varying the viscosities used for the reference model I make use of the strain-rate and temperature dependent viscosity defined via dislocation creep (3.10). The

corresponding creep parameters (table 5.1) are mainly taken from the references provided in Babeyko and Sobolev (2008) and are consistent with data provided by e.g. Sobolev et al. (1994), Hirth and Kohlstedt (2003) and Bürgmann and Dresen (2008).

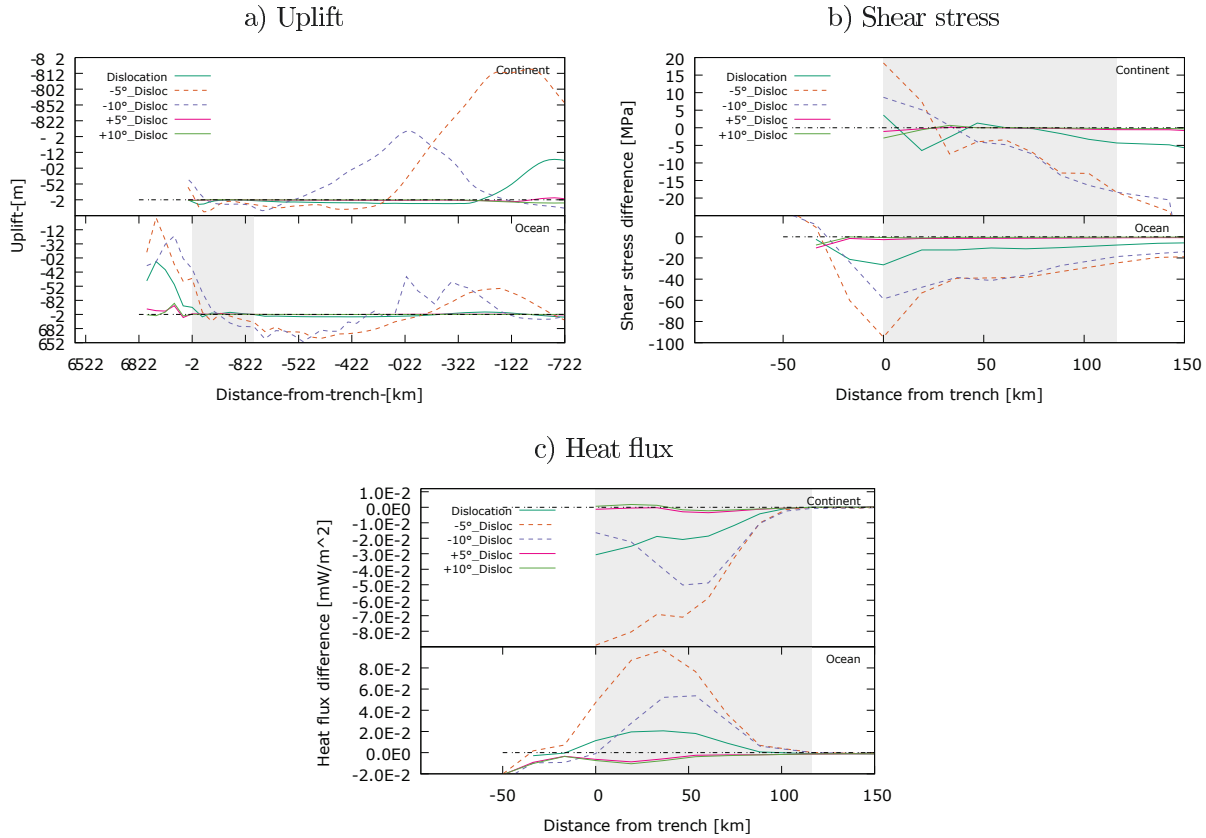


Figure 5.9: Model differences by using a strain-rate dependent viscosity and simultaneously varying the angle of internal friction by $\pm 5^\circ$ and $\pm 10^\circ$

Figure 5.9 shows the results for using dislocation creep and simultaneously varying the angle of internal friction ϕ . The use of a viscosity defined via dislocation creep results in minor changes for the overall model. The variations in vertical movement are negligible except for the regions above the bottom edge of the slab, which is uplifted with respect to the reference model by up to 51 m. The slab itself is nearly unaffected at this position. In the west outside the frictional coupling zone the oceanic plate is uplifted by up to 38 m, but this may be caused by the velocity boundary condition. Decreases in shear stress along the zone of friction are generally below 15 MPa for both plates, while the changes in heat flux are similar to the elasto-plastic crust model, although much smaller in magnitude. If the viscosity and ϕ are varied simultaneously the changes in viscosity amplify the effects observed by solely varying ϕ . As a result the amount of subsidence in the continental plate above the lower edge of the slab is reduced by about 50 m for the case of dislocation creep only and up to 160 m when additionally decreasing ϕ by 5° .

In figure 5.10 the strength profile for the dislocation model is compared to the reference and completely elastic model. In all cases the switches in rheology between the different model parts are at the same position, but the strength is at maximum for the elastic model followed by the dislocation model, whereas the strength in the reference model, in which

Table 5.1: Creep law parameters for the strain-rate dependent viscosity model

	CC	CUL	CLL	CA	OC I	OC II	OC III	OLL I	OLL II	OLL III	OA
N (1)	4.0	4.2	3.5	3.5	4.7	4.7	4.7	3.5	3.5	3.5	3.5
$-\log(A_D)$ ($\text{Pa}^{-N} \text{s}^{-1}$)	27.0	20.0	14.3	14.3	25.9	26.0	26.0	16.0	16.0	16.0	14.3
E_{act} (kJ mol^{-1})	220	440	520	520	480	480	480	530	530	530	520

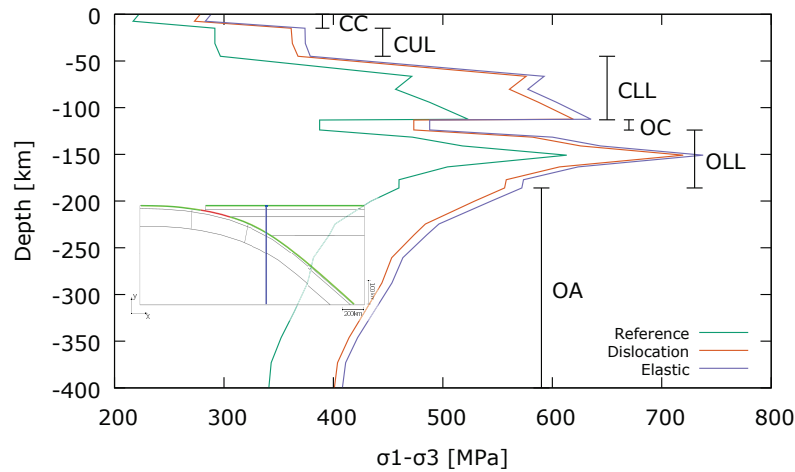


Figure 5.10: Strength profile through the center (blue path in inset) of the model showing the rheological layering for the reference model (depth dependent viscosity) as well as for the model with the viscosity defined via dislocation creep (temperature and strain-rate dependent) and for the fully elastic model.

the viscosity is independent of strain-rate and temperature, is the lowest. Furthermore, at a depth of 150 km the type of deformation switches from frictional to viscous although the LAB is situated at 120 km in the continental and 185 km in the oceanic plate at this position.

5.2.7 Mesh

Using a mesh with a higher resolution of 67.613 instead of 21.180 elements, as done for the reference model, results in a very similar model (figure 5.11b). The most notable effects are less shear stresses and strains as well as less uplift around the eastern and western boundaries and a lower subsidence of the eastern continental plate above the subducting slab. Thus, both models are comparable but with a high resolution mesh one can significantly reduce boundary effects and the upper plate movement is less affected by the subsidence of the slab below the model.

For the final model of northern Chile, tetrahedral elements have to be used to create the mesh for a more realistic geometry. When using this type of elements (figure 5.11c) the model is nearly identical to the reference model but due to the higher resolution, boundary effects are reduced in a similar way as for the high resolution model.

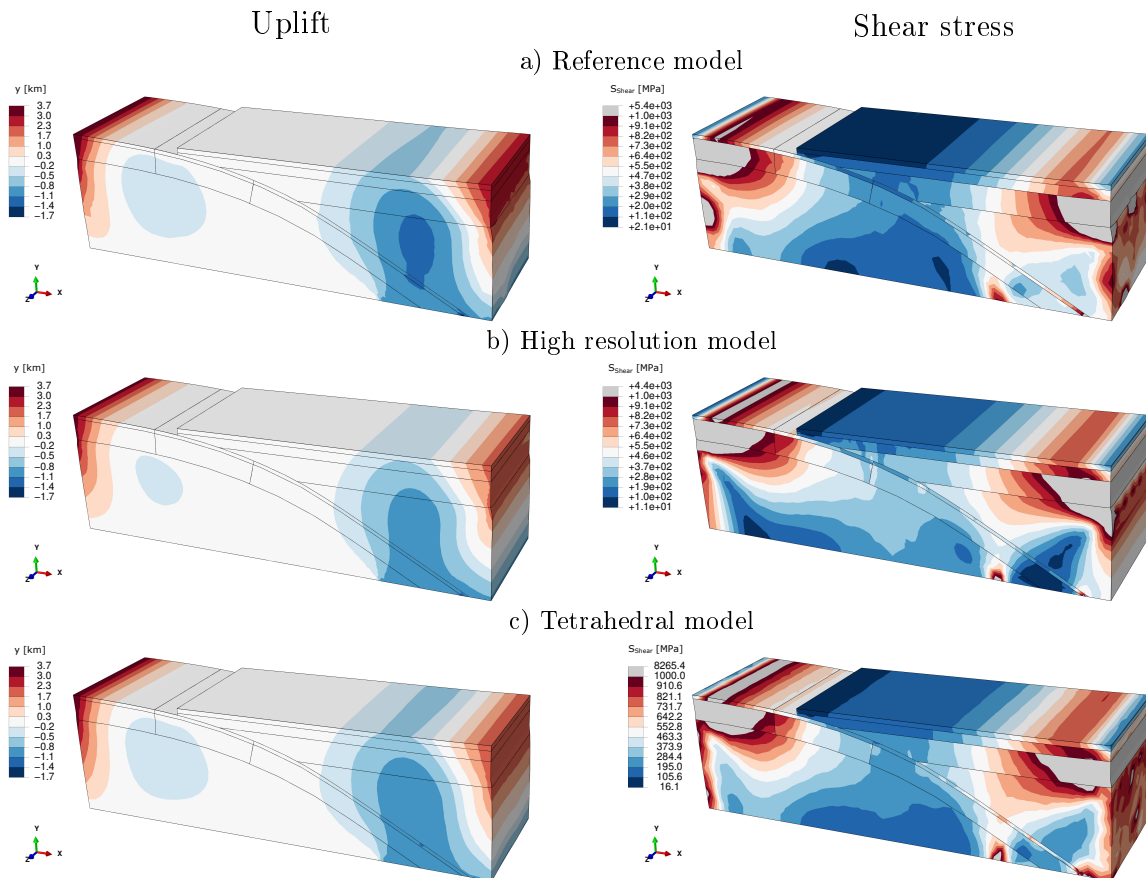


Figure 5.11: Vertical movement (left column) and shear stresses (right column) of the reference (a), high resolution (b), and tetrahedral (c) models after $1.6 \cdot 10^5$ years

6 Modelling South America's subduction zone

This chapter describes the application of the results obtained in the preceding chapters for a generic subduction zone model on the real case scenario in northern Chile (fig. 6.1). The most notable difference to the previous models (chapters 4, 5) lies in the realistic geometry, enabling the direct comparison of the model results with actual measurement data such as topography, bathymetry, GNSS velocities, and earthquake hypocentres. In a second version of the model a slab pull velocity is additionally applied at the bottom of the slab to study its effect on the model results.

6.1 Construction of geometry and mesh

Defining the geometry for the models is the most challenging part, because it determines the quality of the mesh and, therefore, the first order results. The model geometries presented are based on the Bouguer and density model data provided by Tassara et al. (2006) and Tassara and Echaurren (2012) for the range of 17°S - 24°S and 61°W - 78°W (fig. 6.1). This allows for studying the effects of a bended trench including oblique subduction at an angle of 20° to the north similar to previous studies (e.g. Bonnardot et al., 2008; Boutelier and Oncken, 2010; Stegman et al., 2010; Gassmüller, 2011; Iaffaldano et al., 2012; Zeumann, 2013; Contreras-Reyes, 2019). The thickness of the slab is 85 km on average including a crustal thickness of about 6 km, while the average dip angle ranges from 15° to 40° from top to bottom (Tassara et al., 2006).

The point clouds of the model parts as given by Tassara et al. (2006) and Tassara and Echaurren (2012), come in geographic coordinates and I transformed them into units of km via a transverse Mercator projection centered at 68.0°S 22.0°W introducing a maximum distortion of 6 km in height to the model. These data are imported to the software MeshLab 2016.12 (Cignoni et al., 2008), to generate the surface meshes consisting out of triangular faces, using the screened Poisson surface reconstruction algorithm from Kazhdan and Hoppe (2013). I used the software AutoCAD 2017 to manually refine those meshes, i.e. replacing very small triangles and triangles with very acute or obtuse angles, and to define the mesh transitions between intersecting surfaces such as for example the slab surface and the continental Moho. In the last step a cuboid is constructed and cut by the surface meshes, and extended by 150 km to the east and 400 km to the west to reduce boundary effects in the central part of the model during the subduction simulation. The final dimensions of the geometry are thus 2086 km in E-W, 900 km in S-N direction and 410 km from top to bottom, whereas the surface is defined as a flat region situated at 0.5 km above sea level to reduce the amount of very small elements in the mesh. These geometries are exported using the ACIS .sat file format, which can be imported into Abaqus without any limitations. Here the final mesh used for the finite element simulation consists out of 17 parts with different material properties resulting in $1.91 \cdot 10^6$ 4-node tetrahedron coupled temperature-displacement elements and $4.39 \cdot 10^5$ nodes (neglecting additional contact elements and nodes). The mean

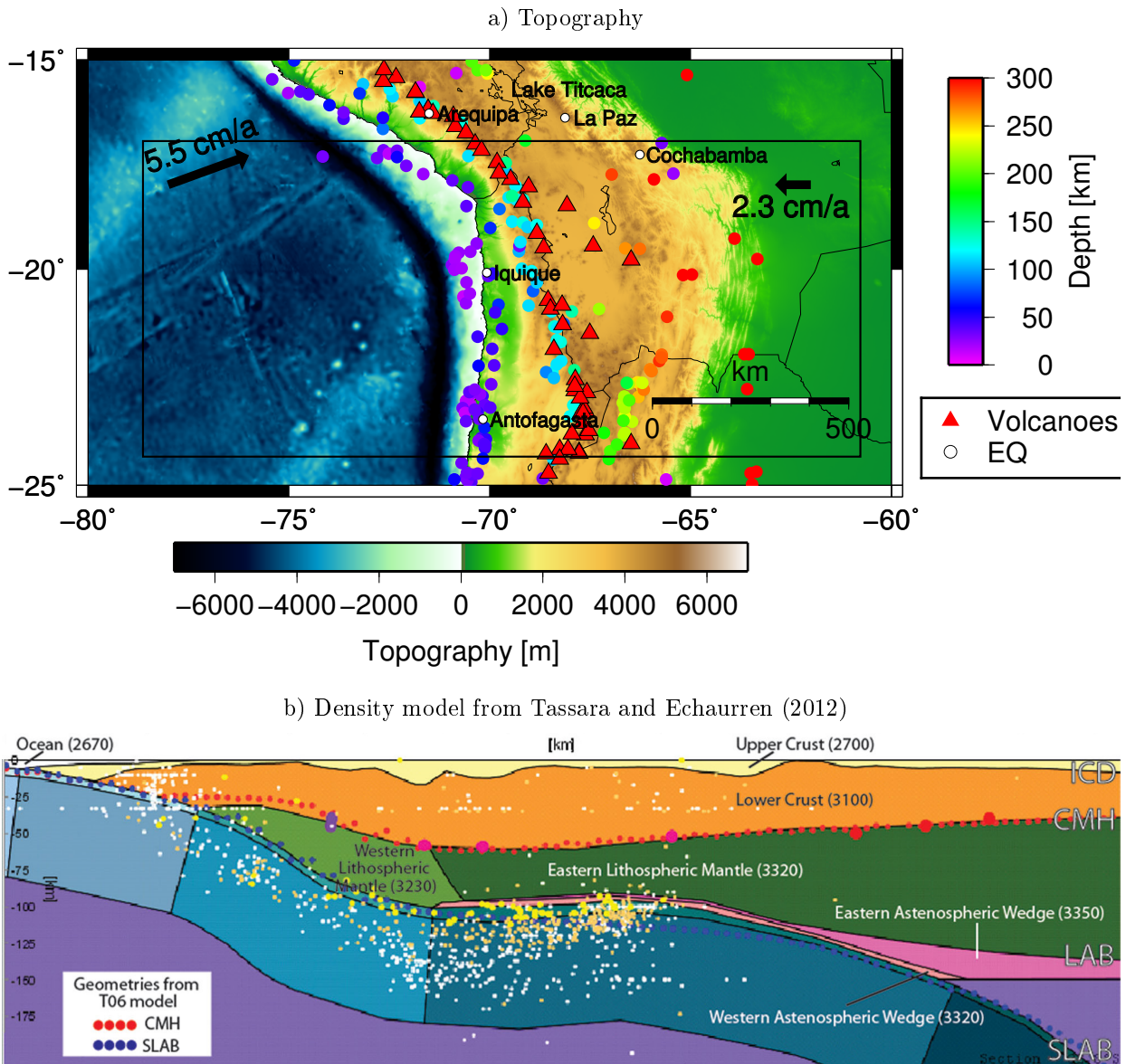


Figure 6.1: a) Detailed topographic map (ETOPO1; Amante and Eakins, 2009) of the study area (rectangle). Red triangles denote volcanoes (<https://www.ngdc.noaa.gov/hazard/volcano.shtml>), circles show earthquakes with magnitudes ≥ 6.0 since 1960-01-01 (USGS), and arrows show the plate velocities (Kreemer, 2009). b) Cross-section of the density model at 32.8°S from Tassara and Echaurren (2012)

maximum element sizes vary from 3 km in the continental and oceanic crust to 25 km in the asthenosphere (figure 6.2a).

6.2 Model properties

Given the mesh the model is defined based on the results of the reference model (chapter 4) and the corresponding parametric study (chapter 5). While the initial stress distribution is very similar to the reference model, the initial temperature distribution does not contain

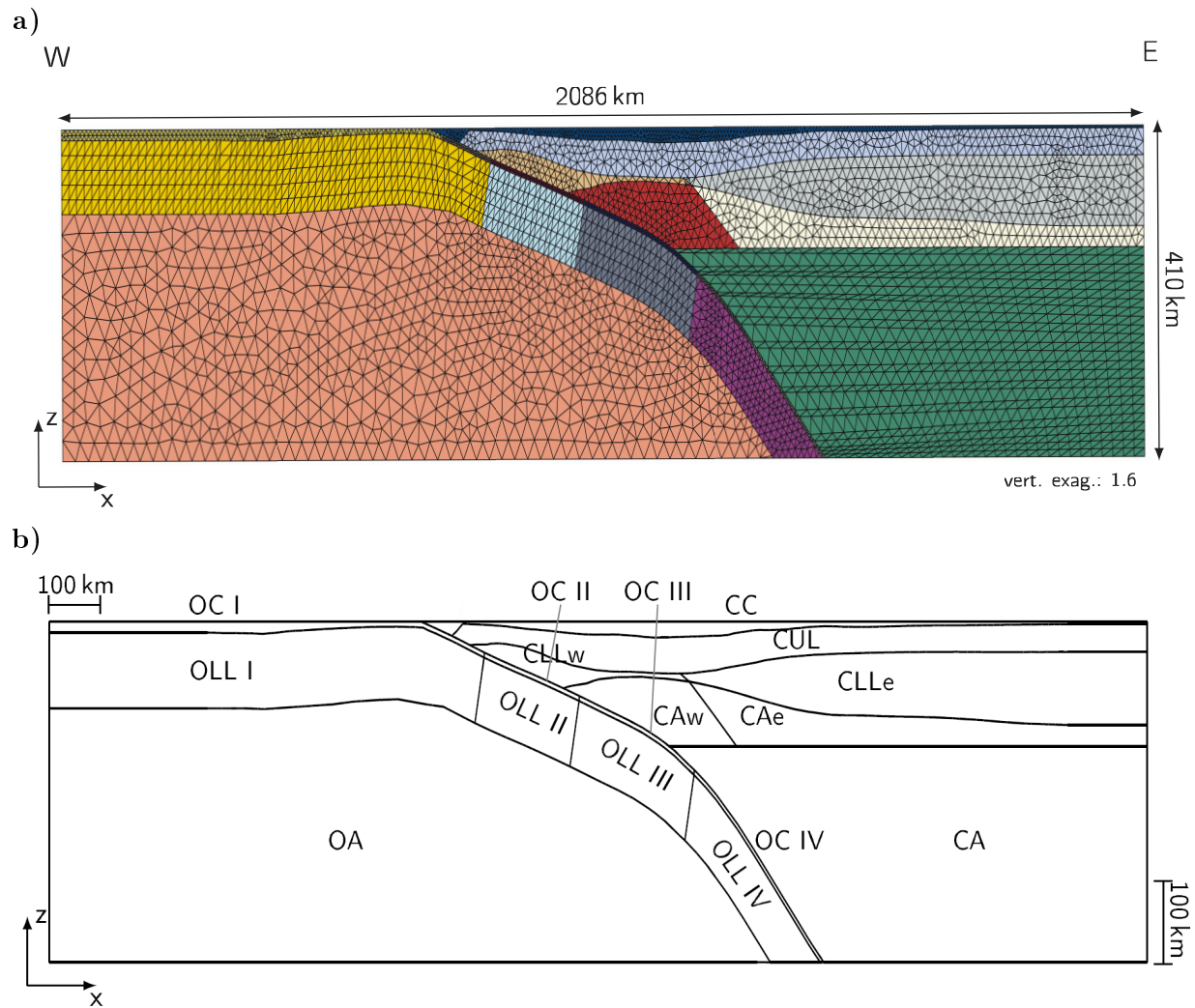


Figure 6.2: Side view showing the mesh (a) and the different parts of the model (b). Abbreviations as in figure 4.1. CLLe-eastern continental lower lithosphere, CLLw-western continental lower lithosphere, CAe-eastern continental asthenosphere, CAw-western continental asthenosphere

any mass flow because this is not available in Abaqus for tetrahedron elements. Thus, the temperature distribution is determined by the temperature at the surface and at the LAB, and by radiogenic heating in the continental plate down to the Moho (figure 6.3).

All boundary conditions applied to the reference model (fig. 4.3) are applied here, too, except that the oceanic Nazca plate moves with a velocity of 5.5 cm/a instead of 6.5 cm/a and the continental South American plate moves with 2.3 cm/a instead of 3.3 cm/a as for the reference model (see Hoffmann-Rothe et al., 2006 for a summary as well as Kremer, 2009). The Nazca plate velocity is split into a W-E and a S-N component with an angle of 20° towards the north. Additionally, radiogenic heating is applied in the continental crust with values of $1.3 \mu\text{Wm}^{-3}$ and $0.35 \mu\text{Wm}^{-3}$ (e.g. Ranalli, 1995; Currie et al., 2002; Turcotte and Schubert, 2014) for the heat production rate in the model units CC and CUL (see fig. 6.2b), respectively.

The geometry of the model allows to include the complete zone of friction, i.e. from updip to downdip limit. According to Hoffmann-Rothe et al. (2006), the updip limit is at about 4 km

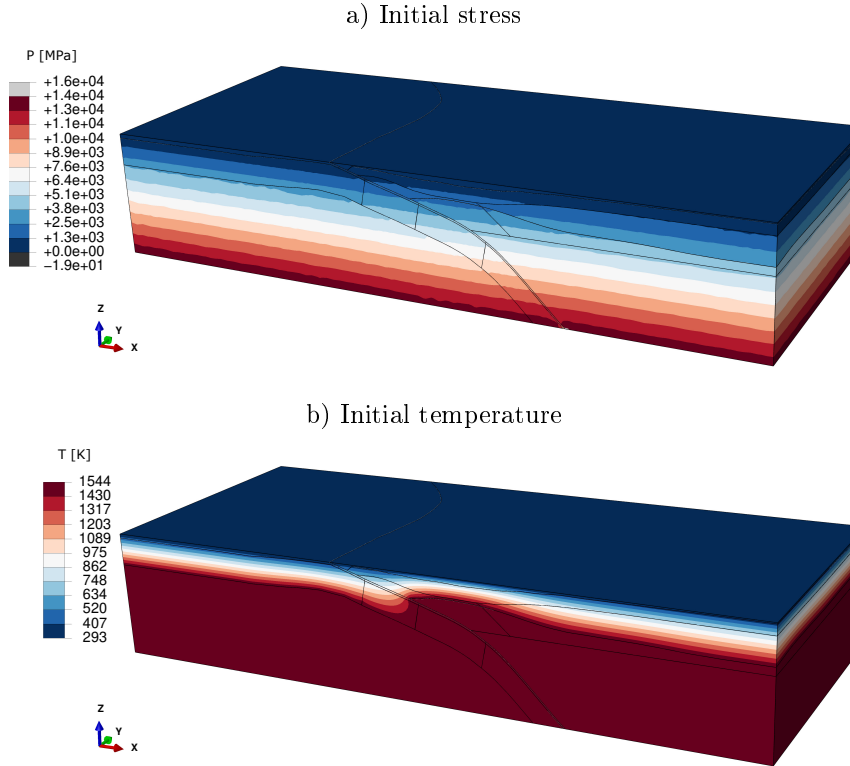


Figure 6.3: Initial stress (a) and temperature distribution (b) of the model for northern Chile

depth, while Hoffmann-Rothe et al. (2006) and Sobolev et al. (2006) found approximately 35 km for the downdip limit. The friction coefficient is set to the most probable value of $\mu = 0.05$ as suggested by e.g. Babeyko and Sobolev (2008), Gerbault et al. (2009), Harris et al. (2010), Middleton and Copley (2013) and Copley (2017).

Due to numerical instabilities (see section 6.3.4) the applied material properties define the model to be fully elastic (6.1) with the density, specific heat capacity, and thermal conductivity as previously defined in table 4.1. The densities for the model units CLLe, CLLw, CAe, CAw, OC IV, OLL IV are taken from Tassara et al. (2006). To compute the Poisson ratio as well as Young's modulus the seismic velocity profiles provided by the ANCORP Working Group (2003) and the 3D tomographic model results by Koulakov et al. (2006) and Dorbath et al. (2008) are used to obtain reasonable v_p and v_s velocities down to 200 km depth, while below a value of $v_p = 8.5$ km/s and a Poisson ratio of 0.25 are assumed. The thermal expansion coefficient is set to $3 \cdot 10^{-5} \text{ K}^{-1}$ for the entire model.

Table 6.1: Material parameters used for the subduction zone of northern Chile: The thermal expansion coefficient is set to $3 \cdot 10^{-5} \text{ K}^{-1}$ and the specific heat capacity to $1250 \text{ J kg}^{-1} \text{ K}^{-1}$ in the model. The thermal conductivity is set to $2.5 \text{ W m}^{-1} \text{ K}^{-1}$ for the oceanic and continental lithosphere and to $6.9 \text{ W m}^{-1} \text{ K}^{-1}$ for the asthenosphere, respectively.

Part	$\rho^{(1)}$ (kg m^{-3})	$v_p^{(2)}$ (km/s)	$v_s^{(2)}$ (km/s)	ν (1)	E (GPa)
CC	2700	5800	3300	0.26	74
CUL	3100	6200	3500	0.27	96

Table 6.1 – Continued from previous page

Part	$\rho^{(1)}$ (kg m^{-3})	$v_p^{(2)}$ (km/s)	$v_s^{(2)}$ (km/s)	ν (1)	E (GPa)
CLLw	3240	8000	4400	0.28	161
CLLe	3320	7800	4300	0.28	157
CAw	3310	8100	4500	0.28	171
CAe	3350	8200	4400	0.30	168
CA	3350	8500	4900	0.25	207
OC I	3050	6200	3600	0.25	98
OC II	3200	6500	3800	0.25	114
OC III	3300	6500	3800	0.25	118
OC IV	3550	6500	3800	0.25	127
OLL I	3355	8100	4600	0.26	179
OLL II	3370	8200	4700	0.25	186
OLL III	3400	8300	4700	0.26	189
OLL IV	3500	8500	4800	0.27	204
OA	3410	8500	4900	0.25	205

References: (1) Tassara and Echaurren (2012), (2) Yuan et al. (2000), Koulakov et al. (2006), Dorbath et al. (2008)

6.3 Results

6.3.1 Final Stage

The overall model subsides by several hundred metres (fig 6.4a). The largest amount of subsidence occurs during the start of the simulation (section 6.3.2). Therefore, the vertical displacement obtained after 7600 years of subduction is subtracted to neglect the warm-up time of the model. The result fits well with the observed average uplift rate in the model (fig. 6.4b). While most parts of the model show near zero uplift, the overall continental crust is uplifted by at least 200 m. The maximum occurs along the continental crust near to the trench with about 900 m, while towards the east a basin at near zero height starts to develop surrounded by regions with several 100 m of uplift. The southern part of the model experiences more uplift than the northern part.

To compare the results with recent observations the uplift rate averaged over the last $3.4 \cdot 10^4$ years of the simulation is shown in figure 6.4b. The features observed are very similar to the ones shown in figure 6.4a whereas it is more clearly visible that the slab sinks. However, only the central parts of the slab subside while the bottom and top regions are nearly fixed in vertical direction. The highest uplift rate in the continental crust is between 10.0 mm/a to 11.0 mm/a and occurs near the trench. The mean uplift rate of the continental crust is 1.0 to 2.8 mm/a. However, results from paleoelevation data (e.g. Gregory-Wodzicki, 2000;

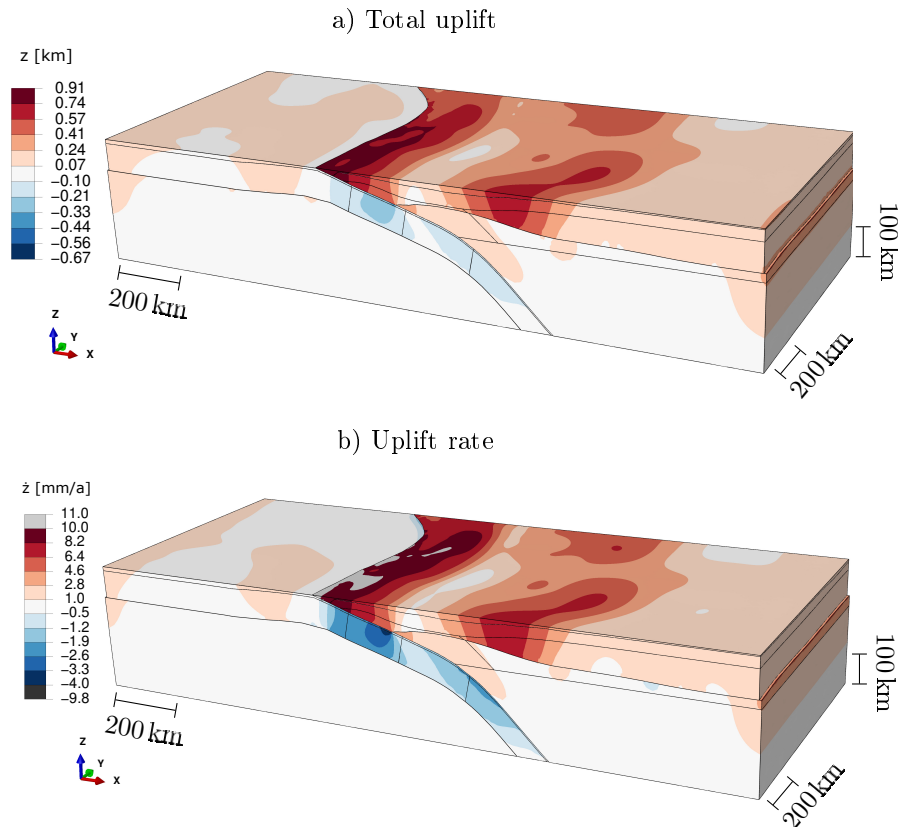


Figure 6.4: Model results in vertical direction after 10^5 years. a) vertical displacement after subtraction of the result after $7.5 \cdot 10^3$ years, b) vertical displacement rate averaged over the last $3.5 \cdot 10^4$ years.

Kukowski and Oncken, 2006; Saylor and Horton, 2014; Melnick, 2016) suggest much lower rates between 0.1 mm/a and 0.2 mm/a.

The horizontal displacement rates are shown in figure 6.5. The west-east rate in the asthenosphere is dominated by the oceanic plate movement with rates between 24 mm/a and 33 mm/a towards the east. Along the continental lithosphere the westernmost regions up to 420 km east of the trench are affected by the oceanic and continental plate motion and show low rates between 0 mm/a and 5 mm/a. The remaining continental lithosphere moves towards the west with rates of up to 23 mm/a increasing to the east. The rate in south-north direction is near zero for most parts of the model except for the oceanic lithosphere and the uppermost continental crust. The most significant feature is that at around the position where the type of subduction switches from oblique to perpendicular, one observes the highest north-directed movement in the continental crust with 3 mm/a decreasing to zero towards the model boundary. Further to the east the movement direction alternates, disappearing 1200 km away from the trench. Figure 6.5c shows the horizontal displacement rates along the continental crust between 20°S and 21°S according to the velocity model VEMOS 2017 (Sanchez and Drewes, 2016; Drewes and Sanchez, 2017). The movement rate towards the north is generally about 10 mm/a higher compared to the rate towards the east.

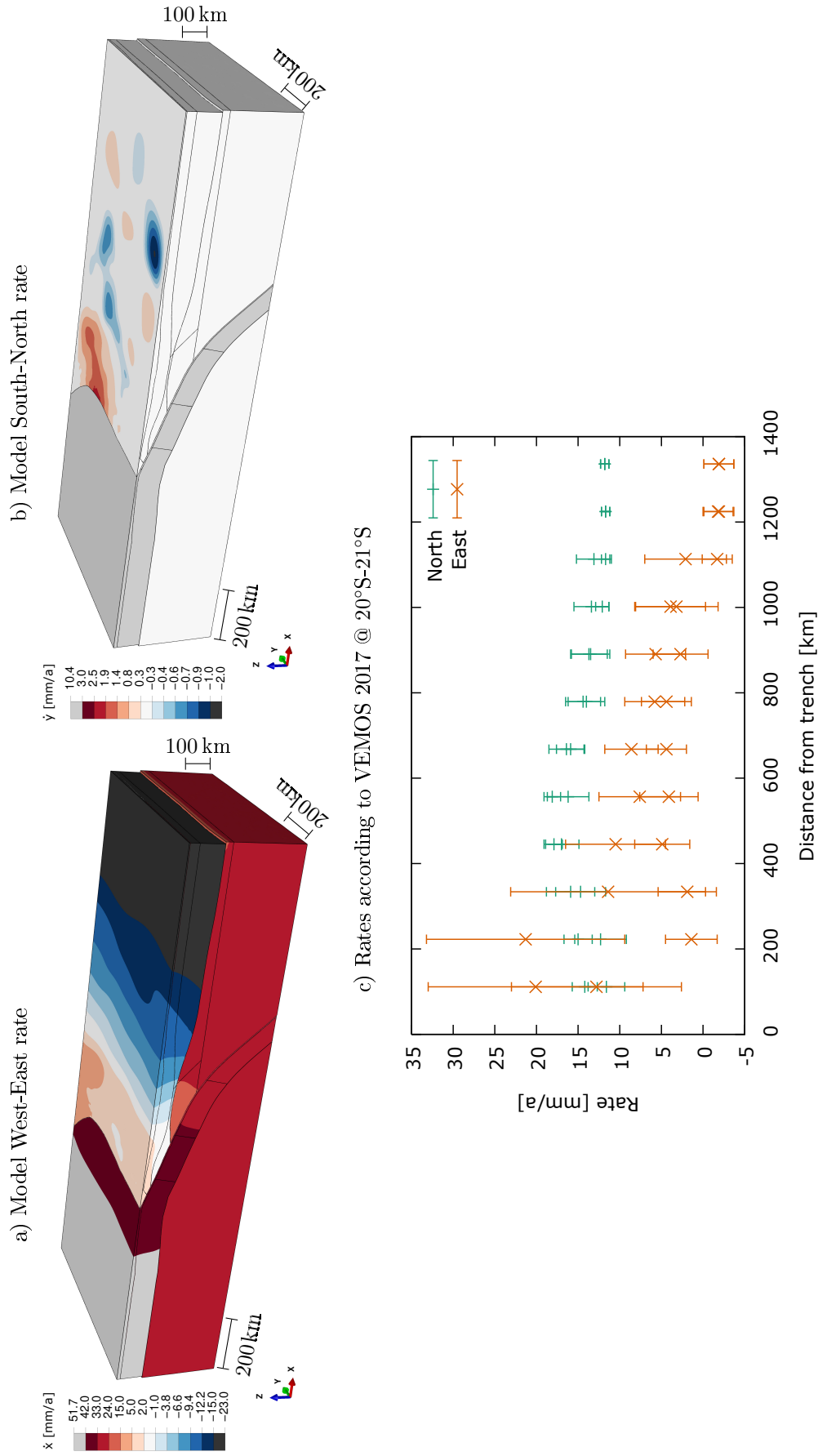


Figure 6.5: a) and b) Model displacement rate in W-E and S-N direction after 10^5 years averaged over the last $3.4 \cdot 10^4$ years. c) W-E and S-N continental crust displacement rates after Sanchez and Drewes (2016) and Drewes and Sanchez (2017) between 20°S and 21°S .

Both increase from the trench towards the backarc of the subduction zone reaching a maximum between 400 km and 600 km distance. The uncertainties in the east components are much higher than those of the north components, especially from the trench up to 300 km distance. These data do not fit my model. The movement rates to the north are much higher in VEMOS 2017 than they are in my finite element model. The maximum rate observed in this study is 10 mm/a occurring at the oceanic plate, whereas according to VEMOS 2017 the continental plate experiences up to 18 mm/a. Furthermore, in this study most continental parts are unaffected by the movement to the north, while VEMOS 2017 predicts that most parts are affected. The rates towards the east are similar near the trench, but they are not unique due to large uncertainties. Further to the east both models show increasing westward motion. In the finite element model the rates are dominated by the applied velocity at the continental plate and are thus much higher.

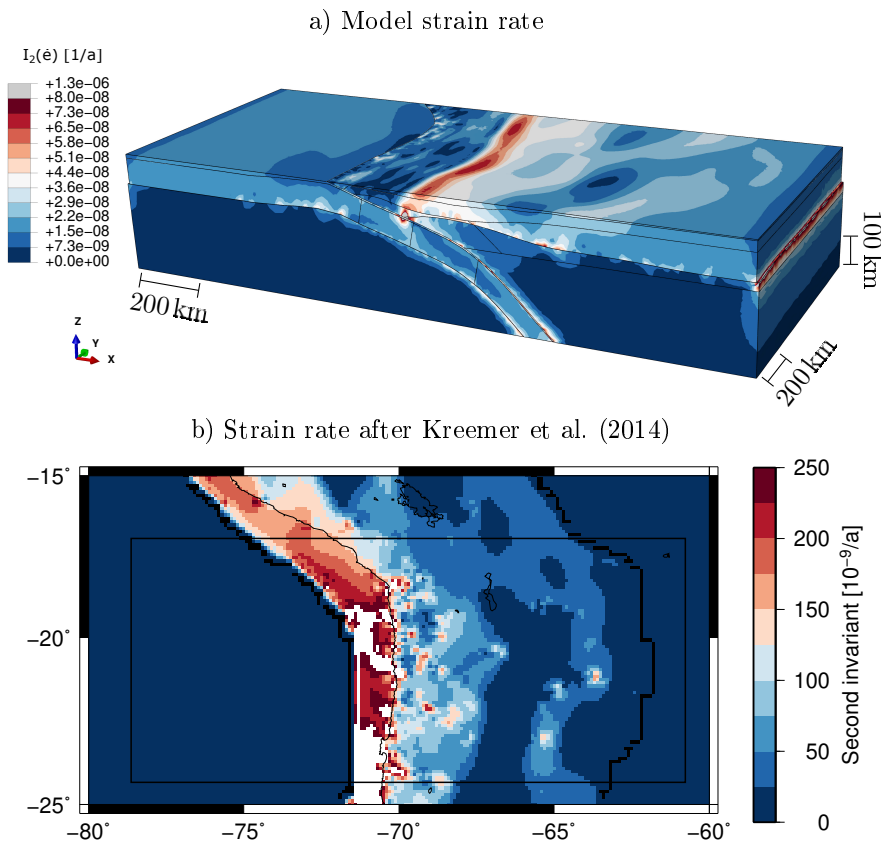


Figure 6.6: Square root of the second invariant of the strain rate tensor (a) in this study after 10^5 years, (b) after Kreemer et al. (2014). Rectangle marks the study area and thick black lines denote the outline of GSRM data.

The strain rate after 10^5 years of subduction (fig. 6.6a) ranges between $1 \cdot 10^{-8}$ 1/a and $3 \cdot 10^{-8}$ 1/a along the entire oceanic lithosphere and decreases to almost zero towards the trench. At the contact with the asthenosphere and upper plate, higher rates of up to $9 \cdot 10^{-8}$ 1/a are observed. Along the continental plate the strain rate east of the trench increases while being splitted into three distinctive regions. Up to about 300 km distance the rate is rather low (no more than $2 \cdot 10^{-8}$ 1/a) and shows an increase from south to north without significant changes directly at the trench. Further apart the rate suddenly increases to $8 \cdot 10^{-8}$ 1/a within about 50 km, while from 400 km distance the rate smoothly decreases to $1.5 \cdot 10^{-8}$ 1/a towards the

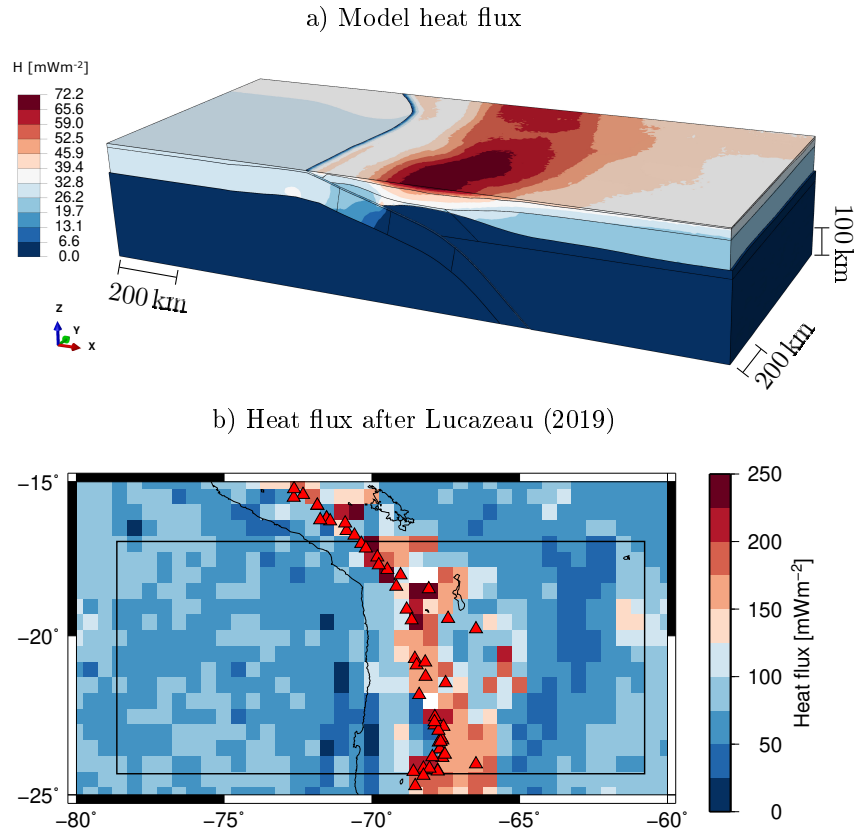


Figure 6.7: Heat flux magnitude (a) in this study after 10^5 years, (b) after Lucazeau (2019). Red triangles denote volcanoes.

eastern boundary of the model. The sudden increase at 300 km appears to be above the contact between oceanic and continental lithosphere at the upper asthenosphere. This is where the highest strain rates of more than 10^{-6} 1/a are observed. In comparison with the global strain rate model (GSRM, Kreemer et al., 2014) (fig. 6.6b) the magnitudes are similar but according to GSRM the location of the maximum strain rate along the continental plate occurs directly beneath the trench. Nevertheless, the strain rates east of the trench along the coast line reach values between $10 \cdot 10^{-8}$ 1/a and $15 \cdot 10^{-8}$ 1/a which is in good agreement with the finite element model.

The resulting heat flow is shown in figure 6.7a. Along the whole asthenosphere the heat flow is 0 mWm^{-2} ; along the upper oceanic plate it is homogeneous and ranges between 24 mWm^{-2} and 36 mWm^{-2} . With increasing depth the heat flow decreases along the slab and reaches 0 mWm^{-2} at a depth of about 140 km. In the continental plate the heat flow is higher along the crust reaching generally more than 30 mWm^{-2} . Along the upper crust moderate values between 30 mWm^{-2} and 50 mWm^{-2} are observed near the trench and in the easternmost regions. Between 250 km and 650 km distance from the trench, the heat flow is increased and reaches up to 72 mWm^{-2} in the south and about 66 mWm^{-2} in the north. Figure 6.7b shows the distribution of surface heat flow after Lucazeau (2019). From this one observes a high heat flux of up to 250 mWm^{-2} around the position of volcanoes in the study area (fig. 6.1). In the finite element model the maximum heat flux occurs at a similar region but with approximately $1/3$ of the heat flow magnitude computed by Lucazeau (2019). Due to the comparatively low resolution of the global heat flow map by Lucazeau (2019), no clear trend

for a good comparison. Figure 6.8 shows the distribution of shear stress along the surface of the slab, for the model of this study and that of Zeumann et al. (2014) as well as the distribution of earthquakes with magnitudes $M_w \geq 6$. The ellipses labeled A and B correspond to the distribution of earthquakes with hypocenter depths between 0 km to 30 km and 70 km to 150 km respectively. In zone A and B the model of Zeumann et al. (2014) shows higher shear stresses compared to the surroundings, which appears to correlate with the distribution of earthquake hypocenters. However, region A may also be further increased to the west in her model where no earthquakes are observed. In the present study one also observes a slightly higher shear stress in zone A, which may extend to the north instead of to the east. At zone B both models show significantly higher shear stresses but in both cases this follows the region of material changes from lithosphere to asthenosphere. Thus, at this position the slab comes into contact with the continental lithosphere and asthenosphere, giving rise to large numerical uncertainties because not only there are three different materials but also three different element sizes which are in contact. Therefore, the observed high shear stresses in region B may result from numerical artefacts. However, in both models the shear stresses directly above region B are comparatively low and a gap in strong earthquakes is observed as well (fig. 6.8c). At the location of Iquique, no increase in shear stress is observed at all in both models although in 2014 a major earthquake occurred at this position.

6.3.2 Temporal evolution

In the following section the temporal evolution of vertical displacement and strain rate is discussed. The results in figures 6.9 and 6.10 show the model after 3, 7.600, 66.000 and 100.000 years respectively. These time steps are solution dependent and are determined by the software Abaqus depending on several convergence criteria including geometric, material and contact aspects. During the subduction process the overall model subsides by several 100 m (fig. 6.9), i.e. relative to the initial configuration there is no uplift at all. However, as discussed in the previous section, the model is subject to a warm-up time. That is, the simulation needs a certain amount of increments / time to reach a dynamically stable state. Figure 6.9 shows that after 7.600 years of subduction the state of maximum subsidence is reached, whereas there are only minor changes in the distribution of vertical displacement after this time. After 66.000 years, large parts of the continental and oceanic lithosphere are slightly uplifted with respect to the state reached after 3 years. Around the trench as well as at the eastern and western boundaries the amount of relative uplift is the highest. The relative uplifting continues up to the final stage after 100.000 years with the results discussed in the previous section. Thus, from the beginning of the simulation the main features observed in the final stage are already present.

The evolution of the strain rate (fig. 6.10) is not as straightforward as that of the vertical displacement, because the final displacement contains the sum of all previous displacements, but the strain rate is unique for each time step. After 3 years of subduction the strain rate is four to five magnitudes higher compared to later states of the simulation, because it is still within the warm-up time. After 7.600 years the strain rate distribution is already similar in magnitude to the final distribution. Furthermore, the strain rate is more homogeneous and the three different regimes along the continental plate observed at the final stage (section 6.3.1) start to develop. The region of high strain rates always starts at 200 km distance from the trench. It ranges to about 600 km distance after 7600 years and diminishes to 300 km distance after 100.000 years. The overall strain rate along the uppermost oceanic and eastern

continental lithosphere after 7.600 years is higher by a factor of almost two compared to the final stage. With increasing time the three distinctive regimes become more clear and after 66.000 years almost the same distribution in strain rate is observed as after 100.000 years.

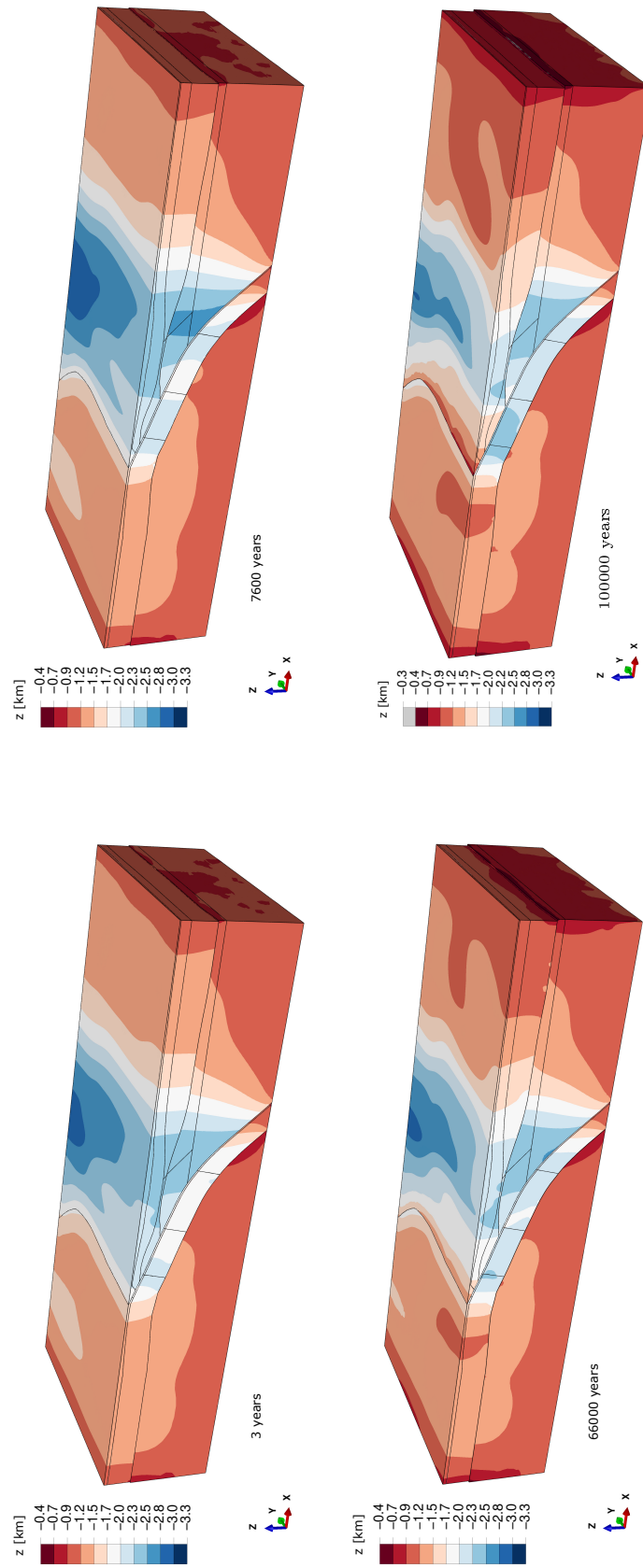


Figure 6.9: Evolution of vertical displacement during the subduction process.

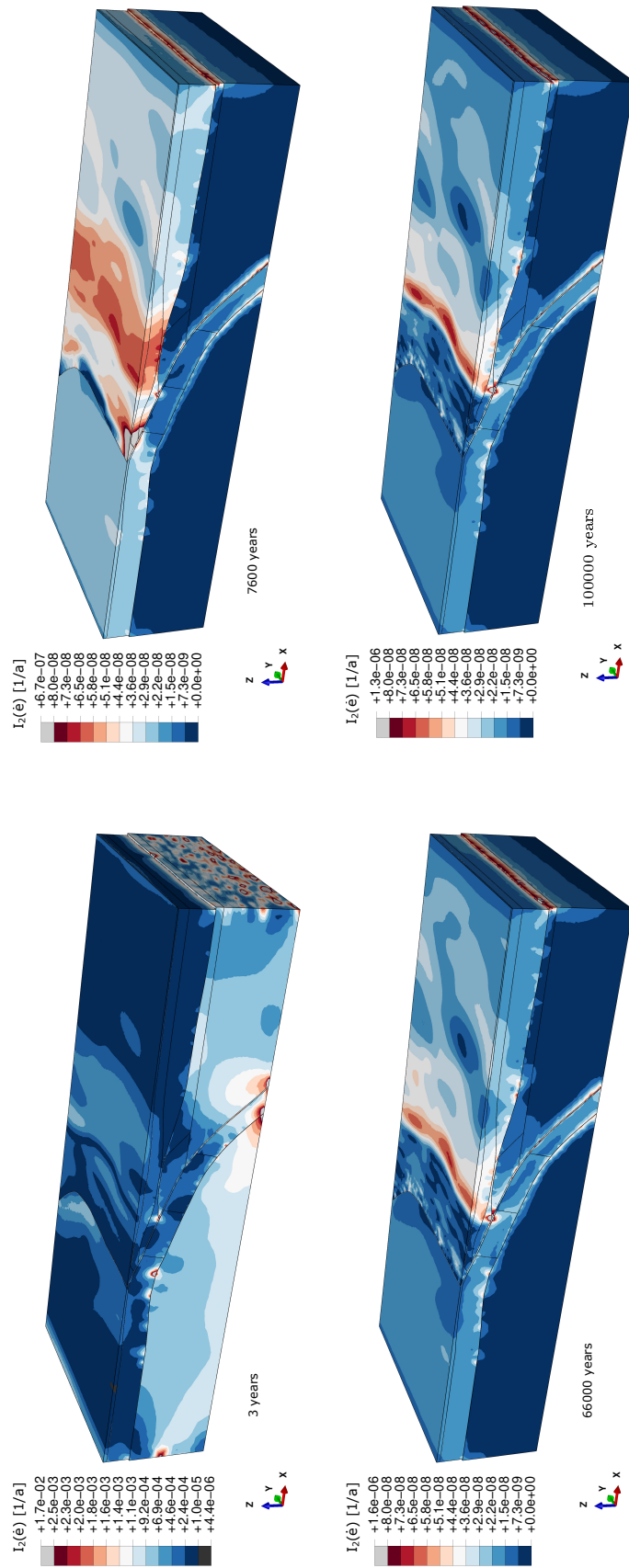


Figure 6.10: Evolution of strain rate during the subduction process. Be aware of the different scaling for the results after 3 years.

6.3.3 Slab Pull velocity

In a second model a velocity at the bottom of the slab is applied with a magnitude of 5.5 cm/a directed 20° towards the north and 40° downwards according to the movement and geometry of the Nazca plate. The results (fig. 6.11) show that the rate of vertical displacement is significantly decreased along major parts of the continental plate (cf. figure 6.4). Near to the trench the uplift rate is increased from 11 mm/a to 14.6 mm/a at maximum. The increase mainly occurs along the N-S directed part of the trench. Further to the east the uplift rate decreases to 1 mm/a at 200 km distance, and decreases further to -2 mm/a at 300 km from the trench. Similar to the first model the uplift rate in the south is higher in most regions compared to the north and the area between 200 km and 400 km distance from the trench is surrounded by areas of higher uplift rate. Along the oceanic plate the rate is slightly increased west of the trench, but from the trench towards the bottom of the slab it is significantly decreased down to -45 mm/a due to the applied velocity at the bottom. Therefore, the model with included slab pull velocity fits much better to the observed uplift rates except at the position of the trench.

As for the uplift rates the strain rates are decreased as well in the model including a slab pull velocity (fig. 6.11b). However, in the northwestern part of the oceanic plate, at the contact between oceanic plate and asthenosphere as well as at the bottom of the slab, the rate is increased. Along the continental plate no clearly distinctive structures in strain rate as in the first model can be observed, but from the distance of about 200 km east of the trench the distribution in strain rate is more homogeneous. Here it is reduced to 0 a⁻¹ at the easternmost boundary. In comparison to the global strain rate model the results are worse than those in the model without a slab pull velocity.

The heat flow (fig. 6.11c) is generally between 5 mWm⁻² to 8 mWm⁻² higher with a slab pull velocity included. Along the zone of friction an increase from 72 mWm⁻² in the model without slab pull velocity to 129 mWm⁻² is observed. However, all structures in the distribution of heat flow remain the same and, therefore, this model yields no significant improvement in comparison to the global heat flow model by Lucazeau (2019).

According to the parametric study (section 5.2.5) the shear stresses are expected to be reduced if the slab pull velocity is applied. From figure 6.11d one observes a significant increase by more than 100 MPa along the entire oceanic crust between about 100 km west of the trench and down to the bottom of the slab. Furthermore, a checkerboard pattern is observed throughout large parts of the slab surface, showing numerical instabilities, which according the Abaqus manual (ABAQUS 6.14, 2014) is due to shear locking of the elements (see also section 6.3.4).

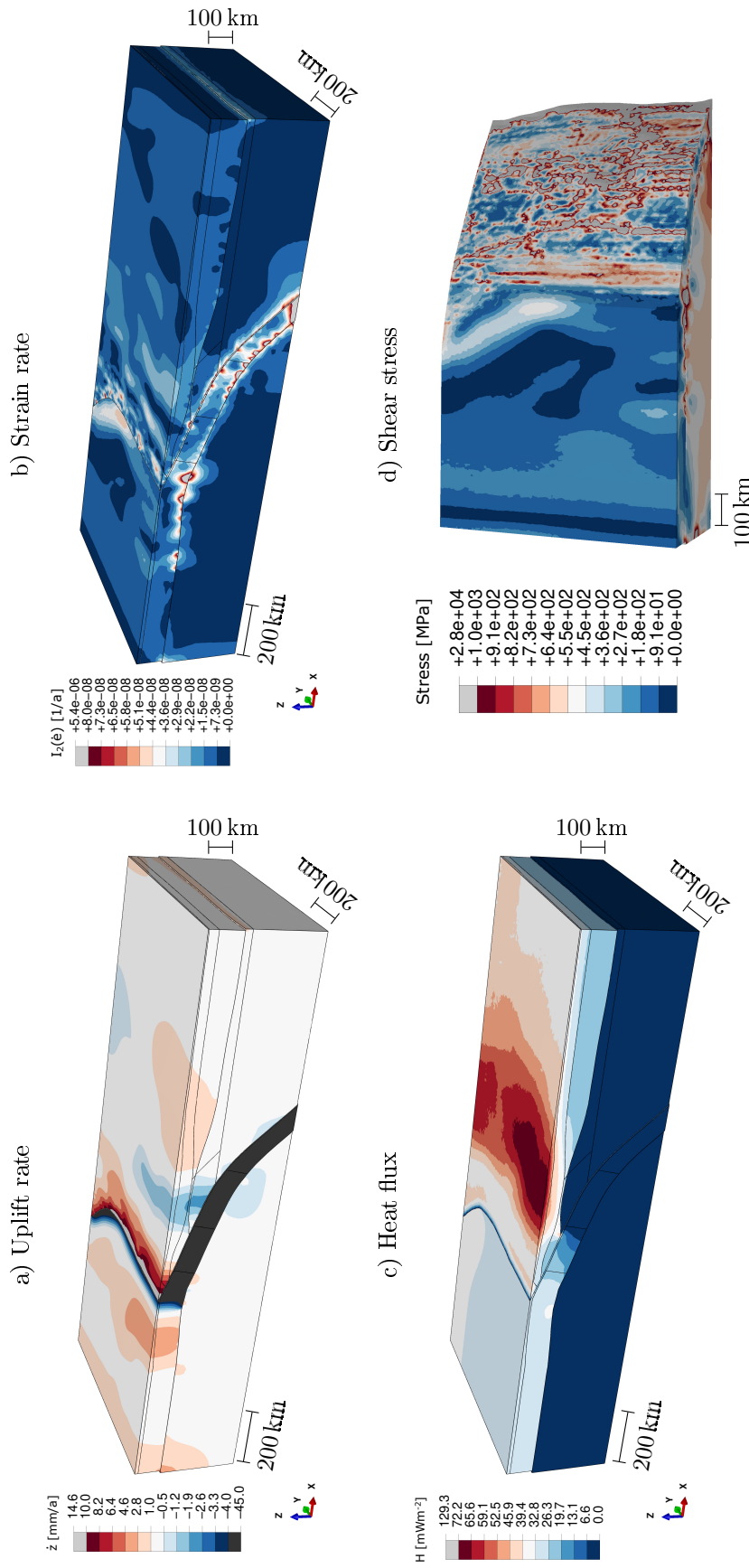


Figure 6.11: Results after 10^5 years for the model with slab pull velocity included. (a) Vertical displacement rate averaged over the last $3.5 \cdot 10^4$ years, (b) second invariant of strain rate tensor, (c) heat flux magnitude, (d) shear stress along the oceanic plate.

6.3.4 Discussion

Originally the simulation was planned to be used together with the Drucker-Prager viscoelastic approach as done for the reference model and the parametric study. To this end the values for dilatancy angle and cohesion provided in table 4.1 and for the angle of internal friction, the viscosity exponent, the viscosity prefactor, and creep activation energy the values suggested by Ranalli (1995) and Gerbault et al. (2009) were chosen. After simulating about 12 years of subduction the model became unstable and failed despite several different test scenarios. A closer inspection of the inelastic deformations revealed very low strains of about three orders of magnitude smaller compared to the total strains. At this stage of the simulation the deformation rates are expected to be higher compared to later model states (see section 6.3.2) and it is thus to be expected that a fully elastic model should yield similar results (see figure 5.4).

With this approach, after 10^5 years of subduction an uplift of several hundred metres is observed near the trench along the continental plate (fig. 6.12b). Due to the fully elastic approach this is not expected to be the evolution of an orogen such as the Andes because by neglecting the external forces the model would relax back to its initial state, whereas an orogen would remain. Instead the uplift is a consequence of elastic bulging because of the frictional coupling between the plates.

In the model a higher amount of uplift and a higher uplift rate are observed in the south compared to the north (fig. 6.4 and 6.12b). According to Bonnardot et al. (2008) an oceanward concave margin implies subsidence of the oceanic and continental crust near the trench. This mechanism fits well to my results because the shape of the oceanic margin in the present model changes from straight in the south to concave in the north. Furthermore, the thickness of the model unit CLL (see figure 6.2b) is highly variable and ranges between 5 km and 80 km, whereas near the trench the thickness in the north is higher than in the south (fig. 6.12a). Due to this additional load in the north the amount of subsidence is increased, whereas the type of convergence reduces this effect. Convergence is oblique in the south but almost perpendicular in the north, therefore, the subsidence in the north is dampened by the perpendicular convergence as predicted by Bonnardot et al. (2008). However, the computed displacement rates do not fit well to the suggested uplift and horizontal rates by Gregory-Wodzicki (2000), Kukowski and Oncken (2006), Saylor and Horton (2014), Melnick (2016), Sanchez and Drewes (2016) and Drewes and Sanchez (2017) although it is shown (section 6.3.3) that with a slab pull velocity included the modelled uplift rates are closer to the expected values. This discrepancy may be because a purely elastic rheology was considered for this model, and topography and bathymetry are not included. While elasticity inhibits inelastic deformations needed to form an orogen as the Andes, the additional topography / bathymetry would add a significant load to the lithosphere. The additional load increases the amount of plate coupling as well as the coupling between crust and mantle (e.g. Arvidsson, 1996; Ziegler et al., 1998; Ziegler et al., 2002; Copley and McKenzie, 2007; Copley et al., 2011; Whitehouse, 2018) and thus potentially lowering the amount of uplift. Especially for the displacement rates towards the north, the reason might be the low coupling between the plates achieved in the model that is seen from the figures in section 6.3.1 as a sharp transition at the contact interfaces for all variables that were discussed. The displacement rate towards the east is strongly affected by the applied plate velocities most notably near the eastern and western model boundaries. Therefore, a comparison with the VEMOS 2017 model beyond the distance of 500 km from the trench must fail because the dimensions of the

finite element model are far too small. Another possible reason for the differences between my model and VEMOS 2017 is again the use of an elastic rheology.

Similar to the uplift rate the strain rate is also influenced by the thickness of the continental lower lithosphere (fig. 6.12c). The highest strain rates are observed between 300 km to 350 km east of the trench. Farther east the unit CLL appears to have its lowest thickness of about 5 km over a range of about 200 km. After 7600 years of subduction (fig. 6.10) the region of highest strain rates coincides with this region of lowest thickness. With ongoing subduction the model reaches a more stable dynamic equilibrium and after 10^5 years the high strain rates are only observed above the intersection of the upper asthenosphere with the continental and oceanic lithosphere. At the same position the shear stresses become exceptionally high and the region is known to trigger strong earthquakes (fig. 6.8a, c). Besides this, there is a gap in the distribution of strong earthquakes from this position towards the trench. Overall this shows that the material changes at the aforementioned intersection is an important indicator for strong earthquakes. However, those changes in material properties do occur at a position at which the finite elements of the asthenosphere have to form a wedge. The corresponding tetrahedrons have obtuse angles and are numerically more difficult to handle, increasing the numerical uncertainties which occur at this region. The Global Strain Rate Model (Kreemer et al., 2014) predicts high strain rates between the trench and the coast of the South American continent (fig. 6.6b) which roughly corresponds to the width of the seismogenic zone lying underneath and is consistent with the occurrence of the most and some of the strongest earthquakes. In my model low surface strain rates are observed between trench and coast (fig. 6.6a) which suggests that an elastic approach is not feasible for this part of the model and that the inelastic strain rates to be expected from a more realistic model are much higher than the elastic strain rates. East of the coast both, the GSRM and my model, predict similar values for the strain rates decreasing towards the continental hinterland. The elastic rheology, thus, seems to be sufficient for first order estimates for earthquakes happening outside the seismogenic zone of coupling.

The surface heat flux follows the thickness of the model unit CLL as well (fig. 6.12d). At around the position of minimum thickness of the unit the heat flux is at maximum, while it is higher in the south compared to the north. At this part of the model the heat flux is determined through radiogenic heating within the lithosphere, and heat conduction. While the radiogenic heat flux is proportional to the thickness of the layer it is applied (see for example Turcotte and Schubert, 2014), the conductive heat flux depends on the temperature gradient. Below the unit CLL the temperature was defined to be constant throughout the asthenosphere. The temperature gradient is at maximum at the lowest thickness of the lithosphere which coincides with the position of maximum heat flux. Accordingly, the heat flux within the oceanic plate is slightly increasing to the north because the thickness of the oceanic lithosphere is increasing to this direction, while both, the heat flux and the thickness, are near constant from west to east. The global surface heat flux model by Lucazeau (2019) and my model (fig. 6.7) are in good correlation for the study area even though the magnitudes in my model are only about half the ones predicted by Lucazeau (2019). This difference is mainly attributed to the high volcanic activity in the area. In my model fluids and corresponding melt generation as well as convection are neglected. As such, the model is not expected to perfectly correlate with the global heat flow model. Nevertheless, the results reveal that the overall heat flux distribution seems to be dominated by thermal conduction, whereas the generation of melts contributes on a local scale that is not resolved by my model.

As previously discussed in section 5.2.5 the application of an additional slab pull velocity is expected to reduce the amount of shear stress and uplift due to the stretching of the slab and the induced subsidence. While the uplift rate decreases similar to the observations by Zeumann (2013), the shear stress greatly increases (fig. 6.11) due to shear locking. Shear locking is caused by large aspect ratios of the elements and greatly increases its stiffness. This may lead to significant numerical errors that may dominate the overall numerical solution (see for example Koschnick, 2004). Without slab pull shear locking was already present in the model (compare with fig. 6.8) but did not dominate it. As slab pull had been applied the additional boundary condition introduced further errors to the simulation that were amplified by the shear locking effect. This further explains why the resulting strain rates do not fit to the Global Strain Rate Model at all after a slab pull velocity is applied.

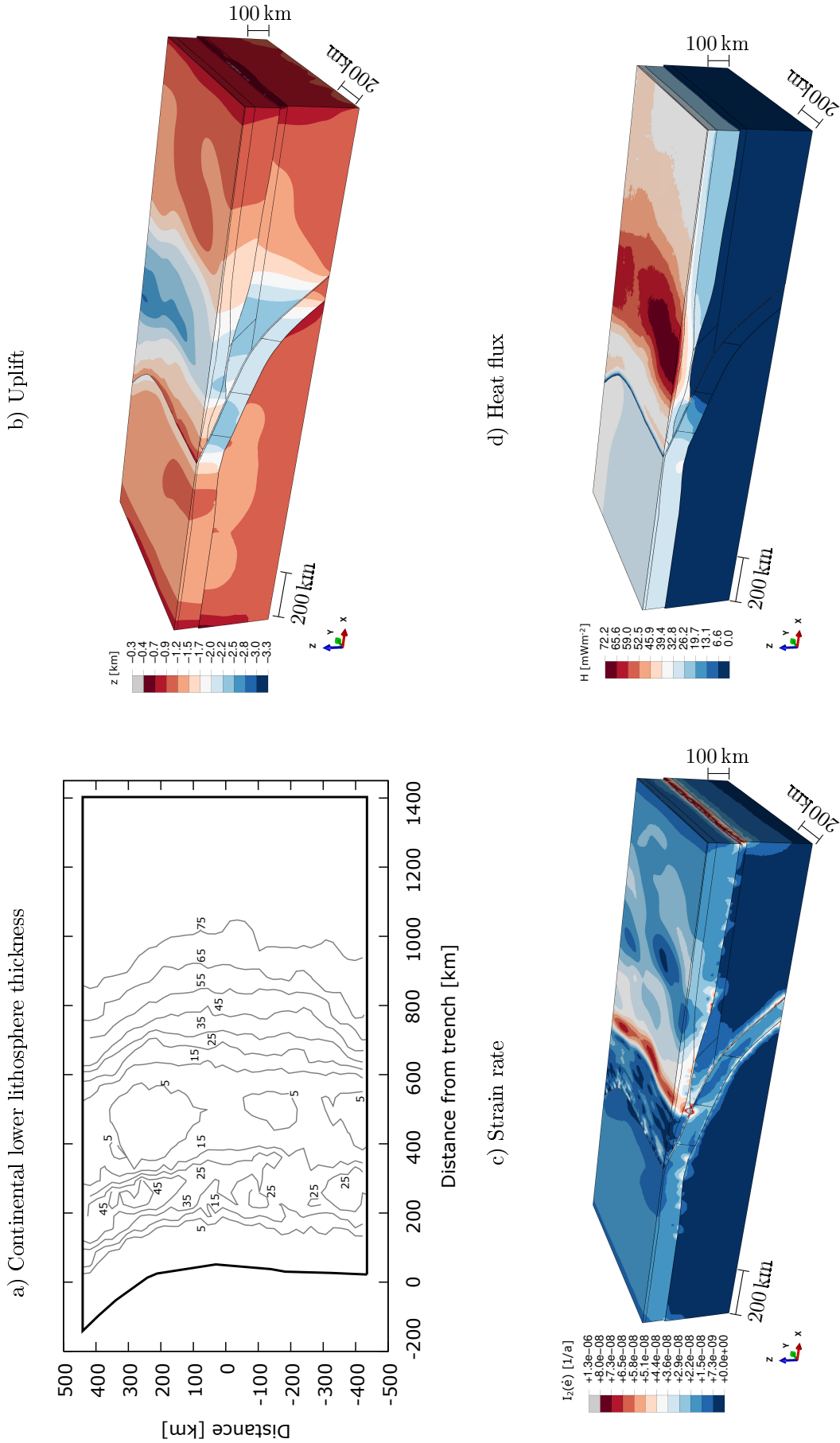


Figure 6.12: Comparison between thickness of the continental lower lithosphere (a) and model results showing uplift (b), strain rate (c) and heat flux (d). Contour lines show the thickness of the model unit CLL. The black line denotes the outline of the continental plate at the model surface. Numbers are given in km.

7 Conclusions and Outlook

In the first part of this thesis the implications of the most important parameters controlling a three-dimensional thermomechanical simulation of subduction zones were studied. In the second part the results were used to develop a model that describes the current state of subduction along the concave trench of South America.

For the parametric study a reference model was created whose geometry is based on a cross-section through the study area. While the geometry was kept simple with this approach, the rheology applied, however, accounts for elasto-viscoplastic deformations including temperature dependence and shear heating. This is the most realistic model. The elastic material parameters source from a well-constrained density model and several seismic reflection and refraction profiles within the area of investigation, while the viscoplastic parameters are typical generic values used for subduction modelling. The uplift rates obtained are already in first-order agreement with observations (e.g Gregory-Wodzicki, 2000). The reference model further allows for an assessment of the expected boundary effects on the final model due to the applied velocities at the eastern and western ends of the lithosphere. In a long-term run simulating 1.6 Ma of subduction, boundary effects start to dominate large parts of the model and the shear stresses increase to exceptionally high values because they are mainly controlled by elastic deformations rather than a subduction channel. Nevertheless, long-term shear heating is observed with a maximum temperature increase of 45 K that is consistent with observations of rocks found along fault zones (e.g. Fukumura et al., 2019). The long-term run further allows for an estimation of time needed for the heat flux along the oceanic plate to reach a stable thermodynamic state, which is about 1 Ma.

Within the framework of a parametric study of the reference model it is found that the following parameters are the most important (sorted by relevance): convergence and slab pull velocity, mesh (number and type of elements), dominant type of rheology (either elastic, elasto-plastic or elasto-viscoplastic), cohesion, friction coefficient and maximum threshold shear stress, angle of internal friction, thermal expansion coefficient. In general the oceanic crust is more affected by variations in these parameters compared to the continental crust. Because of the short time scale of $1.6 \cdot 10^5$ years of the subduction process considered to analyze the effects of parameter changes on the model, the percental changes in heat flux are below 10% even for large variations in the parameters.

The strongest influence on the model results from applying a slab pull velocity. In this case the oceanic and continental crust subside by several hundred metres compared to the reference model. Furthermore, the amount of coupling between the plates is reduced, which decreases the shear stresses along the zone of frictional coupling. Because the oceanic plate is stretched the heat flux within the continental plate is reduced but increased along the oceanic plate. A percental change in the convergence velocity of the plates allows for the scaling of the simulation time by the same percentage. For the final model this has not been used because it was not numerically stable enough to ensure the time scaling. If oblique subduction is considered, i.e. an additional velocity component towards the north is applied for the movement of the oceanic plate, mostly the regions around the frictional coupling zone are affected. Because the overall plate velocity is kept constant, the additional

north component reduces the west-east component of the velocity. However, the resulting model changes around the zone of friction are significantly higher than expected from a corresponding percental decrease in the west-east velocity only.

On increasing the number of elements or changing the type of elements from hexahedrons to tetrahedrons the resulting models are consistent with the reference model. This is important to know because for models with a more complex geometry it can become very difficult to generate a mesh that consists out of hexahedrons. Despite this, the results showed that a model consisting of hexahedral elements should be preferred because the boundary effects are lowest in the high resolution model. This holds true although the tetrahedral model contains a higher amount of elements ($10.1 \cdot 10^4$ compared to $6.7 \cdot 10^4$ in the high resolution model).

Variations in the cohesion show interesting results. For a moderate increase all changes in the model are significantly higher than for a decrease or high increase of the cohesion. Typical values for the cohesion range between 20 MPa-50 MPa. Increasing the values to 200 MPa-500 MPa leads to significant changes in the model. Decreasing the cohesion or increasing it to values beyond 500 MPa affects the model less. For values between 200 MPa-500 MPa an increased subsidence of the crust, and a higher decrease in shear stress and heat flux along the zone of frictional coupling are observed along both plates. For higher or lower values the resulting model behaves more like a purely elastic model as one would expect. In contrast to this, for changes in the angle of internal friction the results are as expected. A decrease in the angle produces more inelastic deformations as is expressed by a higher amount of uplift, while an increase triggers more elastic deformations. If the cohesion is moderately increased and the angle of internal friction is varied as well, a decrease in the angle amplifies the model changes due to the increased cohesion, while an increase in the angle significantly weakens the effects of the increase in cohesion.

The application of a maximum threshold shear stress within the zone of frictional coupling to simulate stick-slip behaviour between the plates yields almost the same results as a reduction in the friction coefficient. In both cases the model is only affected around the zone of friction. While the variations in friction coefficient or threshold stress do affect the heat flux mostly at the upper end of the coupling zone, the largest changes in uplift and shear stress are observed at the lower end of the zone.

If the viscosity is defined via dislocation creep instead of being independent of strain rate and temperature, the resulting model changes are negligible. However, if additionally the angle of internal friction is varied, significant uplift of the eastern continental crust by several tens of metres is observed.

The final model of subduction of the Nazca plate underneath the South American plate makes use of a realistic geometry and density distribution of the study area that is based on a well constrained density model. Because of numerical difficulties an elastic rheology had to be used but, nevertheless, the results are partly in good agreement with geodetical, geological and geophysical observations. The area under investigation includes an oceanward concave trench and oblique subduction of the Nazca plate at an angle of 20° towards the north. In total this causes a switch in the type of subduction from oblique in the southern part of the study area to normal in the northern part. Additionally, the depth of the continental Moho and continental lithosphere-asthenosphere boundary, which defines the thickness of the continental lower lithosphere (CLL), are highly variable. This causes significant differences between the southern and northern model parts.

In accordance with the analysis of Bonnardot et al. (2008) the amount of uplift along the continental plate is lower in the north compared to the south of the study area. This is due to the concave trench. Another reason is that the thickness of the model unit CLL is higher in the north, where it reaches 45 km compared to 25 km in the south. These properties on their own would cause subsidence, but uplift is observed during the last stages of the subduction simulation. The reason lies in the elastic bulging of the continental crust that causes a much higher amount of uplifting. Furthermore, the subsidence is dampened by the switch from oblique to normal subduction from south to north. In comparison with paleoelevation data, however, the acquired uplift rates in the model are up to two orders of magnitude higher, reaching up to 11 mm/a compared to 0.1 to 0.2 mm/a as suggested by these data.

The displacement rates towards the east of the continental crust are similar in comparison to the velocity model VEMOS 2017 (Sanchez and Drewes, 2016; Drewes and Sanchez, 2017) up to a distance of 500 km east of the trench. At greater distances the finite element model starts to become dominated by the applied velocity boundary condition and the results do not fit anymore. The rates towards the north are generally much less in my model compared to VEMOS 2017, because the amount of plate coupling achieved in my model is lower than that needed for higher rates.

A comparison of the strain rates and shear stresses with the distribution of earthquakes shows good coincidences for intermediate depth earthquakes. However, in those regions the model results are also affected by higher numerical uncertainties and so the correlation may be worse or better than predicted by these results. Similar to the uplift rate the strain rate too is affected by the thickness of the model unit CLL. Between 400 km and 600 km east of the trench the thickness becomes very low and the strain rate clearly increases at this position. With ongoing subduction the model reaches a more stable dynamic state and this increase in strain rate diminishes, but is still higher than the average strain rates of the surrounding areas. Further investigation reveals that the applied elastic rheology is insufficient to describe the frictional coupling zone. However, compared to the Global Strain Rate Model (Kreemer et al., 2014) and to the distribution of intermediate depth earthquakes, my model yields good first order results east of the South American coast, i.e. outside the zone of coupling.

In general the heat flux in my model is in good agreement with the global heat flux model of Lucazeau (2019). While the distributions are very similar, the magnitudes along the magmatic arc are lower in my model because fluids and, thus, melt generation is not considered here. This shows that the heat flux on a large scale is determined by thermal conduction but on a local scale it is influenced by volcanic activity. Because of the low resolution of the model of Lucazeau (2019) it is hard to compare the variations between the southern and northern parts. In my model however, the heat flux is clearly higher in the south compared to the north and reaches its maximum at the lowest thickness of the unit CLL. This is in good agreement with the expectations.

If a slab pull velocity is applied to the model, the uplift rate decreases as proposed by the parametric study, while the heat flux is merely affected. In contrast to this, the distribution of shear stress and strain rate change significantly and the resulting variations are totally different from the observations during the parametric study. The results, therefore, seem to

be affected by the effect of shear locking which is a numerical error caused by large aspect ratios of the elements of the finite element mesh.

Developing the elasto-viscoplastic rheology and thermomechanical reference model, and conducting the parametric study has been the main work of this thesis. While it was shown that for a comparatively simple geometry of subduction zones, the results are in good accordance with expectations and observations, a transmission of this knowledge to a model with a realistic geometry needs further improvements. The final model of the South American subduction zone developed during this thesis already showed first-order agreements with some of the geodetical, geological and geophysical observations. However, an enhancement of the mesh would enable the model to become much more stable and yield more serious results. The software Abaqus provides several meshing algorithms and improvements but is, nevertheless, focused on the solution of the equilibrium equations. For complex geometries more advanced meshing software such as HyperMesh (<https://www.altair.com/hypermesh/>) should be used and the mesh is best to be generated with hexahedral instead of tetrahedral elements to reduce boundary effects. The usage of hexahedral elements further allows to include forced convection within the initial temperature model. The utilization of a subduction channel would restrict the shear stresses along the plate interface and is recommended for future studies. During the parametric study it was shown that for short timescales of 10^5 years changes in viscosity become relevant for low angles of internal friction. Thus, the usage of a temperature and strain-rate dependent viscosity as in Babeyko and Sobolev (2008) or Lin and Kuo (2016) can further improve the results especially around the frictional coupling zone. Instead of velocity boundary conditions to simulate the movement of the plates, the application of forces is more realistic because it allows for a dynamic change in the plate velocities over time. These forces may be continuously increased throughout the first stages of the simulation to ensure the numerical stability of the model during the warm-up time. Including topography and bathymetry to the uppermost layer of the model requires a considerable refinement of the mesh and may decrease the numerical stability of the model. Nevertheless, it may be necessary to explain the present day uplift and strain rate observed for the upper crust.

This thesis has been the first approach in combining a realistic geometry together with a realistic rheology to compute the present thermal and mechanical state of the subduction zone along central South America. While not all results do fit to the observations due to numerical difficulties, the model shows good first-order correlations with the observed distribution of heat flux, uplift rate and earthquake hypocentres. In connection with the results from the parametric study the methods developed during this thesis are, therefore, a good starting point to simulate the present state of other subduction zones for which a realistic density distribution is available, such as for example Taiwan (Hsieh and Yen, 2016) or Central America (Lücke, 2012).

References

- ABAQUS 6.14 (2014). *ABAQUS Documentation*. Providence, RI, USA: Dassault Systèmes.
- Adam, J. and C.-D. Reuther (2000). ‘Crustal dynamics and active fault mechanics during subduction erosion. Application of frictional wedge analysis to the north Chilean forearc’. In: *Tectonophysics* 321, pp. 297–325. doi: 10.1016/S0040-1951(00)00074-3.
- Afonso, J. C. and G. Ranalli (2004). ‘Crustal and mantle strengths in continental lithosphere: is the jelly sandwich model obsolete?’ In: *Tectonophysics* 394, pp. 221–232. doi: 10.1016/j.tecto.2004.08.006.
- Afonso, J. C., G. Ranalli and M. Fernandez (2005). ‘Thermal expansivity and elastic properties of the lithospheric mantle: results from mineral physics of composites’. In: *Physics of the Earth and Planetary Interiors* 149, pp. 279–306. doi: 10.1016/j.pepi.2004.10.003.
- Afrouz, A. A. (1992). *Practical Handbook of Rock Mass Classification Systems and Modes of Ground Failure*. CRC Press. ISBN: 0-8493-3711-9.
- Allmendinger, R. and G. González (2010). ‘Invited review paper: Neogene to Quaternary tectonics of the coastal Cordillera, northern Chile’. In: *Tectonophysics* 495(1-2), pp. 93–110. doi: 10.1016/j.tecto.2009.04.019.
- Altamimi, Z., L. Métivier and X. Collilieux (2012). ‘ITRF2008 plate motion model’. In: *J. Geophysical Research* 117(B07402). doi: 10.1029/2011JB008930.
- Alvarez, O., S. Pechuan, M. Gimenez and A. Folguera (2019). ‘Seismic structure along the South American subduction zone using satellite gravity data’. In: *Andean Tectonics*. Ed. by B. K. Horton and A. Folguera. Elsevier. ISBN: 978-0-12-816009-1.
- Amante, C. and B. W. Eakins (2009). *ETOPO1 1 Arc-Minute Global Relief Model: Procedures, Data Sources and Analysis*. NOAA Technical Memorandum NESDIS NGDC 24. doi: 10.7289/V5C8276M.
- ANCORP Working Group (1999). ‘Seismic reflection image of the Andean subduction zone reveals offset of intermediate-depth seismicity into oceanic mantle’. In: *Nature* 349, pp. 341–344. doi: 10.1038/16909.
- ANCORP Working Group (2003). ‘Seismic imaging of an active continental margin - the central Andes (ANCORP ’96)’. In: *J. Geophysical Research* 108, B7. doi: 10.1029/2002JB001771.
- Angermann, D., J. Klotz and C. Reigber (1999). ‘Space-geodetic estimation of the Nazca-South America Euler vector’. In: *Earth and Planetary Science Letters* 171, pp. 329–334. doi: 10.1016/S0012-821X(99)00173-9.
- Antonoli, A., A. Piersanti and G. Spada (1998). ‘Stress diffusion following large earthquakes: a comparison between spherical and flat-earth models’. In: *Geophysical Journal International* 133(1), pp. 85–90. doi: 10.1046/j.1365-246X.1998.1331490.x.
- Argus, D. F., R. G. Gordon, M. B. Helfin, C. Ma, R. J. Eanes, P. Willis, W. R. Peltier and S. E. Owen (2010). ‘The angular velocities of the plates and the velocity of Earth’s centre from space geodesy’. In: *Geophysical Journal International* 180(3), pp. 913–960. doi: 10.1111/j.1365-246X.2009.04463.x.
- Armijo, R., R. Lacassin, A. Coudurier-Curveur and D. Carrizo (2015). ‘Coupled tectonic evolution of Andean orogeny and global climate’. In: *Earth-Science Reviews* 143, pp. 1–35. doi: 10.1016/j.earscirev.2015.01.005.

- Arriagada, C., P. Roperch, C. Mpodozis and P. R. Cobbold (2008). 'Paleogene building of the Bolivian Orocline: Tectonic restoration of the central Andes in 2-D map view'. In: *Tectonics* 27(6). doi: 10.1029/2008TC002269.
- Arvidsson, R. (1996). 'Fennoscandian Earthquakes: Whole Crustal Rupturing Related to Postglacial Rebound'. In: *Science* 274(5288), pp. 744–746.
- Assumpção, M., M. Feng, A. Tassara and J. Julià (2013). 'Models of crustal thickness for South America from seismic refraction functions and surface wave tomography'. In: *Tectonophysics* 609, pp. 82–96. doi: 10.1016/j.tecto.2012.11.014.
- Babeyko, A. Y. and S. V. Sobolev (2008). 'High-resolution numerical modelling of stress distribution in visco-elasto-plastic subducting slabs'. In: *Lithos* 103, pp. 205–216. doi: 10.1016/j.lithos.2007.09.015.
- Baes, M., S. V. Sobolev and J. Quinteros (2018). 'Subduction initiation in mid-ocean induced by mantle suction flow'. In: *Geophysical Journal International* 215(3), pp. 1515–1522. doi: 10.1093/gji/ggy335.
- Banerjee, B. (Nov. 2006). *Basic Thermoelasticity*. University of Utah, Department of mechanical engineering. doi: 10.13140/RG.2.1.1144.2005.
- Banerjee, B. (May 2007). *Basic Thermoplasticity*. University of Utah, Department of mechanical engineering.
- Baumann, T. S. and J. P. Kaus (2015). 'Geodynamic inversion to constrain the non-linear rheology of the lithosphere'. In: *Geophysical Journal International* 202, pp. 1289–1316. doi: 10.1093/gji/ggv201.
- Beavan, J. and J. Haines (2001). 'Contemporary horizontal velocity and strain rate fields of the Pacific-Australian plate boundary zone through New Zealand'. In: *J. Geophysical Research* 106(B1), pp. 741–770. doi: 10.1029/2000JB900302.
- Bessemoulin-Chatard, M. (2012). 'A finite volume scheme for convection-diffusion equations with nonlinear diffusion derived from the Scharfetter-Gummel scheme'. In: *Numerische Mathematik* 121, pp. 637–670. doi: 10.1007/s00211-012-0448-x.
- Bevis, M. E., E. Kendrick, R. Smalley, B. Brooks, R. Allmendinger and B. Isacks (2001). 'On the strength of interplate coupling and the rate of back arc convergence in the central Andes: An analysis of the interseismic velocity field'. In: *Geochemistry, Geophysics, Geosystems* 2(11). doi: 10.1029/2001GC000198.
- Bijwaard, H., W. Spakman and E. R. Engdahl (1998). 'Closing the gap between regional and global travel time tomography'. In: *J. Geophysical Research* 103, pp. 30055–30078. doi: 10.1029/98JB02467.
- Bilek, S. L. (2008). 'Modeling the Dynamics of Subducting Slabs'. In: *Annual Reviews of Earth and Planetary Sciences* 36, pp. 325–356. doi: 10.1146/annurev.earth.36.031207.124129.
- Bilek, S. L. (2010). 'Invited review paper: Seismicity along the South American subduction zone: Review of large earthquakes, tsunamis, and subduction zone complexity'. In: *Tectonophysics* 495(1-2), pp. 2–14. doi: 10.1016/j.tecto.2009.02.037.
- Billen, M. I. (2008). 'Modeling the Dynamics of Subducting Slabs'. In: *Annual Review of Earth and Planetary Sciences* 36, pp. 325–356. doi: 10.1146/annurev.earth.36.031207.124129.
- Billen, M. I. and G. Hirth (2007). 'Rheologic controls on slab dynamics'. In: *Geochemistry, Geophysics, Geosystems* 8(8). doi: 10.1029/2007GC001597.
- Biot, M. A. (1961). 'Theory of folding of stratified viscoelastic media and its implications in tectonics and orogenesis'. In: *Geological Society of America Bulletin* 72, pp. 1595–1620.

- Blanpied, M. L., D. A. Lockner and J. D. Byerlee (1995). 'Frictional slip of granite at hydrothermal conditions'. In: *J. Geophysical Research* 100, pp. 13045–13064. doi: 10.1029/95JB00862.
- Bletery, Q., A. M. Thomas, A. W. Rempel and J. L. Hardebeck (2017). 'Imaging Shear Strength Along Subduction Faults'. In: *Geophysical Research Letters* 44. doi: 10.1002/2017GL075501.
- Bloch, W., J. Kummerow, P. Salazar, P. Wigger and S. A. Shapiro (2014). 'High-resolution image of the North Chilean subduction zone: seismicity, reflectivity and fluids'. In: *Geophysical Journal International* 197, pp. 1744–1749. doi: 10.1093/gji/ggu084.
- Bonnardot, M.-A., R. Hassani, E. Tric, E. Ruellan and M. Régnier (2008). 'Effect of margin curvature on plate deformation in a 3-D numerical model of subduction zones'. In: *Geophysical Journal International* 173, pp. 1084–1094. doi: 10.1111/j.1365-246X.2008.03752.
- Boutelier, D. and O. Oncken (2010). 'Role of the plate margin curvature in the plateau buildup: Consequences for the central Andes'. In: *J. Geophysical Research Solid Earth* 115 (B4). doi: 10.1029/2009JB006296.
- Brace, W. F. and D. L. Kohlstedt (1980). 'Limits on Lithospheric Stress Imposed by Laboratory Experiments'. In: *J. Geophysical Research* 85, B11, pp. 6248–6252. doi: 10.1029/JB085iB11p06248.
- Bürgmann, R. and G. Dresen (2008). 'Rheology of the Lower Crust and Upper Mantle: Evidence from Rock Mechanics, Geodesy and Field Observations'. In: *Annual Review of Earth and Planetary Sciences*.
- Brooks, B. A., M. Bevis, K. X. Whipple, J. R. Arrowsmith, J. Foster, T. Zapata, E. Kendrick, E. Minaya, A. Echalar, M. Blanco, P. Euillades, M. Sandoval and R. J. Smalley (2011). 'Orogenic-wedge deformation and potential for great earthquakes in the central Andean backarc'. In: *Nature Geoscience* 4, pp. 380–383. doi: 10.1038/ngeo1143.
- Brown, M., F. Díaz and J. Grocott (1993). 'Displacement history of the Atacama fault system 25°00'S–27°00'S, northern Chile'. In: *Geological Society of America Bulletin* 105, pp. 1165–1174.
- Burg, J.-P. and S. M. Schmalholz (2008). 'Viscous heating allows thrusting to overcome crustal-scale buckling: Numerical investigation with application to the Himalayan syntaxes'. In: *Earth and Planetary Science Letters* 274, pp. 189–203. doi: 10.1016/j.epsl.2008.07.022.
- Burov, E. B. (2010). 'The equivalent elastic thickness (T_e), seismicity and the long-term rheology of continental lithosphere: Time to burn-out "crème brûlée"? Insights from large-scale geodynamic modeling'. In: *Tectonophysics* 484(1-4), pp. 4–26. doi: 10.1016/j.tecto.2009.06.013.
- Burov, E. B. (2011). 'Rheology and strength of the lithosphere'. In: *Marine and Petroleum Geology* 28, pp. 1402–1443. doi: 10.1016/j.marpetgeo.2011.05.008.
- Byerlee, J. (1978). 'Friction of Rocks'. In: *Pure and Applied Geophysics* 116(4-5), pp. 615–626. doi: 10.1007/BF00876528.
- Capitanio, F. A. and G. Morra (2012). 'The bending mechanics in a dynamic subduction system: Constraints from numerical modelling and global compilation analysis'. In: *Tectonophysics* 522-523, pp. 224–234. doi: 10.1016/j.tecto.2011.12.003.
- Carminati, E., A. M. Negredo, J. L. Valera and C. Doglioni (2005). 'Subduction-related intermediate-depth and deep seismicity in Italy: Insights from thermal and rheological

- modelling'. In: *Physics of the Earth and Planetary Interiors* 149(1-2), pp. 65–79. doi: 10.1016/j.pepi.2004.04.006.
- Chu, S. S., M. L. Lin, W. C. Huang, W. T. Nien, H. C. Liu and P. C. Chan (2015). 'Simulation of growth normal fault sandbox tests using the 2D discrete element method'. In: *Computers & Geosciences* 74, pp. 1–12. doi: 10.1016/j.cageo.2014.10.006.
- Cignoni, P., M. Callieri, M. Corsini, M. Dellepiane, F. Ganovelli and G. Ranzuglia (2008). 'MeshLab: an Open-Source Mesh Processing Tool'. In: *Sixth Eurographics Italian Chapter Conference*, pp. 129–136.
- Cloos, M. and L. Shreve (1988). 'Subduction-channel model of prism accretion, mélange formation, sediment subduction, and subduction erosion at convergent plate margins: 1. Background and description'. In: *Pure and Applied Geophysics* 128(3-4), pp. 455–500. doi: 10.1007/BF00874548.
- Coblentz, D. D., M. Sandiford, R. M. Richardson, S. Zhou and R. Hillis (1995). 'The origins of the intraplate stress field in continental Australia'. In: *Earth and Planetary Science Letters* 133, pp. 299–309. doi: 10.1016/0012-821X(95)00084-P.
- Comte, D. and M. Pardo (1991). 'Reappraisal of Great Historical Earthquakes in the Northern Chile and Southern Peru Seismic Gaps'. In: *Natural Hazards* 4, pp. 23–44. doi: 10.1007/BF00126557.
- Condie, K. C. (2011). *Earth as an Evolving Planetary System*. Elsevier. ISBN: 978-0-12-385227-4.
- Conrad, C. P. and C. Lithgow-Bertelloni (2004). 'The temporal evolution of plate driving forces: Importance of "slab suction" versus "slab pull" during the Cenozoic'. In: *J. Geophysical Research* 109, pp. 1–14. doi: 10.1029/2004JB002991.
- Conrad, C. P., S. Bilek and C. Lithgow-Bertelloni (2004). 'Great earthquakes and slab pull: interaction between seismic coupling and plate-slab coupling'. In: *Earth and Planetary Science Letters* 218(1-2), pp. 109–122. doi: 10.1016/S0012-821X(03)00643-5.
- Contreras-Reyes, E. (2019). 'Control of subduction erosion and sediment accretion processes on the trench curvature of the central Chilean margin'. In: *Andean Tectonics*. Ed. by B. K. Horton and A. Folguera. Elsevier. ISBN: 978-0-12-816009-1.
- Copley, A. (2017). 'The strength of earthquake-generating faults'. In: *J. Geological Society* 175, pp. 1–12. doi: 10.1144/jgs2017-037.
- Copley, A. and D. McKenzie (2007). 'Models of crustal flow in the India-Asia collision zone'. In: *Geophysical Journal International* 169(2), pp. 683–698. doi: 10.1111/j.1365-246X.2007.03343.x.
- Copley, A., J.-P. Avouac and B. P. Wernicke (2011). 'Evidence for mechanical coupling and strong Indian lower crust beneath southern Tibet'. In: *Nature* 472, pp. 79–81. doi: 10.1038/nature09926.
- Cortés, J. A., G. González, S. A. Binnie, R. Robinson, S. P. H. T. Freeman and G. Vargas (2012). 'Paleoseismology of the Mejillones Fault, northern Chile: Insights from cosmogenic ^{10}Be and Optically Stimulated Luminescence determinations'. In: *Tectonics* 31(2). doi: 10.1029/2011TC002877.
- Craig, T. J., A. Copley and T. A. Middleton (2014). 'Constraining fault friction in oceanic lithosphere using the dip angles of newly-formed faults at outer rises'. In: *Earth and Planetary Science Letters* 392, pp. 94–99. doi: 10.1016/j.epsl.2014.02.024.
- Crameri, F., C. P. Conrad, L. Montési and C. R. Lithgow-Bertelloni (2019). 'The dynamic life of an oceanic plate'. In: *Tectonophysics* 760, pp. 107–135. doi: 10.1016/j.tecto.2018.03.016.

- Currie, C. A., R. D. Hyndman, K. Wang and V. Kostoglodov (2002). ‘Thermal models of the Mexico subduction zone: Implications for the megathrust seismogenic zone’. In: *J. Geophysical Research* 107:B12,2370. doi: 10.1029/2001JB000886.
- Dahlen, F. A. (1990). ‘Critical taper model of fold-and-thrust belts and accretionary wedges’. In: *Annual Review of Earth and Planetary Sciences* 18, pp. 55–99. doi: 10.1146/annurev.ea.18.050190.000415.
- Davies, J. H. (2013). ‘Global map of solid Earth surface heat flow’. In: *Geochemistry, Geophysics, Geosystems* 14(10), pp. 4608–4622. doi: 10.1002/ggge.20271.
- DeCelles, P. G., M. N. Ducea, B. Carrapa and P. A. Kapp (2015). *Geodynamics of a Cordillera Orogenic System - The Central Andes of Argentina and Northern Chile*. Geological Society of America. ISBN: 978-0-8137-1212-3.
- Delouis, B., H. Philip, L. Dorbath and A. Cisternas (1998). ‘Recent crustal deformation in the Antofagasta region (northern Chile) and the subduction process’. In: *Geophysical Journal International* 132, pp. 302–338. doi: 10.1046/j.1365-246x.1998.00439.x.
- DeMets, C., R. Gordon, D. Argus and S. Stein (1994). ‘Effect of recent revision to the geomagnetic reversal time scale on estimates of current plate motion’. In: *Geophysical Research Letters* 21, pp. 2191–2194. doi: 10.1029/94GL02118.
- DeMets, C., R. G. Gordon and D. F. Argus (2010). ‘Geologically current plate motions’. In: *Geophysical Journal International* 181(1), pp. 1–80. doi: 10.1111/j.1365-246X.2009.04491.x.
- Dewey, J. F. and S. H. Lamb (1992). ‘Active tectonics of the Andes’. In: *Tectonophysics* 205, pp. 79–95.
- Dorbath, C., M. Gerbault, G. Carlier and M. Guiraud (2008). ‘The Double Seismic Zone of the Nazca Plate in Northern Chile: High Resolution Velocity Structure, Petrological Implications and Thermo-Mechanical Modelling’. In: *Geochemistry, Geophysics, Geosystems* 9(7), pp. 1–29. doi: 10.1029/2008GC002020.
- Drewes, H. and L. Sanchez (2017). *The varying surface kinematics in Latin America: VEMOS 2009, 2014 and 2017*. Symposium SIRGAS2017, Mendoza, Argentina, November 28, 2017.
- Eichelberger, N. and N. McQuarrie (2015). ‘Kinematic reconstructions of the Bolivian orocline’. In: *Geosphere* 11, pp. 445–462. doi: 10.1130/GES01064.1.
- Emmerson, B. and D. McKenzie (2007). ‘Thermal structure and seismicity of subducting lithosphere’. In: *Physics of the Earth and Planetary Interiors* 163(1-4), pp. 191–208. doi: 10.1016/j.pepi.2007.05.007.
- Espurt, N., F. Funicello, J. Martinod, B. Guillaume, C. Faccenna and S. Brusset (2008). ‘Flat subduction dynamics and deformation of the South American plate: Insights from analog modelling’. In: *Tectonics* 27(3). doi: 10.1029/2007TC002175.
- Faccenna, L., A. F. Holt, T. W. Becker, S. Lallemand and L. H. Royden (2018). ‘Dynamics of the Ryukyu/Izu-Bonin-Marianas double subduction system’. In: *Tectonophysics* 746, pp. 229–238. doi: 10.1016/j.tecto.2017.08.011.
- Farrington, R. J., L.-N. Moresi and F. A. Capitanio (2014). ‘The role of viscoelasticity in subducting plates’. In: *Geochemistry, Geophysics, Geosystems* 15, pp. 4291–4304. doi: 10.1002/2014GC005507.
- Filbet, F. and M. Herda (2017). ‘A finite volume scheme for boundary-driven convection-diffusion equations with relative entropy structure’. In: *Numerische Mathematik* 137, pp. 535–577. doi: 10.1007/s00211-017-0885-7.
- FLAC (2018). *FLAC-Explicit Continuum Modeling of Non-linear Material Behaviour in 2D*. URL: <https://www.itascacg.com/software/flac> (visited on 19/02/2019).

- Forsyth, D. and S. Uyeda (1975). ‘On the relative importance of the driving forces of plate motion’. In: *Geophysical Journal of the Royal Astronomical Society* 43, pp. 163–200.
- Fuchs, L., H. Koyi and H. Schmeling (2015). ‘Numerical modeling of the effect of composite rheology on internal deformation in down-built diapirs’. In: *Tectonophysics* 646, pp. 79–95. doi: 10.1016/j.tecto.2015.01.014.
- Fukao, Y. and M. Obayashi (2013). ‘Subducted slabs stagnant above, penetrating through, and trapped below the 660 km discontinuity’. In: *J. Geophysical Research: Solid Earth* 118, pp. 5920–5938. doi: 10.1002/2013JB010466.
- Fukumura, S., K. Okamoto and M. Terabayashi (2019). ‘Metamorphic olivine after dehydration embrittlement in Serpentine: Case study from the Shiraga Serpentine mass in the Sanbagawa high P/T metamorphic belt, central Shikoku, Japan’. In: *Island Arc* e12293. doi: 10.1111/iar.12293.
- Gassmüller, R. (2011). ‘Spannungs- und Deformationsverteilung an gebogenen Subduktionszonen’. Diploma thesis. Jena, Germany: Friedrich-Schiller-University.
- Gerbault, M., J. Cembrano, C. Mpodozis, M. Farias and M. Pardo (2009). ‘Continental Margin Deformation along the Andean Subduction zone: Thermomechanical Models’. In: *Physics of the Earth and Planetary Interiors* 117, pp. 180–205. doi: 10.1016/j.pepi.2009.09.001.
- Gerbault, M., J. Schneider, A. Reverso-Peila and M. Corsini (2018). ‘Crustal exhumation during ongoing compression in the Variscan Maures-Tanneron Massif, France - Geological and thermomechanical aspects’. In: *Tectonophysics* 746, pp. 439–458. doi: 10.1016/j.tecto.2016.12.019.
- Gerbault, M., R. Hassani, C. N. Lizama and A. Souche (2018). ‘Three-Dimensional Failure Patterns Around an Inflating Magmatic Chamber’. In: *Geochemistry, Geophysics, Geosystems* 19(3), pp. 749–771. doi: 10.1002/2017GC007174.
- Gerya, T. V. (2010). *Introduction to numerical geodynamic modelling*. Cambridge University Press. ISBN: 978-0-521-88754-0.
- Gerya, T. V. and D. A. Yuen (2007). ‘Robust characteristic method for modeling multiphase visco-elasto-plastic thermo-mechanical problems’. In: *Physics of the Earth and Planetary Interiors* 163, pp. 83–105. doi: 10.1016/j.pepi.2007.04.015.
- Gülcher, A. J. P., S. J. Beaussier and T. V. Gerya (2019). ‘On the formation of oceanic detachment faults and their influence on intra-oceanic subduction initiation: 3D thermo-mechanical modeling’. In: *Earth and Planetary Science Letters* 506, pp. 195–208. doi: 10.1016/j.epsl.2018.10.042.
- Goes, S., R. Agrusta, J. van Hunen and F. Garel (2017). ‘Subduction-transition zone interaction: A review’. In: *Geosphere* 13(3). doi: 10.1130/GES01476.1.
- González, G., J. Cembrano, D. Carrizo, A. Macci and H. Schneider (2003). ‘Link between forearc tectonics and Pliocene-Quaternary deformation of the Coastal Cordillera, Northern Chile’. In: *J. South American Earth Sciences* 16, pp. 321–342. doi: 10.1016/S0895-9811(03)00100-7.
- González, G., T. Dunai, D. Carrizo and R. Allmendinger (2006). ‘Young displacements on the Atacama Fault System, northern Chile from field observations and cosmogenic ^{21}Ne concentrations’. In: *Tectonics* 25(3). doi: 10.1029/2005TC001846.
- González, G., P. Salazar, J. P. Loveless, R. W. Allmendinger, F. Aron and M. Shrivastava (2015). ‘Upper plate reverse fault reactivation and the unclamping of the megathrust during the 2014 northern Chile earthquake sequence’. In: *Geology* 43(8), pp. 671–674. doi: 10.1130/G36703.1.

- Gordon, R. G. and S. Stein (1992). 'Global tectonics and space geodesy'. In: *Science* 256, pp. 333–342.
- Goutorbe, B., J. Poort, F. Lucazeau and S. Raillard (2011). 'Global heat flow trends resolved from multiple geological and geophysical proxies'. In: *Geophysical Journal International* 187(7), pp. 1405–1419. doi: 10.1111/j.1365-246X.2011.05228.x.
- Gregory-Wodzicki, K. M. (2000). 'Uplift history of the Central and Northern Andes: A review'. In: *Bulletin of the Geological Society of America* 112(7), pp. 1091–1105. doi: 10.1130/0016-7606(2000)112<1091:UHOTCA>2.0.CO;2.
- Groh, U., H. Konietzky, K. Walter and M. Herbst (2011). 'Damage simulation of brittle heterogeneous materials at the grain size level'. In: *Theoretical and Applied Fracture Mechanics* 55, pp. 31–38. doi: 10.1016/j.tafmec.2011.03.001.
- Götze, H.-J. and B. Lahmeyer (1988). 'Application of three-dimensional interactive modeling in gravity and magnetics'. In: *Geophysics* 53(8), pp. 1096–1108. doi: 10.1190/1.1442546.
- Gutknecht, B. D., H.-J. Götze, T. Jahr, G. Jentzsch, R. Mahatsente and S. Zeumann (2014). 'Structure and State of Stress in the Chilean Subduction Zone from Terrestrial and Satellite-Derived Gravity and Gravity Gradient Data'. In: *Surveys in Geophysics*. doi: 10.1007/s10712-014-9296-9.
- Gutscher, M.-A. (2001). 'An Andean model of interplate coupling and strain partitioning applied to the flat subduction zone of WS Japan (Nankai Trough)'. In: *Tectonophysics* 333, pp. 95–109. doi: 10.1016/S0040-1951(00)00269-9.
- Gutscher, M.-A., W. Spakman, H. Bijwaard and E. R. Engdahl (2000). 'Geodynamics of a flat subduction: Seismicity and tomographic constraints from the Andean margin'. In: *Tectonics* 19(5), pp. 814–833. doi: 10.1029/1999TC001152.
- Gutscher, M.-A., R. Maury, J.-P. Eissen and E. Bourdon (2000). 'Can slab melting be caused by flat subduction?' In: *Geology* 28(6), pp. 535–538. doi: 10.1130/0091-7613(2000)28<535:CSMBCB>2.0.CO;2.
- Haines, A. J. and W. E. Holt (1993). 'A procedure for obtaining the complete horizontal motions within zones of distributed deformation from the inversion of strain rate data'. In: *J. Geophysical Research* 98(B7), pp. 12057–12082. doi: 10.1029/93JB00892.
- Hampel, A. and A. Pfiffner (2006). 'Relative importance of trenchward upper plate motion and friction along the plate interface for the topographic evolution of subduction-related mountain belts'. In: *Analogue and Numerical Modelling of Crustal-Scale processes*. Ed. by S. J. H. Buiter and G. Schreurs. Geological Society, London, Special Publications, 253. doi: 10.1144/GSL.SP.2006.253.01.05.
- Hamza, V. M. and M. Munoz (1996). 'Heat flow map of South America'. In: *Geothermics* 25, pp. 599–646. doi: 10.1016/S0375-6505(96)00025-9.
- Hamza, V. M., R. R. Cardoso and C. F. Ponte Neto (2008). 'Spherical harmonic analysis of earth's conductive heat flow'. In: *International Journal of Earth Sciences* 97, pp. 205–226. doi: 10.1007/s00531-007-0254-3.
- Harris, R. N., G. Spinelli, C. R. Ranero, I. Grevemeyer, H. Villinger and U. Barckhausen (2010). 'Thermal regime of the Costa Rican convergent margin: 2. Thermal models of the shallow Middle America subduction zone offshore Costa Rica'. In: *Geochemistry, Geophysics, Geosystems* 11:12. doi: 10.1029/2010GC003273.
- Hassani, R., D. Jongmans and J. Chery (1997). 'Study of plate deformation and stress in subduction processes using two-dimensional numerical model'. In: *J. Geophysical Research* 108, pp. 17951–17965. doi: 10.1029/97JB01354.
- Hasterok, D. (in prep). 'An analysis of the revised global heat flow database'. In.

- Hasterok, D. and D. S. Chapman (2008). ‘Global heat flow: A new database and a new approach’. In: *AGU Fall Meeting Abstracts*.
- Hayes, G. P., D. J. Wald and R. L. Johnson (2012). ‘Slab 1.0: A three-dimensional model of global subduction zone geometries’. In: *J. Geophysical Research* 117(B01302). doi: 10.1029/2011JB008524.
- Heuret, A. and S. Lallemand (2005). ‘Plate motions, slab dynamics and back-arc deformation’. In: *Physics of the Earth and Planetary Interiors* 149, pp. 31–51. doi: 10.1016/j.pepi.2004.08.022.
- Hirth, G. and D. Kohlstedt (2003). ‘Rheology of the Upper Mantle and the Mantle Wedge: A View from the Experimentalists’. In: *Inside the Subduction Factory*. Wiley Online Library, pp. 83–105. doi: 10.1029/138GM06.
- Hoffmann-Rothe, A., N. Kukowski, G. Dresen, H. Echtler, O. Oncken, J. Klotz, E. Scheuber and A. Kellner (2006). ‘Oblique Convergence along the Chilean Margin: Partitioning, Margin-Parallel Faulting and Force Interaction at the Plate Interface’. In: *The Andes-Active Subduction Orogeny*. Ed. by O. Oncken, G. Chong, G. Franz, F. Giese, H.-J. Götze, V. A. Ramos, M. R. Strecker and P. Wigger. Springer. ISBN: 3-540-24329-1.
- Holt, W. E., B. Shen-Tu, A. J. Haines and J. Jackson (2000). ‘On the determination of self-consistent strain rate fields within zones of distributed continental deformation’. In: *The History and Dynamics of Global Plate Motions, Geophysical Monograph Series 121*. Ed. by M. A. Richards, R. G. Gordon and R. D. Van der Hilst. American Geophysical Union. ISBN: 9780875909790. doi: 10.1029/GM121.
- Horton, B. K. (2018). ‘Tectonic Regimes of the Central and Southern Andes: Responses to Variations in Plate Coupling During Subduction’. In: *Tectonics* 37, pp. 402–429. doi: 10.1002/2017TC004624.
- Hsieh, H.-H. and H.-Y. Yen (2016). ‘Three-dimensional density structures of Taiwan and tectonic implications based on the analysis of gravity data’. In: *J. Asian Earth Sciences* 124, pp. 247–259. doi: 10.1016/j.jseaes.2016.05.009.
- Hyndman, R. D. (2007). ‘The Seismogenic Zone of Subduction Thrust Faults: What we know and don’t know’. In: *The Seismogenic Zone of Subduction Thrust Faults*. Columbia University Press. ISBN: 978-0-231-13866-6.
- Iaffaldano, G., E. Di Giuseppe, F. Corbi, F. Funiciello, C. Faccenna and H.-P. Bunge (2012). ‘Varying mechanical coupling along the Andean margin: Implications for trench curvature, shortening and topography’. In: *Tectonophysics* 526–529, pp. 16–23. doi: 10.1016/j.tecto.2011.09.014.
- Ibarra, F., S. Liu, C. Meeßen, C. B. Prezzi, J. Bott, M. Scheck-Wenderoth, S. Sobolev and M. R. Strecker (2019). ‘3D data-derived lithospheric structure of the Central Andes and its implications for deformation: Insights from gravity and geodynamic modelling’. In: *Tectonophysics* 766, pp. 453–468. doi: 10.1016/j.tecto.2019.06.025.
- Isacks, B. (1988). ‘Uplift of the central Andean plateau and bending of the Bolivian orocline’. In: *J. Geophysical Research* 93, pp. 3211–3231. doi: 10.1029/JB093iB04p03211.
- Jaquet, Y. and S. M. Schmalholz (2018). ‘Spontaneous ductile crustal shear zone formation by thermal softening and related stress, temperature and strain rate evolution’. In: *Tectonophysics* 746, pp. 384–397. doi: 10.1016/j.tecto.2017.01.012.
- Ji, Y. and S. Yoshioka (2015). ‘Effects of slab geometry and obliquity on the interplate thermal regime associated with the subduction of three-dimensionally curved oceanic plates’. In: *Geoscience Frontiers* 6(1), pp. 61–78. doi: 10.1016/j.gsf.2014.04.011.

- Jiang, H. and Yongli Xie (2011). 'A note on the Mohr-Coulomb and Drucker-Prager strength criteria'. In: *Mechanics Research Communications* 38, pp. 309–314. doi: 10.1016/j.mechrescom.2011.04.001.
- Kameyama, M., D. A. Yuen and S.-I. Karato (1999). 'Thermal-mechanical effects of low-temperature plasticity (the Peierls mechanism) on the deformation of a viscoelastic shear zone'. In: *Earth and Planetary Science Letters* 168(1-2), pp. 159–172. doi: 10.1016/S0012-821X(99)00040-0.
- Kao, H. and W. P. Chen (1991). 'Earthquakes along the Ryukyu-Kyushu arc: strain segmentation, lateral compression and thermomechanical state of the plate interface'. In: *J. Geophysical Research* 96, pp. 21443–21485. doi: 10.1029/91JB02164.
- Karato, S.-I. (2010). 'Rheology of the deep upper mantle and its implications for the preservation of the continental roots: A review'. In: *Tectonophysics* 481, pp. 82–98. doi: 10.1016/j.tecto.2009.04.011.
- Karato, S.-I., M. S. Paterson and J. D. Fitzgerald (1986). 'Rheology of Synthetic Olivine Aggregates: Influence of Grain Size and Water'. In: *J. Geophysical Research* 91(B8), pp. 8151–8176. doi: 10.1029/JB091iB08p08151.
- Kaus, B. J. P., Y. Liu, T. W. Becker, D. A. Yuen and Y. Shi (2009). 'Lithospheric stress-states predicted from long-term tectonic models: Influence of rheology and possible application to Taiwan'. In: *J. Asian Earth Sciences* 36, pp. 119–134. doi: 10.1016/j.jseaes.2009.04.004.
- Kay, S. M. and B. L. Coira (2009). 'Shallowing and steepening subduction zones, continental lithospheric loss, magmatism, and crustal flow under the central Andean Altiplano-Puna Plateau'. In: *Backbone of the Americas: Shallow Subduction, Plateau Uplift, and Ridge and Terrane Collision*. Ed. by S. M. Kay, V. A. Ramos and W. R. Dickinson. Geological Society of America. ISBN: 978-0-8137-1204-8.
- Kazhdan, M. and H. Hoppe (2013). 'Screened Poisson Surface Reconstruction'. In: *ACM Transactions on Graphics* 32 (3), p. 29. doi: 10.1145/2487228.2487237.
- Kellner, A. (2007). 'Different styles of deformation of the fore-arc wedge along the Chilean convergent margin: Insights from 3D numerical experiments'. PhD thesis. University Potsdam.
- Kennett, B. L. N. and H.-P. Bunge (2008). *Geophysical Continua*. Cambridge University Press. ISBN: 978-0-521-86553-1.
- Kirby, S. H. (1996). 'Interslab earthquakes and phase changes in subducting lithosphere'. In: *Reviews of Geophysics* 34(2), pp. 261–306. doi: 10.1029/96RG01050.
- Kirby, S. H. and A. K. Kronenberg (1987). 'Rheology of the Lithosphere: Selected Topics'. In: *Reviews of Geophysics* 25,6, pp. 1219–1244. doi: 10.1029/RG025i006p01219.
- Kirchner, A., H.-J. Götze and M. Schmitz (1996). '3D-density modelling with seismic constraints in the Central Andes'. In: *Physics and Chemistry of the Earth* 21(4), pp. 289–293. doi: 10.1016/S0079-1946(97)00050-5.
- Kley, J. and C. R. Monaldi (1998). 'Tectonic shortening and crustal thickness in the Central Andes: how good is the correlation?' In: *Geology* 26, pp. 723–726. doi: 10.1130/0091-7613(1998)026<0723:TSACTI>2.3.CO;2.
- Kley, J., C. Monaldi and J. A. Slafity (1999). 'Along-strike segmentation of the Andean foreland: Causes and consequences'. In: *Tectonophysics* 301, pp. 75–94. doi: 10.1016/S0040-1951(98)90223-2.

- Kohlstedt, D. L., B. Evans and S. J. Mackwell (1995). 'Strength of the lithosphere: constraints imposed by laboratory experiments'. In: *J. Geophysical Research* 100(B9), pp. 17587–17602. doi: 10.1029/95JB01460.
- Kohn, M. J., A. E. Castro, B. C. Kerswell, C. R. Ranero and F. S. Spear (2018). 'Shear heating reconciles thermal models with the metamorphic rock record of subduction'. In: *Proceedings of the National Academy of Sciences of the USA* 115(46), pp. 11706–11711. doi: 10.1073/pnas.1809962115.
- Koschnick, F. (2004). 'Geometrische Locking-Effekte bei Finiten Elementen und ein allgemeines Konzept zu ihrer Vermeidung'. PhD thesis. Technische Universität München.
- Koulakov, I., S. V. Sobolev and G. Asch (2006). 'P- and S-velocity images of the lithosphere-aesthenosphere system in the Central Andes from local-source tomographic inversion'. In: *Geophysical Journal International* 167, pp. 106–126. doi: 10.1111/j.1365-246X.2006.02949.x.
- Kreemer, C. (2009). 'Absolute plate motions constrained by shear wave splitting orientations with implications for hot spot motions and mantle flow'. In: *J. Geophysical Research* 114(B10), p. 405. doi: 10.1029/2009.JB006416.
- Kreemer, C., W. E. Holt and A. J. Haines (2003). 'An integrated global model of present-day plate motions and plate boundary deformation'. In: *Geophysical Journal International* 154(1), pp. 8–34. doi: 10.1046/j.1365-246X.2003.01917.x.
- Kreemer, C., G. Blewitt and E. C. Klein (2014). 'A geodetic plate motion and Global Strain Rate Model'. In: *Geochemistry, Geophysics, Geosystems* 15(10), pp. 3849–3889. doi: 10.1002/2014GC005407.
- Krien, Y. and L. Fleitout (2008). 'Gravity above subduction zones and forces controlling plate motions'. In: *J. Geophysical Research* 113(B9). doi: 10.1029/2007JB005270.
- Kösters, M. (1998). '3D-Dichtemodellierung des Kontinentalrandes sowie quantitative Untersuchungen zur Isostasie und Rigidität der Zentralen Anden'. PhD thesis. Berliner Geowissenschaftliche Abhandlungen: Reihe B, Geophysik 32, Freie Universität Berlin.
- Kuhn, H. W. and A. W. Tucker (1951). 'Nonlinear Programming'. In: *Proceedings of the Second Berkeley Symposium on Mathematical Statistics and Probability*. University of California Press, pp. 481–492.
- Kukowski, N. and O. Oncken (2006). 'Subduction Erosion-the "Normal" Mode of Fore-Arc Material Transfer along the Chilean Margin'. In: *The Andes-Active Subduction orogeny*. Ed. by O. Oncken, G. Chong, G. Franz, F. Giese, H.-J. Götze, V. A. Ramos, M. R. Strecker and P. Wigger. Springer. ISBN: 3-540-24329-1.
- Kulm, L. D., W. J. Schweller and A. Masias (1977). 'A preliminary analysis of the geotectonic processes of the Andean continental margin, 6° to 45°S'. In: *Island Arcs, Deep Sea Trenches and Back-arc Basins*. Ed. by M. Talwani and W. C. Pitman III. American Geophysical Union, pp. 285–301. ISBN: 978-0-875-90400-9.
- Lamb, S. (2006). 'Shear stresses on megathrusts: Implications for mountain building behind subduction zones'. In: *J. Geophysical Research* 111(B07401). doi: 10.1029/2005JB003916.
- Lamb, S. (2016). 'Cenozoic uplift of the Central Andes in northern Chile and Bolivia-reconciling paleoaltimetry with the geological evolution'. In: *Canadian Journal of Earth Sciences* 53, pp. 1227–1245. doi: 10.1139/cjes-2015-0071.
- Lamb, S. and L. Hoke (1997). 'Origin of the high plateau in the central Andes, Bolivia, South America'. In: *Tectonics* 16, pp. 623–649. doi: 10.1029/97TC00495.

- Lamb, S., L. Hoke, L. Kennan and J. Dewey (1997). ‘Cenozoic evolution of the Central Andes in Bolivia and northern Chile’. In: *Orogeny Through Time*. Ed. by J.-P. Burg and M. Ford. Geological Society, London, Special Publication, 121. doi: 10.1144/GSL.SP.1997.121.01.10.
- Lücke, O. H. (2012). ‘3D Density Modeling of the Central American Isthmus from Satellite Derived Gravity Data’. PhD thesis. Christian-Albrechts-University, Kiel.
- Lee, E. H. (Mar. 1969). ‘Elastic-Plastic Deformation at Finite Strains’. In: *J. Applied Mechanics* 36(1), pp. 1–6. doi: 10.1115/1.3564580.
- Li, C., R. D. van der Hilst, E. R. Engdahl and S. Burdick (2008). ‘A new global model for P wave speed variations in Earth’s mantle’. In: *Geochemistry, Geophysics, Geosystems* 9(Q05018). doi: 10.1029/2007GC001806.
- Liao, J., T. Gerya and Malusà (2018). ‘3D modeling of crustal shortening influenced by along-strike lithological changes: Implications for continental collision in the Western and Central Alps’. In: *Tectonophysics* 746, pp. 425–438. doi: 10.1016/j.tecto.2018.01.031.
- Lin, S.-C. and B.-Y. Kuo (2016). ‘Dynamics of the opposite-verging subduction zones in the Taiwan region: Insights from numerical models’. In: *J. Geophysical Research Solid Earth* 121. doi: 10.1002/2015JB012784.
- Lindsay, D., M. Zentilli and A. Rivera (1995). ‘Evolution of an active ductile to brittle shear system controlling mineralization at Chuquicamata porphyry copper deposit, northern Chile’. In: *International Geology Review* 37, pp. 945–958.
- Lithgow-Bertelloni, C. and M. A Richards (1998). ‘The dynamics of Cenozoic and Mesozoic plate motions’. In: *Reviews of Geophysics* 36(1), pp. 27–78. doi: 10.1029/97RG02282.
- Liu, L. and J. S. Zhang (2015). ‘Differential contraction of subducted lithosphere layers generates deep earthquakes’. In: *Earth and Planetary Science Letters* 421, pp. 98–106. doi: 10.1016/j.epsl.2015.03.053.
- Liu, Y. and H. Konietzky (2018). ‘Particle-Based Modeling of Pull-Apart Basin Development’. In: *Tectonics* 37, pp. 343–358. doi: 10.1002/2017TC004685.
- Lonsdale, P. (2005). ‘Creation of the Cocos and Nazca plates by fission of the Farallon plate’. In: *Tectonophysics* 404(3-4), pp. 237–264. doi: 10.1016/j.tecto.2005.05.011.
- Lucazeau, F. (2019). ‘Analysis and Mapping of an Updated Terrestrial Heat Flow Data Set’. In: *Geochemistry, Geophysics, Geosystems* 20(8), pp. 4001–4024. doi: 10.1029/2019GC008389. URL: <http://ihfc-iugg.org/products/global-heat-flow-database>.
- Luttrell, K. M., X. Tong, D. T. Sandwell, B. A. Brooks and M. G. Bevis (2011). ‘Estimates of stress drop and crustal tectonic stress from the 27 February 2010 Maule, Chile, earthquake: Implications for fault strength’. In: *J. Geophysical Research* 116(B11401). doi: 10.1029/2011JB008509.
- Maenchen, G. and S. Sacks (1964). ‘The tensor code’. In: *Methods of Computational Physics*. Vol. 3. New York, USA: Academic Press, pp. 181–210.
- Maino, M., L. Casini, A. Ceriani, A. Decarlis, A. Di Giulio, S. Seno, M. Setti and F. M. Stuart (2015). ‘Dating shallow thrusts with zircon (U-Th)/He thermochronometry-The shear heating connection’. In: *Geology* 43(6), pp. 495–498. doi: 10.1130/G36492.1.
- Mareschal, J.-C., C. Jaupart and L. Iarotsky (2017). ‘The Earth Heat Budget, Crustal Radio-activity and Mantle Geoneutrinos’. In: *Neutrino Geoscience*. Ed. by L Ludhova. Open Academic Press, pp. 4.1–4.46.
- Marone, C. (1995). ‘Fault zone strength and failure criteria’. In: *Geophysical Research Letters* 22(6), pp. 723–726. doi: 10.1029/95GL00268.

- Marot, M., T. Monfre, M. Gerbault, G. Nolet, G. Ranalli and M. Pardo (2014). 'Flat versus normal subduction zones: a comparison based on 3-D regional travelttime tomography and petrological modelling of central Chile and western Argentina (29°-35° S)'. In: *Geophysical Journal International* 199, pp. 1633–1654. doi: 10.1093/gji/ggu355.
- McKenzie, D., J. Jackson and K. Priestley (2005). 'Thermal structure of oceanic and continental lithosphere'. In: *Earth and Planetary Science Letters* 233, pp. 337–349. doi: 10.1016/j.epsl.2005.02.005.
- Meeßen, C., J. Sippel, M. Scheck-Wenderoth, C. Heine and M. R. Strecker (2018). 'Crustal Structure of the Andean Foreland in Northern Argentina: Results from Data-Integrative Three-Dimensional Density Modeling'. In: *J. Geophysical Research: Solid Earth* 123(2), pp. 1875–1903. doi: 10.1002/2017JB014296.
- Melnick, D. (2016). 'Rise of the central Andean coast by earthquakes straddling the Moho'. In: *Nature Geoscience* 9, pp. 401–408. doi: 10.1038/NGE02683.
- Michelis, P. N. (1981). 'Work-softening and hardening behaviour of granular rocks'. In: *Rock Mechanics* 14, pp. 187–200. doi: 10.1007/BF01250450.
- Middleton, T. A. and A. Copley (2013). 'Constraining fault friction by re-examining earthquake nodal plane dips'. In: *Geophysical Journal International* 196(2), pp. 671–680. doi: 10.1093/gji/ggt427.
- Miller, T. W. and J. B. Cheatham Jr. (1972). 'A new yield condition and hardening rule for rocks'. In: *International Journal of Rock Mechanics and Mining Sciences & Geomechanical Abstracts* 9, pp. 453–474.
- Mitchell, T. M. and D. R. Faulkner (2009). 'The nature and origin of off-fault damage surrounding strike-slip fault zones with a wide range of displacements: A field study from the Atacama fault system, northern Chile'. In: *J. Structural Geology* 31(8), pp. 802–816. doi: 10.1016/j.jsg.2009.05.002.
- Müller, R. D., M. Sdrolias, C. Gaina and W. R. Roest (2008). 'Age, spreading rates and spreading symmetry of the world's ocean crust'. In: *Geochemistry, Geophysics, Geosystems* 9(4). doi: 10.1029/2007GC001743.
- Molnar, P. and P. England (1990). 'Temperatures, Heat Flux and Frictional Stress Near Major Thrust Faults'. In: *J. Geophysical Research* 95,B4, pp. 4833–4856. doi: 10.1029/JB095iB04p04833.
- Mori, H., S. Wallis, K. Fujimoto and N. Shigematsu (2015). 'Recognition of shear heating on a long-lived major fault using Raman carbonaceous material thermometry: implications for strength and displacement history of the MTL, SW Japan'. In: *Island Arc* 24, pp. 425–446. doi: 10.1111/iar.12129.
- Morishige, M. and P. van Keken (2014). 'Along-arc variation in the 3-D thermal structure around the junction between the Japan and Kurile arcs'. In: *Geochemistry, Geophysics, Geosystems* 15(6), pp. 2225–2240. doi: 10.1002/2014GC005394.
- Morishige, M. and P. van Keken (2017). 'Along-arc variation in short-term slow slip events caused by 3-D fluid migration in subduction zones'. In: *J. Geophysical Research Solid Earth* 122, pp. 1434–1448. doi: 10.1002/2016JB013091.
- Morra, G., P. Chatelain, P. Tackley and P. Koumoutsakos (2009). 'Earth curvature effects on subduction morphology: Modeling subduction in a spherical setting with the Fast Multipole Boundary Element Method'. In: *Acta Geotechnica* 4, pp. 95–105. doi: 10.1007/s11440-008-0060-5.
- Mpodozis, C. and V. Ramos (1989). 'The Andes of Chile and Argentina'. In: *Geology of the Andes and its relation to hydrocarbon and mineral resources*. Ed. by G. E. Ericksen,

- M. T. Canas Pinochet and J. A. Reinemund. Vol. 11. Circum-Pacific Council for Energy and Mineral Resources, Earth Science Series, pp. 59–89.
- Muñoz, J. A., A. Amilibia, N. Carrera, Mon R., G. Chong, E. Roca and F. Sàbat (2005). ‘A geological cross-section of the Andean orogen at 25.5° S’. In: *6th International Symposium on Andean Geodynamics (ISAG 2005, Barcelona), Extended Abstracts: 536-539*. IRD Éditions (Institut de recherche pour le développement). ISBN: 2-7099-1575-8.
- Nagel, T., U.-J. Görke, K. M. Moerman and O. Kolditz (2016). ‘On Advantages of the Kelvin Mapping in Finite Element Implementation of Deformation Processes’. In: *Environmental Earth Sciences* 75(11), pp. 1–11. doi: 10.1007/s12665-016-5429-4.
- National Geophysical Data Center (1993). *5-minute Gridded Global Relief Data (ETOPO5)*. NGDC, NOAA. doi: 10.7289/V5D798BF. (Visited on 04/02/2020).
- Negredo, A. M., J. L. Valera and E. Carminati (2004). ‘TEMSPOL: A MATLAB thermal model for deep subduction zones including major phase transformations’. In: *Computational Geosciences* 30(3), pp. 249–258. doi: 10.1016/j.cageo.2004.01.002.
- Norabuena, E. O., L. Leffler-Griffin, A. Mao, T. Dixon, S. Stein, I. S. Sacks, L. Ocola and M. Ellis (1998). ‘Space Geodetic Observations of Nazca-South America Convergence Across the Central Andes’. In: *Science* 279, pp. 358–362. doi: 10.1126/science.279.5349.358.
- Norabuena, E. O., T. H. Dixon, S. Stein and C. G. A. Harrison (1999). ‘Decelerating Nazca-South America and Nazca-Pacific Plate Motions’. In: *Geophysical Research Letters* 26(22), pp. 3405–3408. doi: 10.1029/1999GL005394.
- Oleskevich, D. A., R. D. Hyndman and K. Wang (1999). ‘The updip and downdip limits to great subduction earthquakes: Thermal and structural models of Cascadia, south Alaska, SW Japan and Chile’. In: *J. Geophysical Research* 104 (B7), pp. 14965–14991. doi: 10.1029/1999JB900060.
- Oncken, O., G. Chong, G. Franz, F. Giese, H.-J. Götze, V. A. Ramos, M. R. Strecker and P. Wigger (2006). *The Andes-Active Subduction Orogeny*. Springer. ISBN: 3-540-24329-1.
- Oncken, O., D. Hindle, J. Kley, K. Elger, P. Victor and K. Schemmann (2006). ‘Deformation of the Central Andean Upper Plate System-Facts, Fiction and Constraints for Plateau Models’. In: *The Andes-Active Subduction Orogeny*. Ed. by O. Oncken, G. Chong, G. Franz, F. Giese, H.-J. Götze, V. A. Ramos, M. R. Strecker and P. Wigger. Springer. ISBN: 3-540-24329-1.
- Osei Tutu, A., S. V. Sobolev, B. Steinberger, A. A. Popov and I. Rogozhina (2018). ‘Evaluating the Influence of Plate Boundary Friction and Mantle Viscosity on Plate Velocities’. In: *Geochemistry, Geophysics, Geosystems* 19(3), pp. 642–666. doi: 10.1002/2017GC007112.
- Ossandón, G., R. Fréaut, L. B. Gustafson, D. D. Lindsay and M. Zentilli (2001). ‘Geology of the Chuquicamata mine: a progress report’. In: *Economic Geology* 96, pp. 249–270. doi: 10.2113/gsecongeo.96.2.249.
- Pardo-Casas, F. and P. Molnar (1987). ‘Relative motion of the Nazca (Farallon) and South American Plates since Late Cretaceous time’. In: *Tectonics* 6(3), pp. 233–248. doi: 10.1029/TC006i003p00233.
- Parks, V. M. B. and N. McQuarrie (2019). ‘Kinematic, flexural and thermal modelling in the Central Andes: Unravelling age and signal of deformation, exhumation and uplift’. In: *Tectonophysics* 766, pp. 302–325. doi: 10.1016/j.tecto.2019.06.008.
- Patzwahl, R., J. Mechie, A. Schulze and P. Giese (1999). ‘2D-velocity models of the Nazca plate subduction zone between 20 and 25 degrees S from wide-angle seismic measurements during CINCA95 project’. In: *J. Geophysical Research* 104, pp. 7293–7317.

- Pavlis, N. K., J. K. Factor and S. A. Holmes (2007). 'Terrain-related gravimetric quantities computed for the next EGM'. In: *Gravity Field of the Earth: Proceedings of the 1st International Symposium of the International Gravity Field Service (IGFS) vol. 18*. Ed. by A. Kiliçoglu and R. Forsberg. Harita Dergisi, Istanbul, pp. 318–323.
- Pavlis, N. K., S. A. Holmes, S. Kenyon and J. K. Factor (2012). 'An Earth gravitational model to degree 2160: EGM2008'. In: *J. Geophysical Research: Solid Earth* 117(B4). doi: 10.1029/2011JB008916.
- Peacock, S. M. (1992). 'Blueshist-facies metamorphism, shear heating and P-T-t paths in subduction shear zones'. In: *J. Geophysical Research* 97(B12), pp. 17693–17707. doi: 10.1029/92JB01768.
- Peacock, S. M. (1996). 'Thermal and Petrologic Structure of Subduction Zones'. In: *Subduction: Top to Bottom*. American Geophysical Union, Geophysical Monograph 96, pp. 119–134.
- Pelecanos, L., S. Kontoe and L. Zdravkovic (2018). 'The Effects of Dam-Reservoir Interaction on the Nonlinear Seismic Response of Earth Dams'. In: *J. Earthquake Engineering*. doi: 10.1080/13632469.2018.1453409.
- Pelz, K. (2000). 'Tectonic erosion along the central Andean forearc (20°-24°S)'. PhD thesis. GeoForschungsZentrum Potsdam.
- Perzyna, P. (1966). 'Fundamental problems in viscoplasticity'. In: *Recent Advances in Applied Mechanics* 9, pp. 243–377.
- Pollack, H. N., S. J. Hurter and J. R. Johnson (1993). 'Heat flow from the Earth's interior: Analysis of the global data set'. In: *Reviews of Geophysics* 31(3), pp. 267–280. doi: 10.1029/93RG01249.
- Popov, A. A., S. V. Sobolev and M. D. Zoback (2012). 'Modeling evolution of the San Andreas Fault system in northern and central California'. In: *Geochemistry, Geophysics, Geosystems* 13(8). doi: 10.1029/2012GC004086.
- Prezzi, C. B., H.-J. Götze and S. Schmidt (2009). '3D density model of the Central Andes'. In: *Physics of the Earth and Planetary Interiors* 177(3-4), pp. 217–234. doi: 10.1016/j.pepi.2009.09.004.
- Ramberg, H. (1962). 'Contact strain and folding instability of a multilayered body under compression'. In: *Geologische Rundschau* 51, pp. 405–439.
- Ramos, V. A. (2010). 'The tectonic regime along the Andes: Present-day and Mesozoic regimes'. In: *Geological Journal* 45, pp. 2–25. doi: 10.1002/gj.1193.
- Ramos, V. A. and A. Folguera (2009). 'Andean flat-slab subduction through time'. In: *Ancient Orogens and Modern Analogues*. Ed. by J. B. Murphy, J. D. Keppie and A. J. Hynes. Geological Society London, Special Publications, 327. doi: 10.1144/SP327.3.
- Ramos, V. A. and S. M. Kay (1992). 'The Southern Patagonian plateau basalts: retroarc testimony of a ridge collision'. In: *Tectonophysics* 205, pp. 261–282.
- Ranalli, G. (1995). *Rheology of the earth*. Chapman and Hall. ISBN: 0-412-54670-1.
- Ranero, C. R., R. von Huene, W. Weinrebe and C. Reichert (2006). 'Tectonic processes along the Chile convergent margin'. In: *The Andes-Active Subduction Orogeny*. Ed. by O. Oncken, G. Chong, G. Franz, F. Giese, H.-J. Götze, V. A. Ramos, M. R. Strecker and P. Wigger. Springer. ISBN: 3-540-24329-1.
- Reuber, G. S., B. J. P. Kaus, A. A. Popov and T. S. Baumann (2018). 'Unraveling the Physics of the Yellowstone Magmatic System using Geodynamic Simulations'. In: *Frontiers in Earth Sciences* 6(117). doi: 10.3389/feart.2018.00117.

- Reutter, K. J., E. Scheuber and D. Helmcke (1991). 'Structural evidence of orogen-parallel strike slip displacements in the Precordillera of northern Chile'. In: *Geologische Rundschau (International Journal of Earth Sciences)* 80, pp. 135–153.
- Reutter, K.-J., E. Scheuber and G. Chong (1996). 'The Precordilleran fault system of Chuquicamata, Northern Chile: evidence for reversals along arc-parallel strike-slip faults'. In: *Tectonophysics* 259(1-3), pp. 213–228. doi: 10.1016/0040-1951(95)00109-3.
- Rietbrock, A. and F. Scherbaum (1998). 'The GIANT analysis system'. In: *Seismological Research Letters* 69(1), pp. 40–45. doi: 10.1785/gssrl.69.1.40.
- Rummel, L., B. J. P. Kaus, R. W. White, D. F. Mertz, J. Yang and T. S. Baumann (2018). 'Coupled petrological-geodynamical modeling of a compositionally heterogeneous mantle plume'. In: *Tectonophysics* 723, pp. 242–260. doi: 10.1016/j.tecto.2017.12.022.
- Rutland, R. W. R. (1971). 'Andean Orogeny and Ocean Floor Spreading'. In: *Nature* 233, pp. 252–255.
- Salazar, P. (2011). 'The upper crustal microseismicity image from the north Chilean subduction zone: implication for tectonics and fluid migration'. PhD thesis. Freie Universität Berlin.
- Salomon, C. (2018). 'Finite element modelling of the geodynamic processes of the Central Andes subduction zone: A Reference Model'. In: *Geodesy and Geodynamics* 9, pp. 246–251. doi: 10.1016/j.geog.2017.11.007.
- Sanchez, L. and H. Drewes (2016). 'Crustal deformation and surface kinematics after the 2010 earthquakes in Latin America'. In: *J. Geodynamics* 102, pp. 1–23. doi: 10.1016/j.jog.2016.06.005.
- Sandiford, M., D. D. Coblenz and R. M. Richardson (1995). 'Ridge torques and continental collision in the Indian-Australian plate'. In: *Geology* 23, pp. 653–656. doi: 10.1130/0091-7613(1995)023<0653:RTACCI>2.3.CO;2.
- Saylor, J. E. and B. K. Horton (2014). 'Nonuniform surface uplift of the Andean plateau revealed by deuterium isotopes in Miocene volcanic glass from southern Peru'. In: *Earth and Planetary Science Letters* 387, pp. 120–131. doi: 10.1016/j.epsl.2013.11.015.
- Schellart, W. P. (2004). 'Quantifying the net slab pull force as a driving mechanism for plate tectonics'. In: *Geophysical Research Letters* 31(7). doi: 10.1029/2004GL019528.
- Schepers, G., D. J. J. van Hinsbergen, W. Spakman, M. E. Kisters, L. M. Boschman and N. McQuarrie (2017). 'South-American plate advance and forced Andean trench retreat as drivers for transient flat subduction episodes'. In: *Nature Communications* 8 (15249). doi: 10.1038/ncomms15249.
- Scheuber, E. and P. A. M. Andriessen (1990). 'The kinematic and geodynamic significance of the Atacama fault zone, northern Chile'. In: *J. Structural Geology* 12(2), pp. 243–257. doi: 10.1016/0191-8141(90)90008-M.
- Scheuber, E., K. Hammerschmidt and H. Friedrichsen (1995). '40Ar/39Ar and Rb-Sr analyses from ductile shear zones from the Atacama Fault Zone, Northern Chile: the age of deformation'. In: *Tectonophysics* 250, pp. 61–87.
- Schmalholz, S. M. and N. S. Mancktelow (2016). 'Folding and necking across the scales: a review of theoretical and experimental results and their applications'. In: *Solid Earth* 7, pp. 1417–1465. doi: 10.5194/se-7-1417-2016.
- Schmalholz, S. M., B. J. P. Kaus and J.-P. Burg (2009). 'Stress-strength relationship in the lithosphere during continental collision'. In: *Geology* 37(9), pp. 775–778. doi: 10.1130/G25678A.1.

- Schmidt, S. and H.-J. Götze (1998). 'Interactive visualization and modification of 3D models using GIS functions'. In: *Physics and Chemistry of the Earth* 23, pp. 289–296. doi: 10.1016/S0079-1946(98)00027-5.
- Schmidt, S., H.-J. Götze, C. Fichler and M. Alvers (2010). 'IGMAS+ a new 3D Gravity, FTG and Magnetic Modeling Software'. In: *Geoinformatik 2010 "Die Welt im Netz"*. Ed. by A. Zipf, K. Behncke, F. Hillen and J. Schefermeyer. Akademische Verlagsgesellschaft AKA GmbH, pp. 57–63. ISBN: 978-3-89838-335-6.
- Schön, J. (1983). *Petrophysik-Physikalische Eigenschaften von Gesteinen und Mineralen*. Stuttgart: Ferdinand Enke Verlag. ISBN: 3-432-92971-4.
- Scholl, D. W. and R. von Huene (2007). 'Crustal recycling at modern subduction zones applied to the past - issues of growth and preservation of continental basement crust, mantle geochemistry, and supercontinent reconstruction'. In: *4-D Framework of Continental Crust*. Ed. by J. R. D. Hatcher, M. P. Carlson, J. H. McBride and J. R. M. Catalán. Vol. 200. Geological Society of America Memoir, pp. 9–32. ISBN: 978-0-813-71200-0. doi: 10.1130/MEM200.
- Scholl, D. W., M. S. Marlow and A. K. Cooper (1977). 'Sediment subduction and offscraping at Pacific margins'. In: *Island Arcs, Deep Sea Trenches and back-arc basins*. Ed. by M. Talwani and W. C. Pitman III. Vol. 1. American Geophysical Union, pp. 199–210. ISBN: 978-0-875-90400-9.
- Schurr, B. (2001). 'Seismic structure of the Central Andean Subduction Zone from Local Earthquake Data'. PhD thesis. GFZ Potsdam.
- Scire, A., G. Zandt, S. Beck, M. Long and L. Wagner (2017). 'The deforming Nazca slab in the mantle transition zone and lower mantle: Constraints from teleseismic tomography on the deeply subducted slab between 6°S and 32°S'. In: *Geosphere* 13(3), pp. 665–680. doi: 10.1130/GES01436.1.
- Scott, E. M., M. B. Allen, C. G. Macpherson, K. J. W. McCaffrey, J. P. Davidson, C. Saville and M. N. Ducea (2018). 'Andean surface uplift constrained by radiogenic isotopes of arc lavas'. In: *Nature Communications* 9(969). doi: 10.1038/s41467-018-03173-4.
- Seno, T. (2009). 'Determination of the pore fluid pressure ratio at seismogenic megathrusts in subduction zones: Implications for strength of asperities and Andean-type mountain building'. In: *J. Geophysical Research* 114(B05405). doi: 10.1029/2008JB005889.
- Senseny, P. E., A. F. Fossum and T. W. Pfeifle (1983). 'Non-Associative constitutive laws for low porosity rocks'. In: *International Journal for Numerical and Analytical Methods in Geomechanics* 7, pp. 101–115. doi: 10.1002/nag.1610070110.
- Sepulveda, S. A., L. B. Giambiagi, S. M. Moreiras, L. Pinto, M. Tunik, G. D. Hoke and M. Farias (2015). 'Geodynamic processes in the Andes of Central Chile and Argentina: an introduction'. In: *Geodynamic Processes in the Andes of Central Chile and Argentina*. Ed. by S. A. Sepulveda, L. B. Giambiagi, S. M. Moreiras, L. Pinto, M. Tunik, G. D. Hoke and M. Farias. Geological Society, London, Special Publications, 399. ISBN: 978-1-86239-653-1.
- Shreve, R. L. and M. Cloos (1986). 'Dynamics of sediment subduction, melange formation, and prism accretion'. In: *J. Geophysical Research* 91(B10), pp. 10229–10245. doi: 10.1029/JB091iB10p10229.
- Silver, P. G., R. M. Russo and C. Lithgow-Berteloni (1998). 'Coupling of South American and African Plate Motion and Plate Deformation'. In: *Science* 279, pp. 60–63. doi: 10.1126/science.279.5347.60.

- Simo, J. C. and T. J. R. Hughes (1998). *Computational Inelasticity*. Ed. by J. E. Marsden, L. Sirovich and S. Wiggins. New York, USA: Springer. ISBN: 0-387-97520-9.
- Sobolev, S. V. and A. Y. Babeyko (2005). ‘What drives orogeny in the Andes?’ In: *Geology* 33, pp. 617–620. doi: 10.1130/G21557.1.
- Sobolev, S. V., A. Y. Babeyko and A. Yu (1994). ‘Modeling of mineralogical composition, density and elastic wave velocities in anhydrous magmatic rocks’. In: *Surveys in Geophysics* 15, pp. 515–544. doi: 10.1007/BF00690173.
- Sobolev, S. V., A. Y. Babeyko, I. Koulakov and O. Oncken (2006). ‘Mechanism of the Andean Orogeny: Insights from Numerical Modelling’. In: *The Andes-Active Subduction Orogeny*. Ed. by O. Oncken, G. Chong, G. Franz, F. Giese, H.-J. Götze, V. A. Ramos, M. R. Strecker and P. Wigger. Springer. ISBN: 3-540-24329-1. doi: 10.1007/978-3-540-48684-8_25.
- Somoza, R. (1998). ‘Updated Nazca (Farallon)-South America relative motions during the last 40 My: implications for mountain building in the central Andean region’. In: *J. South American Earth Sciences* 11(3), pp. 211–215. doi: 10.1016/S0895-9811(98)00012-1.
- Spence, W., C. Mendoza, E. R. Engdahl, G. L. Choy and E. Norabuena (1999). ‘Seismic Subduction of the Nazca Ridge as Shown by the 1996-97 Peru Earthquakes’. In: *Pure and Applied Geophysics* 154, pp. 753–776. doi: 10.1007/s000240050251.
- Stacey, F. D (1977). ‘A Thermal Model of the Earth’. In: *Physics of the Earth and Planetary Interiors* 15, pp. 341–348. doi: 10.1016/0031-9201(77)90096-6.
- Stegman, D. R., R. Farrington, F. A. Capitanio and W. P. Schellart (2010). ‘A regime diagram for subduction styles from 3-D numerical models of free subduction’. In: *Tectonophysics* 483, pp. 29–45. doi: 10.1016/j.tecto.2009.08.041.
- Stern, C. R. (1991). ‘Role of subduction erosion in the generation of Andean magmas’. In: *Geology* 19, pp. 78–81.
- Stern, C. R. (2004). ‘Active Andean volcanism: Its geologic and tectonic setting’. In: *Revista Geologica de Chile* 31(2), pp. 161–206. doi: 10.4067/S0716-02082004000200001.
- Stern, C. R., R. Floody and D. Espiñeira (2011). ‘Olivine-hornblende-lamprophyre dikes from Quebrada los Sapos, El Teniente, Central Chile (34°S): implications for the temporal geochemical evolution of the Andean subarc mantle’. In: *Andean Geology* 38, pp. 1–22.
- Stevenson, D. J. and J. S. Turner (1977). ‘Angle of subduction’. In: *Nature* 270, pp. 334–336.
- Straume, E. O., C. Gaina, S. Medvedev, K. Hochmuth, K. Gohl, J. M. Whittaker, R. Abdulfattah, J. C. Doornenbal and J. R. Hopper (2019). ‘GlobSed: Updated Total Sediment Thickness in the World’s Oceans’. In: *Geochemistry, Geophysics, Geosystems* 20(4), pp. 1756–1772. doi: 10.1029/2018GC008115.
- Strunk, S. (1990). ‘Analyse und Interpretation des Schwerefeldes des aktiven Kontinentalrandes der zentralen Anden (20-26°S)’. PhD thesis. Berliner Geowissenschaftliche Abhandlungen: Reihe B, Geophysik 17, Freie Universität Berlin.
- Syracuse, E. M., P. E. van Keken and G. A. Abers (2010). ‘The global range of subduction zone thermal models’. In: *Physics of the Earth and Planetary Interiors* 183, pp. 73–90. doi: 10.1016/j.pepi.2010.02.004.
- Tassara, A. (2005). ‘Interaction between the Nazca and South American plates and formation of the Altiplano-Puna Plateau: Review of a flexural analysis along the Andean margin (15°-34°S)’. In: *Tectonophysics* 399, pp. 39–57. doi: 10.1016/j.tecto.2004.12.014.
- Tassara, A. (2006). ‘Factors controlling the crustal density structure underneath active continental margins with implications for their evolution’. In: *Geochemistry, Geophysics, Geosystems* 7, Q01001. doi: 10.1029/2005GC001040.

- Tassara, A. and A. Echaurren (2012). ‘Anatomy of the Andean subduction zone: three - dimensional density model upgraded and compared against global-scale models’. In: *Geophysical Journal International* 189, pp. 161–168. doi: 10.1111/j.1365-246X.2012.05397.x.
- Tassara, A., H.-J. Götze and R. Hackney (2006). ‘Three-dimensional density model of the Nazca plate and the Andean continental margin’. In: *J. Geophysical Research* 111, B9, 404. doi: 10.1029/2005JB003976.
- Tavernier, G., H. Fagard, M. Feissel-Vernier, K. Le Bail, F. Lemoine, C. Noll, R. Noomen, J. C. Ries, L. Soudarin, J. J. Valette and P. Willis (2006). ‘The International DORIS Service: genesis and early achievements’. In: 80, pp. 403–417. doi: 10.1007/s00190-006-0082-4.
- Taylor, G. K., J. Grocott, A. Pope and D. E. Randall (1998). ‘Mesozoic fault systems, deformation and fault block rotation in the Andean forearc: a crustal scale strike-slip duplex in the Coastal Cordillera of northern Chile’. In: *Tectonophysics* 299, pp. 93–109. doi: 10.1016/S0040-1951(98)00200-5.
- Thomson, W. (1856). ‘Elements of a Mathematical Theory of Elasticity. Part 1: On Stresses and Strains’. In: *Philosophical Transactions of the Royal Society of London* 146, pp. 481–498. URL: <http://www.jstor.org/stable/108596>.
- Tichelaar, B. W. and J. L. Ruff (1993). ‘Depth of seismic coupling along subduction zones’. In: *J. Geophysical Research* 98, pp. 2017–3027. doi: 10.1029/92JB02045.
- Tomlinson, A. and N. Blanco (1997). ‘Structural evolution and displacement history of the west fault system, Precordillera, Chile: Part 2, postmineral history’. In: *Congreso Geológico Chileno, No. 8, 3*, pp. 1878–1882.
- Turcotte, D. and G. Schubert (2014). *Geodynamics*. Cambridge University Press. ISBN: 978-1-107-00653-9.
- USGS (2020). *U. S. Geological Survey*. URL: <http://earthquake.usgs.gov> (visited on 27/01/2020).
- van Keken, P. E., B. Kiefer and S. M. Peacock (2002). ‘High-resolution models of subduction zones: Implications for mineral dehydration reactions and the transport of water into the deep mantle’. In: *Geochemistry, Geophysics, Geosystems* 3,10. doi: 10.1029/2001GC000256.
- van Summeren, J., C. P. Conrad and C. Lithgow-Bertelloni (2012). ‘The importance of slab pull and a global asthenosphere to plate motions’. In: *Geochemistry, Geophysics, Geosystems* 13(2). doi: 10.1029/2011GC003873.
- Vermeer, P. A. and R. de Borst (1984). ‘Non-Associated Plasticity for Soils, Concrete and Rock’. In: *Heron* 29,3.
- Vigny, C., A. Rudloff, J.-C. Ruegg, R. Madariaga, J. Campos and M. Alvarez (2009). ‘Upper plate deformation measured by GPS in the Coquimbo Gap, Chile’. In: *Physics of the Earth and Planetary Interiors* 175, pp. 86–95. doi: 10.1016/j.pepi.2008.02.013.
- Voigt, W. (1910). *Lehrbuch der Kristallphysik (mit Ausschluß der Kristalloptik)*. Springer. ISBN: 978-3-663-15316-0. doi: 10.1007/978-3-663-15884-4.
- von Huene, R. and C. R. Ranero (2003). ‘Subduction erosion and basal friction along the sediment-starved convergent plate margin off Antofagasta, Chile’. In: *J. Geophysical Research* 108(B2). doi: 10.1029/2001JB001569.
- von Huene, R., W. Weinrebe and F. Heeren (1999). ‘Subduction erosion along the North Chile margin’. In: *J. Geodynamics* 27, pp. 345–358. doi: 10.1016/S0264-3707(98)00002-7.

- Vrolijk, P. (1990). ‘On the mechanical role of smectite in subduction zones’. In: *Geology* 18(8), pp. 703–707. doi: 10.1130/0091-7613(1990)018<0703:OTMROS>2.3.CO;2.
- Wang, K. and K. Suyehiro (1999). ‘How does plate coupling affect crustal stresses in north-east and southwest Japan?’ In: *Geophysical Research Letters* 26(15), pp. 2307–2310. doi: 10.1029/1999GL900528.
- Warren, L. M. (2014). ‘Dominant fault plane orientations of intermediate-depth earthquakes beneath South America’. In: *J. Geophysical Research: Solid Earth* 119, pp. 5762–5785. doi: 10.1002/2013JB010856.
- Wessel, P. and D. Müller (2015). ‘Plate Tectonics’. In: *Treatise of Geophysics*. Ed. by A. Watts and G. Schubert. Vol. 2(6). Elsevier. ISBN: 978-0-444-53802-4. doi: 10.1016/B978-0-444-53802-4.00111-1.
- Whitehouse, P. L. (2018). ‘Glacial isostatic adjustment modelling: historical perspectives, recent advances, and future directions’. In: *Earth Surface Dynamics* 6, pp. 401–429. doi: 10.5194/esurf-6-401-2018.
- Whittington, A. G., A. M. Hofmeister and P. I. Nabelek (2009). ‘Temperature-dependent thermal diffusivity of the Earth’s crust and implications for magmatism’. In: *Nature* 458, pp. 319–321. doi: 10.1038/nature07818.
- Wicht, J. (2002). ‘Inner-core conductivity in numerical dynamo simulations’. In: *Physics of the Earth and Planetary Interiors* 132(4), pp. 281–302. doi: 10.1016/S0031-9201(02)00078-X.
- Wilkins, M. L. (1964). ‘Calculation of elastic-plastic flow’. In: *Methods of Computational Physics*. Ed. by B. Alder, S. Fernbach and M. Rotenberg. Vol. V.3. New York, USA: Academic Press, pp. 211–263.
- Winkler, E. (1867). *Vorträge über Eisenbahnbau*. Dominicus.
- Winkler, E. (1867). *Die Lehre von der Elasticität und Festigkeit*. Dominicus.
- Woodward, D. J. (1977). ‘Stress due to phase changes in subduction zones and an empirical equation of state for the mantle’. In: *Geophysical Journal of the Royal Astronomical Society* 50, pp. 459–472. doi: 10.1111/j.1365-246.X.1977.tb04183.x.
- Yañez, G., G. R. Ranero, R. von Huene and J. Diaz (2001). ‘Magnetic anomaly interpretation across a segment of the southern Central Andes (32–34°S): implications on the role of the Juan Fernández ridge in the tectonic evolution of the margin during the Upper Tertiary’. In: *J. Geophysical Research* 106, pp. 6325–6345. doi: 10.1029/2000JB900337.
- Yuan, X., S. V. Sobolev, R. Kind, O. Oncken and Andes Seismology Group (2000). ‘Subduction and collision processes in the Central Andes constrained by converted seismic phases’. In: *Nature* 408, pp. 958–961. doi: 10.1038/35050073.
- Zeumann, S. (2013). ‘3D Finite Element Modelling of the Central Andean subduction zone with realistic geometry’. PhD thesis. Jena, Germany: Friedrich-Schiller University.
- Zeumann, S. and A. Hampel (2015). ‘Deformation of erosive and accretive forearcs during subduction of migrating and non-migrating aseismic ridges: Results from 3-D finite element models and application to the Central American, Peruvian, and Ryukyu margins’. In: *Tectonics* 34. doi: 10.1002/2015TC003867.
- Zeumann, S., R. Sharma, R. Gassmöller, T. Jahr and G. Jentzsch (2014). ‘New Finite-Element Modelling of Subduction Processes in the Andes using realistic Geometries’. In: *Earth on the Edge: Science for a Sustainable Planet*. Ed. by C. Rizos and P. Willis. Vol. 139. International Association of Geodesy Symposia, pp. 105–111. doi: 10.1007/978-3-642-37222-3_13.

- Zhang, W., Y. Zhuang and E. T. Chung (2016). ‘A new spectral finite volume method for elastic wave modelling on unstructured meshes’. In: *Geophysical Journal International* 206, pp. 292–307. doi: 10.1093/gji/ggw148.
- Ziegler, P. A., J.-D. Van Wees and S. Cloetingh (1998). ‘Mechanical controls on collision-related compressional intraplate deformation’. In: *Tectonophysics* 300(1-4), pp. 103–129. doi: 10.1016/S0040-1951(98)00236-4.
- Ziegler, P. A., G. Bertotti and S. Cloetingh (2002). ‘Dynamic processes controlling foreland development - the role of mechanical (de)coupling of orogenic wedges and forelands’. In: *Stephan Mueller Special Publication Series* 1, pp. 17–56. doi: 10.5194/smsps-1-17-2002.
- Zienkiewicz, O. C. and R. L. Taylor (2000). *The Finite Element Method, Volume 1: The Basis*. Oxford, UK: Butterworth-Heinemann. ISBN: 0-7506-5049-4.
- Zienkiewicz, O. C. and R. L. Taylor (2000). *The Finite Element Method, Volume 2: Solid Mechanics*. Oxford, UK: Butterworth-Heinemann. ISBN: 0-7506-5055-9.

Appendix

A Voigt notation and formulary

All of the tensor equations in three dimensions, can be converted into matrix equations in six dimensions, due to the fact that the stress and strain tensors are symmetric. This simplifies the equations in section 3.2 and 3.3 and reduces the amount of memory needed to save the quantities, for all fourth-rank tensors from 81 to 36 and for all second-rank tensors from 9 to 6. The most noticeable notations were proposed by Thomson (1856) (Lord Kelvin) and Voigt (1910). In Kelvin notation the stress and strain vector components are defined as

$$\vec{\sigma} = \begin{pmatrix} \sigma_{11} \\ \sigma_{22} \\ \sigma_{33} \\ \sqrt{2}\sigma_{12} \\ \sqrt{2}\sigma_{13} \\ \sqrt{2}\sigma_{23} \end{pmatrix}, \quad \vec{\epsilon} = \begin{pmatrix} \epsilon_{11} \\ \epsilon_{22} \\ \epsilon_{33} \\ \sqrt{2}\epsilon_{12} \\ \sqrt{2}\epsilon_{13} \\ \sqrt{2}\epsilon_{23} \end{pmatrix}$$

preserving the tensor character (e.g. Nagel et al., 2016). In Voigt notation we have

$$\vec{\sigma} = \begin{pmatrix} \sigma_{11} \\ \sigma_{22} \\ \sigma_{33} \\ \sigma_{12} \\ \sigma_{13} \\ \sigma_{23} \end{pmatrix}, \quad \vec{\epsilon} = \begin{pmatrix} \epsilon_{11} \\ \epsilon_{22} \\ \epsilon_{33} \\ 2\epsilon_{12} \\ 2\epsilon_{13} \\ 2\epsilon_{23} \end{pmatrix}$$

which does not preserve the tensor character.

A.1 Voigt notation

The Voigt notation is the most widely used notation among finite element programmes including Abaqus, although the violation of the tensor character results in several drawbacks as compared to the Kelvin notation.

To be able to effectively use the Voigt notation I introduce the following quantities

$$\delta_i = \begin{cases} 1, & i \in \{1, 2, 3\} \\ 0, & \text{else} \end{cases}$$

$$p_{ik} = \begin{cases} 2\delta_{ik}, & i, k \in \{1, 2, 3\} \\ \delta_{ik}, & \text{else} \end{cases}$$

$$y_{ik} = \begin{cases} 1, & i, k \in \{1, 2, 3\} \\ 2, & \text{else} \end{cases}$$

with $i, k \in \{1, 2, 3, 4, 5, 6\}$. Then a scalar product between two vectors $a_i \neq \epsilon_i$, $b_i \neq \epsilon_i$ is given by

$$\vec{a} \cdot \vec{b} = a_i y_{ik} b_k$$

Due to this the definition of the stress invariants do change, e.g. we have

$$J_2 = \frac{1}{2} s_i y_{ik} s_k$$

$$\frac{\partial J_2}{\partial \sigma_i} = y_{ik} s_k$$

with the stress deviator

$$s_i = \sigma_i - \frac{I_1}{3} \delta_i$$

$$I_1 = \sigma_i \delta_i = \sigma_1 + \sigma_2 + \sigma_3$$

The isotropic elastic stiffness matrix and its inverse read

$$C_{ik} = \mu p_{ik} + \lambda \delta_i \delta_k$$

$$S_{ik} = C_{ik}^{-1} = \frac{1}{\mu} p_{ik}^{-1} - \frac{\nu}{E} \delta_i \delta_j$$

with the Poisson ratio ν , Youngs modulus E and

$$p_{ik}^{-1} = \begin{cases} \frac{1}{2} \delta_{ik}, & i, k \in \{1, 2, 3\} \\ \delta_{ik}, & \text{else} \end{cases}$$

Multiplication of C_{ik} with an arbitrary vector a_i results in

$$a_i C_{ik} = \mu p_{ik} a_k + \lambda \delta_k (a_1 + a_2 + a_3) = C_{ik} a_k$$

A.2 Formulary for Drucker-Prager viscoplasticity

This section provides a formulary of all formulas used to define the Abaqus UMAT subroutine that specifies the relationship between stress and strain. The subduction simulation depends on temperature and, therefore, the subroutine must provide temperature dependent quantities additional to the ones derived in section 3.2 (ABAQUS 6.14, 2014). To account for frictional heating due to inelastic deformations, the rate of inelastic work converted into heat (short: dissipated heat) as well as its derivatives with respect to temperature and strain are needed. Furthermore, if a thermal expansion coefficient is given the derivative of stress with respect to temperature must be provided.

The following is a listing of all relevant formulas in full tensor notation used throughout this study for the return mapping algorithm (section 3.3) as well as the temperature dependent parameters.

- Isotropic elastic stiffness tensor and its inverse

$$C_{iklm} = \mu (\delta_{il} \delta_{km} + \delta_{im} \delta_{kl}) + \lambda \delta_{ik} \delta_{lm}$$

$$S_{iklm} = C_{iklm}^{-1} = \frac{1}{\mu} (\delta_{il} \delta_{km} + \delta_{im} \delta_{kl}) - \frac{\nu}{E} \delta_{ik} \delta_{lm}$$

with the Poisson ratio ν and Young's modulus E (see eqn. 2.1)

- Drucker-Prager yield function, plastic potential and overstress function

$$\begin{aligned}
f(\sigma_{ik}) &= \alpha(\phi)I_1 + \sqrt{J_2} - \tau_Y(\phi) \\
g(\sigma_{ik}) &= \alpha(\phi_{dil})I_1 + \sqrt{J_2} - \tau_Y(\phi_{dil}) \\
\Phi(f) &= \tau_Y(\phi) \left(\frac{f}{\tau_Y(\phi)} \right)^N \\
\alpha(\phi) &= \frac{2 \sin \phi}{\sqrt{3}(3 - \cos \phi)}, \quad \tau_Y(\phi) = \frac{6C \cos \phi}{\sqrt{3}(3 - \sin \phi)} \\
I_1 &= \sigma_{ii} = \sigma_{11} + \sigma_{22} + \sigma_{33} \\
J_2 &= \frac{1}{2} s_{ik} s_{ki} = \sigma_{12}^2 + \sigma_{13}^2 + \sigma_{23}^2 + \frac{1}{6} [(\sigma_{11} - \sigma_{22})^2 + (\sigma_{22} - \sigma_{33})^2 + (\sigma_{33} - \sigma_{11})^2] \\
s_{ik} &= \sigma_{ik} - \frac{I_1}{3} \delta_{ik}
\end{aligned}$$

- Derivatives

$$\begin{aligned}
\frac{\partial f}{\partial \sigma_{ik}} &= \alpha(\phi) \delta_{ik} + \frac{s_{ik}}{2\sqrt{J_2}} \\
\frac{\partial g}{\partial \sigma_{ik}} &= \alpha(\phi_{dil}) \delta_{ik} + \frac{s_{ik}}{2\sqrt{J_2}} \\
\frac{d\Phi}{df} &= N \cdot \frac{\Phi(f)}{f}
\end{aligned}$$

- Denominator

$$\begin{aligned}
H &= \frac{d\Phi}{df} [3\alpha(\phi)\alpha(\phi_{dil})B + \mu] + \frac{\eta(T)}{\Delta t} \\
B &= 2\mu + 3\lambda \\
\eta(T) &= \frac{1}{2} A_D^{-1/N} \dot{\epsilon}_{II}^{1/N-1} \exp\left(\frac{E_{act}}{RT}\right) \\
\dot{\epsilon}_{II} &= \sqrt{\dot{\epsilon}_{12}^2 + \dot{\epsilon}_{13}^2 + \dot{\epsilon}_{23}^2 + \frac{1}{6} [(\dot{\epsilon}_{11} - \dot{\epsilon}_{22})^2 + (\dot{\epsilon}_{22} - \dot{\epsilon}_{33})^2 + (\dot{\epsilon}_{33} - \dot{\epsilon}_{11})^2]}
\end{aligned}$$

- Residuals

$$\begin{aligned}
R_{ik} &= \Delta \epsilon_{ik} - \frac{2}{\mu} \Delta \sigma_{ik} + \frac{\nu}{E} (\Delta \sigma_{11} + \Delta \sigma_{22} + \Delta \sigma_{33}) \delta_{ik} - \lambda^{vp} \frac{\partial g}{\partial \sigma_{ik}} \\
r &= -\Phi(f) - \lambda^{vp} \frac{\eta(T)}{\Delta t}
\end{aligned}$$

- Viscoplastic strain

$$\epsilon_{ik}^{vp} = \lambda^{vp} \frac{\partial g}{\partial \sigma_{ik}}$$

- Consistent tangent modulus

$$C_{iklm}^{vp} = C_{iklm} - \frac{1}{H} \left(\alpha(\phi) \alpha(\phi_{dil}) \delta_{ik} \delta_{lm} B^2 + \mu^2 \frac{s_{ik} s_{lm}}{J_2} \right)$$

- Increments

$$\begin{aligned}\Delta\lambda^{vp} &= \frac{Z - r}{H} \\ \Delta\sigma_{ik} &= 2\mu R_{ik} + \lambda R_{ii}\delta_{ik} - \Delta\lambda^{vp} D_{ik} \\ R_{ii} &= \Delta\epsilon_{ii} + \left(\frac{3\nu}{E} - \frac{2}{\mu}\right)\Delta\sigma_{ii} - 3\alpha(\phi_{dil})\lambda^{vp} \\ Z &= \frac{d\Phi}{df} \frac{\partial f}{\partial\sigma_{ik}} C_{iklm} R_{lm} = \frac{d\Phi}{df} \left[B\alpha(\phi)R_{ii} + \mu(s_{ik}\Delta\epsilon_{ik} - \lambda^{vp}\sqrt{J_2}) - 2\frac{s_{ik}\Delta\sigma_{ik}}{\sqrt{J_2}} \right] \\ D_{ik} &= B\alpha(\phi_{dil})\delta_{ik} + \mu\frac{s_{ik}}{\sqrt{J_2}}\end{aligned}$$

- Temperature dependent parameters (see ABAQUS 6.14, 2014, Theory Guide sec. 4)
 - Dissipated heat

$$\begin{aligned}\dot{w}^h &= \frac{\beta}{2\Delta t} g_0 \lambda^{vp} \\ g_0 &= \alpha(\phi_{dil})I_1 + \sqrt{J_2}\end{aligned}$$

- Derivatives

$$\begin{aligned}\frac{\partial\sigma_{ik}}{\partial T} &= \alpha_T B \left[\frac{3\alpha(\phi)}{H} D_{ik} - \delta_{ik} \right] \\ \frac{\partial\dot{w}^h}{\partial T} &= \frac{-3\beta}{2\Delta t} \alpha_T \frac{d\Phi}{df} \alpha(\phi) B \frac{g_0}{H} \\ \frac{\partial\dot{w}^h}{\partial\epsilon_{ik}} &= \frac{\beta}{2\Delta t} \left[\alpha(\phi_{dil})\lambda^{vp}\delta_{lm}C_{lmik}^{vp} + \frac{g_0}{H} \left(\frac{d\Phi}{df} \alpha(\phi) B \delta_{ik} + \mu \frac{s_{ik}}{\sqrt{J_2}} \right) \right]\end{aligned}$$

with the fraction of inelastic energy converted into heat β and the linear thermal expansion coefficient α_T .

B Results of parameter changes

In this section further results from the parametric study are presented. The differences with respect to the reference model shown here are either comparatively low in case of a single parameter change or in case of simultaneous parameter changes the resulting differences are similar to the sum of the differences of solely varying the according parameters. Additional parameters have been varied throughout this study, however the resulting differences are even smaller than the ones presented in this section and thus, at least for short-term simulations, they are hardly important. Those parameters are the angle of dilatancy, the percentage of inelastic energy converted into heat as well as the exponent N defining the dependence of the viscosity from the shear strain rate. Furthermore, the following simultaneous parameter variations were tested, but the differences to the reference model are the same as the sum of the single differences: The angle of internal friction together with the slab pull velocity and the friction coefficient together with either slab pull velocity, maximum threshold shear stress along the zone of friction or the type of rheology, i.e. elastic, elasto-plastic or elasto-viscoplastic.

Figure B.1 shows the differences in vertical displacement with respect to the reference model along the continental (top panel) and oceanic (bottom panel) crust (green paths in figure 4.8) and in shear stress along the zone of friction (red path in figure 4.8) for four different parameter changes. When simultaneously varying the convergence velocity and the angle of internal friction (fig. B.1a) or the friction coefficient (fig. B.1b), no combined effects are observed, neither in the differences in height along the crusts nor in the shear stress along the zone of friction. On varying the velocity by $\pm 5\%$ together with varying the friction coefficient by ± 0.05 the differences due to a change in friction dominate at the frictional coupling zone and above (compare with figure 5.7), while outside of it the influence of the friction coefficient is negligible and, thus, the change in velocity dominates the result. This is true for the differences in uplift and shear stress as well. For the simultaneous variation of velocity and angle of internal friction the situation is vice versa (compare with figure 5.5). Near the trench up to about 200 km distance, the change in velocity dominates the changes in uplift and further to the east the differences due to varying the angle of internal friction become more important. Because a change in the angle has nearly no impact on the distribution of shear stresses along the zone of friction, these differences are dominated by a change in velocity.

For the reference model and all subsequent models a gravitational acceleration of 9.81 m/s^2 is assumed. But strictly speaking this is the acceleration near to the geographic poles, while the study area of northern Chile is beneath the equator where the typical value is 9.78 m/s^2 . Therefore, two model runs are accomplished wherein the acceleration is varied by $\pm 0.03 \text{ m/s}^2$ (fig. B.1c) for comparison. For this purpose the initial stress distributions had to be recomputed. Despite the very small changes in gravity the resulting differences in height are comparable with for example large changes in cohesion or angle of internal friction (fig. 5.5). Along the continental and oceanic crust changes between 10 m and 20 m of respective uplift in case of lower gravity and subsidence in case of higher gravity are observed. At the oceanic crust the variations are between 10 m to 15 m. At the continental crust the differences are similar up to a distance of 500 km east of the trench. Further towards

the model boundary the amount of subsidence decreases to near zero for an acceleration of 9.84 m/s^2 , whereas the amount of uplift increases up to 25 m for 9.78 m/s^2 . The respective changes in shear stress along the zone of friction are comparatively low being below 5 MPa in the continental and below 10 MPa in the oceanic plate. An increase in gravity seems to have a stronger influence on shear stress than a corresponding decrease. The reason might be that it is numerically more difficult to generate a lithostatic stress distribution for higher gravity.

On including linear thermal expansion into the model (fig. B.1d) the results hardly change but nevertheless the changes are systematic. With an increasing thermal expansion coefficient the continental crust subsides increasingly with the maximum amount of subsidence occurring at about 500 km distance from the trench. Large parts of the elevation of the oceanic crust are not affected by thermal expansion but from 350 km east of the trench, the crust is uplifted by a similar amount as observed in the continental crust. The changes in shear stress throughout the zone of friction are below 1 MPa along the continental plate. At 50 km distance to the trench, i.e. at about the center of the frictional coupling zone, the stress is not affected at all, while towards the updip limit a small increase and towards the downdip limit a similar decrease is observed. Along the oceanic plate the shear stress is generally increased with the maximum observed west of the trench, i.e. towards the western model boundary. Within the oceanic part of the zone of friction the shear stress differences are about twice the maximum magnitudes observed throughout the continental plate. The position of maximum increase in shear stress is almost the same as in the continental plate, however, from this position it is continuously decreasing to zero towards the downdip limit of the zone.

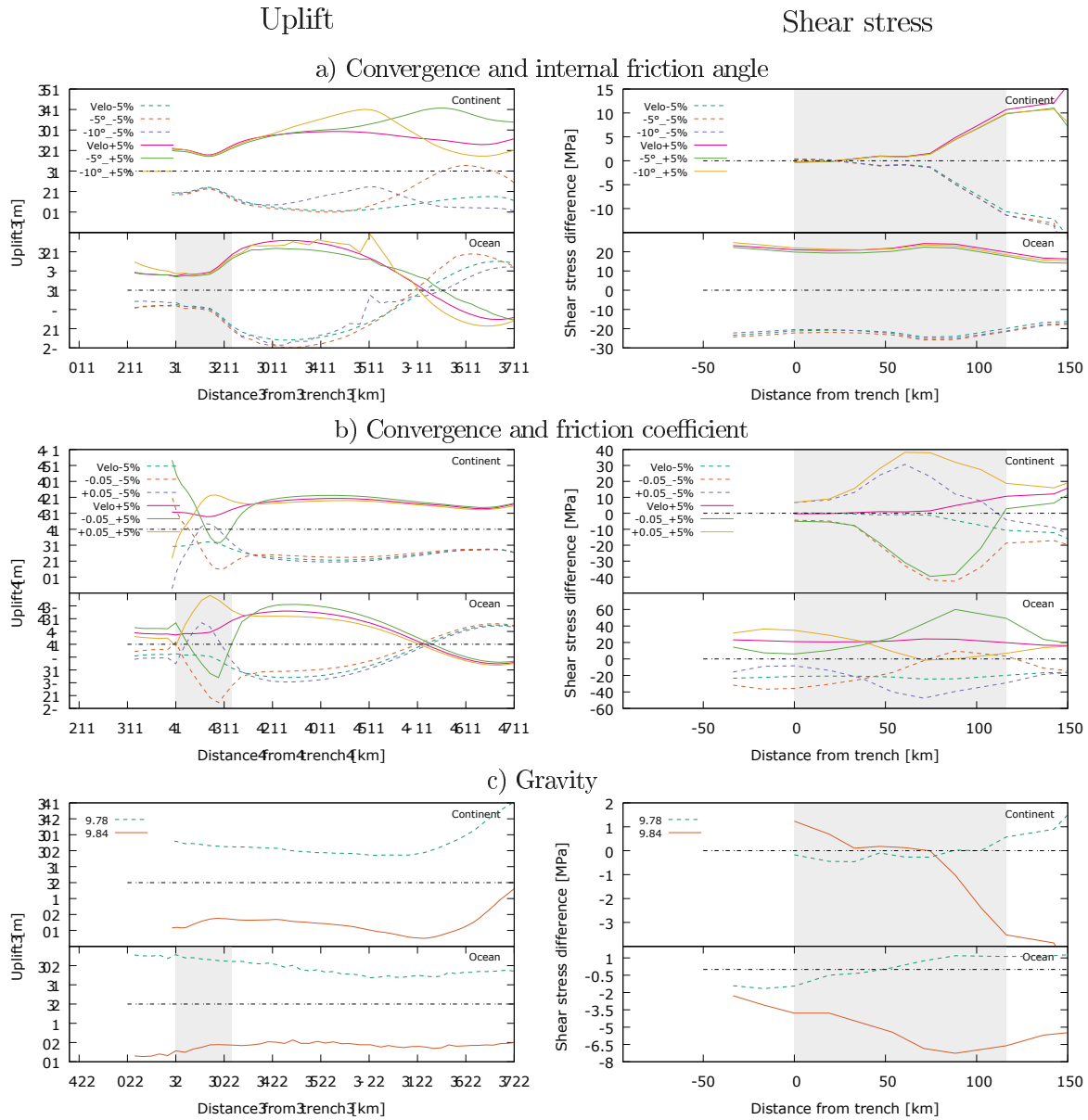


Figure B.1: Model differences along the continental (top panel) and oceanic (bottom panel) plate in vertical displacement (left column) and shear stress (right column). The convergence velocity is simultaneously varied with either the angle of internal friction (a) or the friction coefficient (b). The velocity changes are $\pm 5\%$, the angle of internal friction has been decreased by 5° and the friction coefficient is varied by ± 0.05 . The gravitational acceleration ranges between 9.78 and 9.84 m/s^2 (c) and the linear thermal expansion coefficient between $1.0 \cdot 10^{-3} \text{ 1/K}$ and $6.0 \cdot 10^{-3} \text{ 1/K}$ (d). The grey shaded area marks the zone of friction.

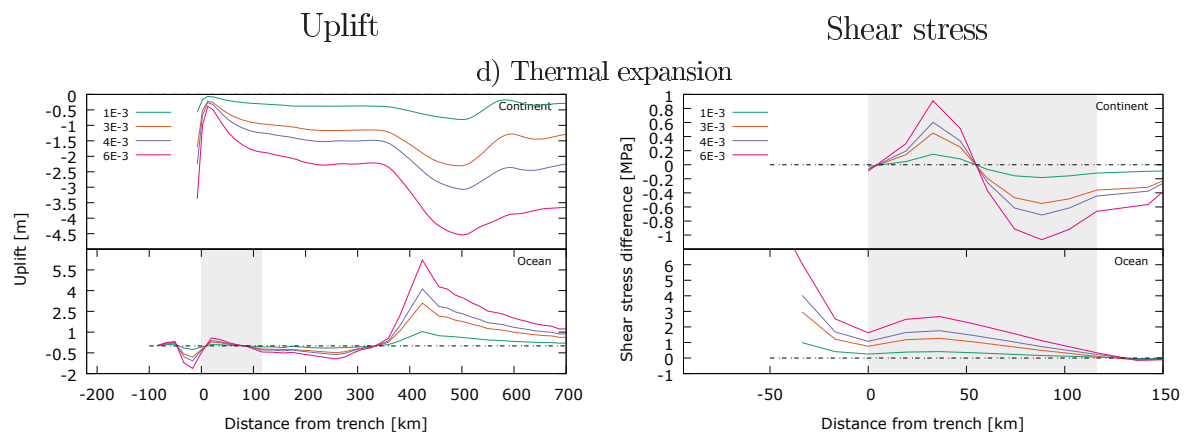
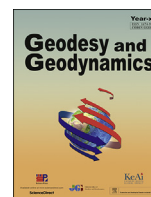


Figure B.2: Continued from previous page

C Finite element modelling of the geodynamic processes of the central Andes subduction zone: A Reference Model

Chris Salomon

Published in: *Geodesy and Geodynamics* 9 (2018), 246-251



Finite element modelling of the geodynamic processes of the Central Andes subduction zone: A Reference Model

Chris Salomon

Institute of Geosciences, General Geophysics and Structural Geology Group, Friedrich Schiller University, 07749, Jena, Burgweg 11, Germany



ARTICLE INFO

Article history:

Received 25 April 2017

Received in revised form

13 November 2017

Accepted 27 November 2017

Available online 3 February 2018

Keywords:

Abaqus

Andes subduction zone

Finite element modelling

Thermomechanical models

Viscoplasticity

ABSTRACT

This paper presents preliminary results of three-dimensional thermomechanical finite-element models of a parameter study to compute the current temperature and stress distribution in the subduction zone of the central Andes (16°S–26°S) up to a depth of 400 km, the bottom of the asthenosphere. For this purpose a simulation running over c. 50,000 years will be realized based on the geometry of a generic subduction zone and an elasto-viscoplastic Drucker–Prager rheology. The kinematic and thermal boundary conditions as well as the rheological parameters represent the current state of the study area. In future works the model will be refined using a systematic study of physical parameters in order to estimate the influence of the main parameters (e.g. viscosity, fault friction, velocity, shear heating) on the results of the reference model presented here. The reference model is kept as simple as possible to be able to estimate the influence of the parameters in future studies in the best possible way, whilst minimizing computational time.

© 2018 Institute of Seismology, China Earthquake Administration, etc. Production and hosting by Elsevier B.V. on behalf of KeAi Communications Co., Ltd. This is an open access article under the CC BY-NC-ND license (<http://creativecommons.org/licenses/by-nc-nd/4.0/>).

1. Introduction

Subduction zone seismicity accounts for more than two thirds of the global seismic energy release (e.g. [1]) and is hence an integral process accompanying the recycling of lithospheric plates along convergent plate boundaries. Most subduction earthquakes, including ‘giant’ ones with moment magnitudes $M_w \geq 8$, are generated at intermediate depths between c. 50 and 300 km (e.g. [2]) and many factors have been invoked to explain their occurrence. The classical concept is that ‘embrittlement’ induced by metamorphic dehydration reactions in the downgoing slab is responsible for triggering intermediate depth seismic dislocations (e.g. [3,4]). ‘Embrittlement’ essentially means overcoming the brittle shear strength along the plate interface in the presence of a free fluid phase that counteracts normal stresses on faults. As an

alternative mechanism for intermediate depth earthquakes, John et al. [5] and Prieto et al. [6] suggested that, in the absence of free fluids, so-called ‘thermal runaway melting’, induced by self-localising shear heating, might control seismogenic material failure at differential stresses lower than those needed for inducing brittle failure along a plate interface. Recent ideas on the occurrence of $M_w \geq 8$ earthquakes also suggested that they occur preferably along accretionary, i.e. addition of material to the overriding plate, rather than erosive margins, i.e. removal of material from the upper plate basement ([7] and references therein), implying that the presence vs. absence of large volumes of low-friction pelitic material constituting a trench-fill effectively controls fault friction and, in turn, when dynamically weakened during seismic slip (‘velocity weakening’ [8,9]), the size of the ruptured area and hence the seismic moment released along a subduction plate interface. However, the Tohoku $M_w = 9.1$ earthquake of 2011 [10] occurred along a clearly erosive subduction segment, rendering the notion of [7] at best contradictory and suggesting that possibly still other factors exert a control on where seismicity localises. The above examples highlight how strongly interdependent the rheological, geometrical and physical parameters (such as pressure, temperature as well as the presence vs. absence of volatile phases) are in triggering subduction zone seismicity; and controversies still prevail.

E-mail address: chris.salomon@uni-jena.de.

Peer review under responsibility of Institute of Seismology, China Earthquake Administration.



Production and Hosting by Elsevier on behalf of KeAi

<https://doi.org/10.1016/j.geog.2017.11.007>

1674-9847/© 2018 Institute of Seismology, China Earthquake Administration, etc. Production and hosting by Elsevier B.V. on behalf of KeAi Communications Co., Ltd. This is an open access article under the CC BY-NC-ND license (<http://creativecommons.org/licenses/by-nc-nd/4.0/>).

This study addresses the temperature-dependent rheology of subducting lithosphere by means of three-dimensional numerical finite-element modelling using an elasto–viscoplastic rheological model, to obtain a better understanding of the stress distribution in subduction zones. For this the subduction zone of the central Andes (16°S–26°S) serves for scaling and calibration of the models (Fig. 1).

2. The reference model

The FEM (finite-element method) is a widely used technique among geophysicists for simulating plate movements along subduction zones. Using three-dimensional geometries enables us to do most realistic numerical simulations. However, these computations require very robust and time efficient numerical algorithms. This work therefore makes use of the FEM package Abaqus 6.14–2 [12], which is a widely accepted tool for a large range of applications in geosciences (e.g. www.ruhr-uni-bochum.de/geoqus). For testing purposes the geometry of the current reference model describes a generic subduction zone using a two-dimensional cross section extended to the third dimension (Fig. 2).

The size of the reference model is 650 km from west to east (x-direction), 400 km from south to north (z-direction) and 400 km from bottom to top (y-direction), resulting in approx. 27,000 three-

dimensional finite elements. The boundary conditions (Fig. 3) applied include a constant gravitational acceleration acting on the overall model, the horizontal motion of the oceanic and continental plate, slab pull on the subducting slab into the lower earth's mantle, as well as friction including shear heating between the oceanic and continental crust along the plate interface (Fig. 3). During the simulation the eastern and western boundary elements of the asthenosphere are only allowed to move in vertical direction (y) while fixing the horizontal directions (x and z) to account for surrounding materials. The bottom of the oceanic as well as continental asthenosphere is completely fixed. The applied plate velocities are typical mean values according to Refs. [13–15]. The coefficient of friction along the plate interface was set to $\mu = 0.3$ down to the base of the upper plate Moho and $\mu = 0$ between the Moho and the lithosphere–asthenosphere boundary (LAB). This strict simplification was necessary for obtaining a numerically stable solution. In developing the models further, the author intends to modify the downdip variation in a more realistic way. The simulations intend to reflect the current subduction state before the occurrence of large earthquakes. To achieve this a dynamically stable equilibrium must be realized, which is considered to appear after c. 100,000 years of simulation duration. Due to this long-term effects such as erosion, convection and serpentinization in the forearc mantle are to be neglected.

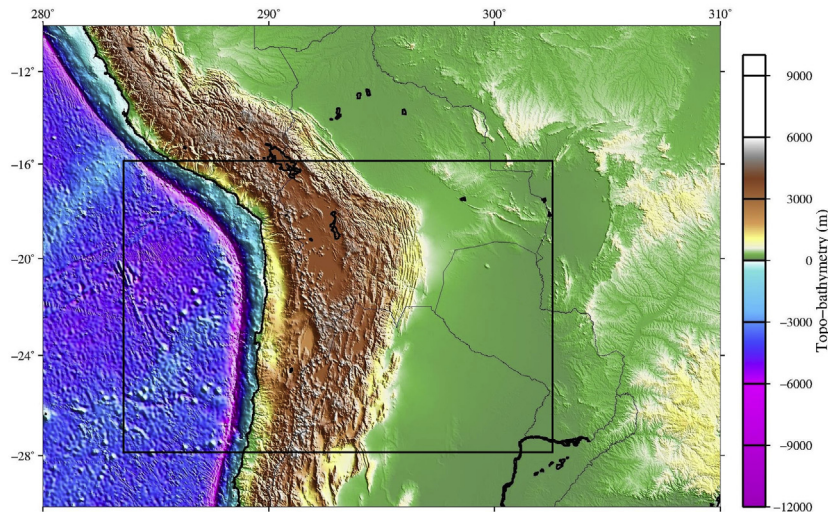


Fig. 1. Topographic map of the central Andes (conceived with Submap 4.0 [11]). The rectangle denotes the study area.

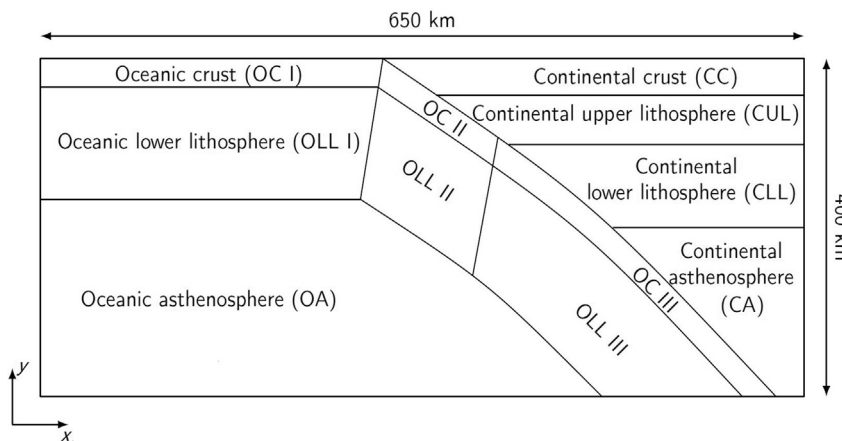


Fig. 2. Different parts of the model and their abbreviations.

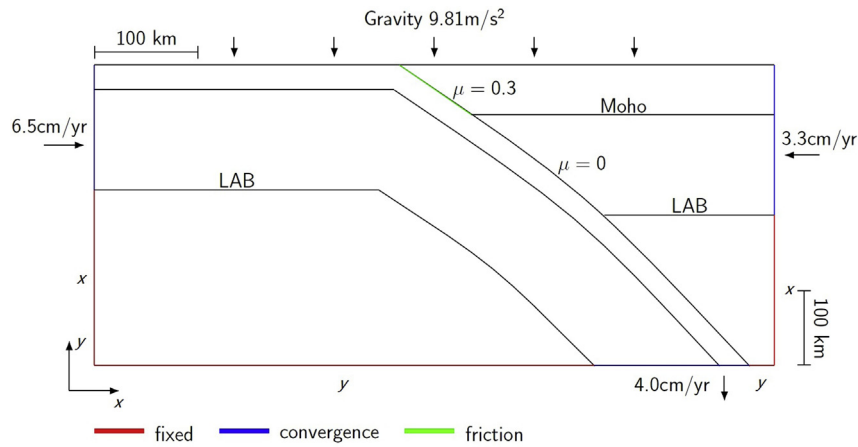


Fig. 3. 2D cross section through the reference model illustrating boundary conditions applied. LAB marks the lithosphere-asthenosphere boundary, Moho marks the Mohorovičić discontinuity.

To successfully integrate gravity a lithostatic stress distribution at the beginning of the simulation is needed. This is computed by additionally fixing the eastern and western boundary elements of the lithosphere in horizontal direction (x, z) and the bottom slab elements in vertical direction (y) for that gravity alone, as a load acting on all elements, determines the plate movements. On assuming an overall elastic rheology a static stress simulation is done by using the implicit FE method Abaqus/Standard (Fig. 4a). Furthermore a static temperature model is needed to complete the starting conditions. For simplicity this is currently achieved by defining isothermals for the top surface temperature (275 K), the continental Moho and lower boundary of the oceanic lithosphere (1523 K) as well as the bottom temperature (1873 K) of the model. In most studies a temperature of 1523 K is used at the LAB instead of at the continental Moho. But for the present model a constant temperature gradient of 30 °C/km was assumed resulting in the Moho temperature presented in this work. In upcoming models this value will be decreased to study its effect on the model results. Again Abaqus/Standard is used to compute the resulting temperature distribution (Fig. 4b).

The material parameters needed to define the rheology of the subduction model are taken from published theoretical and experimental studies and are presented in Table 1. For simplicity the Poisson ratio ν was set to a constant value of 0.25 although it is known to vary between c. 0.23 and 0.27 [16,17]. The thermal expansion coefficient α is also known to vary between c. $2 - 4 \cdot 10^{-5} \text{K}^{-1}$ [18,19] but for this reference model it was set to 0.0K^{-1} in the overall model, to later be able to investigate its

influences on the model results. The definitions of all parameters except the Poisson ratio ν , Young's modulus E and density ρ are given in section 3.

3. Drucker–Prager viscoplasticity

For describing thermo-mechanical processes one has to solve the coupled system of conservation equations for momentum (1), mass (2) and energy (3).

$$\frac{dv_i}{dt} = \frac{\partial \sigma_{ik}}{\partial x_k} + g_i \quad (1)$$

$$\frac{\partial \rho}{\partial t} + \frac{\partial}{\partial x_i} (\rho v_i) = 0 \quad (2)$$

$$\rho C_p \frac{dT}{dt} = \frac{\partial}{\partial x_i} \left(\kappa \frac{\partial T}{\partial x_i} \right) + \sigma_{ik} \frac{\partial v_k}{\partial x_i} + h \quad (3)$$

In these equations Einstein's summation rule applies and x_i are the coordinates, t –time, v_i –velocities, σ_{ik} –stress tensor, g_i –gravity vector, $d/dt = \partial/\partial t + (\partial/\partial x_j) \cdot (dx_j/dt)$ –material time derivative, ρ –mass density, C_p –heat capacity, κ –heat conductivity, h –internal heat generation.

By additionally solving the constitutive equations, which relate the stress to the strain tensor, all quantities are defined. This work uses a temperature dependent elasto-viscoplastic Drucker–Prager

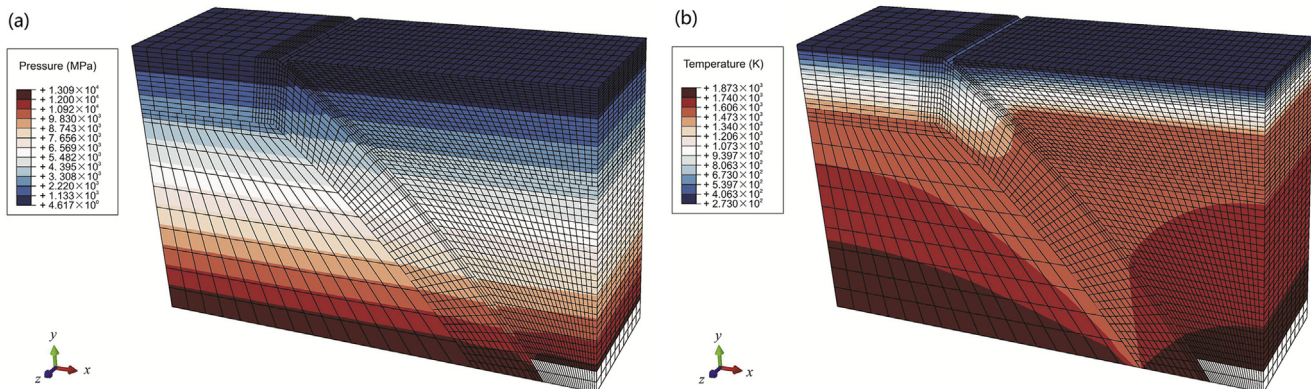


Fig. 4. Starting conditions of the model: a) Lithostatic pressure distribution in units of 1 MPa b) Static temperature distribution in units of 1 K.

Table 1

Rheological parameters used for the reference model: ν –Poisson ratio, ρ –mass density, E –Young's modulus, ϕ –internal friction angle, ϕ_{dil} –dilatancy angle, C –cohesion, N –power law coefficient, η_0 –viscosity at $T = T_{melt}$, E_A –creep activation energy, T_{melt} –melting temperature, α –linear thermal expansion coefficient, C_p –heat capacity, κ –heat conductivity; for abbreviations see Fig. 2.

Parameter	Model part	Value	Reference	
ν	All	0.25	–	
ρ (kg/m ³)	CC	2700	[20]	
	CUL	3100		
	CLL	3320		
	CA	3430		
	OC I	3050		
	OLL I	3350		
	OC II	3300		
	OLL II	3400		
	OC III	3550		
	OLL III	3500		
	OA	3410		
	E (GPa)	CC	80	[21]
		CUL	100	
		CLL	150	
		CA	180	
OC I		98		
OLL I		183		
OC II		116		
OLL II		186		
OC III		125		
OLL III		191		
OA		205		
ϕ		ALL	40°	[22]
		ALL	10°	[23]
ϕ_{dil}		CC, CUL, OC I–III	20	[19,22,24]
		CLL, OLL I–III	30	
	CA, OA	50		
N	CC, CUL, CLL, OC I–III, OLL I–III	2.5	[22,25,26]	
	CA, OA	3.5		
η_0 (MPa)	CC, CUL	10 ²⁵	[26]	
	CLL	10 ²²		
	OC I–II	10 ²⁷		
	OLL I–III	10 ²⁴		
	CA, OA	10 ²¹		
E_A (kJ mol ⁻¹)	CC, CUL, OC I–II	150	[22,26]	
	OLL I–III, OC III	180		
	CLL, CA, OA	520		
T_{melt} (K)	CC, CUL, OC I–III, OLL I–III	2000	[27,28]	
	CLL, CA, OA	2170		
α (K ⁻¹)	All	0.0	–	
C_p (J kg ⁻¹ K ⁻¹)	CC, CUL, CLL, OC I–III, OLL I–III	1.7	[29,30]	
	CA, OA	1.3		
κ (W m ⁻¹ K ⁻¹)	CC, CUL, CLL, OC I–III, OLL I–III	2.5	[22,30]	
	CA, OA	6.9		

relationship in which the total strain rate is decomposed into elastic, viscoplastic and temperature components:

$$\dot{\epsilon}_{ik} = \dot{\epsilon}_{ik}^{(e)} + \dot{\epsilon}_{ik}^{(v)} + \alpha \dot{T} \quad (4)$$

The viscoplastic components are defined by

$$\dot{\epsilon}_{ik}^{(v)} = \dot{\lambda} \frac{\partial g}{\partial \sigma_{ik}} \quad (5)$$

with the Lagrangian multiplier $\dot{\lambda}$ and the plastic potential function $g = 2 \sin \phi_{dil} / [\sqrt{3} (3 - \sin \phi_{dil})] I_1 + \sqrt{J_2}$. $\dot{\lambda}$ is computed according to Alfano et al. [31] by solving the consistency condition

$$df = d\Phi^{-1}(\dot{\lambda}) \quad (6)$$

with $f = 2 \sin \phi / [\sqrt{3} (3 - \sin \phi)] I_1 + \sqrt{J_2}$ –Drucker–Prager yield function, $\Phi^{-1}(\dot{\lambda})$ –inverse of Perzyna [32] overstress function $\Phi(f) = \sigma_{eff} (f / \sigma_Y)^N = \langle \eta \dot{\lambda} \rangle$, $\langle \dots \rangle$ –McCauley brackets, ϕ_{dil}

–dilatancy angle, ϕ –angle of internal friction, σ_{eff} –effective viscoplastic stress, $\sigma_Y = 6C \cos \phi / (3 - \sin \phi)$ –yield stress, C –cohesion, N –power law coefficient, $\eta = \eta_0 \exp[E_A / R(1/T - 1/T_{melt})]$ –viscosity, η_0 –viscosity at $T = T_{melt}$, E_A –creep activation energy, R –universal gas constant, T_{melt} –melting temperature, α –linear thermal expansion coefficient, I_1 –mean normal stress, J_2 –second invariant of deviatoric stress tensor.

On assuming isotropic linear elasticity the increments of the stress components are therefore given by

$$d\sigma_{ij} = C_{ijkl} (d\epsilon_{kl} - d\epsilon_{kl}^{(v)}) \quad (7)$$

with the elastic stiffness tensor

$$C_{ijkl} = \mu (\delta_{ik} \delta_{jl} + \delta_{il} \delta_{jk}) + \lambda_L \delta_{ij} \delta_{kl} \quad (8)$$

where μ –shear modulus or second Lamé constant, λ_L –first Lamé constant, δ_{ik} –identity tensor. Given the Poisson ratio ν and Young's modulus E the Lamé constants are defined by

$$\mu = \frac{E}{2(1 + \nu)} \quad (9)$$

$$\lambda_L = \frac{E\nu}{(1 + \nu)(1 - 2\nu)} \quad (10)$$

4. Results and discussion

The final simulation of the current subduction reference model is carried out using the explicit FE method Abaqus/Explicit. Due to this several 100,000's of time increments are needed to achieve a dynamic equilibrium state of the subduction process. Numerical uncertainties, e.g. because of round off errors, can thus have a significant influence on the stability of the computation. Currently the models are able to simulate up to c. 50,000 years of subduction using the conditions described in section 2, which is considered to be the minimum simulation duration to achieve the acquired equilibrium.

Fig. 5 shows the final distributions of the translation in y-direction (i.e. upwards), the pressure, the heat flux as well as the temperature in the model. The model has an increasing downwards translation towards the trench (Fig. 5a). Especially the subducting oceanic plate is downlifted by several kilometres. According to observations of subduction zones in reality one would expect uplifting of near trench regions of the continental instead of downlifting of the oceanic plate. The reasons for this discrepancy maybe the steep dipping angle of the slab of up to 50° at the bottom of the model, the low depth of the continental Moho of 40 km or the missing horizontal component of the slab pull velocity.

The pressure gradient of the continental plate has decreased during the subduction process in comparison to the gradient of the oceanic plate (Fig. 5b). In the bottom of the model, between slab and continental asthenosphere, a high pressure has been accumulated. The left and right ends of the model are dominated by boundary effects. In the uppermost layer of the continental crust tensional stresses are present around the trench. This is considered to be another boundary effect because no corresponding uplifting can be seen in Fig. 5a. The oceanic asthenosphere is dominated by artefacts due to the coarse mesh. Nevertheless the overall pressure is lower than in the continental asthenosphere.

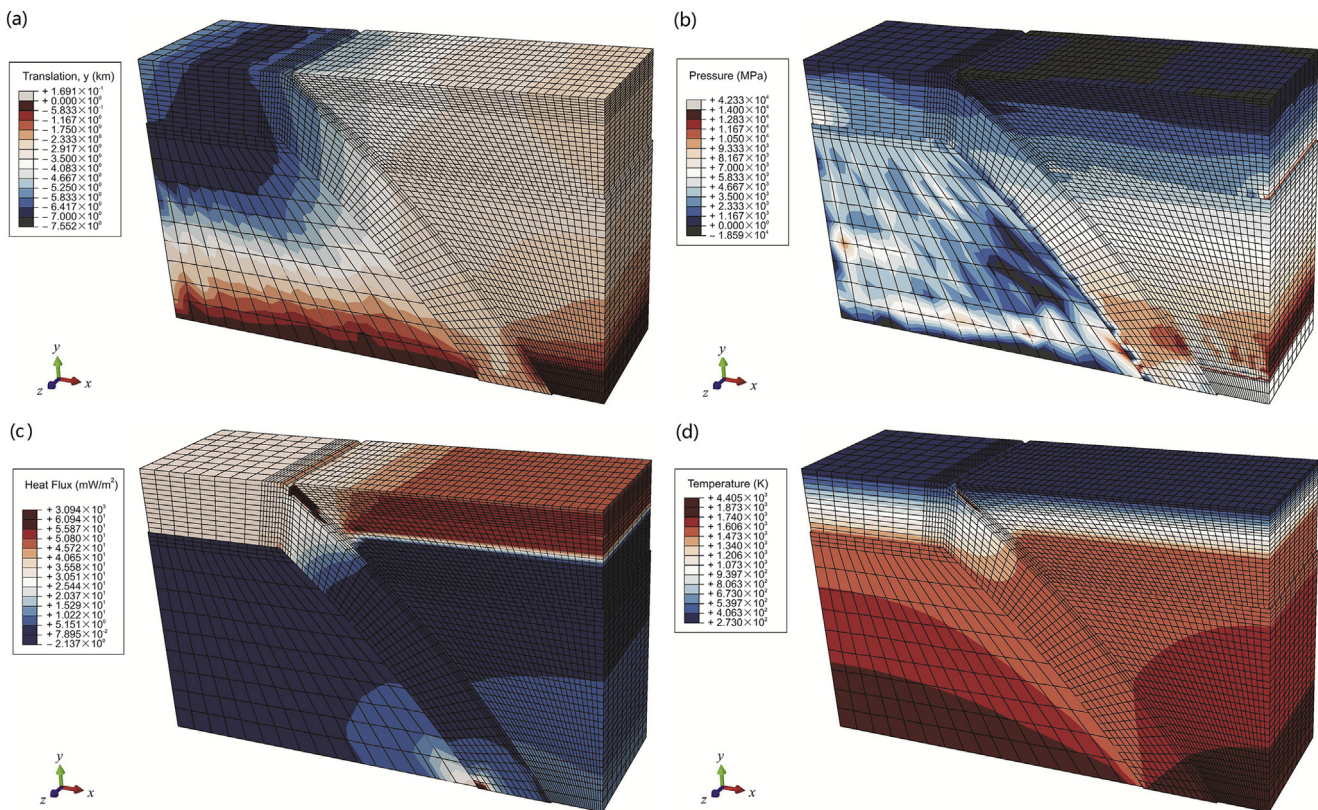


Fig. 5. Final results of the simulation after c. 50,000 years of subduction. a) Translation in y - (i.e. upwards-) direction in units of 1 km; b) pressure in units of 1 MPa; c) heat flux magnitude in units of 1 mW/m^2 ; d) temperature in units of 1 K.

The heat flux magnitude (Fig. 5c) in the oceanic lithosphere is nearly constant while in the continental lithosphere the heat flux down to the Moho is significantly higher than in the lower lithosphere. Below the depth of the Moho the heat flux decreases significantly in the lower continental lithosphere and overall asthenosphere but with increasing depth a slight increase can be observed. Furthermore around the frictional coupling zone of the plates a very high heat flux is observed being two magnitudes higher than in the surroundings, resulting in an increase of the temperature to more than 4000 K (Fig. 5d) which is clearly the effect of shear heating in the model. These values are quite high and have to be improved in future model runs by adjusting different parameters such as the friction coefficient and the dipping angle of the slab. All remaining parts of the temperature distribution have hardly changed in comparison to the starting distribution (Fig. 4b).

5. Conclusions

In this work a three-dimensional thermomechanical finite element model of a generic subduction zone was created using available data from the subducting region around the central Andes. The current reference model already includes all boundary conditions as well as material properties belonging to the desired region and shows a dynamically stable subduction process of up to c. 50,000 years. Despite the geologically short simulation duration the model already starts being in a dynamically stable equilibrium including shear heating in the frictional coupling zone, a change in the pressure gradient between the continental and oceanic plate and vertical movements of the plates. Thus the model presented here can already serve as reference model for a subsequent

parameter study. During this parameters such as the dipping angle of the slab, the friction coefficient, downdip limit, viscosity and the amount of shear heating will be refined to estimate their influence on the results of the reference model.

Acknowledgements

I greatly appreciate Thomas Jahr, Kamil Ustaszewski and the structural geology team for very constructive discussions and helpful hints related to this work.

References

- [1] J.F. Pacheco, L.R. Sykes, Seismic moment catalog of large shallow earthquakes, 1900 to 1989, *Bull. Seism. Soc. Am.* 82 (3) (1992) 1306–1349.
- [2] S. Stein, M. Wysession, *An Introduction to Seismology, Earthquakes and Earth Structure*, Blackwell Publishing, 2005.
- [3] H.W. Green, H. Houston, The mechanics of deep earthquakes, *Ann. Rev. EPS* 23 (1) (1995) 169–213.
- [4] B.R. Hacker, S.M. Peacock, G.A. Abers, S.D. Holloway, Subduction factory 2. Are intermediate-depth earthquakes in subducting slabs linked to metamorphic dehydration reactions?, *J. Geophys. Res.* 108 (B1) (2003), <https://doi.org/10.1029/2001JB001129>.
- [5] T.S. John, S. Medvedev, L.H. Rupke, T.B. Andersen, Y.Y. Podladchikov, H. Austrheim, Generation of intermediate-depth earthquakes by self-localizing thermal runaway, *Nat. Geosci.* 2 (2) (2009) 137–140, <https://doi.org/10.1038/ngeo419>.
- [6] G.A. Prieto, M. Florez, S.A. Barrett, G.C. Beroza, P. Pedraza, J.F. Blanco, E. Poveda, Seismic evidence for thermal runaway during intermediate-depth earthquake rupture, *Geophys. Res. L.* 40 (23) (2013) 6064–6068, <https://doi.org/10.1002/2013GL058109>.
- [7] S.L. Bilek, The role of subduction erosion on seismicity, *Geology* 38 (2010) 479–480, <https://doi.org/10.1130/focus052010.1>.
- [8] C. Marone, C.H. Scholz, The depth of seismic faulting and the upper transition from stable to unstable slip regimes, *Geophys. Res. L.* 15 (6) (1988) 621–624, <https://doi.org/10.1029/GL0151006p00621>.

- [9] K. Ujje, G. Kimura, Earthquake faulting in subduction zones: insights from fault rocks in accretionary prisms, *Prog. EPS* 1 (1) (2014) 7, <https://doi.org/10.1186/2197-4284-1-7>.
- [10] D. Bassett, D.T. Sandwell, Y. Fialko, A.B. Watts, Upper-plate controls on coseismic slip in the 2011 magnitude 9.0 Tohoku-Oki earthquake, *Nature* 531 (2016) 92–96, <https://doi.org/10.1038/nature16945>.
- [11] A. Heuret, S. Lallemand, Plate motions, slab dynamics and back-arc deformation, *PEPI* 149 (2005) 31–51, <https://doi.org/10.1016/j.pepi.2004.08.022>.
- [12] Dassault Systèmes SIMULIA, 2017. <http://www.3ds.com>. (Accessed 20 April 2017).
- [13] E. Norabuena, L. Leffler-Griffin, A. Mao, T. Dixon, S. Stein, I.S. Sacks, L. Ocola, M. Ellis, Space geodetic observations of nazca-south America convergence across the central Andes, *Science* 279 (1998) 358–362, <https://doi.org/10.1126/science.279.5349.358>.
- [14] E. Kendrick, M. Bevis, R. Smalley Jr., B. Brooks, R.B. Vargas, E. Lauría, L.P.S. Fortes, The Nazca-South America Euler vector and its rate of change, *J. S. Am. Earth Sci.* 16 (2003) 125–131, [https://doi.org/10.1016/S0895-9811\(03\)00028-2](https://doi.org/10.1016/S0895-9811(03)00028-2).
- [15] E.M. Syracuse, P.E. van Keken, G.A. Abers, The global range of subduction zone thermal models, *PEPI* 183 (2010) 73–90, <https://doi.org/10.1016/j.pepi.2010.02.004>.
- [16] I. Koulakov, S.V. Sobolev, G. Asch, P- and S-velocity images of the lithosphere-aesthenosphere system in the Central Andes from local-source tomographic inversion, *Geophys. J. Int.* 167 (2006) 106–126, <https://doi.org/10.1111/j.1365-246X.2006.02949.x>.
- [17] Y. Dzierma, W. Rabbel, M. Thorwart, I. Koulakov, H. Wehrmann, K. Hoernle, D. Comte, Seismic velocity structure of the slab and continental plate in the region of the 1960 Valdivia (Chile) slip maximum – insights into fluid release and plate coupling, *EPSL* 331–332 (2012) 164–176, <https://doi.org/10.1016/j.epsl.2012.02.006>.
- [18] J.C. Afonso, G. Ranalli, M. Fernandez, Thermal expansivity and elastic properties of the lithospheric mantle: results from mineral physics of composites, *PEPI* 149 (2005) 279–306, <https://doi.org/10.1016/j.pepi.2004.10.003>.
- [19] A.Y. Babeyko, S.V. Sobolev, High-resolution numerical modelling of stress distribution in visco-elasto-plastic subducting slabs, *Lithos* 103 (2008) 205–216, <https://doi.org/10.1016/j.lithos.2007.09.015>.
- [20] A. Tassara, H.-J. Götze, R. Hackney, Three-dimensional density model of the Nazca plate and the Andean continental margin, *J. Geophys. Res.* 111 (B9, 404) (2006), <https://doi.org/10.1029/2005JB003976>.
- [21] ANCORP Working Group, Seismic imaging of a convergent continental margin and plateau in the central Andes (Andean Continental Research Project 1996/ANCORP'96), *J. Geophys. Res.* 108 (B7) (2003) 2328, <https://doi.org/10.1029/2002JB001771>.
- [22] G. Ranalli, *Rheology of the Earth*, Chapman and Hall, 1995. ISBN: 0-412-54670-1.
- [23] P.N. Michelis, Work-softening and hardening behaviour of granular rocks, *Rock Mech.* 14 (1981) 187–200, <https://doi.org/10.1007/BF01250450>.
- [24] S. Zeumann, *3D Finite Element Modelling of the Central Andean Subduction Zone with Realistic Geometry* (Ph.D. Thesis), Friedrich-Schiller University, Jena, Germany, 2013.
- [25] P. Wu, Deformation of an incompressible viscoelastic flat earth with power-law creep: a finite element approach, *Geophys. J. Int.* 108 (1992) 35–51, <https://doi.org/10.1111/j.1365-246X.1992.tb00837.x>.
- [26] S.-I. Karato, Rheology of the deep upper mantle and its implications for the preservation of the continental roots: a review, *Tectonophysics* 482 (2010) 82–98, <https://doi.org/10.1016/j.tecto.2009.04.011>.
- [27] L.M. Barron, *Thermodynamic multicomponent silicate equilibrium phase calculations*, *Am. Mineral.* 57 (1972) 809–823.
- [28] D.C. Presnall, M.J. Walter, Melting of forsterite, Mg₂SiO₄, from 9.7 to 16.5 GPa, *J. Geophys. Res.* 98 (B11) (1993) 19777–19783, <https://doi.org/10.1029/93JB01007>.
- [29] R.G. Berman, L.Y. Aranovich, Optimized standard state and solution properties of minerals: 1. Model calibration for olivine, orthopyroxene, cordierite, garnet and ilmenite in the system FeO-MgO-CaO-Al₂O₃-TiO₂-SiO₂, *Contrib. Mineral. Petrol.* 126 (1996) 1–24, <https://doi.org/10.1007/S004100050232>.
- [30] A.G. Whittington, A.M. Hofmeister, P.I. Nabelek, Temperature-dependent thermal diffusivity of the Earth's crust and implications for magmatism, *Nature* 458 (2009) 319–321, <https://doi.org/10.1038/nature07818>.
- [31] G. Alfano, F. De Angelis, L. Rosati, General solution procedures in elasto/viscoplasticity, *Comput. Meth. Appl. Mech. Eng.* 190 (2001) 5123–5147, [https://doi.org/10.1016/S0045-7825\(00\)00370-4](https://doi.org/10.1016/S0045-7825(00)00370-4).
- [32] P. Perzyna, *Fundamental problems in viscoplasticity*, *Red. Adv. Appl. Mech.* 9 (1966) 243–377.



Chris Salomon, 2007 to 2013 Friedrich-Schiller-University Jena (FSU), Physics Diploma
2013–2014 research assistant at Institute of Geosciences FSU (IGW)
Since 2014 PhD candidate at IGW.

Acknowledgements

First of all, I want to thank my supervisors Thomas Jahr and Kamil Ustaszewski for spending their time for numerous discussions. Their support and suggestions helped to improve this work a lot. I thank them together with the colleagues of the working groups of Applied and General Geophysics and Structural Geology for providing a nice working environment.

Furthermore, I thank Christoph Grützner for his participations in some of the discussions and all of his hints and suggestions. This work has really benefitted of them.

I am thankful to Corné Kreemer for providing his data from the GSRM project as well as Kasper Fischer and Mishel Zucko for their hints related to Abaqus.

Finally I want to thank my parents, family and friends for their support and motivation over all those years.

Selbständigkeitserklärung

Ich erkläre, dass ich die vorliegende Arbeit selbständig und unter Verwendung der angegebenen Hilfsmittel, persönlichen Mitteilungen und Quellen angefertigt habe.

Ort, Datum

Chris Salomon